

## Structure, magnetism and excitations in some Mn-based magnetocaloric effect compounds

Michael Gottschlich





Forschungszentrum Jülich GmbH  
Peter Grünberg Institut (PGI)  
Streumethoden (PGI-4 / JCNS-2)

# **Structure, magnetism and excitations in some Mn-based magnetocaloric effect compounds**

Michael Gottschlich

Schriften des Forschungszentrums Jülich  
Reihe Schlüsseltechnologien / Key Technologies

Band / Volume 62

---

ISSN 1866-1807

ISBN 978-3-89336-874-7



Bibliographic information published by the Deutsche Nationalbibliothek.  
The Deutsche Nationalbibliothek lists this publication in the Deutsche  
Nationalbibliografie; detailed bibliographic data are available in the  
Internet at <http://dnb.d-nb.de>.

Publisher and  
Distributor:                   Forschungszentrum Jülich GmbH  
                                  Zentralbibliothek  
                                  52425 Jülich  
                                  Tel:     +49 2461 61-5368  
                                  Fax:     +49 2461 61-6103  
                                  Email:  zb-publikation@fz-juelich.de  
  www.fz-juelich.de/zb

Cover Design:                Grafische Medien, Forschungszentrum Jülich GmbH

Printer:                        Grafische Medien, Forschungszentrum Jülich GmbH

Copyright:                    Forschungszentrum Jülich 2013

Schriften des Forschungszentrums Jülich  
Reihe Schlüsseltechnologien / Key Technologies, Band / Volume 62

D 82 (Diss., RWTH Aachen University, 2013)

ISSN 1866-1807  
ISBN 978-3-89336-874-7

The complete volume is freely available on the Internet on the Jülicher Open Access Server (JUWEL)  
at [www.fz-juelich.de/zb/juwel](http://www.fz-juelich.de/zb/juwel)

Neither this book nor any part of it may be reproduced or transmitted in any form or by any  
means, electronic or mechanical, including photocopying, microfilming, and recording, or by any  
information storage and retrieval system, without permission in writing from the publisher.

# Zusammenfassung

Der magnetokalorische Effekt bewirkt das Kühlen oder Erwärmen eines Materials aufgrund des Einflusses eines angelegten magnetischen Feldes. Dieser Mechanismus bietet unter Verwendung von günstigen und umweltfreundlichen Materialien ein alternatives Kühlverfahren, das ohne das mechanische Bewegen von Partikeln funktioniert. Aus diesem Grund ist er Gegenstand aktueller Forschungsthemen. Der magnetokalorische Effekt wird mit dem Messen (oder Berechnen) der Entropie-änderung charakterisiert.

Polykristalline Proben der Zusammensetzungen  $\text{Mn}_{5-x}\text{Fe}_x\text{Si}_3$   $x=0,1,2,3,4$  und ein Einkristall der Verbindung  $\text{Mn}_{5-x}\text{Fe}_x\text{Si}_3$   $x=0$  wurden hergestellt, um den magnetokalorischen Effekt in diesen Materialien zu untersuchen. Alle Proben wurden mit Magnetisierungsmessungen charakterisiert, wobei ferro- und antiferromagnetisches Verhalten diagnostiziert wurde. Diffraktogramme wurden auf dem time-of-flight Pulverdiffraktometer POWGEN an der Spallationsquelle im Oak Ridge National Laboratory aufgenommen, um die magnetischen Strukturen der Materialien zu untersuchen. Inelastische Neutronenstreuexperimente wurden an dem Einkristall  $\text{Mn}_{5-x}\text{Fe}_x\text{Si}_3$   $x=4$  auf dem thermischen 3-Achsen-Spektrometer 2T1 im Laboratoire Léon Brillouin durchgeführt, um die dynamischen Eigenschaften zu analysieren.

Die verfeinerten Daten, die bei Raumtemperatur an den Proben  $\text{Mn}_{5-x}\text{Fe}_x\text{Si}_3$   $x=0,1,2,3,4$  an POWGEN aufgenommen wurden, bestätigen, dass die Struktur der Einheitszelle mit hexagonaler Symmetrie beschrieben werden kann. Dies stimmt mit veröffentlichten Resultaten überein. Anomalitäten wurden in verschiedenen kristallographischen Parametern als Funktion des Fe-Gehalts der Proben entdeckt.

Die bei Temperaturen zwischen 70K und 90K an der Komposition  $\text{Mn}_{5-x}\text{Fe}_x\text{Si}_3$   $x=0$  aufgenommenen Diffraktogramme konnten mit einer orthorhombischen antiferromagnetischen Struktur verfeinert werden. Unterhalb des antiferromagnetischen Phasenübergangs bei 62K wurde die beste Verfeinerung mit einer monoklinen Einheitszelle durchgeführt. Ausserdem hat diese Struktur einen schwachen ferromagnetischen Charakter, der unter dem Einfluss eines angelegten magnetischen Feldes aufgehoben wird. Dieser Mechanismus bewirkt vermutlich die negative Entropie-änderung in dieser Zusammensetzung.

Die Auswertung der Diffraktogramme, die in der ferromagnetischen Phase von  $\text{Mn}_{5-x}\text{Fe}_x\text{Si}_3$   $x=4$  aufgenommenen wurden, legen ein unterschiedliches Verhalten der magnetischen Atome auf den beiden kristallographischen Plätzen dar (der dritte wird von Si besetzt). Dieses Verhalten hat vermutlich einen starken Einfluss auf die Entropieänderung in diesem Material.

Phononenzweige in der Dispersionsrelation von  $\text{Mn}_{5-x}\text{Fe}_x\text{Si}_3$   $x=4$  verlaufen anisotropisch, was auf die hexagonale Struktur zurückgeführt wird.

Um den Effekt von Fe und Mn auf die Entropieänderung zu analysieren, wurde die Komposition  $\text{Mn}_{5-x}\text{Fe}_x\text{Si}_3$   $x=4$  mit Co dotiert (jeweils für Fe oder Mn). Die Auswertungen der Pulverdiffraktogramme, welche auf POWGEN aufgenommen wurden, belegen die Anwesenheit von mindestens einer Fremdphase in jeder Probe. Ähnlich wie in dem Fall von  $\text{Mn}_{5-x}\text{Fe}_x\text{Si}_3$   $x=4$ , haben auch Verfeinerungen an den Co-dotierten Materialien verschiedene Verhalten der magnetischen Momente der Atome auf den von Mn/Fe/Co besetzten Plätzen ergeben.

# Abstract

The magnetocaloric effect causes the cooling or heating of a material due to the influence of an applied magnetic field. This mechanism provides an alternative technique for cooling, when using cheap and environment friendly materials. Heating and cooling takes place without moving any mechanical parts. Therefore, this effect attracts the attention of many scientific studies. The magneto caloric effect is characterized by the entropy change.

Polycrystalline samples of the compositions  $\text{Mn}_{5-x}\text{Fe}_x\text{Si}_3$   $x=0,1,2,3,4$  and a single crystal of the composition  $\text{Mn}_{5-x}\text{Fe}_x\text{Si}_3$   $x=4$  were prepared in order to analyze the magnetocaloric effect in those materials. All samples were characterized with magnetization measurements. Ferro- and antiferromagnetic behaviour could be detected. Diffraction patterns were taken on the time-of-flight powder diffractometer POWGEN at the Spallation Neutron Source (SNS), Oak Ridge National Laboratory to analyze the magnetic structures of the compounds. Inelastic neutron data were collected on the single crystal  $\text{Mn}_{5-x}\text{Fe}_x\text{Si}_3$   $x=4$  on the thermal neutron triple axis spectrometer 2T1 at Laboratoire Léon Brillouin to investigate the dynamic properties.

The refined data taken on samples  $\text{Mn}_{5-x}\text{Fe}_x\text{Si}_3$   $x=0,1,2,3,4$  on POWGEN at room temperature confirm the hexagonal structure. This has already been reported in literature. Anomalies could be identified in several crystallographic parameters as function of the Fe-content of the samples

Diffraction patterns taken on sample  $\text{Mn}_{5-x}\text{Fe}_x\text{Si}_3$   $x=0$  between the phase transitions at 70K and 90K could be refined with an orthorhombic unit cell including antiferromagnetism. Below the phase transition at 62K the best refinements could be performed using a monoclinic unit cell. Also, the structure seems to exhibit weak ferromagnetism, which can be annihilated with an applied magnetic field. This mechanism is proposed to cause the negative magnetocaloric effect in this compound.

The analysis of diffraction patterns taken in the ferromagnetic phase of  $\text{Mn}_{5-x}\text{Fe}_x\text{Si}_3$   $x=4$  indicate different behaviours of the magnetic atoms occupying the two crystallographic positions (the third is occupied by Si). This property is proposed to influence significantly the entropy in this material.

Phonon branches in the dispersion relation of  $\text{Mn}_{5-x}\text{Fe}_x\text{Si}_3$   $x=4$  are anisotropic, which is due to the hexagonal structure.

In order to investigate the effect of Fe and Mn on the change of the entropy the composition  $\text{Mn}_{5-x}\text{Fe}_x\text{Si}_3$   $x=4$  was doped with Co (for Mn and Fe). The analysis of the diffraction patterns which were taken on POWGEN identified at least one impurity phase in every sample. Different behaviours of the magnetic moments of the atoms in these compounds could also be verified, which is similar to the composition  $\text{Mn}_{5-x}\text{Fe}_x\text{Si}_3$   $x=4$ .

# Contents

<b>1 Motivation</b>	<b>7</b>
1.1 The magneto caloric effect (MCE)	7
1.1.1 The magneto caloric effect (MCE) and why it is useful for application	7
1.1.2 How the magneto caloric effect works	8
1.2 Why the system $Mn_{5-x}Fe_xSi_3$ is a good candidate for studies	10
1.3 The idea of modifying the MCE in $Mn_{5-x}Fe_xSi_3$ $x=4$ : Co-doping	11
1.3.1 Inelastic neutron scattering: The key role for MCE-investigations	12
<b>2 Basics of MCE and neutron scattering</b>	<b>13</b>
2.1 The MCE	13
2.1.1 Measuring the MCE	13
2.2 Basics of diffraction	14
2.2.1 Bragg's law	14
2.2.2 Scattering amplitude	15
2.2.3 Neutron scattering	16
2.2.4 Basics of powder diffraction	16
2.2.5 Constant wave length (CW) instruments	17
2.2.6 Time-of-flight (TOF) instruments	19
2.2.7 Single crystal versus powder diffraction	20
2.3 Performing refinements with Jana2006	20
2.3.1 Basic parameters	20
2.3.2 Calculating Intensities	21
2.3.3 Profile function	22
2.3.4 Rietveld refinement	22
2.3.5 Quality of refinements	23
2.4 Inelastic neutron scattering	24
2.4.1 Magnons	26
<b>3 Instruments</b>	<b>27</b>
3.1 Experiments on POWGEN	27
3.2 Experiments on HB2A	28
3.3 Experiments on 2T1	29
<b>4 Preparation and quality check of samples</b>	<b>31</b>
4.1 Synthesis of polycrystalline samples: "kalter Schwebetiegel"	31
4.2 Details of prepared samples	32
4.3 Synthesis of single crystal $Mn_{5-x}Fe_xSi_3$ $x=4$	34
<b>5 Magnetization measurements</b>	<b>37</b>
5.1 Experimental conditions	37

5.2	$\text{Mn}_{5-x}\text{Fe}_x\text{Si}_3$ . . . . .	37
5.3	$\text{Mn}_{1-x}\text{Co}_x\text{Fe}_4\text{Si}_3$ and $\text{MnFe}_{4-x}\text{Co}_x\text{Si}_3$ . . . . .	43
5.4	Summary . . . . .	45
<b>6</b>	<b>DSC measurements to unravel the MCE</b>	<b>47</b>
6.1	Experimental conditions . . . . .	47
6.2	Inverse MCE in $\text{Mn}_{5-x}\text{Fe}_x\text{Si}_3$ $x=0$ . . . . .	47
6.3	MCEs of $\text{Mn}_{5-x}\text{Fe}_x\text{Si}_3$ $x=4$ , $\text{Mn}_{1-x}\text{Co}_x\text{Fe}_4\text{Si}_3$ and $\text{MnFe}_{4-x}\text{Co}_x\text{Si}_3$ . . . . .	49
6.4	Summary . . . . .	50
<b>7</b>	<b>Neutron powder diffraction</b>	<b>51</b>
7.1	Analysis of diffraction patterns . . . . .	51
7.2	$\text{Mn}_{5-x}\text{Fe}_x\text{Si}_3$ . . . . .	51
7.2.1	Experimental setups . . . . .	51
7.2.2	Details of refinements performed on diffraction patterns taken on sample $\text{Mn}_{5-x}\text{Fe}_x\text{Si}_3$ $x=0$ . . . . .	52
7.2.3	Details of refinements performed on diffraction patterns taken on samples $\text{Mn}_{5-x}\text{Fe}_x\text{Si}_3$ $x>0$ . . . . .	56
7.2.4	Results of refinements of $\text{Mn}_{5-x}\text{Fe}_x\text{Si}_3$ at room temperature . . . . .	61
7.2.5	Results of refinements of $\text{Mn}_{5-x}\text{Fe}_x\text{Si}_3$ $x=0$ at low temperatures . . . . .	68
7.2.6	Results of refinements on $\text{Mn}_{5-x}\text{Fe}_x\text{Si}_3$ $x=4$ at low temperatures . . . . .	75
7.3	$\text{Mn}_{1-x}\text{Co}_x\text{Fe}_4\text{Si}_3$ and $\text{MnFe}_{4-x}\text{Co}_x\text{Si}_3$ . . . . .	86
7.3.1	Experimental setups . . . . .	86
7.3.2	Details of refinements . . . . .	86
7.3.3	Results of refinements . . . . .	98
7.4	Co-doped materials and $\text{Mn}_{5-x}\text{Fe}_x\text{Si}_3$ $x=4$ at room temperature . . . . .	110
7.5	Summary . . . . .	112
<b>8</b>	<b>Inelastic neutron scattering</b>	<b>115</b>
8.1	Experimental setups and data treatment . . . . .	115
8.2	Analyzing and fitting of data . . . . .	116
8.2.1	Phonons . . . . .	116
8.2.2	Magnons . . . . .	120
8.3	Results . . . . .	121
8.3.1	Dispersion relation . . . . .	121
8.3.2	Properties of the magnon . . . . .	122
8.4	Summary . . . . .	125
<b>9</b>	<b>Conclusion</b>	<b>127</b>
<b>10</b>	<b>Outlook</b>	<b>129</b>
10.1	Further modification of the MCE in $\text{Mn}_{5-x}\text{Fe}_x\text{Si}_3$ $x=0$ and $\text{Mn}_{5-x}\text{Fe}_x\text{Si}_3$ $x=4$ with doping . . . . .	129
10.1.1	$\text{Mn}_{5-x}\text{Fe}_x\text{Si}_3$ $x=0$ . . . . .	129
10.1.2	$\text{Mn}_{5-x}\text{Fe}_x\text{Si}_3$ $x=4$ . . . . .	129
10.2	Neutron diffraction measurements on single crystals . . . . .	130
10.3	Inelastic neutron scattering measurements . . . . .	130

---

<b>11 Acknowledgements</b>	<b>133</b>
<b>A Additional Information</b>	<b>135</b>
A.1 The Curie Weiss law . . . . .	135
A.2 Profile function for TOF-diffraction . . . . .	135
A.3 Instrumental parameters for CW-diffraction . . . . .	136
A.4 Magnetic form factors . . . . .	136
A.5 X-ray powder diffraction . . . . .	137
A.6 Magnetization measurements . . . . .	139
A.7 Neutron powder diffraction . . . . .	140
A.7.1 $\text{Mn}_{5-x}\text{Fe}_x\text{Si}_3$ . . . . .	140
A.7.2 Details of the refinement performed on sample $\text{MnFe}_{4-x}\text{Co}_x\text{Si}_3$ $x=0.2$ at 310K . . . . .	140
<b>B Bibliography</b>	<b>159</b>
<b>C List of Figures</b>	<b>167</b>
<b>D List of Tables</b>	<b>173</b>
<b>E Index</b>	<b>175</b>



# Chapter 1

## Motivation

### 1.1 The magneto caloric effect (MCE)

#### 1.1.1 The magneto caloric effect (MCE) and why it is useful for application

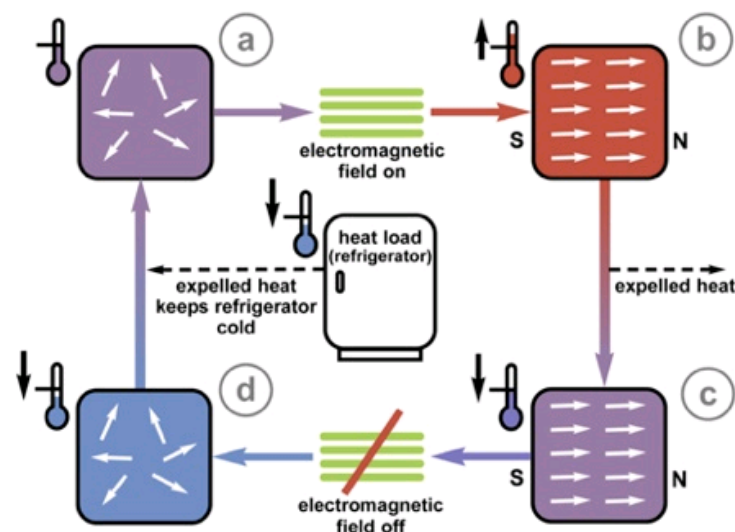


**Figure 1.1:** Performance of one cycle of magnetocaloric refrigeration taken from [1]. a) A magnetic material is considered. b) When applying a magnetic field the magnetic moments align. Therefore the magnetic part of the entropy is decreased forcing the lattice part of the entropy to increase keeping the change of total entropy zero for an adiabatic process. This causes the material to heat up. c) After heat is pumped away due to the contact with an external heat bath the material's temperature is lower and reaches the equilibrium value of step a. Notice that magnetic moments are still aligned. d) The magnetic field is turned off causing the magnetic part of the entropy to rise and the lattice part to decrease. Finally the temperature of the material is lower than at the beginning a). From here on the material can be used for the performance of more cycles of cooling.

The magnetocaloric effect (MCE) was first discovered in 1881 in Fe [2] and is based on the influence of an applied magnetic field on a magnetic material. Using this effect for adiabatic



cooling was first proposed in the 1920s by [3, 4]. It holds the potential to be periodically used for cycles of refrigerating or heating. In figure 1.1 the performance of one cycle of cooling is illustrated.

The cooling/heating process takes place without moving any mechanical parts. They are less harmful to environment than vapor-compression refrigerators, since they do not use chlorofluorocarbons and hydrofluorocarbons as working fluids which cause damage to the ozone layer [5, 6].

In 1997 it was demonstrated that a magnetic refrigerator is a competitive cooling technology in comparison to vapor cycle refrigerator [7]. Cooling powers exceeding 500 Watts could be produced by magnetic refrigeration using a 5T field which is a record performance. There are a lot of applications [8] for the MCE ranging from supermarket to household refrigerators [9].

A lot of scientific groups have investigated materials in the context of the MCE [10, 11]. The giant magnetocaloric effect (GMCE) was discovered in 1997 in  $Gd_5Si_2Ge_2$  [12]. Since then a lot of papers have been published about investigations of rare earth compounds such as  $R_5T_4$  compounds (R=rare earth element and T=Si, Ge or Sn) [10]. For example,  $Gd_5(Si_{1-x}Ge_x)_4$  has been reported in numerous papers (for example [13–15]). Substitutions of Gd in  $Gd_5Si_4$  were reported in [16]. Near room temperature magnetic refrigerators attracted the attention of a lot of scientific groups [17–21].

## 1.1.2 How the magneto caloric effect works

Literature distinguishes between two different types of MCE materials: The first order (FOMT) and second order (SOMT) magnetic phase transition compounds [22]. In both cases the name refers to the nature of phase transition which can be of first or second order.

In FOMT materials, the maximum magnetic entropy change is principally defined by the difference in the entropies of the low- and high-magnetic field phases. Here, the MCE can be quantified with heat capacity measurements.  $Gd_5(Si_{1-x}Ge_x)_4$ , MnAs and  $Mn_{5-x}Fe_xSi_3$   $x=0$ , for example, are FOMT [10].

In SOMT compounds, the largest MCE is proposed when the heat capacity of a material is strongly influenced by the magnetic field providing the option to calculate the MCE with magnetization measurements.  $Mn_{5-x}Fe_xSi_3$   $x=4$  and  $Mn_5Ge_3$  are SOMT materials [10].

The value of the MCE strongly depends on magnetic and structural ordering which influences the entropy of the system. The total entropy change of a material can be written as summation of the lattice, the magnetic and the conduction-electron subsystem as presented in equation 1.1 [23]. Here, it is assumed that the magnetism originates from localized magnetic moments. The MCE is characterized by the isothermal magnetic entropy change  $\Delta S_m$  and the adiabatic temperature change  $\Delta T_{ad}$  [11], which are observed upon magnetic field changes.

$$\Delta S_{total} = \Delta S_l + \Delta S_m + \Delta S_e = 0 \quad (1.1)$$

$$\Delta S_m = \mu_0 \int_{H_i}^{H_f} \left( \frac{\partial M}{\partial T} \right) dH \quad (1.2)$$

$$\Delta T_{ad} = -\mu_0 \int_{H_i}^{H_f} \frac{T}{C_p(T, H)} \left( \frac{\partial M}{\partial T} \right) dH \quad (1.3)$$

The MCE is emanently high close to points of phase transitions as illustrated in figure 1.2. This is due to the fact that phase transitions influence the magnetization and therefore the magnetic part of the entropy (equations 1.2 and 1.3). Phase transitions can also influence the nuclear structure, which would in first place affect the lattice part of the entropy in equation 1.1. The GMCE in  $\text{Gd}_5\text{Si}_2\text{Ge}_2$  originates from structural and magnetic ordering taking place simultaneously [11]. In that case the entropy change of the system can be calculated with the specific heat [23]:

$$\Delta S_H = \int_{T_0}^T \left( \frac{c_p(T', B_f) - c_p(T', B_i)}{T'} \right) dT' \quad (1.4)$$

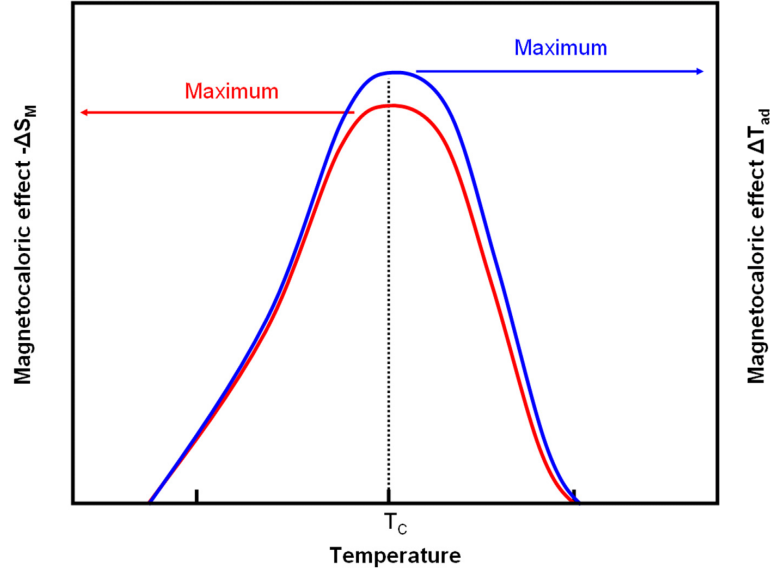


**Figure 1.2:** Schematic drawing of entropy change.

If the temperature derivative of the magnetization in equations 1.2 and 1.3 is negative, as is the case of ferromagnetic materials, the thermodynamic formulation of  $\Delta S_m$  and  $\Delta T_{ad}$  predicts  $\Delta S_m < 0$  and  $\Delta T_{ad} > 0$  (the direct MCE). In this case the sample heats up when the external magnetic field is applied adiabatically. On the other hand, an opposite effect occurs if the temperature derivative of the magnetization is positive. This predicts  $\Delta S_m > 0$  and  $\Delta T_{ad} < 0$ , the so-called inverse MCE. Here, the sample cools down when the external magnetic field is applied adiabatically.

The inverse MCE is actually less common and exists in diverse kinds of magnetic materials. However, it seems quite common in antiferromagnetic arrangements such as Ni-Mn-Sn alloys [24], for example. A large inverse MCE was reported in  $\text{Ni}_{50}\text{Mn}_{34}\text{In}_{16}$  [25]. The inverse MCE

in antiferromagnetic compounds is obviously associated with a modification of magnetic sublattices due to the influence of the applied magnetic field. This was first noted by [26] and [27] investigating Tutton salts.

## 1.2 Why the system $\text{Mn}_{5-x}\text{Fe}_x\text{Si}_3$ is a good candidate for studies

For large scale room temperature applications, investigations of materials in the context of the MCE compounds consisting of cheap and nontoxic elements seems to be accurate as a starting point. At least one of the elements should carry a magnetic moment, even though this does not for sure induce but increase chances for the compound to exhibit magnetic features. Furthermore, a flexible structure is proposed, too, since this could easily cause phase transitions. Atoms with magnetic moments should occupy atomic positions enabling strong magnetic interactions. This could be fulfilled with small distances between atoms with magnetic moments, or via nonmagnetic atoms carrying induced moments.

$\text{Mn}_{5-x}\text{Fe}_x\text{Si}_3$  fulfills all these conditions. Elements are cheap and Fe carries a magnetic moment. Hexagonal space group  $P6_3/mcm$  (193) includes two flexible atomic positions in  $\text{Mn}_{5-x}\text{Fe}_x\text{Si}_3$  [28]. A lot of materials which are investigated in the context of the MCE, especially with doping, crystallize in hexagonal space group  $P6_3/mmc$  [29]. MnAs, for example, crystallizes in hexagonal space group  $P6_3/mmc$  [30] and exhibits a coupled structural/magnetic FOMT [31, 32]. Substitution of Sb for As ( $\text{MnAs}_{1-x}\text{Sb}_x$ ) results in decreasing  $T_C$  and the change of entropy [33–35]. For  $x \geq 0.1$  the character in the vicinity of the MCE is changed from FOMT to SOMT.

The negative magnetic entropy change ( $-\Delta S_m$ ) of  $\text{Mn}_{5-x}\text{Fe}_x\text{Si}_3$   $x=0$  is proposed to be  $\sim -0.5$  J/kgK and the magnetic entropy change of  $\text{Mn}_{5-x}\text{Fe}_x\text{Si}_3$   $x=4$   $\sim 2$  J/kgK for magnetic field changes of 0T-2T [36]. For comparison the magnetic entropy change of the GMCE material  $\text{Gd}_5\text{Ge}_2\text{Si}_2$  is proposed to be 27 J/kgK [10].

Small distances between two neighbored atoms of  $2.4 \text{ \AA}$  could enable magnetic interactions in  $\text{Mn}_{5-x}\text{Fe}_x\text{Si}_3$ . The presence of two different atomic positions occupied by Mn and Fe [28] could induce a large magnetoelastic effect, as it is proposed in Mn-Fe-P-Si compounds [37].  $\text{Mn}_{5-x}\text{Fe}_x\text{Si}_3$  is reported to exhibit a rich phase diagram [28, 36, 38]. This family of materials has already been investigated in the context of the MCE [36] proposing a negative MCE for antiferromagnetic  $\text{Mn}_{5-x}\text{Fe}_x\text{Si}_3$   $x=0$  and direct MCEs for  $\text{Mn}_{5-x}\text{Fe}_x\text{Si}_3$   $x=3,4,5$ .

The structure of  $\text{Mn}_{5-x}\text{Fe}_x\text{Si}_3$   $x=0$  has already been analyzed with neutron scattering [28, 38–43] presenting results disagree to each other. To the best of the knowledge of the author of this thesis, details of the structure of ferromagnetic  $\text{Mn}_{5-x}\text{Fe}_x\text{Si}_3$   $x=4$  have not been published. In [28, 38] no diagrams presenting magnetic moments or lattice constants in dependence of temperature were published.

All these properties leave  $\text{Mn}_{5-x}\text{Fe}_x\text{Si}_3$  as a promising candidate for further studies.

## 1.3 The idea of modifying the MCE in $Mn_{5-x}Fe_xSi_3$ $x=4$ : Co-doping

hydrogen 1 H 1.0079																	helium 2 He 4.0026	
lithium 3 Li 6.941	beryllium 4 Be 9.0122											boron 5 B 10.811	carbon 6 C 12.011	nitrogen 7 N 14.007	oxygen 8 O 15.999	fluorine 9 F 18.998	neon 10 Ne 20.180	
sodium 11 Na 22.990	magnesium 12 Mg 24.305											aluminum 13 Al 26.982	silicon 14 Si 28.086	phosphorus 15 P 30.974	sulfur 16 S 32.065	chlorine 17 Cl 35.453	argon 18 Ar 39.948	
potassium 19 K 39.098	calcium 20 Ca 40.078	scandium 21 Sc 44.956	titanium 22 Ti 47.867	vanadium 23 V 50.942	chromium 24 Cr 51.996	manganese 25 Mn 54.938	iron 26 Fe 55.845	cobalt 27 Co 58.933	nickel 28 Ni 58.693	copper 29 Cu 63.546	zinc 30 Zn 65.39	gallium 31 Ga 69.723	germanium 32 Ge 72.61	arsenic 33 As 74.922	selecnium 34 Se 78.96	bromine 35 Br 79.904	krypton 36 Kr 83.80	
rubidium 37 Rb 85.468	strontium 38 Sr 87.62	yttrium 39 Y 88.906	zirconium 40 Zr 91.224	niobium 41 Nb 92.906	molybdenum 42 Mo 95.94	technetium 43 Tc [98]	ruthenium 44 Ru 101.07	rhodium 45 Rh 102.91	palladium 46 Pd 106.42	silver 47 Ag 107.87	cadmium 48 Cd 112.41	indium 49 In 114.82	tin 50 Sn 118.71	antimony 51 Sb 121.76	tellurium 52 Te 127.60	iodine 53 I 126.90	xenon 54 Xe 131.29	
cesium 55 Cs 132.91	barium 56 Ba 137.33	* 57-70	lanthanum 57 La 138.91	hafnium 58 Hf 178.49	tantalum 59 Ta 180.95	tungsten 60 W 183.84	rhenium 61 Re 186.21	osmium 62 Os 190.23	iridium 63 Ir 192.22	platinum 64 Pt 195.08	gold 65 Au 196.97	mercury 66 Hg 200.59	thallium 67 Tl 204.38	lead 68 Pb 207.2	bismuth 69 Bi 208.98	polonium 70 Po [209]	astatine 71 At [210]	radon 72 Rn [222]
francium 87 Fr [223]	radium 88 Ra [226]	* * 89-102	actinium 89 Ac [227]	thorium 90 Th 232.04	protactinium 91 Pa 231.04	uranium 92 U 238.03	neptunium 93 Np [237]	plutonium 94 Pu [244]	americium 95 Am [243]	curium 96 Cm [247]	berkelium 97 Bk [247]	californium 98 Cf [251]	einsteinium 99 Es [252]	fermium 100 Fm [257]	mendelevium 101 Md [258]	nobelium 102 No [259]		
		* Lanthanide series	lanthanum 57 La 138.91	cerium 58 Ce 140.12	praseodymium 59 Pr 140.91	neodymium 60 Nd 144.24	promethium 61 Pm [145]	samarium 62 Sm 150.36	europlum 63 Eu 151.96	gadolinium 64 Gd 157.25	terbium 65 Tb 158.93	dysprosium 66 Dy 162.50	holmium 67 Ho 164.93	erbium 68 Er 167.26	thulium 69 Tm 168.93	ytterbium 70 Yb 173.04		
		* * Actinide series	actinium 89 Ac [227]	thorium 90 Th 232.04	protactinium 91 Pa 231.04	uranium 92 U 238.03	neptunium 93 Np [237]	plutonium 94 Pu [244]	americium 95 Am [243]	curium 96 Cm [247]	berkelium 97 Bk [247]	californium 98 Cf [251]	einsteinium 99 Es [252]	fermium 100 Fm [257]	mendelevium 101 Md [258]	nobelium 102 No [259]		

Figure 1.3: Periodic table of elements taken from [44].

Once the MCE of base compound  $Mn_{5-x}Fe_xSi_3$   $x=4$  was measured and analyzed the question rises how the entropy change could be modified by substitution. In order to do a step by step approach, it is useful to first substitute only one element since doping several elements at the same time might cause complex results which cannot be understood that easily. Second, promising elements of the base compound have to be selected for doping. Third, another element which could replace the original one has to be chosen.

The base compound consists of Mn, Fe and Si. The MCE is linked to the magnetism. Literature reports about magnetic moments on atoms Mn/Fe [28, 39] but not on Si. Therefore, promising candidates for elements that could be substituted are Mn and Fe.

Addressing the third step, looking at the periodic table a neighboured 3d element of Mn or Fe can be a good choice. This is useful, since the addition of more than one electron to an atom could easily result in a new structure due to different bonding lengths.

Cr has a melting point of 2180K. This does not fit to the other elements (Mn has a melting point of 1519K and Fe of 1811K). Preparing samples with Mn, Fe and Cr would result in evaporation of Mn. Small evaporation effects are already noted for the synthesis of  $Mn_{5-x}Fe_xSi_3$  at the Forschungszentrum Juelich.

This makes Co (melting point is 1768K) a promising candidate for doping in the base compound. The saturation moment of a lot of compounds seem to be influenced by Co-doping. One interesting material is  $MnFe_{1-x}Co_xGe$ , for example, crystallizing in  $P6_3/mmc$  [45]. Saturation moment and entropy change increase with Co content for  $0 < x \leq 0.85$ . Another compound is  $Mn_{3-x}Co_xGaC$ . Here, the entropy change is decreased for small contents of Co [46]. Therefore, doping with Co seems to be a good starting point to modify the MCE.

### 1.3.1 Inelastic neutron scattering: The key role for MCE-investigations

Performing magnetization and neutron powder diffraction measurements seems to be quite reasonable, since the entropy change strongly depends on the magnetic properties of a sample. How can inelastic neutron scattering measurements push studies of the MCE?

It has already been mentioned in this work that the driving force of the MCE is the change between lattice, electronic and magnetic parts of entropy due to shifting the applied magnetic field on a sample (equation 1.1). This gives rise to questioning how those parts of the entropy are coupled with each other.

In [37] coupling between degrees of freedom of lattice and spin in magnetic materials is proposed to be useful for magnetic refrigeration. In [47] a simulation is presented. Here, energy transfer from quasimagnons to quasiphonons is proposed to induce a negative entropy change in ferromagnetic materials. Therefore, investigating the dynamics of the system could reveal the coupling of phonons and magnons. Such properties can be investigated with inelastic neutron scattering.

In [48] inelastic neutron scattering measurements were performed on  $\text{Er}_x\text{Pr}_{1-x}$   $x=0.6, 0.8$  to develop a theoretical model in order to investigate magnetothermal properties in the context of the MCE. They considered the crystalline electric field as carrier of the magnetic entropy in the pure lanthanide material and developed a theoretical model which can describe the magnetothermal properties of the system. However, when inelastic neutron scattering measurements were performed no magnetic field was applied. Still, field dependence of magnetic excitations (which is reported in  $\text{CeCu}_2$  [49], for example) could play an important role to analyze its influence on the MCE.

In order to perform inelastic neutron scattering measurements on a sample it is useful determine phonon and magnon branches first. Once phonon and magnon branches have been qualified, next step is to develop a theoretical model for the dynamics of the system. This model can be refined by comparison with the measured branches. In case points of coupling between phonons and magnons could not be determined with measurements they could be qualified by the calculations. Third, proposed points of phonon-magnon coupling in reciprocal space could be investigated with inelastic neutron scattering in dependence of the applied magnetic field.

## Chapter 2

# Basics of MCE and neutron scattering

## 2.1 The MCE

### 2.1.1 Measuring the MCE

There are a lot of ways to measure the MCE [23]. The temperature of the sample can directly be measured as it was done in [50–52] with setup used in [53]. Other techniques to measure the MCE are indirect such as performing magnetization or specific heat measurements. Making use of one of these methods, the MCE has finally to be calculated.

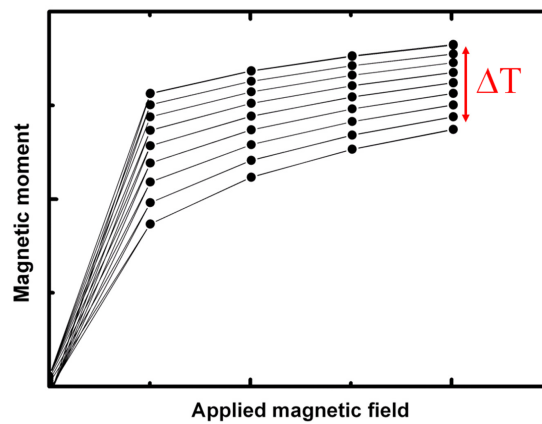


**Figure 2.1:** Schematic magnetization measurements performed at constant temperatures under varying the applied magnetic field.

In this thesis the MCE was always calculated indirectly by magnetization or by heat capacity measurements.

In figure 2.1 a schematic magnetization measurement is presented performed at constant temperature under varying the applied magnetic field. Magnetization measurements performed at

constant field under varying temperatures can also be used. The MCE can be determined by evaluating integral (1.2) numerically [23]:

$$\Delta S_m = \sum_i \left( \frac{M_i(T'_i, B_i) - M_i(T_i, B_i)}{T'_i - T_i} \right) \Delta B \quad (2.1)$$

When the MCE is determined with specific heat measurements, integral (1.4) has to be evaluated in the same way.

## 2.2 Basics of diffraction

### 2.2.1 Bragg's law

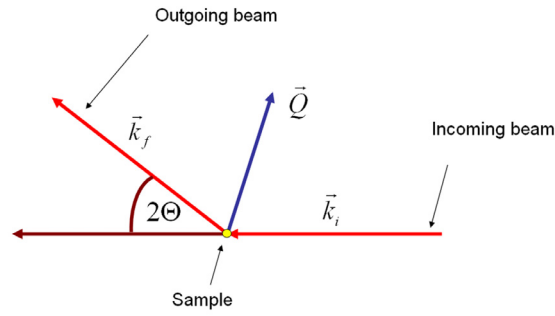


**Figure 2.2:** Schematic drawing of a diffraction experiment.

In a diffraction experiment an incoming beam of neutrons with wave vector  $\vec{k}_i$  interacts with the sample. For diffraction, the energy transfer between sample and radiation is zero by definition. The basic geometry is presented in figure 2.2. Because of this interaction outgoing neutrons are reflected into a certain direction having wave vector  $\vec{k}_f$ . The scattering vector is defined as  $\vec{Q} = \vec{k}_f - \vec{k}_i$ .

A simple equation calculating angles at which reflections are generated due to diffraction is the Bragg's law presented in equation (2.2). This equation only takes into account the wave length  $\lambda$  of the incoming beam and the geometry of the unit cell which describes symmetries of the sample.  $d$  is the interplanar distance.

$$n\lambda = 2d \sin\theta \quad (2.2)$$

Notice that equation 2.2 is only one-dimensional. This formula only considers the angle between incoming and outgoing beam and interplanar distances. The orientation of the sample (if it would be a single crystal) is not taken into account: Constructive interference can only take place, when certain angles  $\theta$  are chosen. The path difference between neighbouring waves has

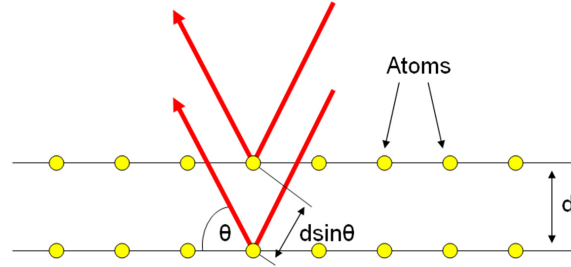


**Figure 2.3:** Schematic drawing of scattering at two planes of atoms with respect to Bragg's law.

to be an integer multiple  $n$  of the incident wave length. Under such conditions the scattered waves are in phase with each other and a diffraction maximum can be observed.

## 2.2.2 Scattering amplitude

When analyzing diffraction patterns, not only the angle at which reflections appear, but also intensities of diffraction maximums are crucial. When calculating intensities of reflections a formula takes into account which elements occupy which positions inside the unit cell is useful. Finally, a certain  $Q$ -vector has to be selected focusing on a certain point which fulfills Bragg's law. The amplitude of the scattered beam can be written as shown in equation (2.3).

$$f(\vec{Q}) = \frac{m}{2\pi\hbar^2} \int V(\vec{r}') e^{-i\vec{Q}\vec{r}'} d^3r' \quad (2.3)$$

$m$  is the mass and  $\hbar$  the Planck constant. The scattering potential  $V(\vec{r}')$  and the propagating wave  $e^{-i\vec{Q}\vec{r}'}$  are integrated over space. Notice that the scattering amplitude is proportional to the Fourier transform of the scattering potential  $V(\vec{r}')$  which is considered to be weak.

In solid state physics the scattering potential can be calculated with the structure factor:

$$F(\vec{Q}) = \sum_i f_i T_i(\vec{Q}) e^{-i\vec{Q}\vec{r}_i} \quad (2.4)$$

This equation holds for x-ray scattering where the summation depends on the atomic form factors  $f_i$  taking every atom in the unit cell into account. In the case of neutrons the scattering lengths  $b_i$  are used. Both, the structure factor and the scattering length depend on the element.

$$T_i(\vec{Q}) = \exp\left[-\frac{1}{2} \langle (\vec{Q}\vec{u}_i)^2 \rangle\right] \quad (2.5)$$

The temperature factor for harmonic oscillations can be calculated with Gaussian form as presented in equation (2.5) with the scattering vector  $\vec{Q}$  and the displacement  $\vec{u}$ . Notice that atomic



displacement parameters include thermal displacement, too, since displacement of an atom depends on temperature.

### 2.2.3 Neutron scattering

#### Nuclear scattering

Neutrons scatter from the nuclei of atoms in a sample. The scattering potential can be calculated with the Fermi pseudo potential, because the radius of a nucleus is much smaller than the wavelength of the neutrons.

$$V_{Fermi}(\vec{R}) = \frac{2\pi\hbar^2}{m} b\delta(\vec{r} - \vec{R}) \quad (2.6)$$

$\vec{R}$  is a point in real space and  $\vec{r}$  the location of the nuclei. The potential only depends on the strength of the interaction which is the scattering length  $b$ . The strength of the interaction is determined by the inner structure of the nucleus, respectively.

#### Magnetic scattering

Furthermore, the neutron carries a magnetic moment. Therefore magnetic ordering of samples causes the emergence of additional reflections, additional intensities and decrease of intensities. The magnetic part can be calculated with equation

$$\vec{M}(\vec{Q}) = -2\mu_B f_m(\vec{Q}) \sum_i e^{-i\vec{Q}\vec{R}_i} \vec{S}_i \quad (2.7)$$

Only magnetic moments aligned perpendicular to the scattering vector  $\vec{Q}$  give a contribution to the corresponding intensities.

### 2.2.4 Basics of powder diffraction

Single crystal diffraction might be considered superior to powder diffraction concerning investigating physical properties of materials. Still, powder diffraction measurements can be performed on a wide variety of materials [54], since not every compound is available in a form of a single crystal. A lot of materials are twinned (for example ferroelectrics [55]). Sometimes samples also contain phases of impurity. Furthermore, polycrystalline or powder samples can easily be investigated in a wide range of environments.

In neutron (or x-ray) powder diffraction measurements intensity is measured as a function of an angle. This also holds for polycrystalline materials. Such materials consist of many crystallites of varying size and orientation. Sometimes polycrystal samples are composed of crystallites with preferred orientation, which is due to the preparation. Basic drawing of such an experiment is presented in figure 2.4. An incoming neutron beam interacts with the sample. The

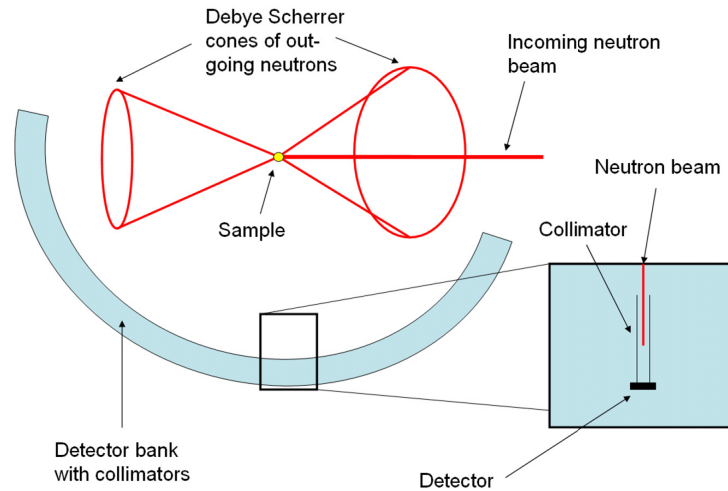


**Figure 2.4:** Schematic drawing of powder diffraction instrument.

outgoing beam is reflected according to Bragg's law. Therefore, a one dimensional diffraction pattern is generated. This is due to random orientation of crystallites in the sample. Concerning measurements performed on single crystals, where a three-dimensional (two angles) pattern, the Ewald-sphere, of the reciprocal space is taken. Here, points of reciprocal lattice are replaced by rings (also illustrated in figure 2.4) in a powder diffraction experiment.

Diffraction patterns taken on a sample can be analyzed by refining a model on the data. Making use of this method microstructural properties, for example nuclear structure, can be revealed. In case of neutron powder diffraction the magnetic structure can be determined, too.

Performing neutron powder diffraction measurements today (2012) two different types of instruments are available for such experiments. One class is the so-called constant wavelength (CW) and the other time of flight (TOF) instruments.

### 2.2.5 Constant wave length (CW) instruments

The phrase "CW" already reveals the characteristics of a CW-instrument. First, one wave length has to be selected of a continuous spectrum. For this, a monochromator is used. This monochromator consists of a set of single crystals which are aligned with the same orientation. The monochromator has to be aligned with respect to the outgoing wave length as shown in figure 2.5. Another wave length can be selected by simply rotating the monochromator. Every neutron with a certain wave length is reflected at a certain angle of the monochromator. This is due to the fact that the monochromator simply makes use of the nature of diffraction, i.e. scattering takes place with respect to Bragg's law. Finally only the wave length passes through the slit. Still, this is not only one single wave length, but a very small interval of wave lengths.

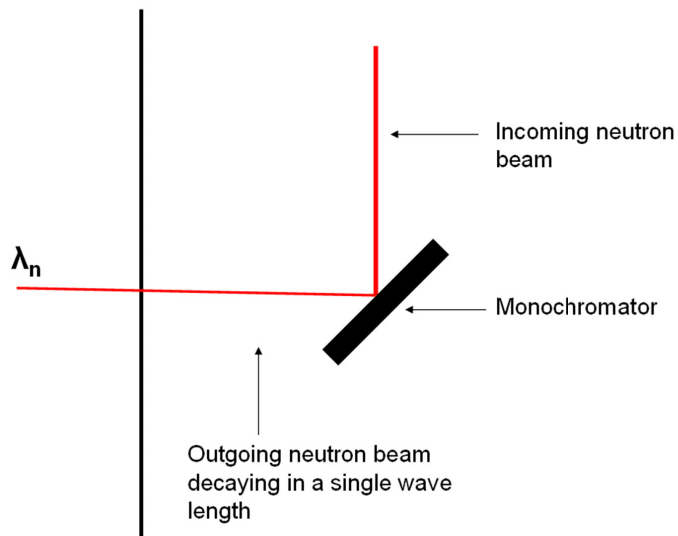


**Figure 2.5:** Schematic drawing of a monochromator.

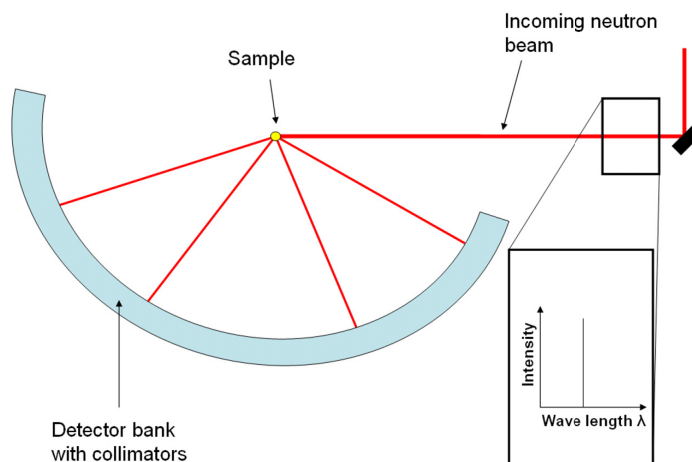


**Figure 2.6:** Schematic drawing of CW instrument used for powder diffraction.

In figure 2.6 the setup of a CW-instrument is illustrated. After having been reflected on the monochromator the beam interacts with the sample. With respect to Bragg's law the powder diffraction pattern emerges. Making use of Bragg's law the diffraction pattern can be transformed from  $\theta$ - to d-spacing.

### 2.2.6 Time-of-flight (TOF) instruments

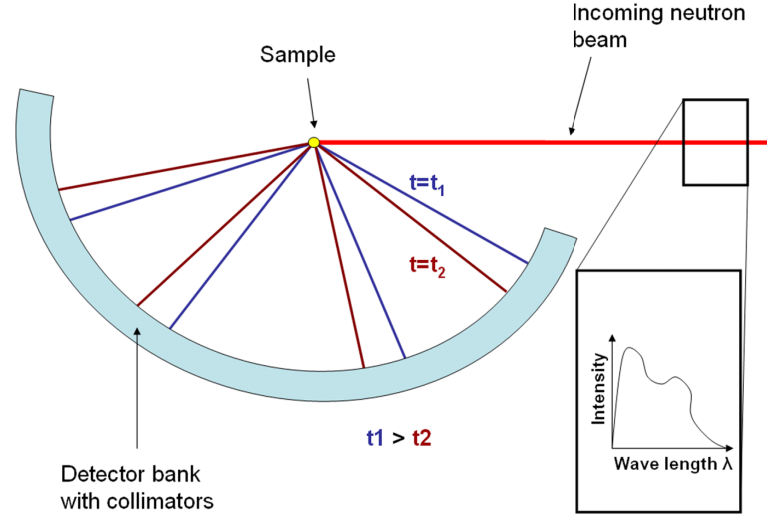


**Figure 2.7:** Schematic drawing of TOF instrument used for powder diffraction. Reflections impinging on the detector bank are drawn at two different time frames. In the right part a spectrum of intensities of a pulse of neutrons as a function of wave length is illustrated.

In the previous section the design of a CW-instrument was explained. Topic of this chapter is time-of-flight (TOF) instruments. Here pulses of neutrons interact with the sample. Basic setup of a TOF instrument used for powder diffraction measurements is presented in figure 2.7. In contrast to CW-instruments reflections move on the detectors as function of time (also indicated in figure). Therefore, the final diffraction pattern measures intensity as function of time while intensity as function of angle is measured on a CW-instrument.

The phrase instrumental parameters refers in the context of TOF-data to transformation between  $t$ - and  $d$ -spacing. For this transformation a polynomial of second degree (equation 2.8) with parameters zero,  $difc$  and  $difa$  or the formula developed by Jason Hodges (equation 2.12) could be used. Equation 2.8 is simply a Taylor series to the second differentiation. Therefore, it only works properly for small values of  $d$ . The formula developed by Jason Hodges by fitting experimental data [56] is complex dealing with parameters ZeroT, CT, AT, ZeroE, CE, Wcross and Tcross. Notice that these parameters have other names when using FullProf (table 2.1).

$$TOF = Zero + difc(d) + difa(d^2) \quad (2.8)$$

$$TOF_t = ZeroT + CT(d) + AT(d^2) \quad (2.9)$$

$$TOF_e = ZeroE + CE(d) \quad (2.10)$$

$$n_{cross} = 0.5erfc(Wcross(Tcross - (d^{-1}))) \quad (2.11)$$

$$TOF = n_{cross}TOF_e + (1 - n_{cross})TOF_t \quad (2.12)$$

Jana2006	ZeroT	CT	AT	ZeroE	CE	Wcross	Tcross
FullProf	Zerot	Dtt1t	Dtt2t	Zero	Dtt1	Width	x-cross

**Table 2.1:** Parameters of formula used for transformation from t- to d-spacing in Jana2006 and FullProf.

## 2.2.7 Single crystal versus powder diffraction

When diffraction measurements on a single crystal are performed one can take equation 2.3 into account. Here, intensities of reflections can only be equal to each other due to symmetry conditions of unit cell (or if equation 2.3 gives the same intensity by chance). Therefore one can consider the Ewald-sphere with points of intensities around the sample. This sphere is always generated with respect to the orientation of the single crystal, i.e. if the single crystal is rotated with the source of radiation around a certain axis (this axis has to pass through the single crystal, of course) the sphere will rotate around the very same axis, too.

This is in contrast to powder diffraction. In powder diffraction there is not only one, but a finite number of orientations. This means that rotating sample should not effect the diffraction pattern at all. Still, Bragg's law has to be valid. This gives rise to a diffraction pattern which only depends on one angle, i.e.  $\theta$ . So, performing diffraction measurements on powder samples implies losing information about reflections that overlap with and are not equivalent to each other.

## 2.3 Performing refinements with Jana2006

### 2.3.1 Basic parameters

Today diffraction patterns can be analyzed with the right software easily. No matter which software is used they all propose a model which is mathematically refined to measured data. All models consist of the following parts: Background treatment, instrumental parameters, scale factors, profile function for peak shape, absorption corrections, asymmetry, space group, lattice constants, atomic displacement, texture and atomic parameters.

For this dissertation all diffraction patterns were refined using program Jana2006. Program Fullprof was only used to analyze measurements to confirm structure. There are some manuals providing detailed mathematical and technical information concerning programs like Jana2006 [57–60].

Space group and lattice constants affect positions of peaks. As the space group describes symmetries of the unit cell of a sample, the same symmetries can be identified in diffraction patterns again. Lattice constants affect the position of peaks. Space group and lattice constants are directly included in scattering potential in equation (2.3).

The background of a diffraction pattern was treated by making use of so-called linear interpolation or of a polynom of a certain degree. For linear interpolation Jana2006 provides the option selecting background points by default, which can be modified manually.

### 2.3.2 Calculating Intensities

The total diffracted intensity of a reflection is calculated by the sum of the squared nuclear and magnetic diffracted intensities:

$$F^2 = F_{nuclear}^2 + F_{magnetic}^2 \quad (2.13)$$

$$F_{nuclear}^2 = A^2 + B^2 \quad (2.14)$$

$$f = xT(f_0 + f' + if'') \quad (2.15)$$

$$T = e^{[8\pi^2 U \sin^2(\theta/\lambda)]} \quad (2.16)$$

$f$  is the structure factor which also includes anomalous distributions. Equation 2.16 is only valid in the case of x-ray diffraction. In the case of neutron diffraction the parts of the structure factor is replaced by the neutron scattering lengths

$$f = xT(b_0 + b' + ib'') \quad (2.17)$$

and has exactly the same mathematical structure as for the case of x-rays.  $x$  is the atomic fraction or the occupation of an atom on a position in the unit cell.  $T$  is related to the atomic displacement which is calculated with equation 2.16.  $U$  is the displacement. Here, isotropy is considered.

The factors  $A$  and  $B$  consist of the following part:

$$A = xT(A_0 + A' - B''), B = xT(B_0 + B' + A'') \quad (2.18)$$

$$A_0 = \sum_i x_i T_i f_{0i} \cos(2\pi \vec{Q}_i \vec{r}_i), B_0 = \sum_i x_i T_i f_{0i} \sin(2\pi \vec{Q}_i \vec{r}_i) \quad (2.19)$$

$$A' = \sum_i x_i T_i f'_i \cos(2\pi \vec{Q}_i \vec{r}_i), B'_0 = \sum_i x_i T_i f'_i \sin(2\pi \vec{Q}_i \vec{r}_i) \quad (2.20)$$

$$A'' = \sum_i x_i T_i f''_i \cos(2\pi \vec{Q}_i \vec{r}_i), B''_0 = \sum_i x_i T_i f''_i \sin(2\pi \vec{Q}_i \vec{r}_i) \quad (2.21)$$

Equations 2.19 to 2.21 involve sums over the atoms in the unit cell. This is also the case for the magnetic part of the intensity:

$$F_{magnetic} = \sum_i \vec{q}_i p_i e^{2\pi i \vec{Q}_i \vec{r}_i} \quad (2.22)$$

Here,  $\vec{q}_i$  is the magnetic interaction vector and  $p_i$  the magnetic cross section.

Concerning scale factor and absorption correction, both of them refer just to one parameter in every refinement. For TOF-data linear absorption was assumed:

$$A = e^{-A_B \lambda} \quad (2.23)$$

### 2.3.3 Profile function

The peak function was always refined with a mixture of Gaussian and Lorentzian profile which is explained in detail in [57, 58].

In the case of neutron TOF-data Parameters used for Gaussian part are Sig0, Sig1 and Sig2, for Lorentzian part Gam0, Gam1 and Gam2. Asymmetries of peaks were calculated with parameters alpha0e, alpha1e, beta02, beta1e, alpha0t, alpha1t, beta0t and beta1t. Parameters alpha refer to the rising and beta to the decay constant of an pulse of waves. All those parameters effect the shape of the peak. The mathematical formulation of those parameters can be found in section A.2.

### 2.3.4 Rietveld refinement

Refinements can already be performed just by having applied the parameters which were introduced in previous subsection (for example atomic fraction, displacement). Physical properties that can be determined this way is space group and lattice constants. Of course a proposed model has to be available. This way the structure of the unit cell can be confirmed. Scale factors are not supposed to be refined. Intensities are only calculated due to symmetry conditions of the unit cell of the model. Such a refinement was named after Le Bail who developed this method [61].

A method which is called after its developer Rietveld [62, 63] also consideres the atomic structure. Here, a model including all atomic locations such as atomic occupations, atomic posiiions and atomic displacement is applied.

Concerning atomic occupations equation 2.17 is taken into account.

Detailed mathematical information of the structure of a sample influencing the refinement can be found in [57, 58]. Notice that mathematical notation used in Gsas was used in Jana2006, too. In table 2.2 effection of reflections by certain conditions is presented.

Name	Position of peaks	Peak shape	Intensity of Peaks	Background
Time of measuring			x	x
Symmetries (space group)	x			
Lattice constants	x			
Instrumental parameters	x			
Asymmetry parameters		x		
Resolution function		x		
Atomic occupations			x	x
Atomic displacement			x	
Atomic positions			x	

**Table 2.2:** Influence of parameters of the model of the Rietveld refinement of reflections.

### 2.3.5 Quality of refinements

The quality of a refinement is characterized by the goodness of fit (GOF) value. This value is calculated as presented in equation (2.24) with the total number of observations  $N_{obs}$  and the number of variables  $N_{var}$  in the refinement.  $M$  is defined in equation 2.25. The weight factors are derived from an error propagation scheme and  $I_o$  and  $I_c$  refer to observed and calculated intensities.

$$GOF = \frac{M}{(N_{obs} - N_{var})} \quad (2.24)$$

$$M = \sum_i w_i (I_{o,i} - I_{c,i})^2 \quad (2.25)$$

Concerning qualities of diffraction patterns, in every refinement the difference pattern is indicated. This value is just calculated by  $I_o - I_c$  and is illustrated below the diffraction pattern in every refinement (figure 2.8). The summation takes place over every measured point in the diffraction pattern. In the case of having a model applied fitting 100% to the measured data  $GOF=1$ . Therefore, the value is expected to be slightly above 1.



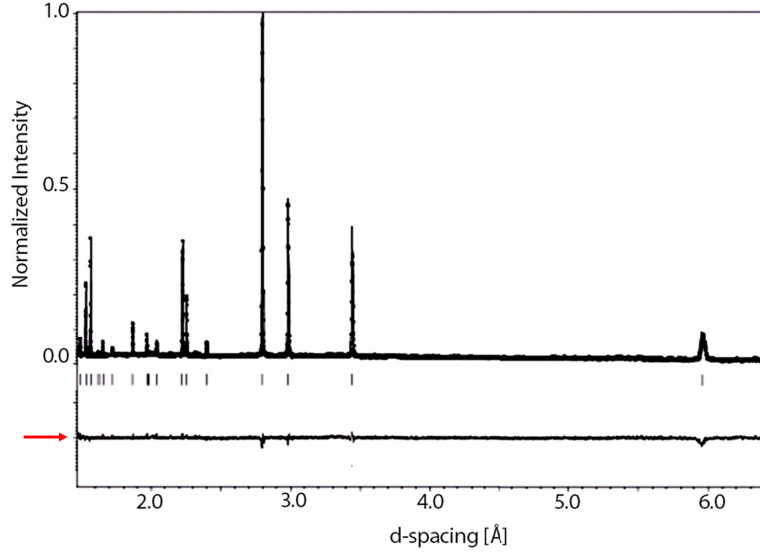


**Figure 2.8:** Powder diffraction pattern performed on  $Mn_{5-x}Fe_xSi_3$ ,  $x=0$  at 100 K with refinement. Red arrow points at line of difference pattern.

## 2.4 Inelastic neutron scattering

### Nuclear inelastic scattering

The purpose of inelastic neutron scattering is to revolve the change in energy that occurs when neutrons interact with the nuclei. In the case of inelastic scattering a momentum and an energy transfer from the neutron to the nucleus or vice versa takes place [64, 65]. Therefore, the wave vectors of incoming and outgoing beam,  $k_i$  and  $k_f$  (initial and final wave vectors) are not equal. The double differential cross section can be written as [65]:

$$\begin{aligned} \frac{d^2\sigma}{d\Omega d\omega} &= \frac{k_f}{k_i} \frac{2\pi}{v_0} \sum_{\tau} \sum_{j,q} \\ &\cdot \left| \sum_i \frac{b_i}{\sqrt{m_i}} \exp[-W_i(\vec{Q} + i\vec{Q}\vec{R}_i)] (\vec{Q}\vec{e}_i^j) \right|^2 \\ &\cdot \omega_j^{-1} (n(\omega_j(\vec{q})) + \frac{1}{2} \pm \frac{1}{2}) \delta(\omega \mp \omega_j(\vec{q})) \delta(\vec{Q} \mp \vec{q} - \vec{\tau}) \end{aligned} \quad (2.26)$$

$b_i$  is the scattering length.  $W(\vec{Q})$  is the Debye-Waller factor taking atomic displacement of atoms into account and  $\tau$  the nearest reciprocal lattice vector. The intensity scales with the factor  $(\vec{Q}\vec{e}_i^j)$ .

$\vec{e}$  is the polarization of the phonon mode. In case of  $\vec{e}$  is perpendicular to  $\vec{q}$  (left part in figure 2.9) the transverse component of a phonon is measured. In the case of  $\vec{e}$  is parallel to  $\vec{q}$  (right part in figure 2.9) the longitudinal component of a phonon is measured.

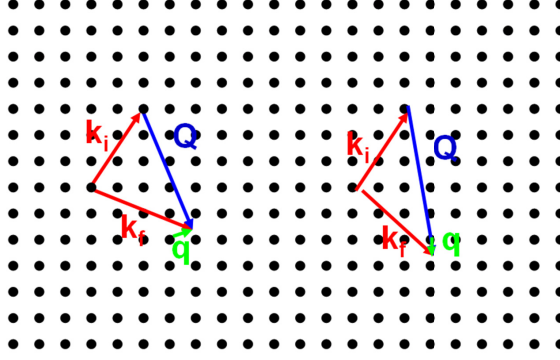


Figure 2.9: Scattering with illustration of the values  $\vec{Q}$ ,  $\vec{q}$ ,  $\vec{k}_i$  and  $\vec{k}_f$ .

### Magnetic inelastic scattering

Analogue to inelastic scattering at nuclei, inelastic magnetic scattering revolves the energy change that occurs due to the magnetic interactions between neutrons and the sample.

$$\frac{d^2\sigma}{d\Omega d\omega} = \frac{k_f}{k_i} (r_m)^2 \sum_{\alpha,\beta} \left( \delta_{\alpha\beta} - \frac{Q_\alpha Q_\beta}{Q^2} \right) \frac{1}{(2\mu_B)^2} S_{\langle MM \rangle}(Q, E) \quad (2.27)$$

$$S_{\langle MM \rangle}(Q, E) = \int e^{\frac{-iEt}{\hbar}} \langle M_Q^\alpha(t) M_{-Q}^\beta(t) \rangle \frac{dt}{2\pi\hbar} \quad (2.28)$$

$$r_m = -2\mu_B \frac{2m}{\hbar^2} \mu_n \quad (2.29)$$

$M$  is the magnetic moments which are perpendicular to the wave vector  $Q$ ,  $E$  the energy,  $\mu_n$  the magnetic moment of the neutron and  $\mu_B$  the Bohr magneton [66].

### Focusing and defocusing

A triple axis spectrometer for inelastic neutron scattering measurements is considered. In figure 2.10 the effect of the orientation of the resolution ellipsoid illustrated. Measuring in focussing setup will provide data with narrow sharp peaks, since the ellipsoid only cuts the branch for a short range in energy but the shape of the branch perfectly fits to the ellipsoid. Measuring in the defocussing mode on the other hand will provide broad peaks with low intensity (in comparison to focussing mode).

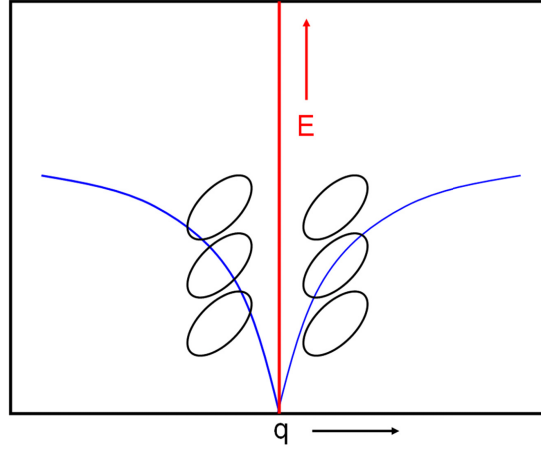


**Figure 2.10:** Dispersion of one branch in defocussing (left) and focussing (right) mode.

### 2.4.1 Magnons

A magnon branch can similar to a phonon branch cut the point  $E=0\text{meV}$  in the dispersion relation curve. This branch can be mathematically fitted with a model considering the spins as a chain with only next neighbour interactions which was introduced in [67]. Since magnons are quantized spin waves the energy can be calculated by considering wave functions. The energy finally scales with  $J$  the exchange parameter,  $S$  the spin and  $a$  the distance between two magnetic atoms [67]:

$$\hbar\omega = 4JS(1 - \cos(ka)) \quad (2.30)$$

Taking anisotropy into account, the whole dispersion of this magnon branch does not cut the point  $E=0\text{meV}$  but a point  $E>0\text{meV}$ . This anisotropy term does not depend on  $Q$ . This anisotropy term can be written analoge to [68].

In order to extract the exchange parameters from experimental data points of measurements the following model can be adapted to the points of measurements:

$$\hbar\omega = \sum_{i=1}^N J_i(1 - \cos(ka_i)) + c \quad (2.31)$$

In the summation in equation (2.31)  $N$  spin waves are considered. No interaction between spin waves are considered, which would have led to a Hamiltonian that has to be diagonalized to extract the interaction constants which was done in [68, 69], for example.

## Chapter 3

### Instruments

#### 3.1 Experiments on POWGEN

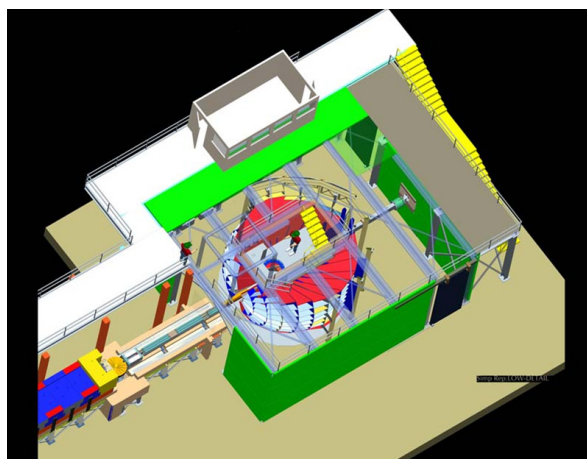


**Figure 3.1:** Schematic picture of TOF instrument POWGEN at SNS Oak Ridge National Laboratory. Detectors are planned to be placed around the sample holder taken from [70].

Time-of-flight (TOF) neutron data were collected on samples  $\text{Mn}_{5-x}\text{Fe}_x\text{Si}_3$   $x=0,1,2,3,4$ ,  $\text{Mn}_{1-x}\text{Co}_x\text{Fe}_4\text{Si}_3$   $x=0.1,0.2$  and  $\text{MnFe}_{4-x}\text{Co}_x\text{Si}_3$   $x=0.2,0.5$  on the new powder diffractometer POWGEN (layout presented in figure 3.1) at the Spallation Neutron Source (SNS), Oak Ridge National Laboratory. In contrast, all other TOF neutron powder diffractometers, the design of POWGEN is based on combining the diffracted neutrons detected at all angles into a single pattern rather than assigning them to a series of different profiles that traditionally were based on grouping detectors with respect to the scattering angle. This unique approach yields to a high count rate while preserving a resolution of  $\Delta d/d=0.0015$  at  $d=1 \text{ \AA}$ . Further information on the design of POWGEN can be obtained by reading reference [56].

As can be seen in figure 3.2 there are three choppers build in the neutron guide at certain distances to the source to select a wave length band.

Concerning TOF-instruments the resolution strongly depends on the distance between source and sample. This is simply due to measuring intensities as function of time. The distance

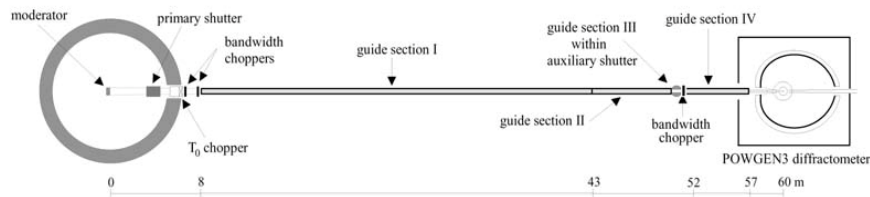


**Figure 3.2:** Technical layout of TOF-instrument POWGEN taken from [70]

between source and sample influences the width of package of wave lengths and therefore the resolution. This is due to the fact that a package of wave length includes neutrons with different velocities. Therefore, the longer the distance the larger the width of the package and the higher the resolution, respectively. Unfortunately long distances are also equivalent to loss of neutrons, i.e. loss of intensity, since neutrons might not be 100% reflected by the guide. The equipment of the sample environment was build in a distance of 60m to the source (figure 3.2).

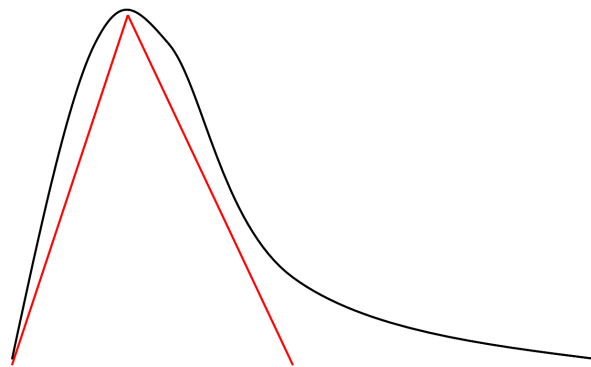


**Figure 3.3:** Proposed outgoing beam of neutron with (red) and without (black) using choppers.

The choppers in the neutron guide have been installed to influence the shape of the pulse of neutrons. In figure 3.3 a pulse of neutrons is presented with and without using choppers. When choppers are applied the shape of the rise and decay of a pulse is sharper which is due to the fact that choppers absorb neutrons. The influence of the choppers on the shape of the pulse is crucial for refinements since rise and decay of the pulse, which are sharp, are easier to refine with asymmetric parameters. Asymmetric parameters are still useful for the calculation of the shape of a pulse, since the choppers do not work perfectly due to their texture.

## 3.2 Experiments on HB2A

Constant wavelength (CW) neutron data was collected on sample  $\text{Mn}_{5-x}\text{Fe}_x\text{Si}_3$   $x=0$  at High Flux Isotope Reactor (HFIR), Oak Ridge National Laboratory on the powder diffractometer HB2A. The measurement was performed using a wavelength of  $\lambda=2.41 \text{ \AA}$  (Germanium 113

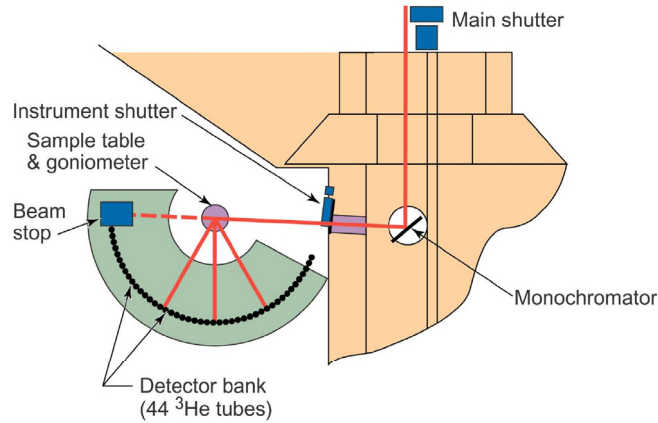


**Figure 3.4:** Schematic picture of CW instrument HB2A at HFIR Oak Ridge National Laboratory taken from [71].

as monochromator). Data taken on this instrument is perfectly suited for refinements with the Rietveld method. For the measurements which will be subject of this dissertation the cryomagnet equipment was applied. Magnetic fields up to 7 T could be applied on the sample. The resolution of the instrument is  $\Delta d/d = 0.002$ .

A sketch of the setup is presented in figure 3.4.

### 3.3 Experiments on 2T1

Inelastic neutron data were collected on sample  $\text{Mn}_{5-x}\text{Fe}_x\text{Si}_3$   $x=4$  on thermal neutron triple axis spectrometer 2 T1 at LLB (layout presented in figure 3.5).

For unpolarized neutrons monochromator and analyzer of type PG 002 (Pyrolytic Graphite) were used. The (002)-direction is orientated perpendicular to the surface which reflects the neutron beam.

The final wave length was  $\lambda=2.662 \text{ \AA}$ .

This unique approach yields a high count rate while preserving a resolution of  $\Delta\delta=0.8 \text{ meV}$  ( $E_F=14.7\text{meV}$ ) at the elastic line. Further information on the design of 2T1 can be found at [72].

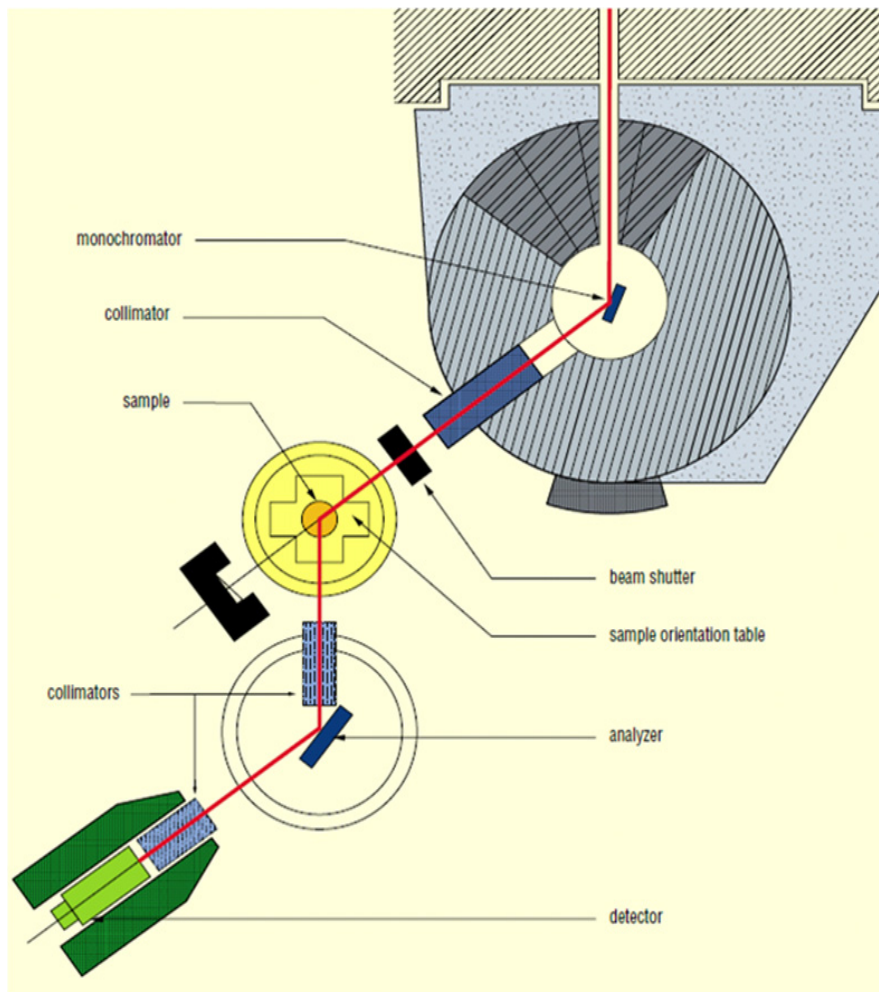


**Figure 3.5:** Schematic picture of triple axis spectrometer 2T1 at LLB taken from [72].

## Chapter 4

# Preparation and quality check of samples

### 4.1 Synthesis of polycrystalline samples: "kalter Schwebetiegel"

Polycrystalline samples have been prepared by inductive melting using a cold crucible designed in the Forschungszentrum Juelich [74]. The schematic layout of the kalter Schwebetiegel (KST) is presented in figure 4.1.

The crucible, which is cooled by a water cycle, consists of several segments. The induction coils induce a high frequency alternating magnetic field in the crucible. The segments of the crucible work as carrier of the magnetic field, which finally generates alternating current in the sample. This causes the material to heat up due to resistive losses.

The whole equipment is sealed with a recipient which consists of silica allowing to melt samples under argon.



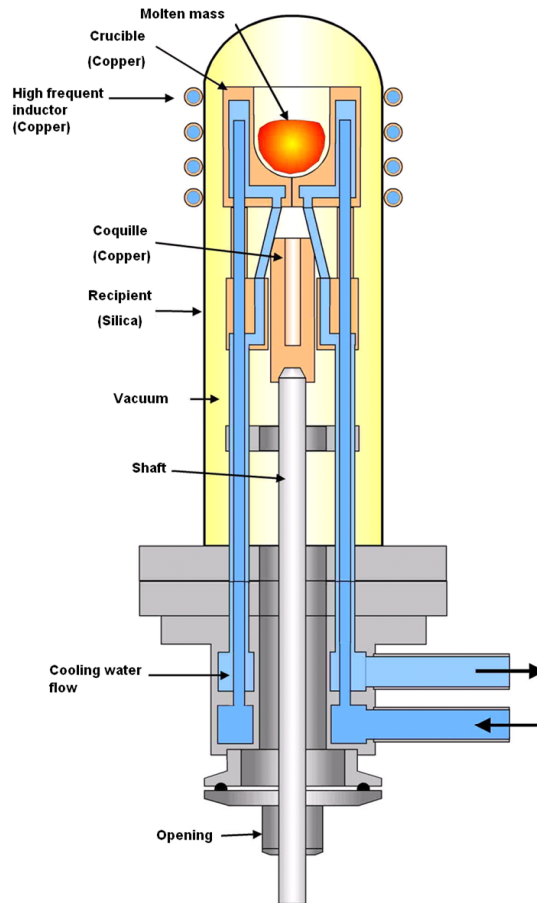


Figure 4.1: Technical layout of the KST taken from [73].

## 4.2 Details of prepared samples

All polycrystalline samples  $Mn_{5-x}Fe_xSi_3$ ,  $x=0,1,2,3,4$ ,  $Mn_{1-x}Co_xFe_4Si_3$   $x=0.1,0.2$  and finally  $MnFe_{4-x}Co_xSi_3$ ,  $x=0.2,0.5$  have been prepared by inductive melting under Argon. Every batch was melted and annealed at least four times to get good quality samples. Mn (Aldrich, 99.99%), Fe (Aldrich, 99.99%), Si (Aldrich, 99.99%) and Co (Aldrich, 99.99%) were used as starting materials. The metal pieces have been preliminary etched with hydrochloric acid to remove the oxidation coating from the surface. Before melting all samples were heated under vacuum to remove impurities like absorbed water. All final products remain with a metallic luster and visibly stable upon exposure to both air and moisture over several weeks.

The structure of every sample was confirmed with x-ray scattering at room temperature using Si as reference material to determine instrumental parameters. Program FullProf 1.10 was used for refining models on the diffraction patterns. As an example for refinements a diffraction pattern with refinement and Si used as reference is presented in figure 4.2.

#### 4.2 Details of prepared samples

Sample	prepared weights				Calculated weights			
	Mn [g]	Fe [g]	Si [g]	Co [g]	Mn [g]	Fe [g]	Si [g]	Co [g]
$\text{Mn}_{5-x}\text{Fe}_x\text{Si}_3$								
x=0	15.315(5)	0	4.702(5)		15.305	0	4.695	
x=1	12.244(5)	3.103(5)	4.688(5)		12.244	3.104	4.683	
x=2	9.190(5)	6.195(5)	4.679(5)		9.183	6.192	4.671	
x=3	6.127(5)	9.264(5)	4.665(5)		6.122	9.265	4.659	
x=4	3.060(5)	12.325(5)	4.655(5)		3.061	12.322	4.648	
Single crystal $\text{Mn}_{5-x}\text{Fe}_x\text{Si}_3$ x=4								
	15.313(5)	61.608(5)	23.235(5)		15.305	61.609	23.238	
	15.308(5)	61.609(5)	23.238(5)		15.305	61.609	23.238	
$\text{Mn}_{1-x}\text{Co}_x\text{Fe}_4\text{Si}_3$								
x=0.1	0.678(5)	3.077(5)	1.163(5)	0.077(5)	0.681	3.077	1.161	0.081
x=0.2	0.605(5)	3.072(5)	1.161(5)	0.164(5)	0.605	3.074	1.159	0.162
$\text{MnFe}_{4-x}\text{Co}_x\text{Si}_3$								
x=0.2	0.756(5)	2.922(5)	1.159(5)	0.162(5)	0.756	2.921	1.160	0.162
x=0.5	0.754(5)	2.690(5)	1.159(5)	0.409(5)	0.754	2.684	1.157	0.405

**Table 4.1:** Weights of elements used for preparation.

In table 4.1 prepared and calculated weights for all the samples are presented. Two times 50g of composition  $\text{Mn}_{5-x}\text{Fe}_x\text{Si}_3$  x=4 were first prepared with the KST to get a final value of weight of ca. 100g for the single crystal synthesis.

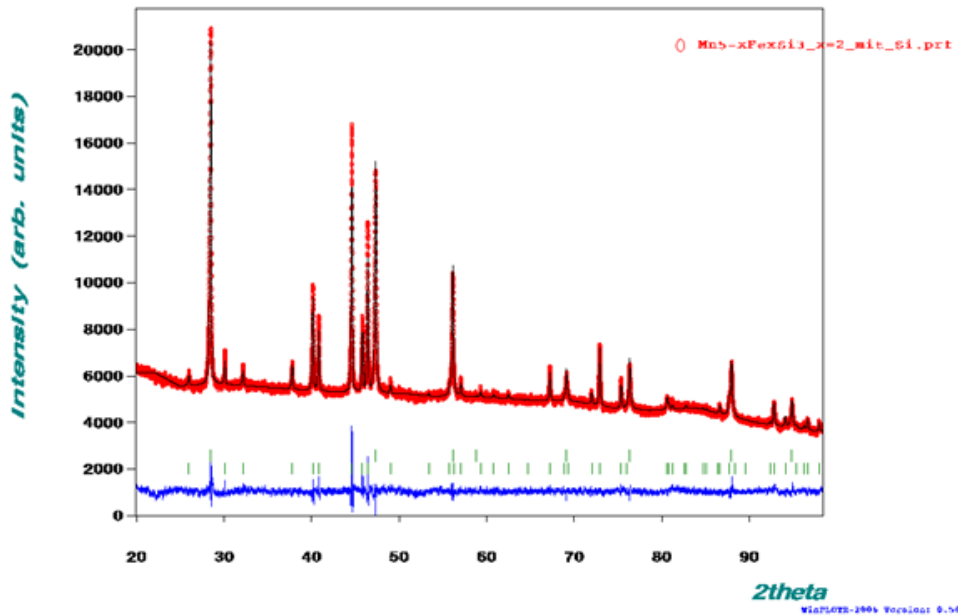


**Figure 4.2:** Diffraction pattern taken on  $\text{Mn}_{5-x}\text{Fe}_x\text{Si}_3$  x=2 with refinement. Si was used as reference.

The detailed results of a typical refinement is presented in chapter A.5.

The background of those diffraction patterns was refined with linear interpolation.

The Si-phase was refined using the profile matching mode which is equivalent to the LeBail-setting (no atomic and scale factors, chapter 2.3.1). The cell parameters of phase 1 were kept constant to determine the instrumental parameters (Cos- and Sin-shift parameters). Second, the halfwidth parameters of the Si-phase were refined and applied to use them for the second phase (in this case  $\text{Mn}_{5-x}\text{Fe}_x\text{Si}_3$   $x=2$ ).

When the parameters of the second phase were refined, parameters of the Si-phase were only included in the refinement as constants without being refined anymore.

Values for the preferred orientation were refined in either phase but kept constant during the cycles of the final refinement. The preferred orientation in both phases was low, since a value of 1 indicates the absence of any preferred orientation.

### 4.3 Synthesis of single crystal $\text{Mn}_{5-x}\text{Fe}_x\text{Si}_3$ $x=4$

The single crystal  $\text{Mn}_{5-x}\text{Fe}_x\text{Si}_3$   $x=4$  was prepared by the method of Czochralski under Argon. The working process of this equipment is presented in figure 4.3. The molten mass is placed into a crucible consisting of Wolfram, which is heated up by induction with the same technique as described in section 4.1.

A seed crystal is dipped into the melt. The shaft with the seed crystal is pulled up with a certain velocity. Shaft and crucible slowly rotate against each other. The single crystal is finally grown in a shape of a cylinder. A detailed description of the working process of a Czochralski equipment can be found in [75].

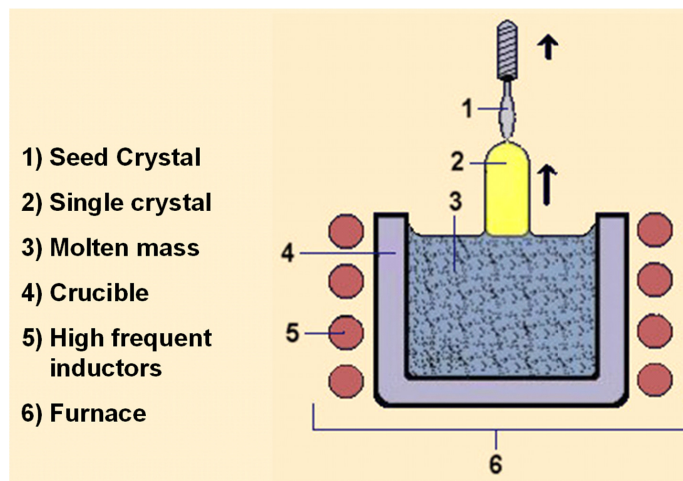


Figure 4.3: Czochralski method for single crystal preparation taken from [76].

---

### 4.3 Synthesis of single crystal $Mn_{5-x}Fe_xSi_3$ $x=4$

---

At the beginning the seed was pulled out of the molten mass with a velocity of 15mm per hour. This had to be done to decrease the chance of growing a single crystal consisting of several parts with different orientations. Finally, the seed crystal of the equipment was pulled out of the molten mass with a velocity of 9mm per hour to grow a cylindrical single crystal with a diameter of ca. 8mm.



# Chapter 5

## Magnetization measurements

### 5.1 Experimental conditions

The magnetization as a function of temperature of all samples were measured on a Quantum design (QD) Magnetic Property Measurement System (MPMS). Magnetization data in dependence of temperature were collected after having polycrystalline samples fixed with batting in a gel-capsule which was put in a straw. Every straw was pierced with a needle in front, behind and through the capsule, improving evacuation conditions.

All magnetization measurements were performed using RSO-equipment, except measurements on  $\text{Mn}_{5-x}\text{Fe}_x\text{Si}_3$ ,  $x=4$  at 1T and 2T where dc-equipment was applied.

Magnetization measurements on sample  $\text{MnFe}_{4-x}\text{Co}_x\text{Si}_3$   $x=0.5$  were performed on a Cryo Cooler Measurement system (CCMS) of the company Cryogenic Limited using VSM equipment. These measurements were performed to calculate the MCE.

Every magnetization measurement consists of a first part in which temperature was lowered and a second in which temperature was increased (the applied magnetic field remained constant). Under these conditions any hysteresis effect can be detected.

### 5.2 $\text{Mn}_{5-x}\text{Fe}_x\text{Si}_3$

#### Points of phase transitions and magnetic behaviour

In figure 5.1 (a-f) magnetization measurements performed on  $\text{Mn}_{5-x}\text{Fe}_x\text{Si}_3$   $x=0,1,2,3,4$  are presented. Every measurement was performed at a magnetic field of 100 Oe except figure 5.1f. Here, a field of 200 Oe was applied. As can be seen in figures 5.1 (a and b), some points of measurement do not fit into the whole magnetizations. In the magnetization of sample  $\text{Mn}_{5-x}\text{Fe}_x\text{Si}_3$   $x=0$  at 175K one point lies slightly above the curve. The magnetization of sample  $\text{Mn}_{5-x}\text{Fe}_x\text{Si}_3$   $x=1$  reveals similar anomalies at 152K and close to 250K. These anomalies are due to the equipment. No anomalies at these temperatures are reported in literature.

The magnetization measurements are very similar to measurements presented in literature. The shapes of the measurement of all compositions perfectly reproduce data in [36, 41, 77]. This leaves no doubt about the quality of the samples and their macroscopic properties.

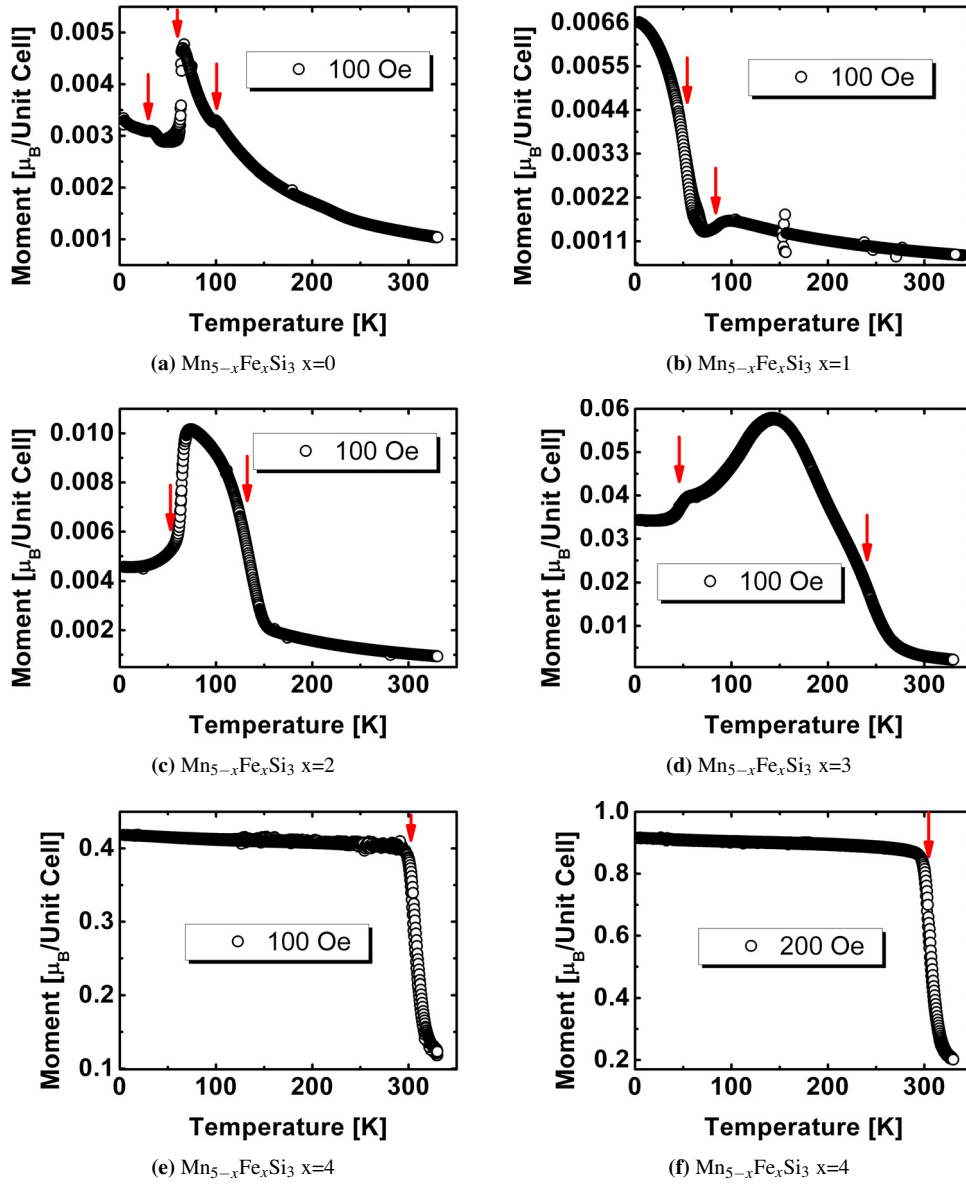


**Figure 5.1:** RSO-magnetization measurements performed on  $\text{Mn}_{5-x}\text{Fe}_x\text{Si}_3$  at 100Oe and 200Oe (only  $\text{Mn}_{5-x}\text{Fe}_x\text{Si}_3$   $x=4$ ). Red arrows indicate points of phase transitions.

The values of the magnetization measurements are not reliable due to the following facts: 1) The applied field is too small for having saturated the moments and all samples were polycrystalline. Moments do not point into the same but random directions under such conditions. 2) The way samples were prepared should have caused the engagement of preferred orientations of unit cells inside a polycrystalline sample which was explained in previous chapters.

Still, magnetic behaviour and points of phase transitions, which are linked to the macroscopic magnetic moment of a sample, can be easily extracted from the data. Points of phase transitions were extracted from the first derivatives of the magnetizations. An example of a phase transition that could be detected in  $Mn_{5-x}Fe_xSi_3$   $x=4$  can be found in figure A.1. The sharp peak in the red line is due to technical errors which have occurred during the measurement.

Magnetic structures of compositions  $Mn_{5-x}Fe_xSi_3$   $x=0,1,2,3$  are antiferromagnetic and  $Mn_{5-x}Fe_xSi_3$   $x=4$  is ferromagnetic.

Phase transitions were detected at 100(1)K, 62(1)K and 30(1)K for  $Mn_{5-x}Fe_xSi_3$   $x=0$ , at 89(1)K and 51(1)K for  $Mn_{5-x}Fe_xSi_3$   $x=1$ , at 134(1)K and 64(1)K for  $Mn_{5-x}Fe_xSi_3$   $x=2$  and at 244(1)K and 53(1)K for  $Mn_{5-x}Fe_xSi_3$   $x=3$ , respectively. The phase transition in sample  $Mn_{5-x}Fe_xSi_3$   $x=4$  takes place close to  $T_C=302(1)K$ . No hysteresis effects are visible in the magnetization measurements of these compounds.

Publication	$T_{N1}$ [K]	$T_{N2}$ [K]	$T_{N3}$ [K]
Diss	100(1)	62(1)	30(1)
[40, 42, 43]	99	66	-
[41]	106	60	-
[78]	-	68	-

**Table 5.1:** Temperatures of phase transition determined with derivatives of magnetization measurements performed for this thesis (Diss) and proposed temperatures of phase transitions in publications of sample  $Mn_{5-x}Fe_xSi_3$   $x=0$ .

In literature composition  $Mn_{5-x}Fe_xSi_3$   $x=0$  is reported to have antiferromagnetic phase transitions at Neel temperatures of 99K and 66K [40, 42, 43, 78]. Points of phase transitions of composition  $Mn_{5-x}Fe_xSi_3$   $x=0$  differ in publications (table 5.1). They all report about a complex microscopic structure ranging from an orthorhombic unit cell for  $66K < T < 99K$ . The existence of a monoclinic unit cell below 66K is mentioned in [43]. These microscopic structures cannot be investigated with the magnetization measurement. Still, points of phase transitions and magnetic behaviour extracted from the magnetization measurements seem to be very close to those presented at least in one publication. Differences could be due to synthesis or due to the presence of impurities (no impurities were detected in the sample used for the measurements presented here). The third phase transition which takes place at 30(1)K seems to be unknown in literature.

According to literature [38] the structure of  $Mn_{5-x}Fe_xSi_3$   $x=1$  exhibits commensurate antiferromagnetism between 70K and 95K. Below 70K an orthorhombic structure similar to  $Mn_{5-x}Fe_xSi_3$   $x=0$  is proposed. A point of phase transition could be detected at 89(1)K which is close to 95K. According to the magnetization presented in this thesis there is another phase transition at 51(1)K and not at 70K. Unfortunately in [38] no details of the proposed magnetic structures are mentioned. Even a refinement is missing.



For composition  $\text{Mn}_{5-x}\text{Fe}_x\text{Si}_3$   $x=2$  the magnetic structure is proposed to be commensurate antiferromagnetic [38] between 125K and 50K. Below 50K the emergence of an additional reflection could be detected and is reported to have appeared due to a reorientation of the spins.

In [36] phase transitions are proposed to take place close to 250K and 50K, which is close to the temperatures presented in this thesis. This is in disagreement to [38]. Here, only one phase transition is proposed to take place close to 145K. Maybe the magnetic structure is too complex to be characterized by only observing intensities of reflections as it was obviously done in [38]. Furthermore  $\text{Mn}_{5-x}\text{Fe}_x\text{Si}_3$   $x=3$  is reported to exhibit an incommensurate antiferromagnetic ordering. [28] proposes helical antiferromagnetic ordering at 77K (which is not proposed to be a phase transition temperature). The phase transition for composition  $\text{Mn}_{5-x}\text{Fe}_x\text{Si}_3$   $x=3$  at 53(1)K in the magnetization measurement, could be due to a reorientation of the magnetic moments.

The ferromagnetic structure of compound  $\text{Mn}_{5-x}\text{Fe}_x\text{Si}_3$   $x=4$  is also known in literature [28, 36, 38]. The phase transition is proposed to take place close to 300K [36, 38], which is in agreement with the measurements presented in this thesis (figures 5.1 e and f). Furthermore, they report about the presence of two different magnetic moments on the two atomic positions of Mn and Fe [28, 38].

The value of the magnetization obviously increases with content of Fe. Furthermore, the structure seems to loose complexity. The value of the magnetization increases by a factor  $>2$  when comparing measurements performed on sample  $\text{Mn}_{5-x}\text{Fe}_x\text{Si}_3$   $x=4$  at fields of 100Oe and 200Oe (same measurement with the same technical conditions). This is a sign for sensitivity to magnetic fields and to magnetic moments which are far away from being saturated. At low temperatures below the phase transition the magnetization still increases a little bit. This could be due to the presence of the two different magnetic moments (reported in [28, 38]) on atoms acting differently, since magnetizations measure the macroscopic moment of the whole sample. Neutron diffraction measurements could be the key for understanding this phenomenon (as it was done in literature).

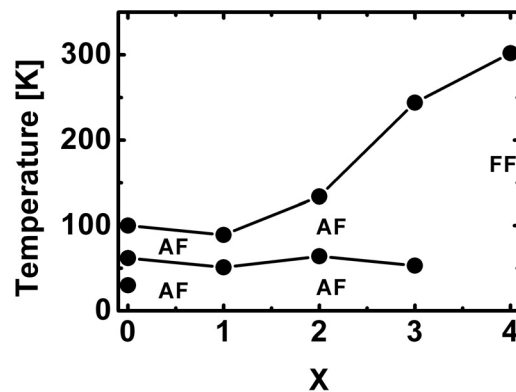


**Figure 5.2:** Phase diagram of  $\text{Mn}_{5-x}\text{Fe}_x\text{Si}_3$  redetermined by magnetization measurements.

After having identified points of phase transition and the nature of the magnetism, the phase diagram in dependence of composition and temperature can be redetermined. Figure 5.2 presents

the results. They fit to work published in literature [36, 38].

Magnetization measurements performed at applied fields of 1T and 2T exhibit a much bigger magnetic moment than those performed at magnetic fields of 100Oe and 200Oe. This is due to the fact that the niveau of the magnetization is moved closer to its saturation. This also explains why the value of the magnetization does not increase that much when comparing measurements performed at 1T and 2T and measurements performed at 100Oe and 200Oe.

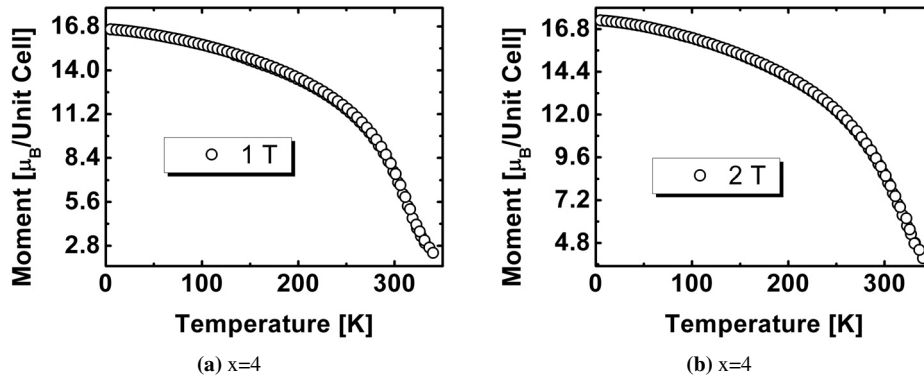


**Figure 5.3:** DC-magnetization measurements performed on  $Mn_{5-x}Fe_xSi_3$   $x=4$  at 1T (left) and 2T (right).

The nature of the phase transition looks completely different. In those measurements no paramagnetic behaviour is visible anymore. The phase transition could have been shifted to higher temperatures or even have completely disappeared due to the applied field. Ferromagnetic behaviour can still easily be identified.

Therefore, even at an applied field of 1T the magnetic moments can be considered saturated. This explains the small differences between 1T and 2T measurements concerning values of the moments. Since there are 10 magnetic atoms in the unit cell the average saturated momentum of a single atom is  $1.7\mu_B$  which is close to the values of Fe and Mn.

### Fitting of susceptibilities

The susceptibilities can easily be calculated with the measured data and used for fitting. Theory concerning susceptibility measurements and phases transitions can be found in [67, 79].

In figures 5.4 (a-d) inverse susceptibilities of compositions  $Mn_{5-x}Fe_xSi_3$   $x=0,1,2,3$  are presented. In the paramagnetic phase they obey the Curie Weiss law (explained in section A.1) with Weiss temperatures, Curie constants and effective magnetic moments presented in table 5.2.

In the inverse susceptibility of  $Mn_{5-x}Fe_xSi_3$   $x=0$  a bump is visible close to 260K. No anomaly is reported in any publication, to the best of th knowledge of this thesis' author. If this effect has originated from the sample its nature remains unclear. A fitting of the inverse susceptibility above 250K (figure A.2) resulted in a Weiss temperature of 33.0(2)K.

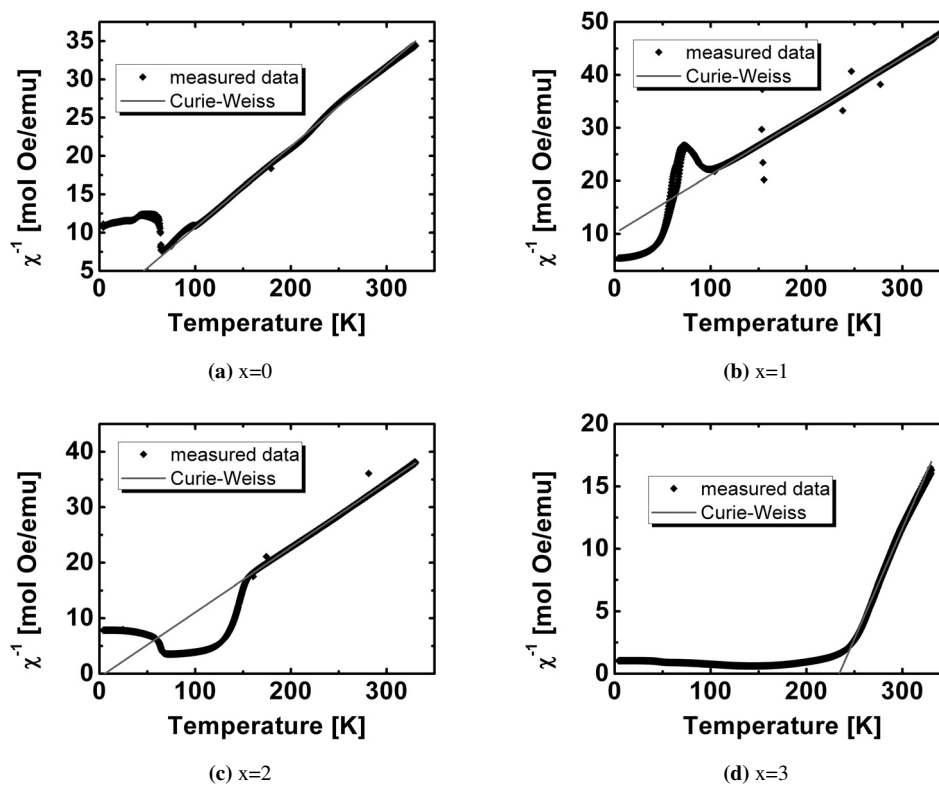


Figure 5.4: Inverse susceptibilities with Curie-Weiss fits.

composition	C [K]	$\mu_{eff}$ [ $\mu_B$ ]	$\Theta$ [K]
x=0	9,4607(1)	2.75(3)	1.0(3)
x=1	9,1058(1)	2.70(3)	93.5(3)
x=2	8,5412(1)	2.61(3)	-5.6(3)
x=3	5,5701(8)	2.11(8)	-235(1)

**Table 5.2:** Curie constants  $C$ , Weiss temperatures  $\Theta$  and effective magnetic moments  $\mu_{eff}$  for  $Mn_{5-x}Fe_xSi_3$   $x=0,1,2,3$ .

Unfortunately, there are not enough points of measurements above the transition temperature in the magnetization of sample  $Mn_{5-x}Fe_xSi_3$   $x=4$ . Therefore, no reasonable fitting could be performed.

### 5.3 $Mn_{1-x}Co_xFe_4Si_3$ and $MnFe_{4-x}Co_xSi_3$

#### Points of phase transitions and magnetic behaviour

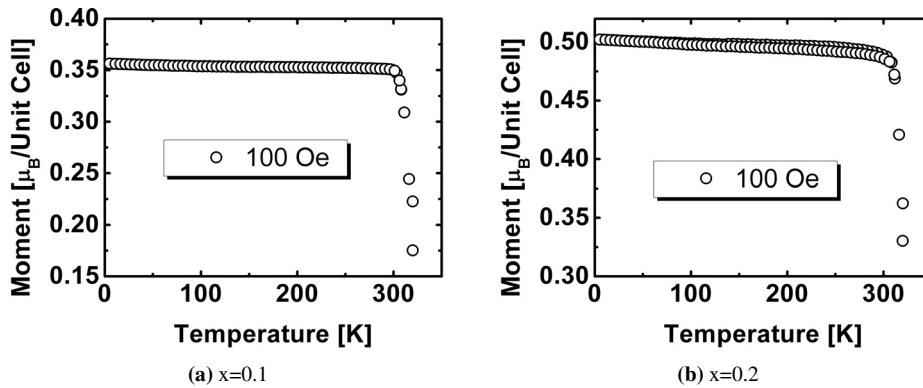


**Figure 5.5:** RSO-magnetization measurements performed on  $Mn_{1-x}Co_xFe_4Si_3$ . Numbers in boxes in diagrams indicate applied fields when measurement was performed.

For both series of compositions magnetization measurements indicated ferromagnetic behaviour with transition temperatures above 310K (maximum temperature of the measurement) for  $Mn_{1-x}Co_xFe_4Si_3$ -series and 299(1)K for  $MnFe_{4-x}Co_xSi_3$   $x=0.2$  (figure 5.5 (a)) and 288(1)K for  $MnFe_{4-x}Co_xSi_3$   $x=0.5$  (figure 5.6 (b)). The fact that values of magnetization measurements differ (quantitatively) when two samples are compared with each other does not necessarily have a physical meaning. Those results cannot be compared quantitatively with each other due to the mentioned conditions in section 5.2 concerning polycrystalline samples.

The same phenomenon concerning increase of magnetization of sample  $Mn_{5-x}Fe_xSi_3$   $x=4$  at low T is observed here. The magnetization is not constant but increases with decreasing temperature.

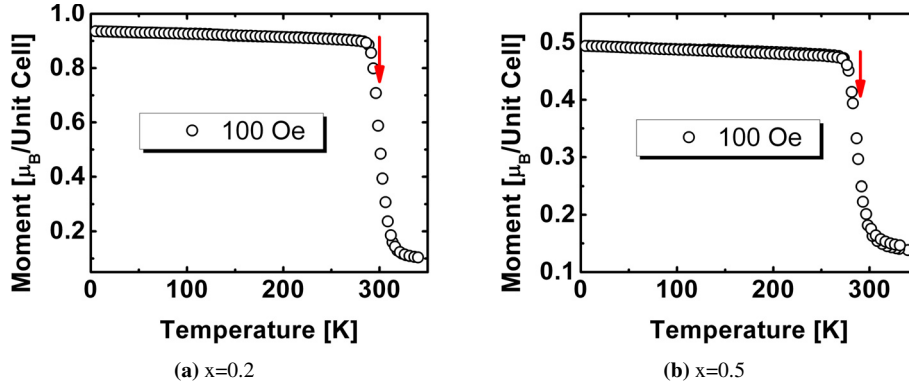


**Figure 5.6:** RSO-magnetization measurements performed on  $\text{MnFe}_{4-x}\text{Co}_x\text{Si}_3$ . Numbers in boxes in diagrams indicate applied fields when measurement was performed.

For samples  $\text{Mn}_{1-x}\text{Co}_x\text{Fe}_4\text{Si}_3$   $x=0.2$  and  $\text{MnFe}_{4-x}\text{Co}_x\text{Si}_3$   $x=0.5$  weak hysteresis effects are visible close to the transition temperature. For now, the appearance of those features remains unclear.

### Fitting susceptibilities with the Curie Weiss-law in the paramagnetic phases

Attempts to fit the susceptibilities for compositions  $\text{MnFe}_{4-x}\text{Co}_x\text{Si}_3$   $x=0.2, 0.5$  in the paramagnetic phase failed. The resulted transition temperatures were 182K ( $x=0.2$ ) and 113K ( $x=0.5$ ). These values do not make any sense, since phase transitions of both samples take place between close to 300K. The fact that fitting the susceptibilities failed is due to the small number of points of measurements.

Therefore, calculating and fitting susceptibilities of those compounds does not provide additional information about the magnetic phase transitions.

### Magnetic behaviour of $\text{MnFe}_{4-x}\text{Co}_x\text{Si}_3$ $x=0.5$ at 0Oe

When magnetization measurements were performed on sample  $\text{MnFe}_{4-x}\text{Co}_x\text{Si}_3$   $x=0.5$  in order to calculate the MCE, a second phase transition could be detected (figure 5.7). The nature of this phase transition (assuming it is only one phase transition) could be due to the presence of a second phase or due to different magnetic ordering of the two magnetic atoms in the unit cell. Two magnetic moments ordering differently on two atomic sites has been reported for  $\text{Mn}_{5-x}\text{Fe}_x\text{Si}_3$   $x=4$  in [38]. When magnetic fields  $\geq 100\text{Oe}$  the second phase transition disappears.

It has to be mentioned that the piece of sample which was used for the magnetization measurements at 100Oe exhibited a moment which was too large for the instrument when a field of 1T was applied. Therefore, a small part of this piece was used for measurements to calculate the magnetic entropy change.

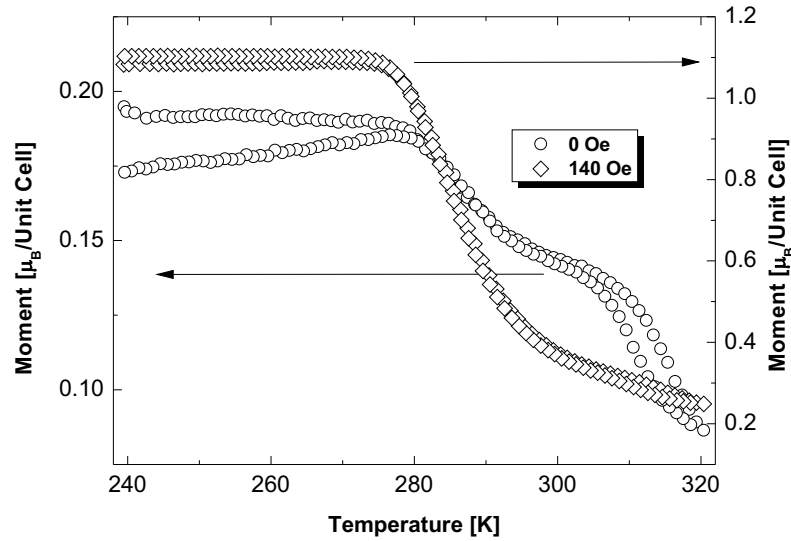


**Figure 5.7:** VSM-magnetization measurements performed on sample  $\text{MnFe}_{4-x}\text{Co}_x\text{Si}_3$   $x=0.5$  at applied fields of 0T and 140Oe.

However, this is the only sample exhibiting two phase transitions that could be detected in a magnetization measurement with small applied field of 0T. This could be due to different instrumental setups or due to phase transition temperatures outside of the measured regions.

## 5.4 Summary

The complex nature of the magnetism in  $\text{Mn}_{5-x}\text{Fe}_x\text{Si}_3$   $x=0,1,2,3,4$  was reinvestigated with magnetization measurements. The magnetic behaviours range from antiferro- ( $x=0,1,2,3$ ) to ferromagnetism ( $x=4$ ). The Co-doped materials  $\text{Mn}_{1-x}\text{Co}_x\text{Fe}_4\text{Si}_3$   $x=0.1,0.2$  and  $\text{MnFe}_{4-x}\text{Co}_x\text{Si}_3$   $x=0.2,0.5$  exhibit ferromagnetism at low temperatures.

Phase transitions take place at low temperatures for samples  $\text{Mn}_{5-x}\text{Fe}_x\text{Si}_3$   $x=0,1,2,3$  and close to room temperature for  $\text{Mn}_{5-x}\text{Fe}_x\text{Si}_3$   $x=4$ . The phase diagram of these compounds in dependence of  $x$  could be redetermined (figure 5.2) and is in agreement with publications. No hysteresis effect could be detected for any of the mentioned compounds.

Fitting of inverse susceptibilities allowed to determine the characteristic temperatures for the antiferromagnetic compounds. The moments of ferromagnetic  $\text{Mn}_{5-x}\text{Fe}_x\text{Si}_3$   $x=4$  indicate saturation at an applied field of 1T. The average magnetic moment on a magnetic atom is  $1.7\mu_B$ .

Magnetization measurements indicate ferromagnetic behaviour of the samples  $\text{Mn}_{1-x}\text{Co}_x\text{Fe}_4\text{Si}_3$   $x=0.1,0.2$  and  $\text{MnFe}_{4-x}\text{Co}_x\text{Si}_3$   $x=0.2,0.5$ . Similar to  $\text{Mn}_{5-x}\text{Fe}_x\text{Si}_3$   $x=4$  phase transitions take place close to and above room temperature.

Weak hysteresis effects were observed in the magnetization measurements of the samples  $\text{Mn}_{1-x}\text{Co}_x\text{Fe}_4\text{Si}_3$   $x=0.2$  and  $\text{MnFe}_{4-x}\text{Co}_x\text{Si}_3$   $x=0.5$ .

In the magnetization measurement performed on  $\text{MnFe}_{4-x}\text{Co}_x\text{Si}_3$   $x=0.5$  at 0T an anomaly is visible, which could be due to an ordering of the magnetic moments on another atomic site or due to the presence of impurities. At larger applied fields only one phase transition and no additional anomaly was visible.

# Chapter 6

## DSC measurements to unravel the MCE

### 6.1 Experimental conditions

The magnetocaloric effect of the sample  $\text{Mn}_{5-x}\text{Fe}_x\text{Si}_3$   $x=0$  was calculated with specific heat measurements which were performed at applied fields of 0T and 3T on a Physical Property Measurement System (PPMS).

All other MCEs were calculated with magnetization measurements performed at constant fields, or hysteresis measurements performed at constant temperatures.

DC-magnetization measurements at constant fields were performed on sample  $\text{Mn}_{5-x}\text{Fe}_x\text{Si}_3$   $x=4$  at ORNL on an MPMS instrument. RSO-hysteresis measurements at constant temperatures were performed on  $\text{Mn}_{1-x}\text{Co}_x\text{Fe}_4\text{Si}_3$   $x=0.1$  and  $\text{MnFe}_{4-x}\text{Co}_x\text{Si}_3$   $x=0.2$  on an MPMS. VSM-magnetization measurements at constant fields were performed on sample  $\text{Mn}_{1-x}\text{Co}_x\text{Fe}_4\text{Si}_3$   $x=0.2$  on a PPMS. All devices mentioned so far in this section were designed by the company Quantum Design.

As already mentioned in section 5.1 the magnetization measurements on sample  $\text{MnFe}_{4-x}\text{Co}_x\text{Si}_3$   $x=0.5$  were performed on a CCMS instrument.

### 6.2 Inverse MCE in $\text{Mn}_{5-x}\text{Fe}_x\text{Si}_3$ $x=0$

In figure 6.1 the determined entropy change exhibited by antiferromagnetic sample  $\text{Mn}_{5-x}\text{Fe}_x\text{Si}_3$   $x=0$  is presented ( $\Delta B=3\text{T}$ ). The value of the negative entropy change is similar to results presented in [36]. The shape, however, is quite different since the negative entropy change in [36] exhibits a sharp jump between negative and positive values of  $\Delta S$ .

In literature both types of inverse MCE materials can be found. For example, the negative MCEs in  $\text{CoMnSi}_{1-x}\text{Ge}_x$  [80],  $\text{Mn}_3\text{GaC}$  [81], Ni-Fe-Mn-Ga alloys [82] and  $\text{SmMn}_2\text{Ge}_2$  [83] do not exhibit sharp jumps as proposed in material  $\text{Mn}_{5-x}\text{Fe}_x\text{Si}_3$   $x=0$  by [36]. Still there are materials, for example  $\text{La}_{0.125}\text{Ca}_{0.875}\text{MnO}_3$  [84] and  $\text{PrNi}_5$  [85], which exhibit such a jump in the MCE, too.



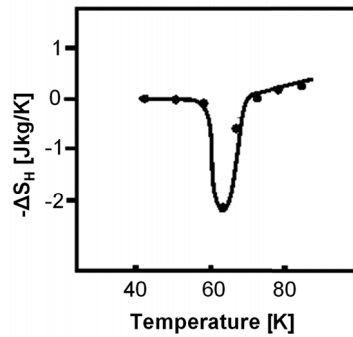


**Figure 6.1:** MCE in  $Mn_{5-x}Fe_xSi_3$   $x=0$  with  $\Delta B=3T$ . Error bars are smaller than the points in the diagram. The line between points of measurement is only a guide to the eye.

One can hardly determine which entropy change in  $Mn_{5-x}Fe_xSi_3$   $x=0$  is correct. It might be the case that the heat capacity measurement is very delicate. Not having taken enough points of measurements (if that is the case) could have led to such a different shape.

### 6.3 MCEs of $Mn_{5-x}Fe_xSi_3$ $x=4$ , $Mn_{1-x}Co_xFe_4Si_3$ and $MnFe_{4-x}Co_xSi_3$

The entropy changes of ferromagnetic samples  $Mn_{5-x}Fe_xSi_3$   $x=4$ ,  $Mn_{1-x}Co_xFe_4Si_3$   $x=0.1, 0.2$  and  $MnFe_{4-x}Co_xSi_3$   $x=0.2, 0.5$  are presented in figure 6.2. The maxima of the entropy changes of all the samples are between 0.9J/kgK and 1.1J/kgK. The largest entropy change is exhibited by sample  $Mn_{1-x}Co_xFe_4Si_3$   $x=0.1$ , the smallest by sample  $Mn_{1-x}Co_xFe_4Si_3$   $x=0.2$ .

The entropy change of  $Mn_{5-x}Fe_xSi_3$   $x=4$  is in the order of 1J/kgK with a narrow shape. This fits to results presented in [36]. They determined the entropy change with magnetic field changes of 2T (order of 2 J/kgK) and 5T (order of 4 J/kgK).

The maximum of the entropy change in each sample in dependence of the total number of electrons of Mn, Fe and Co (number of electrons of Si are excluded) is illustrated in figure 6.3. Error bars of 0.02 were considered because of the limited number of points of measurements. This shows clearly that the entropy change in these compounds cannot simply be understood just by taking the number of electrons into account.

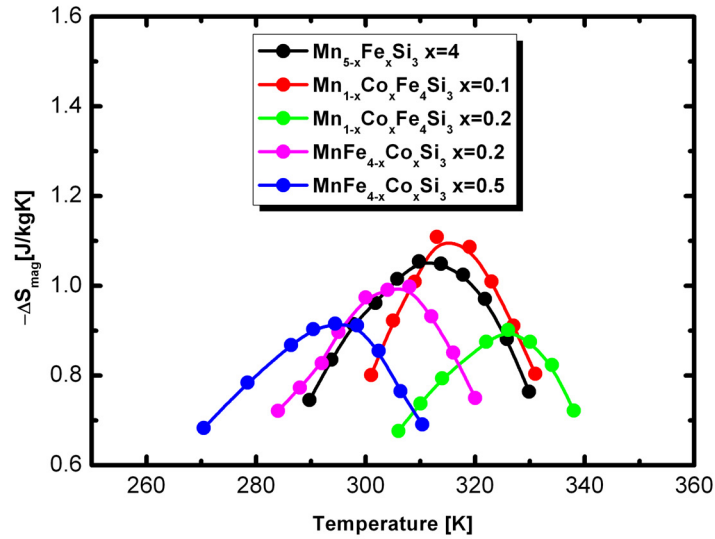


**Figure 6.2:** MCE of  $Mn_{5-x}Fe_xSi_3$   $x=4$ ,  $Mn_{1-x}Co_xFe_4Si_3$  and  $MnFe_{4-x}Co_xSi_3$  and with  $\Delta B=1T$ . Error bars are smaller than the points in the diagram. Lines between points of measurement are only guides to the eye.

The fact that the experimentally determined entropy changes are quite different in each sample could be due to the electronic part of the entropy in equation 1.1 which was not taken into account here, since its value is so far unknown. In that case phonons and magnetism should be considered. Furthermore, various magnetic and nuclear configurations could play an important role. Finally, the presence of impurities could influence the entropy change in each sample.

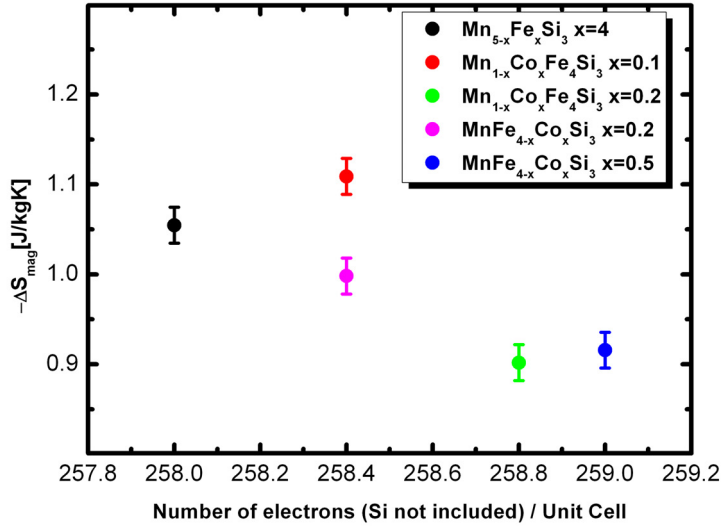


**Figure 6.3:** MCE in dependence of number of electrons in one unit cell. Number of electrons of Si are not included.

## 6.4 Summary

The MCE in materials  $\text{Mn}_{5-x}\text{Fe}_x\text{Si}_3$   $x=0,4$  have been reinvestigated via magnetization and specific heat measurements. Material  $\text{Mn}_{5-x}\text{Fe}_x\text{Si}_3$   $x=4$  was doped with Co in order to study the influence of substitution of atoms on the entropy change.

The entropy changes of  $\text{Mn}_{5-x}\text{Fe}_x\text{Si}_3$   $x=0,4$  could reproduce results presented in publication [36]. They proposed an inverse MCE in  $\text{Mn}_{5-x}\text{Fe}_x\text{Si}_3$   $x=0$  at  $\sim 60\text{K}$  and direct MCE in  $\text{Mn}_{5-x}\text{Fe}_x\text{Si}_3$   $x=4$  at  $\sim 310\text{K}$ .

Enhanced entropy changes could be measured for  $\text{Mn}_{1-x}\text{Co}_x\text{Fe}_4\text{Si}_3$   $x=0.1$  (maximum is  $\sim 1.11\text{J/kgK}$ ) in comparison to  $\text{Mn}_{5-x}\text{Fe}_x\text{Si}_3$   $x=4$  (maximum is  $\sim 1.09\text{J/kgK}$ ), while the entropy changes of all other Co-doped materials are smaller than the MCE in  $\text{Mn}_{5-x}\text{Fe}_x\text{Si}_3$   $x=4$  (minimum is  $\sim 0.9\text{J/kgK}$ ). The maximum of the entropy change in each material strongly varies with  $T_C$ .

# Chapter 7

## Neutron powder diffraction

### 7.1 Analysis of diffraction patterns

For data analysis program Jana2006 was used. Performing refinements a damping factor of 0.3 was applied. The damping factor defines the shift of the values between the sets of parameters of two cycles during the process of refining. The higher the damping factor the faster the values change.

In case of having not only one (as it is usually the case for x-ray diffraction) but several output files being part of the same measurement the pattern of one output file will be called "block". These blocks are due to the number of detectors applied at different angles. Therefore, it makes sense to call the final product of the collection of all blocks which are part of the same measurement "diffraction pattern". If a diffraction pattern consists of several blocks one refinement was performed on all blocks simultaneously. Peak shape functions, absorption corrections (pseudo-absorption correction), scale factors and background functions were refined separately on each block. The profile of the peak shape was always modeled with Pseudo Voigt. The Pseudo Voigt is a mixture of Gaussian and Lorentzian distribution.

In every refinement lattice constants, atomic displacement parameters, atomic distributions and phase fractions were refined and can be considered the link between different blocks of one refinement. Cycles of refinement were performed until all parameters have converged naturally.

Details such as correlations values between parameters of a typical refinement can be found in section A.7.2. All other refinements were performed analog.

### 7.2 $\text{Mn}_{5-x}\text{Fe}_x\text{Si}_3$

#### 7.2.1 Experimental setups

In table 7.1 details of setups are presented. Samples with points of temperatures where measurements were taken. Every diffraction pattern is projected into an imaginary diffraction pattern with a characteristic angle of center (AC) and a constant wave length (CW). If no notifications denoted measurement was performed on POWGEN.

The measurements on POWGEN were performed under different settings. This is due to the fact that the equipment of this instrument was still in progress of being installed. The number of

Mn <sub>5-x</sub> Fe <sub>x</sub> Si <sub>3</sub> x=0			
Temperatures [K]	300, 100, 90, 80, 70, 60, 50, 40, 30, 12		
Ranges in d-spacing [Å]	0.33 to 3.21	1.5 to 6.42	
Temperatures [K]	50, measurement performed on HB2A, λ=2.41 Å, Ge (113)		
Ranges in degrees [°]	8.0 to 126		
Mn <sub>5-x</sub> Fe <sub>x</sub> Si <sub>3</sub> x=1			
Temperatures [K]	300		
AC	115°	85°	45°
Ranges in d-spacing [Å]	0.2 to 1.283	0.2 to 1.57	0.2 to 3.52
Mn <sub>5-x</sub> Fe <sub>x</sub> Si <sub>3</sub> x=2			
Temperatures [K]	300		
AC	115°	85°	45°
Ranges in d-spacing [Å]	0.2 to 1.283	0.2 to 1.57	0.2 to 3.52
Mn <sub>5-x</sub> Fe <sub>x</sub> Si <sub>3</sub> x=3			
Temperatures [K]	270		
AC	115°	85°	45°
Ranges in d-spacing [Å]	0.2 to 1.283	0.2 to 1.57	0.2 to 3.52
Mn <sub>5-x</sub> Fe <sub>x</sub> Si <sub>3</sub> x=4			
Temperatures [K]	300, 270, 250, 220, 190, 160, 130, 100, 80, 50, 30, 10		
AC	115°	85°	45°
Ranges in d-spacing [Å]	0.2 to 1.283	0.2 to 1.57	0.2 to 3.52

**Table 7.1:** Details of instrumental setups for the various measurements.

detectors, for example, used to change year by year at that time (2010/2011). Even the software tools to determine instrumental parameters have not been fully developed at the beginning of 2010. That is why two different functions were used to calculate the transformation from t- to d-spacing.

## 7.2.2 Details of refinements performed on diffraction patterns taken on sample Mn<sub>5-x</sub>Fe<sub>x</sub>Si<sub>3</sub> x=0

For operating TOF-instruments the transformation from t- to d-spacing is very crucial. For transformation from time- to d-spacing the formula developed by Jason Hodges was used for all refinements performed on measurements on sample Mn<sub>5-x</sub>Fe<sub>x</sub>Si<sub>3</sub> x=0 on POWGEN. Besides its complexity, this formula holds the potential to mathematically describe the transformation properly even at high d-spacing which is not the case for a polynomial of second degree (section 2.2.6).

The refinements performed on diffraction patterns taken on Mn<sub>5-x</sub>Fe<sub>x</sub>Si<sub>3</sub> x=0 on POWGEN are considered to have very good quality (figures 7.1 and 7.2). One reason for this is the fact that due to instrumental setups reflections close to 6 Å in d-spacing could be captured which is valuable for magnetic structures since intensity originating from magnetic ordering depends on d-spacing (magnetic form factors).

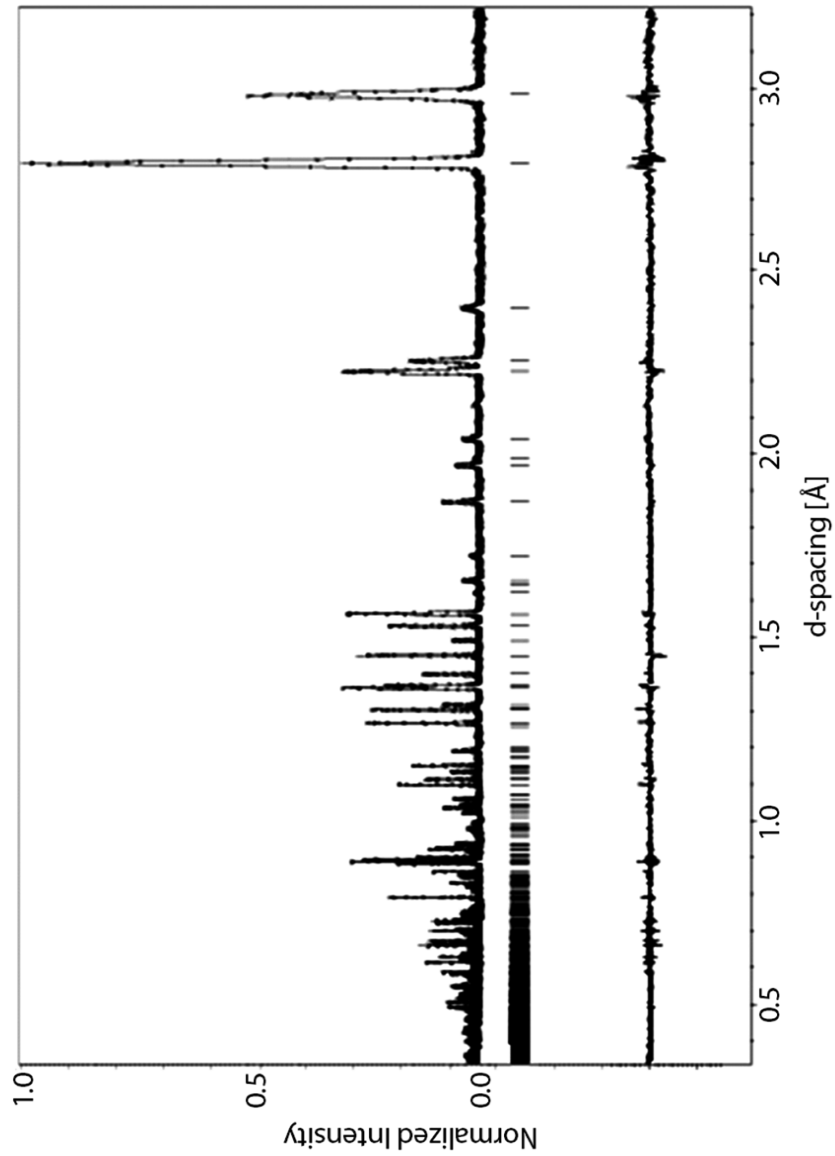


**Figure 7.1:** Block with center of wave lengths  $CWL=1.066 \text{ \AA}$  of powder diffraction pattern performed on  $Mn_{5-x}Fe_xSi_3$   $x=0$  at 100K with refinement. The intensity was normalized to the peak with the highest intensity.

Background of those diffraction patterns is small. Characteristic for this is a narrow line indicating differences between measured data and calculated profile.

In figures 7.1 and 7.2 two blocks (due to two different setups) with refinements are presented. No traces of impurities are visible in each pattern.

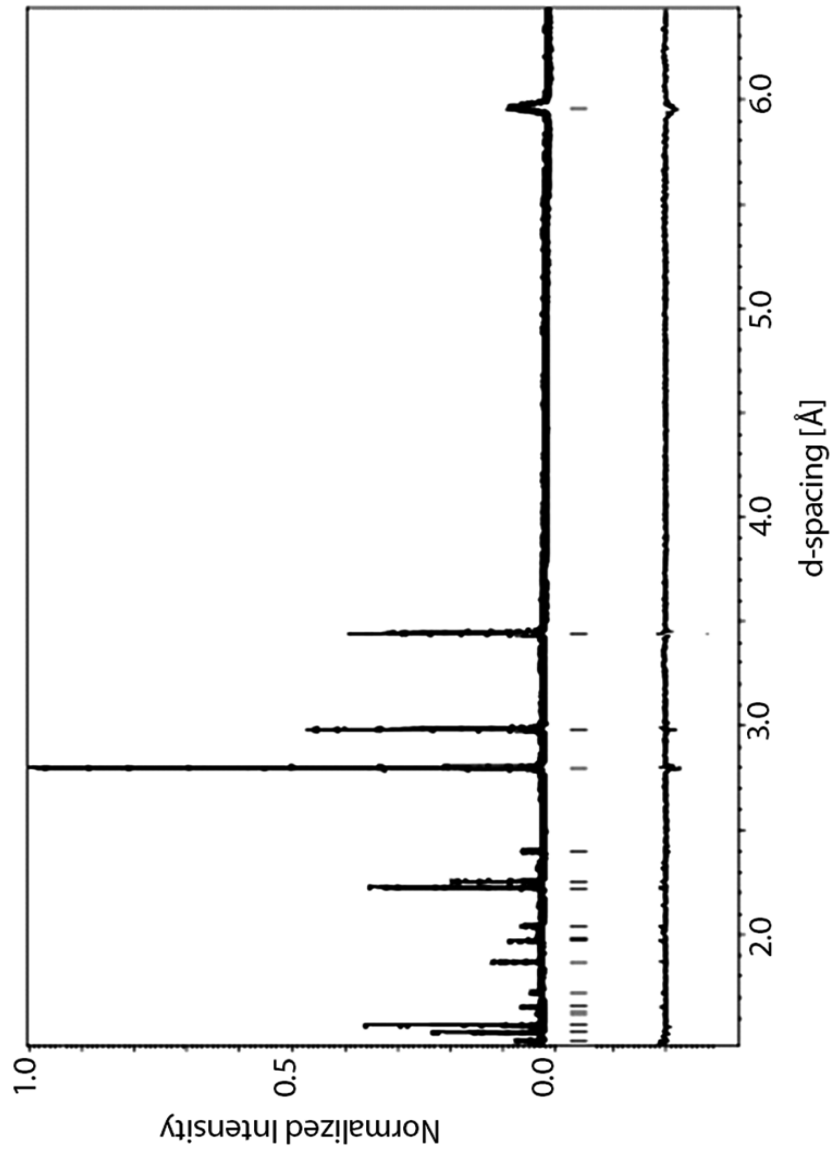


**Figure 7.2:** Block with  $CWL=3.198 \text{ \AA}$  of powder diffraction pattern performed on  $Mn_{5-x}Fe_xSi_3$ ,  $x=0$  at 100K with refinement.

One measurement was performed on  $Mn_{5-x}Fe_xSi_3$   $x=0$  (same batch which was used for measurements on POWGEN) on HB2A at 50K. Diffraction pattern with refinement is presented in figure 7.3. Since HB2A is a CW-instrument the transformation from degree- to d-spacing is calculated simply by using Bragg's law. As instrumental parameters shift, sycos and sysin were used (explained in section A.3).

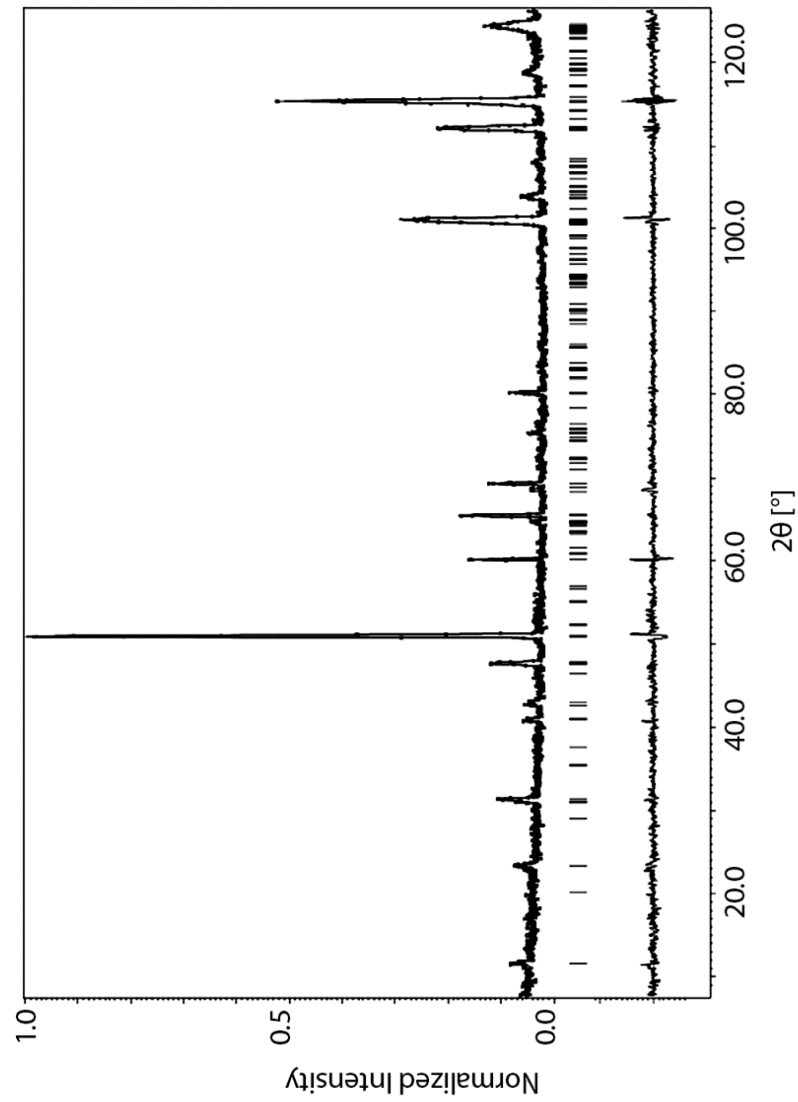


**Figure 7.3:** Neutron powder diffraction pattern taken on  $Mn_{5-x}Fe_xSi_3$   $x=0$  at 50K with a wave length of 2.41 Å. A magnetic field of 4T was applied.



### 7.2.3 Details of refinements performed on diffraction patterns taken on samples $\text{Mn}_{5-x}\text{Fe}_x\text{Si}_3$ $x>0$

#### General qualities of the refinements

In every diffraction pattern taken on one of the samples  $x>0$  regions were excluded as presented in table 7.2. Those regions were excluded in sense of using global cut offs at high or low t-spacing on every block individually. Excluded regions are visible in every block that is presented with refinement.

	block 1 (115°)	block 2 (85°)	block 3 (45°)
Excluded region 1	$5.34 < t < 11.48$	$4.31 < t < 9.97$	$2.47 < t < 8.21$
Excluded region 2	$33.97 < t < 34.32$	$33.83 < t < 34.79$	$46.04 < t < 48.25$

**Table 7.2:** Excluded regions defined in t-spacing used on every diffraction pattern taken on  $x>0$  consisting of the three blocks.

As mathematical formula for transformation from t- to d-spacing polynoms of second degree order was used which. This caused small discrepancies at high values in d-spacing (close to 3 Å and higher).

For every diffraction pattern taken on  $\text{Mn}_{5-x}\text{Fe}_x\text{Si}_3$   $x=1$  and  $x=2$  background was refined using a polynom of 12th degree on a single block. In case of  $\text{Mn}_{5-x}\text{Fe}_x\text{Si}_3$   $x=3$  and  $x=4$  only polynoms of 9th degree were used.

Concerning profile function of peaks (Pseudo Voigt in TOF setting), only parameters Gam1, Gam2, Sig1 and Sig2 were refined leaving all the others zero. No asymmetry was applied.

Atomic occupations and anisotropic displacement parameters were only refined on diffraction patterns taken at 300K for all samples. At low temperatures ( $\text{Mn}_{5-x}\text{Fe}_x\text{Si}_3$   $x=4$ ) displacement parameters were refined using an isotropic model.

Figures 7.4 to 7.6 give an impression of the quality of the refinements especially when looking at the difference patterns. Since one impurity could be detected in  $\text{Mn}_{5-x}\text{Fe}_x\text{Si}_3$   $x=4$  and because of measurements that were performed at low temperature on this material all three blocks are presented here. For each block one GOF value is calculated. Qualities of measurements taken on samples  $\text{Mn}_{5-x}\text{Fe}_x\text{Si}_3$   $x=1,2,3,4$  are very similar.

For  $\text{Mn}_{5-x}\text{Fe}_x\text{Si}_3$   $x=4$  in every diffraction pattern two additional reflections that cannot be indexed with either of the symmetries of the two phases could be detected between 1.21 Å and 1.22 Å on blocks 1 and 2 (centers 115° and 85°) visible in figures A.6 and A.7. The very same reflections could not be detected on forward scattering part of the detectors (figure A.6). This is due to the fact that these peaks were not generated by physical but software conditions. Therefore, such reflections were considered "ghosting", i.e. generated by software used for data processing at the instrument.

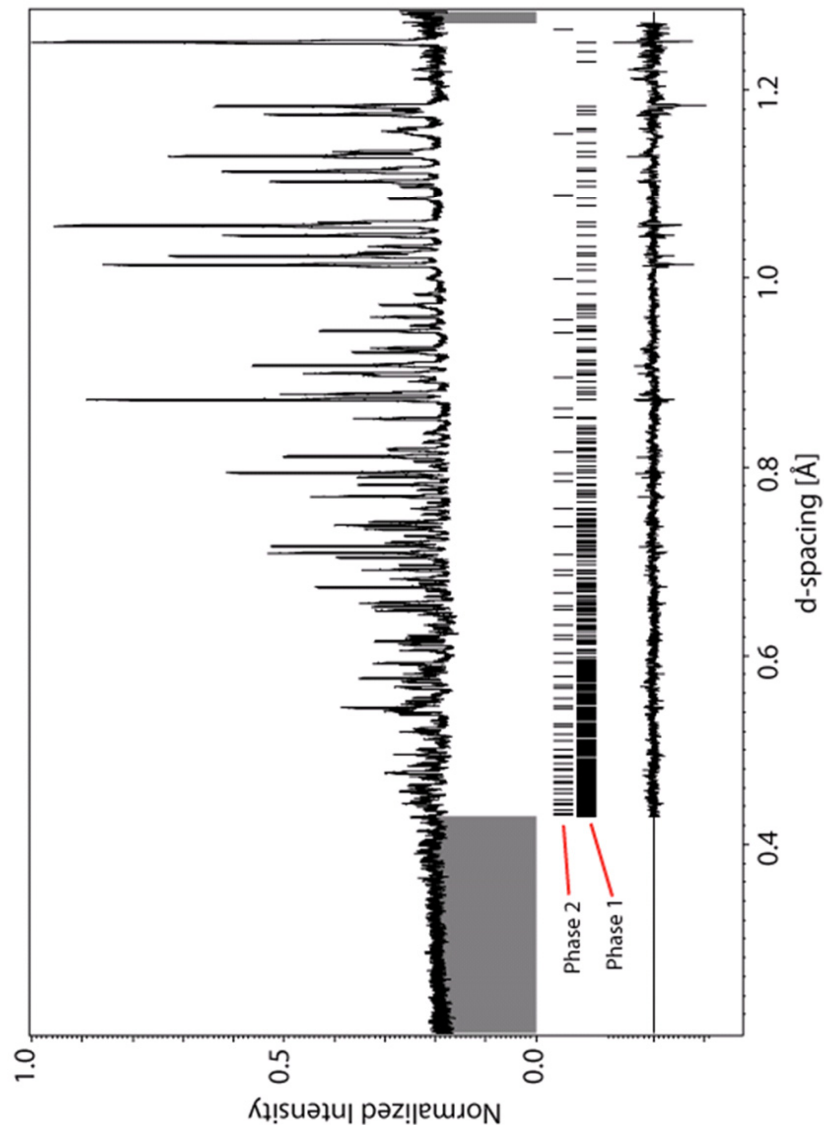


**Figure 7.4:** Block with center at  $115^\circ$  of powder diffraction pattern of  $Mn_{5-x}Fe_xSi_3$   $x=4$  taken at 300K with refinement. GOF-value of this block is 1.32. Stripes in the upper line marked with "phase 2" emerged from impurity (section 7.2.3).

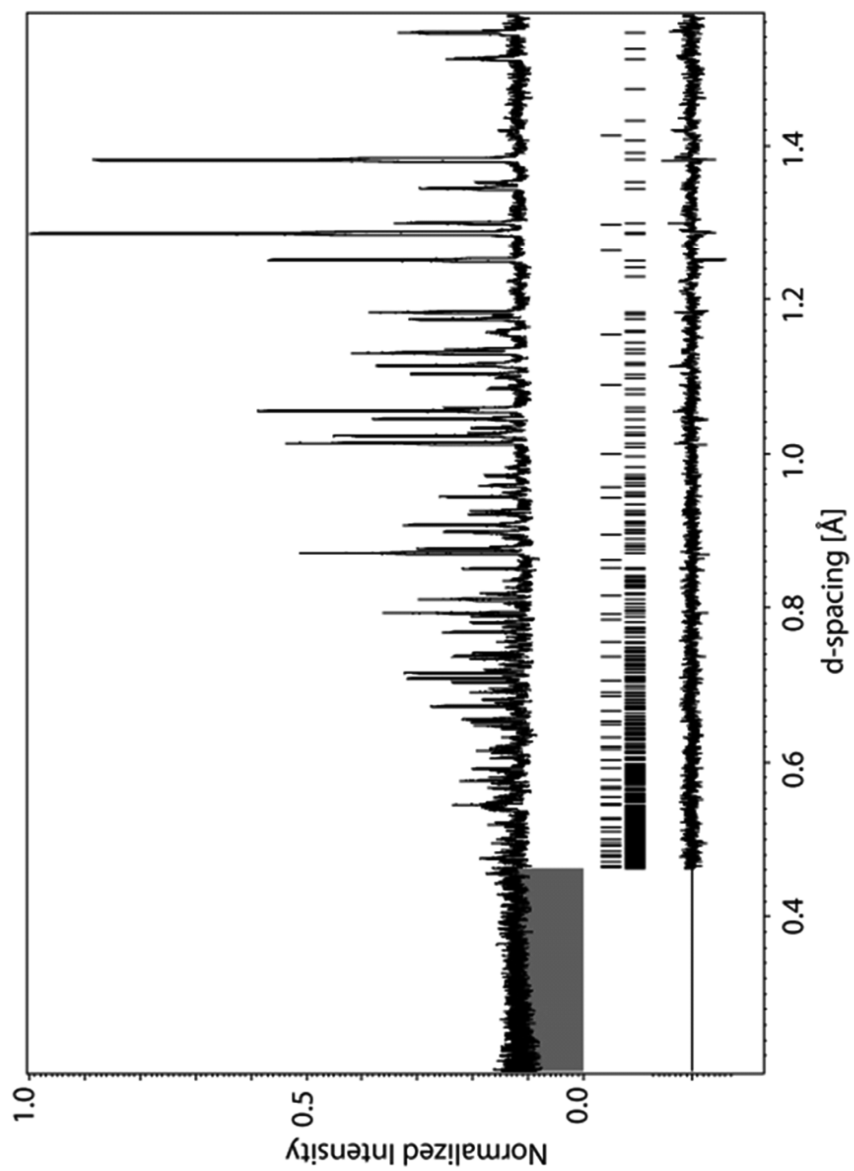


**Figure 7.5:** Block with center at  $85^\circ$  of powder diffraction pattern of  $\text{Mn}_{5-x}\text{Fe}_x\text{Si}_3$   $x=4$  taken at 300K with refinement. GOF-value of this block is 1.08.

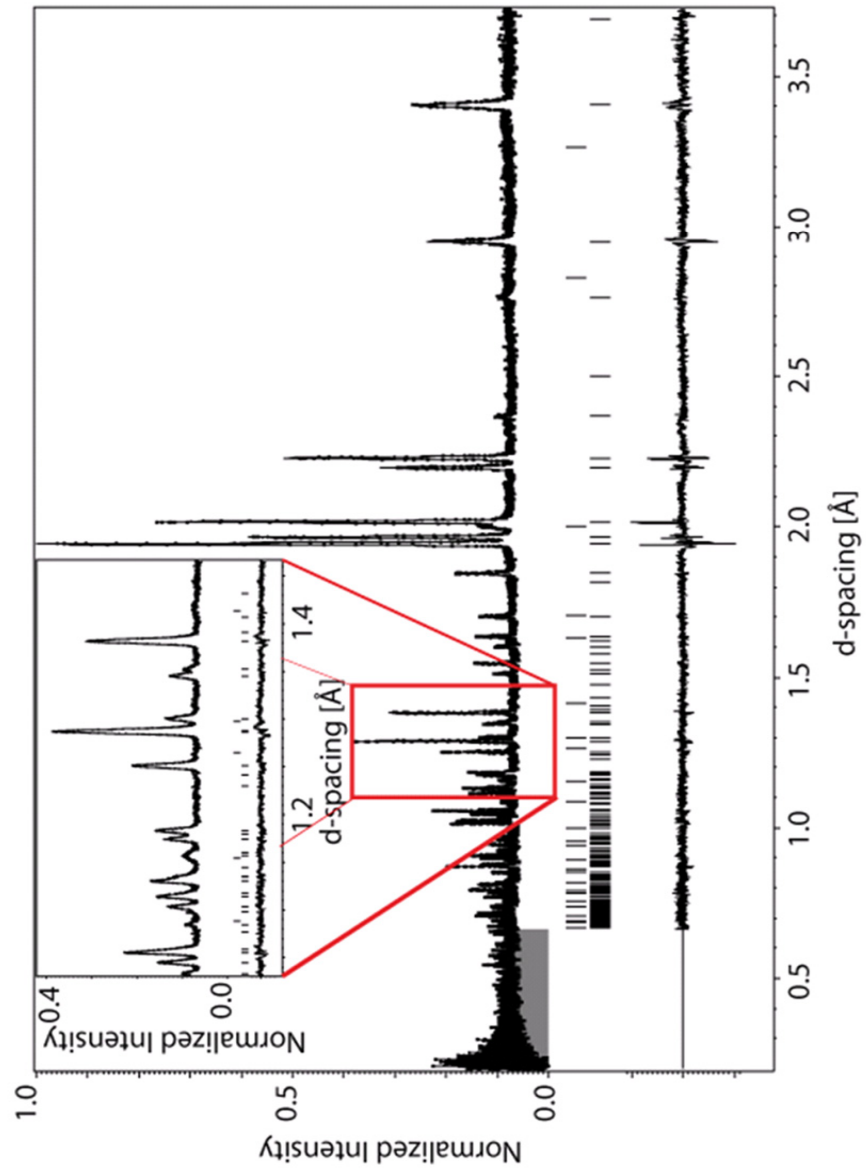


**Figure 7.6:** Block with center at  $45^\circ$  of powder diffraction pattern of  $Mn_{5-x}Fe_xSi_3$   $x=4$  taken at 300K with refinement. GOF-value of this block is 1.21. Left inset presents the part in d-spacing where "ghosting" reflections appeared in the patterns of the other two blocks.

### Impurity phase in sample $\text{Mn}_{5-x}\text{Fe}_x\text{Si}_3$ $x=4$

On diffraction patterns taken on  $\text{Mn}_{5-x}\text{Fe}_x\text{Si}_3$   $x=4$  two phases were used as model for refinements. This additional phase could be identified as  $\text{Mn}_{1.69(3)}\text{Fe}_{1.31(3)}\text{Si}$  with a content of 10.5(9)%. The unit cell of this structure is isometric to the unit cells of  $\text{Fe}_3\text{Si}$  and  $\text{Fe}_3\text{Si}$  [86, 87]. In table 7.3 results of two different refinements performed on diffraction patterns taken on  $\text{Mn}_{5-x}\text{Fe}_x\text{Si}_3$   $x=4$  at 270K are presented (results of all three blocks). Since there are significant differences in the results between the two refinements (especially GOF-value) the phase of impurity was chosen to be included in every model used for refinements performed on diffraction patterns taken on sample  $\text{Mn}_{5-x}\text{Fe}_x\text{Si}_3$   $x=4$ .

			M1		M2		Si	
I	$a$ [Å]	$c$ [Å]	U [Å <sup>2</sup> ]	M [ $\mu_B$ ]	U [Å <sup>2</sup> ]	M [ $\mu_B$ ]	U [Å <sup>2</sup> ]	GOF
Y	6.80814(2)	4.73022(2)	0.0040(1)	-0.1(6)	0.0042(1)	1.67(4)	0.0044(1)	1.18
N	6.80811(2)	4.73021(2)	0.0045(1)	-0.1(6)	0.0050(1)	1.70(4)	0.0050(1)	1.24

**Table 7.3:** Comparing results of refinements of non-impurity compounds when phases of impurities are included (first one, marked with Y) and not included (second one, marked with N) in the refinement. Conducted on data taken on sample  $\text{Mn}_{5-x}\text{Fe}_x\text{Si}_3$   $x=4$  at 270K.

Concerning the impurity in compound  $\text{Mn}_{5-x}\text{Fe}_x\text{Si}_3$   $x=4$ , still, the driving force of the MCE is the pure composition. This is due to the fact that the magnetization measurements do not indicate the presence of another phase which can only mean that the part of the sample used for these measurements is pure or that the magnetism of the impurity does not have an impact.

$\text{Mn}_{5-x}\text{Fe}_x\text{Si}_3$   $x=4$  is the only compound in this family exhibiting magnetic ordering at 300K. Therefore a magnetic model with moments alligned parallel to the  $c$ -axis was applied. The refined values of the magnetic moments turned out to be very much depending on the starting values used for the refinement. Just refining magnetic and nuclear structures at the same time resulted in ferrimagnetic behaviour. This could be due to an overload of the refinement because of the number of refined parameters. Therefore, the existence of another more stable model cannot be ruled out. The results of the refined magnetic structure cannot be considered reliable. Notice that no additional (magnetic) reflections were detected in any diffraction pattern taken on  $\text{Mn}_{5-x}\text{Fe}_x\text{Si}_3$   $x=4$  (except ghosting and impurity).

The quality of diffraction patterns taken on samples with  $x>0$  is very similar (except for  $\text{Mn}_{5-x}\text{Fe}_x\text{Si}_3$   $x=3$ ) since they were all performed with the same instrumental setup. This does not only mean that every data set of a measurement consists of three blocks, but that for transformation between  $t$ - and  $d$ -spacing a polynomial of second degree was used. Therefore small discrepancies between diffraction patterns and refined models appear often at high  $d$ -spacing. This is not the case for  $\text{Mn}_{5-x}\text{Fe}_x\text{Si}_3$   $x=0$ , a different model for the transformation from  $t$ - to  $d$ -spacing was used here.

In samples  $x<4$  no impurities could be detected. No special regions were excluded.

### Qualities of refinements

In figure 7.7 GOF-values of refinements are presented. Even though having used two different setups for taking diffraction patterns GOF-values are very similar when compared to each other.

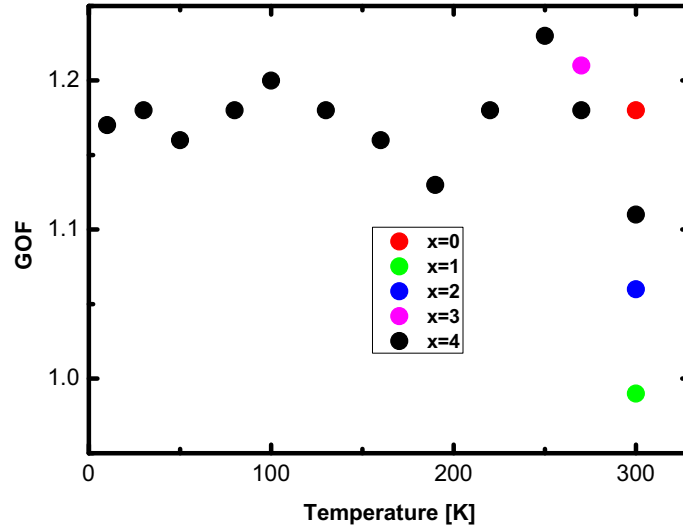


**Figure 7.7:** GOF-values of refinements performed on diffraction patterns of  $Mn_{5-x}Fe_xSi_3$  as function of  $x$  and temperature. All diffraction patterns taken at 300K except  $Mn_{5-x}Fe_xSi_3$   $x=3$ , which was taken at 270K.

Those values give rise to consider results of these refinements reasonable. Notice that those GOF-values emerged from taking all of the three blocks into account.

## 7.2.4 Results of refinements of $Mn_{5-x}Fe_xSi_3$ at room temperature

### Nuclear structure

Site	Atom	Coordination	Multiplicity	Wyckoff letter
M1	Mn/Fe	(1/3,1/3,0)	4	d
M2	Mn/Fe	(x,0,1/4)	6	g
Si	Si	(x,0,1/4)	6	g

**Table 7.4:** Multiplicities and Wyckoff letter of atoms in hexagonal space group  $P6_3/mcm$  (193) of samples  $Mn_{5-x}Fe_xSi_3$  [28, 88]. Name is reference which is used from now on for atoms occupying the corresponding Wyckoff position.

At room temperature all samples crystallize in hexagonal space group  $P6_3/mcm$  (193) which was already reported in [28, 77]. In table 7.4 atomic positions with crystallographic conditions are presented.

Figure 7.8 illustrates a projection of the hexagonal unit cell of  $Mn_{5-x}Fe_xSi_3$  along the  $c$ -axis. In the right part of this figure the magnetic unit cell used for refinements on  $Mn_{5-x}Fe_xSi_3$   $x=4$

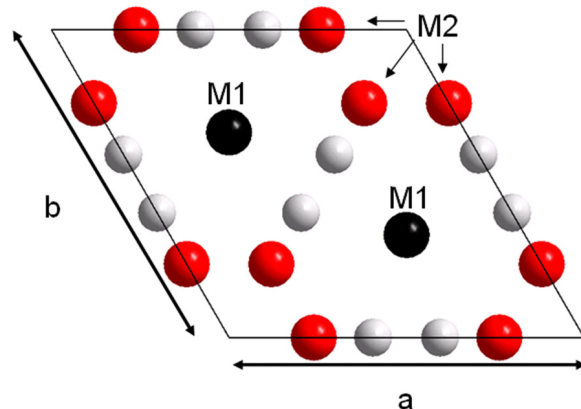


**Figure 7.8:** Projection along the  $c$ -axis of the unit cell of  $\text{Mn}_{5-x}\text{Fe}_x\text{Si}_3$  for compositions  $0 < x < 4$ . Black and red spheres represent Mn or Fe while silver spheres Si atoms, respectively.

is presented. A classical way to describe this structure is to divide the local environments into two Mn/Fe atoms (here called M1 and M2) which occupy Wyckoff positions 4d and 6g. The M1 atom is surrounded by 6 equidistant Si atoms with a distance of  $2.4305(5) \text{ \AA}$  ( $\text{Mn}_{5-x}\text{Fe}_x\text{Si}_3$   $x=0$ ) which can be considered as distorted octahedra. Those  $[\text{M1Si}_6]$  polyhedra are bicapped, through  $\text{Si}_3$  triangular faces, by two additional M1 atoms. The M1-M1 range arranged parallel to  $c$ -axis is the shortest distances observed in the crystal structure of  $\text{Mn}_{5-x}\text{Fe}_x\text{Si}_3$ -series with  $d_{\text{M1-M1}}=2.4089(5) \text{ \AA}$  ( $\text{Mn}_{5-x}\text{Fe}_x\text{Si}_3$   $x=0$ ). These  $[\text{Mn1Si}_6]$  polyhedra share triangular faces with their analogs forming quasi infinite  $1_{\infty} [\text{M1Si}_3]$  chains. Surrounding these chains atoms occupying M2-site are connected forming vacant  $[\infty(\text{M2})_6]$  distorted octahedron with distances of  $2.9054(3) \text{ \AA}$  ( $\text{Mn}_{5-x}\text{Fe}_x\text{Si}_3$   $x=0$ ) between two neighboured M2 atoms. These  $[\square(\text{M2})_6]$  octahedra share triangular faces creating quasi infinite  $1_{\infty} [\square(\text{M2})_3]$  chains. This unique description concerning quasi-infinite chains is illustrated in figure 7.9.

Lattice constants as function of Fe content extracted from refinements performed on measurements taken at 300K (except  $\text{Mn}_{5-x}\text{Fe}_x\text{Si}_3$   $x=3$ , which was taken at 270K) are presented in figure 7.10. Both lattice constants are contracted when content of Fe is increased. The effect of contraction of the lattice constants is in the order of  $0.12 \text{ \AA}$  and therefore significant, even though it is "only one electron which was added to a certain atom".

Lattice constant  $a$  seems to scale linear in Fe-content. The fact that lattice constant  $c$  does not scale linear could be the result of different features due to magnetism at low temperatures (phase transitions are discussed in section 5.2), for example, which effect lattice constant  $c$  in the first place. This would make sense since the magnetic behaviour in this family of compounds is rather complex (figures 5.1 (a-f) and 5.2).

Lattice constant  $a$  obeys Vegard's law which proposes a linear relation between crystal lattice and concentration of a constituent element [89]. The intersection extrapolated to  $x=0$  of the linear fits for lattice constant  $a$  is  $6.9148(1) \text{ \AA}$ . Within an deviation of  $0.0003 \text{ \AA}$  the value coincides with the lattice constant  $a$  refined for  $\text{Mn}_{5-x}\text{Fe}_x\text{Si}_3$   $x=0$  (table 7.5).

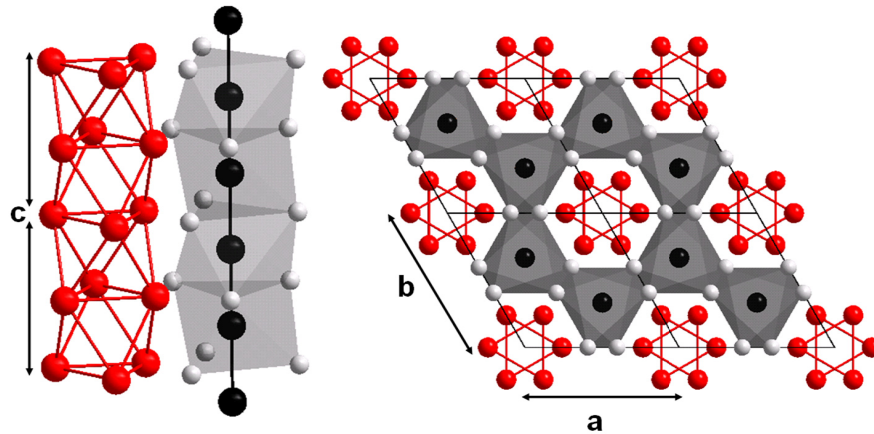


**Figure 7.9:** From left to right:  $1_{\infty}[\square(M2)_3]$  chains,  $1_{\infty} [M1Si_3]$  chains and unit cell from above indicating the two chains.

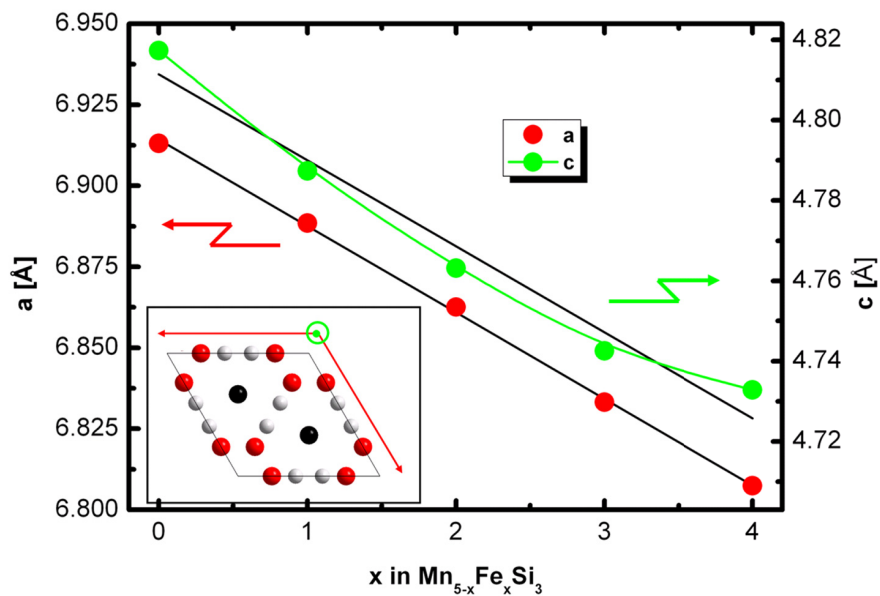


**Figure 7.10:** Lattice constants  $a$  and  $c$  of  $Mn_{5-x}Fe_xSi_3$  as function of  $x$ . All taken from refinements on diffraction patterns taken at 300K except  $Mn_{5-x}Fe_xSi_3$   $x=3$ , which was taken at 270K. Black lines are linear fits. The green curve is a guide to the eye. Colors of points in diagram refer to colors of marked lattice constants in unit cell in the inset. Error bars are smaller than points in diagram.

Lattice constant  $c$  does not obey Vegard's law. The intersection is  $4.808(6)\text{Å}$  for this constant. This is an error of  $0.01\text{Å}$  in comparison to lattice constant  $c$  of  $Mn_{5-x}Fe_xSi_3$   $x=0$ . Furthermore, the dependence of this lattice constant does not seem to be linear in temperature. The fact that this lattice constant does not obey Vegard's law can be considered anomalous.



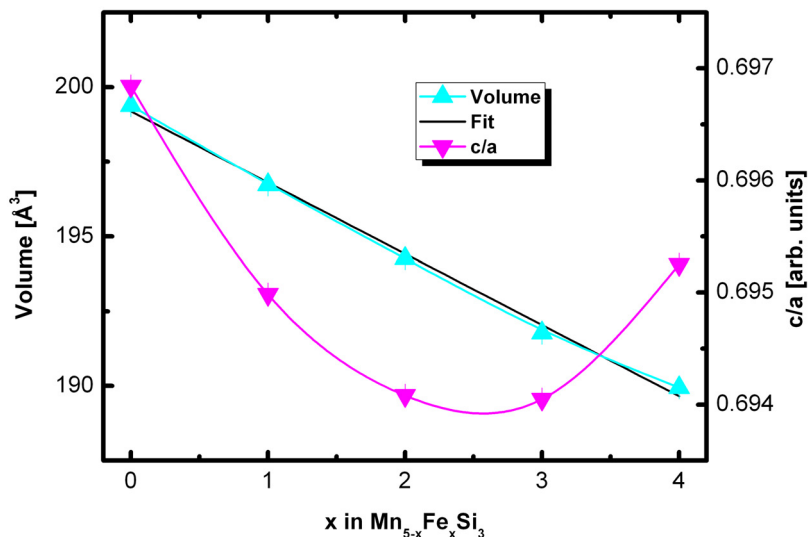


**Figure 7.11:** Volume and  $c/a$  of  $\text{Mn}_{5-x}\text{Fe}_x\text{Si}_3$  as function of  $x$ . All taken from refinements on diffraction patterns taken at 300K except  $\text{Mn}_{5-x}\text{Fe}_x\text{Si}_3$   $x=3$ , which was taken at 270K. The black line is a linear fit. The other two lines are only guides to the eye.

The additional electron which is added when Mn is substituted with Fe obviously leads to different orbital distributions with less spatial extension. This is probably another link between magnetic complexity and the content of Fe. Differences of the presented lattice constants to [28, 77] could originate from different sets of instrumental parameters. For example, the value of the lattice constant  $a$  for the composition  $\text{Mn}_{5-x}\text{Fe}_x\text{Si}_3$   $x=4$  is proposed to be  $6.8054(7)\text{Å}$  and  $c$   $4.7290(5)\text{Å}$  [28]. In [77] the lattice constants are reported to be  $6.8004(5)\text{Å}$  ( $a$ ) and  $4.7298(8)\text{Å}$  ( $c$ ). This is an offset of up to  $\sim 0.07\text{Å}$  in lattice constant  $a$  in comparison to the value presented in table 7.5. Lattice constant  $c$  is obviously less affected.

The fact that two different values are presented for each constant of  $\text{Mn}_{5-x}\text{Fe}_x\text{Si}_3$   $x=4$  could be due to the possible impurity content and the corresponding difference of stoichiometry of  $\text{Mn}_{5-x}\text{Fe}_x\text{Si}_3$ . In [77] the crystallization of impure phases ( $\text{Fe}_{1-x}\text{Mn}_x\text{Si}$  and  $\text{Fe}_{3-x}\text{Mn}_x\text{Si}$ ) is reported. Furthermore, in [77] the lattice constants were determined by Guinier-Haegg photographs.

In [28] all samples are claimed to be pure. Here, since the neutron diffraction measurements were performed in the 70s on an old instrument the quality of the data was maybe not sufficient to determine the exact composition.

The volume of the unit cell and  $c/a$  as function of Fe content is presented in figure 7.11. Both values do not depend linear on the content of Fe.

The fact that the volume depends almost linear of the content is due to lattice constant  $a$ , which obeys Vegard's law.

The value  $c/a$  has a minimum between  $x=2$  and  $x=3$ . The value increases between  $x=3$  and  $x=4$ . This complex behaviour fits to lattice constant  $c$  as function of the Fe-content (7.10) and the magnetism (figure 5.2).

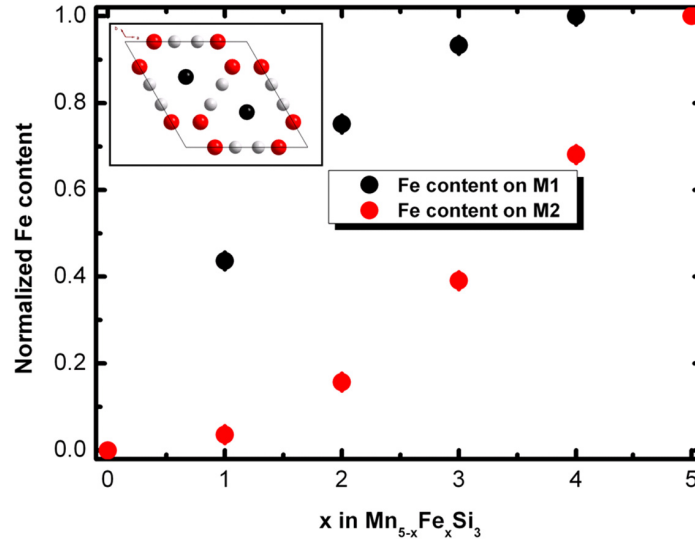


**Figure 7.12:** Occupations of Fe of the two atomic positions M1 and M2 in  $Mn_{5-x}Fe_xSi_3$  as function of  $x$ . All taken from refinements on diffraction patterns taken at 300K except  $Mn_{5-x}Fe_xSi_3$   $x=3$ , which was taken at 270K. Inset presents the unit cell of these structures. Colors of points in diagram refer to colors of atoms in unit cell in the inset. Error bars are smaller than points in diagram.

When Mn is substituted with Fe one could expect a 50:50 occupation of the two atoms on the two atomic positions M1 and M2. This assumption does not hold as can be seen in figure 7.12, which is simply due to the fact that atomic positions M1 and M2 are not equivalent. They differ for example in bonding lengths which is very clear, since neighbored atoms on position M2 share very short distances of  $2.4089(5) \text{ \AA}$  ( $Mn_{5-x}Fe_xSi_3$   $x=0$ ) to each other. There are no similar features for position M1. No vacancies were proposed

Results of refinements reveal that Fe prefers to occupy position M2. For composition  $Mn_{5-x}Fe_xSi_3$   $x=4$  no Mn could be detected on this position anymore even though there is still 20% of Mn in the compound. This is qualitatively in agreement with [28]. The occupation of Fe presented in the figure of this work is a little broader than the one presented in [38] but they still look very similar.

Isotropic displacement parameters of those compositions as function of Fe-content are presented in figure 7.13.

The displacement parameter on M1 almost seems to be constant. The total difference between minimum ( $x=2$ ) and maximum (at  $x=1$ ) is  $\sim 0.0004 \text{ \AA}^2$ . Therefore, the Fe content dependence of the displacement parameter on M1 can be considered weak.

This is in contrast to the displacement of atoms on sites M2 and Si with maximum values occurring at  $x=0$ , go down when Fe content is increased until they have reached a minimum

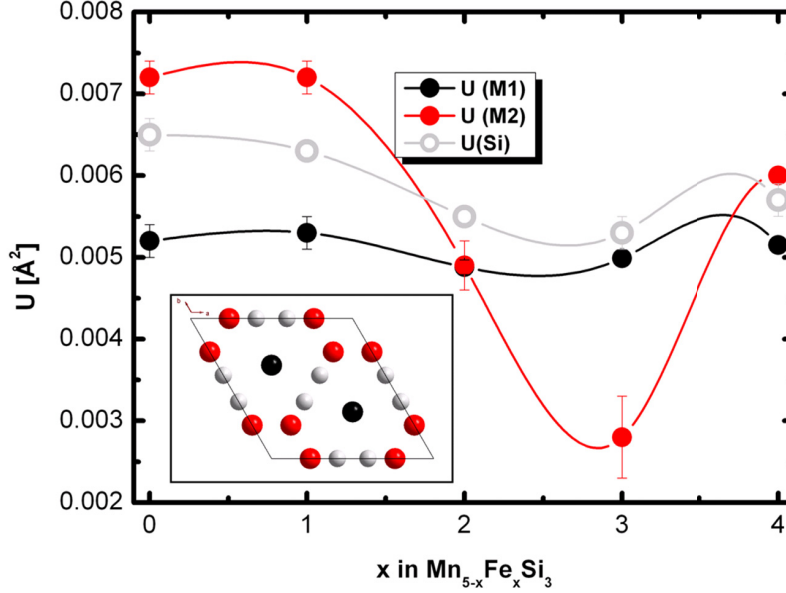


**Figure 7.13:** Isotropic displacement parameters of  $\text{Mn}_{5-x}\text{Fe}_x\text{Si}_3$  as function of  $x$ . All taken from refinements on diffraction patterns taken at 300K except  $\text{Mn}_{5-x}\text{Fe}_x\text{Si}_3$   $x=3$ , which was taken at 270K. Inset presents the unit cell of these structures. Colors of points in diagram refer to colors of atoms in unit cell in the inset. Lines between points of measurements are only guides to the eye.

at  $x=3$ . At  $x=4$  thermal displacement parameters increase again. The total difference between minima and maxima is  $\sim 0.004 \text{ \AA}^2$  for M2 and  $\sim 0.001 \text{ \AA}^2$  for Si.

The Fe content dependence of lattice constant  $c$ , quotient  $c/a$  and displacement parameters on M2 and Si coincide qualitatively with each other. The diagrams with maximum values at  $x=0$  and minimum values at (or close to)  $x=3$  look similar.

One might conclude that these values reflect the varying magnetic behaviour of  $\text{Mn}_{5-x}\text{Fe}_x\text{Si}_3$  as function of  $x$  at low temperatures, even though all compounds are paramagnetic close to 300K (except  $x=4$  with ferromagnetic behaviour). The magnetic structures range from commensurate ( $x=0,1,2$ ) to incommensurate antiferromagnetism ( $x=3$ ) and finally ferromagnetism ( $x=4$ ). These features were discussed in section 5.2.

In literature for  $\text{Mn}_{5-x}\text{Fe}_x\text{Si}_3$   $x=0$  the values of the magnetic moments on M1 or positions which are equivalent to M1 (orthorhombic [39, 42] and monoclinic [40] structures are proposed at low temperatures) is always small in comparison to moments on other positions. This is similar to  $\text{Mn}_{5-x}\text{Fe}_x\text{Si}_3$   $x=4$  with large magnetic moments on M2 and small moments on M1 [28, 38]. To the best of the knowledge of the author of this thesis, no paper reports for any composition in  $\text{Mn}_{5-x}\text{Fe}_x\text{Si}_3$  about magnetic moments which are larger on M1 than on M2.

Unfortunately, detailed information about the magnetic structures of  $\text{Mn}_{5-x}\text{Fe}_x\text{Si}_3$   $0 < x < 4$  is missing. Still, a general proposal how the nuclear structure is linked to the magnetic behaviour can be introduced:

The bondings on position M2 are the driving force of the magnetic behaviour, since the magnetic moments on site M1 tend to be small (information about  $Mn_{5-x}Fe_xSi_3$   $0 < x < 4$  is missing). The change of the crystal structure, for example the contraction of the unit cell alter the exchange interaction. Therefore, all properties which are linked to the atom on site M2 reflect this behaviour (even in the paramagnetic state). Since lattice constant  $c$  does not obey Vegard's law in contrast to  $a$ , magnetic interactions along the  $c$ -axis could play an important role.

The lattice constant of the impurity  $Mn_{1.69(3)}Fe_{1.31(3)}Si$  converged to a value of  $5.6580(3)\text{\AA}$ . Comparing this to literature [90] reveals a difference of  $\sim 0.02\text{\AA}$ , assuming the composition of the impurity is  $Mn_{1.7}Fe_{1.3}Si$ . This is another hint for discrepancies with the instrumental parameters.

x	a [ $\text{\AA}$ ]	c [ $\text{\AA}$ ]	Fe(M1)	Fe(M2)	x(M2)	x(Si)	GOF
0	6.91312(3)	4.81735(3)	0	0	0.2358(1)	0.5991(1)	1.18
1	6.88848(2)	4.78739(2)	0.436(2)	0.036(1)	0.23223(5)	0.59830(6)	0.99
2	6.86256(2)	4.76318(2)	0.752(2)	0.157(1)	0.2236(2)	0.59813(8)	1.06
3	6.83318(2)	4.74256(2)	0.933(2)	0.391(1)	0.2539(2)	0.5992(1)	1.21
4	6.80742(2)	4.73286(2)	1	0.682(2)	0.24310(5)	0.6007(1)	1.11

**Table 7.5:** Lattice constants  $a$  and  $c$ , occupation of Fe on M1 and M2,  $x(M2)$ ,  $x(Si)$  of  $Mn_{5-x}Fe_xSi_3$  as function of  $x$ . All taken from refinements on diffraction patterns at 300K and 270K just for  $x=3$ .

## Magnetic structure

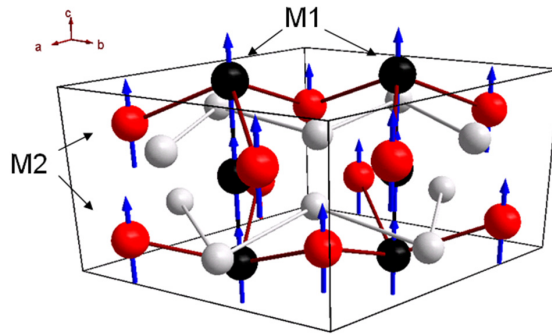


**Figure 7.14:** Unit cell with magnetic moments applied parallel to  $c$ -axis used as model for refinements on diffraction patterns taken on  $Mn_{5-x}Fe_xSi_3$   $x=4$ . Atomic positions of Mn are denoted in both parts.

Material with composition  $Mn_{5-x}Fe_xSi_3$   $x=4$  is the only compound of the family exhibiting magnetic ordering at 300K. The diffraction pattern could be refined with the space  $P6_3/mc'm'$  with magnetic moment applied parallel to the  $c$ -axis as it is proposed in [28]. The used magnetic form factors are discussed in section A.4. On atomic position M1 the magnetic moment converged to a value of  $1.12(7)\mu_B$  and the moment on atomic position M2 to a value of  $1.06(5)\mu_B$ . The magnetic moments have not fully aligned at 300K, as can be seen in the magnetization

measurement (figure 5.1 (e,f)). Therefore the refined magnetic moments could not have been evaluated properly due to the effect of fluctuations. The magnetic structure is discussed in detail in section 7.2.6.

The magnetic properties of the phase  $\text{Fe}_{3-x}\text{Mn}_x\text{Si}$  vary with the content of Mn [91]. The Curie temperature of the impurity is proposed to be below 250K, even for compositions with less Mn [90, 92]. The magnetic moments are in the order of  $0.5\mu_B$  [90], which is too small to get refined properly. This is due to the small content of 10.5(9)%. Intensities of magnetic reflections depend on  $d$  in  $d$ -spacing. Therefore, the magnetism of this phase would have to be refined on the reflection at  $\sim 2.0\text{\AA}$  in  $d$ -spacing, which is the only reflection at high  $d$ -spacing with a reasonable intensity. The magnetic structure of this impurity was therefore not refined.

## 7.2.5 Results of refinements of $\text{Mn}_{5-x}\text{Fe}_x\text{Si}_3$ $x=0$ at low temperatures

Neutron powder diffraction data have been collected at 100K, 90K, 80K and 70K in order to analyze and understand the antiferromagnetic phase stable between  $T_N1=100(1)\text{K}$  and  $62(1)\text{K}$  (figure 5.1 (a) and table 5.1). Lattice constants refined on diffraction pattern taken at 100K converged to  $a=b=6.88965(2)\text{\AA}$  and  $c=4.80011(2)\text{\AA}$ . Displacement parameters did not show any significant changes as function of temperature.

At 90K the best refinement could be performed using orthorhombic space group Cmmm which is a subgroup of hexagonal space group  $P6_3/mcm$ . Mathematic transformation from hexagonal to orthorhombic space group is  $a = ah$ ,  $b = ah + 2bh$  and  $c = ch$ .  $ah$ ,  $bh$  and  $ch$  refer to the hexagonal unit cell. The cell parameters of the orthorhombic structure used in the refinement converge to  $a=6.89695(2)\text{\AA}$ ,  $b= 11.9085(3)\text{\AA}$  and  $c= 4.79666(3)\text{\AA}$ .

Comparing results of refinements performed on data taken at 100K and 90K  $a$  distortion of the lattice parameters was seen. Cell parameter  $a$  increased and  $b$  decreased due to the phase transition. Still the volume of the unit cells remained almost constant.

90K, cell parameters: $a= 6.89695(2)\text{\AA}$ , $b=11.9085(3)\text{\AA}$ and $c=4.79666(3)\text{\AA}$					
Atom	Wyckoff letter	x	y	z	U [ $\text{\AA}^2$ ]
M1	8e	0	0.33245(14)	0	0.00208(15)
M21	4c	-0.2637(3)	0.5	-0.25	0.0011(3)
M22	8g	-0.6175(2)	0.38271(11)	-0.25	0.0035(2)
Si1	4c	0.1002(2)	0.5	-0.25	0.0023(4)
Si2	8g	-0.29949(19)	0.70028(10)	-0.25	0.0033(2)

**Table 7.6:** Refined atomic parameters.

Due to the structural phase transition in  $\text{Mn}_{5-x}\text{Fe}_x\text{Si}_3$   $x=0$  atomic position M2 in hexagonal setting was split into two atomic positions M21 and M22 which are introduced in the orthorhombic space group Cmmm. The phase transition could be identified in the diffraction pattern by splitting of peaks and emerging of additional reflections. Additional peaks appeared close to  $3.3\text{\AA}$  and  $3.4\text{\AA}$  and  $4.4\text{\AA}$  and  $4.5\text{\AA}$  in  $d$ -spacing. The magnetic propagation vector for this new structure is parallel to the  $b$ -axis in the orthorhombic unit cell, which is in agreement with [39, 41] and in contrast to [42]. With respect to the propagation vector the new magnetic superspace

group is  $Ccmm1'$  ( $0\beta 0$ ) $00ss$  with  $\mathbf{q} = (0, \beta, 0) = \beta^*$ . The magnetic structure was refined using the option of magnetic waves in program Jana2006. GOF-value of the final refinement including 36 parameters is 1.85. Results of the refinement performed on diffraction pattern taken at 90K are presented in table 7.6.

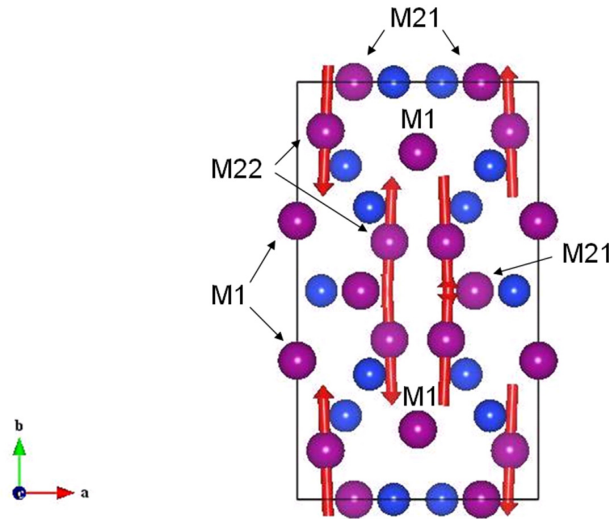


**Figure 7.15:** Magnetic unit cell of  $Mn_{5-x}Fe_xSi_3$   $x=0$  extracted from refinement performed on diffraction pattern taken at 90K.

The 1D antiferromagnetic structure is shown in figure 7.15. Magnetic moments point almost antiparallel to each other along  $b$ -axis with a small rotation around the  $c$ -axis. This is exactly the same magnetic unit cell proposed by [39]. The value of the refined magnetic moment on site M22 is  $1.53(6)\mu_B$  which fits to value ( $1.48\mu_B$ ) presented in literature [39]. Those values meet physical expectations and therefore strengthens the use of this model for the refinement.

There are a lot of reasons explaining why only 1/3 of all the Mn atoms carry an ordered magnetic moment in that phase. One reason could be the very short distance of atoms occupying position M1. Furthermore M21 atoms and M22 atoms form triangular arrangements around M1. Therefore a model proposing magnetic frustration would meet expectations [93] since antiferromagnetic ordering could only be exhibited by moments pointing into the direction of position M1. Assuming the existence of magnetic frustration the nature of short range ordering observed in the magnetization measurement could be explained. Refinements on diffraction patterns taken at lower temperatures indicate bigger magnetic moments with values of  $1.74(6)\mu_B$  (80K) and  $1.89(6)\mu_B$  (70K). Additionally the magnetic moment starts to tilt which can be seen in figure 7.16.

At 60K the magnetic ordering is altered due to the phase transition taking place at 62(1)K (figure 5.1 (a) and table 5.1). In the diffraction pattern this transition could be detected due to the splitting of magnetic peaks at  $4.5\text{ \AA}$  (inset in figure 7.18). The reflections could be indexed as  $(0\ 1\ 1\ 0)$  and  $(1\ 2\ 0\ 0)$ . This change in the diffraction pattern can only be refined using a model

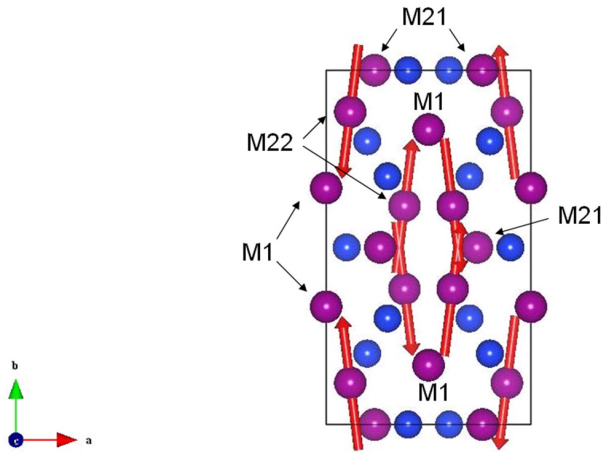


**Figure 7.16:** Magnetic unit cell of  $\text{Mn}_{5-x}\text{Fe}_x\text{Si}_3$   $x=0$  extracted from refinement performed on diffraction pattern taken at 70K.

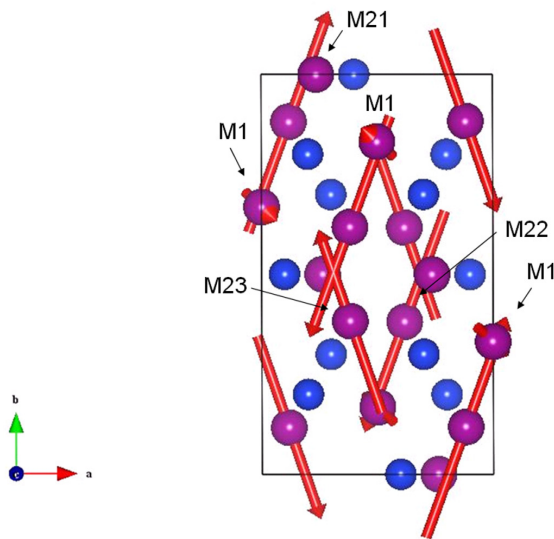


**Figure 7.17:** Magnetic unit cell of  $\text{Mn}_{5-x}\text{Fe}_x\text{Si}_3$   $x=0$  extracted from refinement performed on diffraction pattern taken at 60K. The second atom on position M21 has disappeared due to the different space group in comparison to the unit cell at 70K 7.16.

with a monoclinic magnetic unit cell. Even though first attempts for refining the data made use of a model with superspace group  $\text{P}2_1/\text{m}1'(\frac{1}{2}00)0\text{ss}$ , a better refinement could be performed

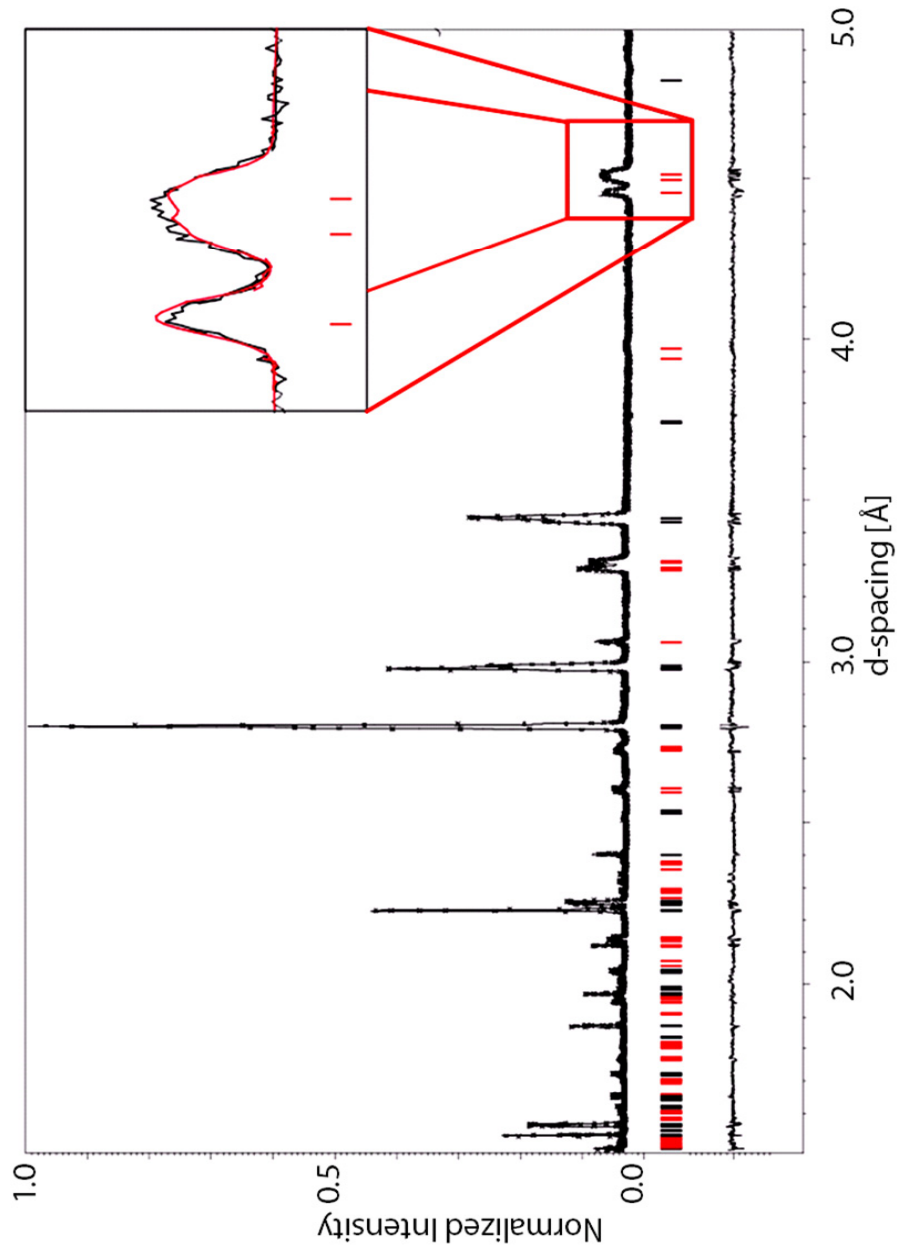


**Figure 7.18:** Block with  $CWL=1.066 \text{ \AA}$  of powder diffraction pattern performed on  $Mn_{5-x}Fe_xSi_3$   $x=0$  at 60K on POWGEN with refinement.



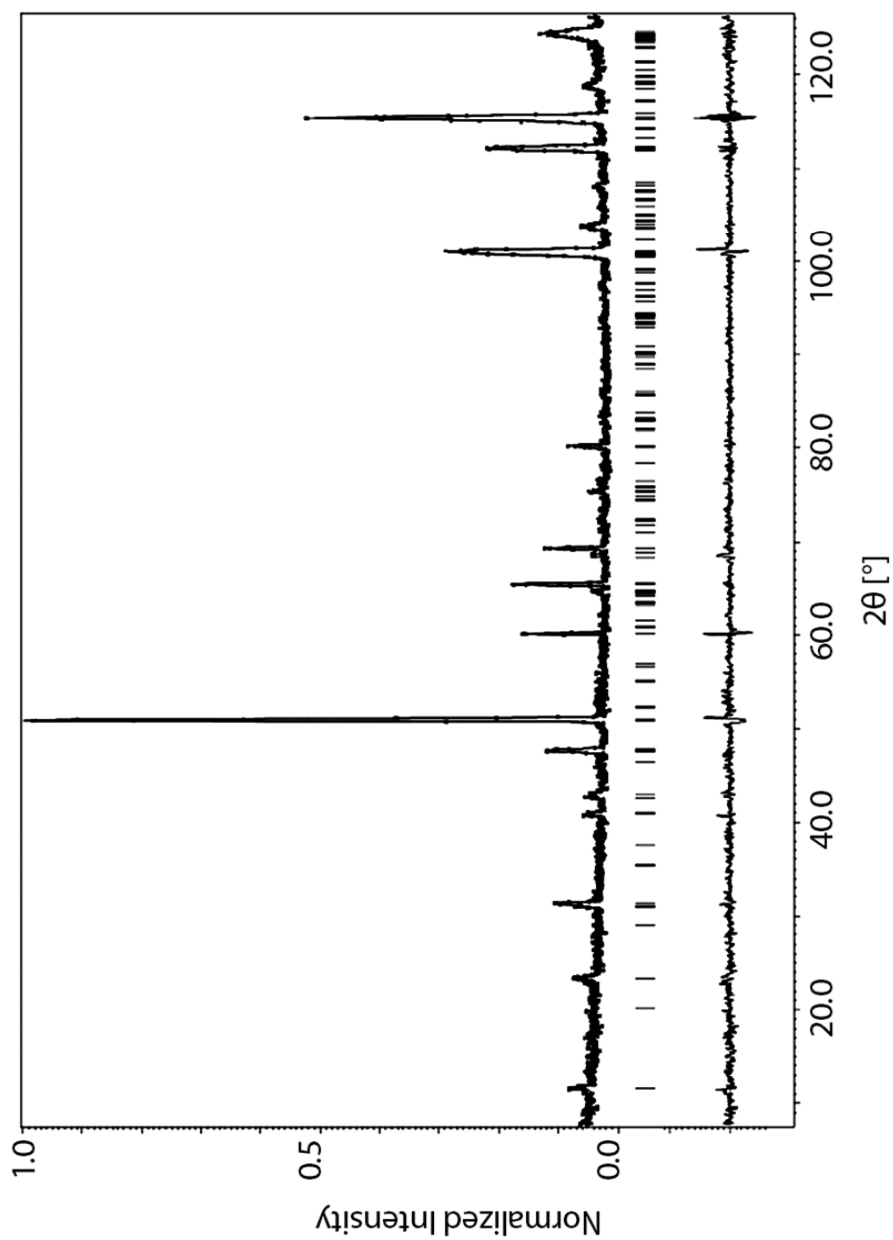


**Figure 7.19:** Block with  $CWL=1.066\text{ \AA}$  of powder diffraction pattern performed on  $Mn_{5-x}Fe_xSi_3$   $x=0$  at 50K on HB2A at an applied field of 4T with refinement.

using non-standard setting  $C21/m1'(010)0ss$ . In the context of the simultaneous appearance of nuclear and magnetic ordering this space group seems to be most reasonable since many other space groups have been attempted to be used in the model for refinements. In figure 7.16 the magnetic unit cell used for refinements is presented. The very same magnetic unit cell was used to refine data taken at temperatures below 60K.

As the magnetic moment on site M2 starts to tilt at low temperatures a weak magnetic moment on site M1 is introduced in the refinement carrying a moment of  $0.2 \mu_B$ . The coupling between two M1-atoms appears to be weakly ferromagnetic. This ferromagnetic ordering is accompanied by an expansion of lattice constant  $c$ .

The nuclear and magnetic structures of  $Mn_{5-x}Fe_xSi_3$   $x=0$  as function of an applied magnetic field were investigated with neutron powder diffraction measurements on HB2A which is the powder diffractometer at the High Flux Isotope Reactor (at Oak Ridge National Laboratory). Data has been collected at low temperatures at 50K down to 5K under a magnetic field of 4T. Refinements using the monoclinic super space group  $C2_1/m1'(010)0ss$  performed on data taken at 50K without magnetic field are consistent with results presented in the previous section. Cell parameters converged to  $a=6.8968(3) \text{ \AA}$ ,  $b=11.9052(5) \text{ \AA}$ ,  $c=4.8081(4) \text{ \AA}$  and  $\gamma=90.218(3)^\circ$ . Those values do not agree with respect to error bars with the parameters presented in table 7.8. Refinements performed on the diffraction patterns show evidence of a modification of both the nuclear and the magnetic structure of this compound.

Despite some lack of information at high-Q as well as a lowest resolution at high-d spacing, as presented in figure 7.19 the diffraction pattern with refinement is presented. The addition of the magnetic field clearly causes a change in configuration and symmetry from the monoclinic to the orthorhombic space group. The data collected at 50K under 4 Tesla magnetic field has been refined with the super space group  $Ccmm1'(0\beta 0)00ss$ . Lattice constants converged to  $a=6.8853(3) \text{ \AA}$ ,  $b=11.8589(5) \text{ \AA}$  and  $c=4.7914(4) \text{ \AA}$  and a volume of  $391.22(1) \text{ \AA}^3$ . Therefore, one may conclude that: 1) the magnetic moment on the M1 atomic site is annihilated as observed above 60K where a phase transition has been detected in the magnetization measurement (figure 5.1 (a) and table 5.1) and (2) a contraction of  $\sim 1\%$  of the volume of the unit cell. Using the monoclinic space group for refinements could not improve its quality.

Therefore, the magnetic field is assumed to be able to perturb the weak ferromagnetism associated with the coupling of two neighboring atoms on site M1. So, the stability of the orthorhombic arrangement in this phase is strengthened. No change in symmetry of the unit cell takes place at temperatures down to 5K when the magnetic field of 4T is applied.

The interplay between the monoclinic and orthorhombic arrangements at low temperatures due to the influence of an applied magnetic field are considered to be the driving force of the inverse MCE in this compound. In [94, 95] a model for antiferromagnetism with two magnetic sublattices is proposed for the inverse MCE to occur in antiferromagnetic systems. In the "simplest" case introduced in [94] two sublattices are considered. Nearest neighbour atoms always refer to the other sublattice. In material  $Mn_{5-x}Fe_xSi_3$   $x=0$  the magnetism is more complex. Three sublattices should be considered in the AF2 structure stable at 60K (no magnetic field applied). They are formed by the magnetic moments on M1, M22 and M23. Since the nearest neighbour on site M1 is an atom on site M1 again, interactions within this sublattice would have to be considered, too, as it was done in [95]. This is due to the fact that the magnetism on M1 seems to play an important role for the phase transition due to an applied magnetic field.

Nevertheless, a model considering three sublattices of magnetic atoms can be considered for material  $\text{Mn}_{5-x}\text{Fe}_x\text{Si}_3$   $x=0$ . Especially the weak ferromagnetism gives this composition a unique character.

cell parameters: $a=6.8924(4)\text{ \AA}$ , $b=11.9164(5)\text{ \AA}$ , $c=4.80483(4)\text{ \AA}$ and $\gamma=90.200(3)^\circ$						
Atom	Wyckoff position	x	y	z	U [ $\text{\AA}^2$ ]	M [ $\mu_B$ ]
M1	4f	-0.0004(5)	0.3318(4)	-0.0056(7)	0.00141(15)	0.51(3)
M21	2e	0.2636(15)	0.5003(7)	0.25	0.0026(13)	0.14(3)
M22	2e	0.6172(16)	0.6170(5)	0.25	0.0018(3)	2.66(4)
M23	2e	0.6181(12)	-0.6185(8)	0.25	0.0017(12)	2.21(4)
Si1	2e	0.0989(17)	0.5002(8)	-0.25	0.0023(11)	0
Si2	2e	-0.2999(17)	0.3004(9)	-0.25	0.0030(12)	0
Si3	2e	-0.299(2)	-0.3000(7)	0.75	0.0024(3)	0

**Table 7.7:** Refined atomic parameters at 60K.

cell parameters: $a=6.8929(3)\text{ \AA}$ , $b=11.9152(5)\text{ \AA}$ , $c=4.8061(4)\text{ \AA}$ and $\gamma=90.222(3)^\circ$						
Atom	Wyckoff position	x	y	z	U [ $\text{\AA}^2$ ]	M [ $\mu_B$ ]
M1	4f	-0.0008(4)	0.3314(3)	-0.0054(7)	0.00125(15)	0.53(3)
M21	2e	0.2639(13)	0.5000(7)	0.25	0.0026(11)	0.15(3)
M22	2e	0.6173(15)	0.6170(5)	0.25	0.0020(3)	2.80(6)
M23	2e	0.6184(12)	-0.6187(7)	0.25	0.0016(10)	2.37(6)
Si1	2e	0.0987(14)	0.5001(7)	-0.25	0.0025(10)	0
Si2	2e	-0.3001(14)	0.3006(7)	-0.25	0.0028(10)	0
Si3	2e	-0.2999(17)	-0.3000(6)	0.756	0.0024(3)	0

**Table 7.8:** Refined atomic parameters at 50K.

cell parameters: $a=6.8931(2)\text{ \AA}$ , $b=11.9150(4)\text{ \AA}$ , $c=4.80675(3)\text{ \AA}$ and $\gamma=90.247(2)^\circ$						
Atom	Wyckoff position	x	y	z	U [ $\text{\AA}^2$ ]	M [ $\mu_B$ ]
M1	4f	0.0010(7)	0.3333(7)	-0.0046(9)	0.00141(14)	0.52(3)
M21	2e	0.2638(13)	0.5003(7)	0.25	0.0023(12)	0.15(3)
M22	2e	0.6170(14)	0.6169(5)	0.25	0.0010(2)	3.01(6)
M23	2e	0.6182(11)	-0.6189(7)	0.25	0.0010(11)	2.40(6)
Si1	2e	0.1003(14)	0.5008(7)	-0.25	0.0021(11)	0
Si2	2e	-0.3001(14)	0.2995(8)	-0.25	0.0028(12)	0
Si3	2e	-0.3006(16)	-0.2997(6)	0.75	0.0022(3)	0

**Table 7.9:** Refined atomic parameters at 40K.

cell parameters: $a=6.8939(5)\text{Å}$ , $b=11.9135(5)\text{Å}$ , $c=4.80731(4)\text{Å}$ and $\gamma=90.262(2)^\circ$						
Atom	Wyckoff letter	x	y	z	U [ $\text{Å}^2$ ]	M [ $\mu_B$ ]
M1	4f	0.0000(6)	0.3322(6)	-0.0049(8)	0.00139(16)	0.51(3)
M21	2e	0.2633(14)	0.5002(7)	0.25	0.0026(13)	0.17(3)
M22	2e	0.6172(15)	0.6169(5)	0.25	0.0018(3)	2.95(6)
M23	2e	0.6182(12)	-0.6188(8)	0.25	0.0015(11)	2.68(6)
Si1	2e	0.0990(14)	0.5004(7)	-0.25	0.0016(10)	0
Si2	2e	-0.3001(14)	0.3004(8)	-0.25	0.0035(11)	0
Si3	2e	-0.3000(18)	-0.2999(6)	0.75	0.0025(3)	0

Table 7.10: Refined atomic parameters at 30K.

cell parameters: $a=6.8943(3)\text{Å}$ , $b=11.9131(5)\text{Å}$ , $c=4.80742(5)\text{Å}$ and $\gamma=90.268(3)^\circ$						
Atom	Wyckoff position	x	y	z	U [ $\text{Å}^2$ ]	M [ $\mu_B$ ]
M1	4f	0.0003(7)	0.3326(7)	-0.0055(7)	0.00142(15)	0.52(3)
M21	2e	0.2634(14)	0.5003(7)	0.25	0.0029(13)	0.19(3)
M22	2e	0.6175(15)	0.6169(5)	0.25	0.0018(3)	2.97(6)
M23	2e	0.6181(11)	-0.6188(8)	0.25	0.0014(12)	2.60(6)
Si1	2e	0.0992(15)	0.5005(7)	-0.25	0.0017(11)	0
Si2	2e	-0.3002(15)	0.3001(9)	-0.25	0.0034(12)	0
Si3	2e	-0.3003(18)	-0.2999(6)	0.75	0.0027(3)	0

Table 7.11: Refined atomic parameters at 12K.

## 7.2.6 Results of refinements on $Mn_{5-x}Fe_xSi_3$ $x=4$ at low temperatures

### Nuclear structure of $Mn_{5-x}Fe_xSi_3$ $x=4$

Lattice constants as function of temperature are presented in figure 7.20. Lattice constant  $c$  is contracted when the temperature is lowered. No anomalies can be seen in the dependence of temperature of lattice constant  $c$ . The temperature dependence of the lattice constant  $a$  reminds of a shape of a wave: It decreases between 0K and 80K, increases between 80K and 250K and decreases above 250K again. The decrease of  $a$  above 250K could be due to the ferromagnetic ordering at  $T_C=302(1)\text{K}$  (section 5.2). Maybe the two atomic sites order at different temperatures.

Still, regarding values of both lattice constants quantitatively, the orders of change  $\sim 0.002\text{Å}$  are small in comparison to  $Mn_{5-x}Fe_xSi_3$   $x=0 \sim 0.02\text{Å}$  (section 7.2.5).

The volume and  $ca$  do not indicate any anomalies (figure 7.21), which is due to the fact that the change in lattice constant  $a$  is in the order of  $10^{-4}\text{Å}$  and the change in lattice constant  $c$  in the order of  $10^{-3}\text{Å}$ . Additional measurements would have to be performed slightly above and below the phase transition to extract the influence of the phase transition in detail.

The same phenomenon is visible in the derivatives of the lattice constants in figure 7.22, which should indicate the presence of the phase transition analog to [96]. There is no sharp peak

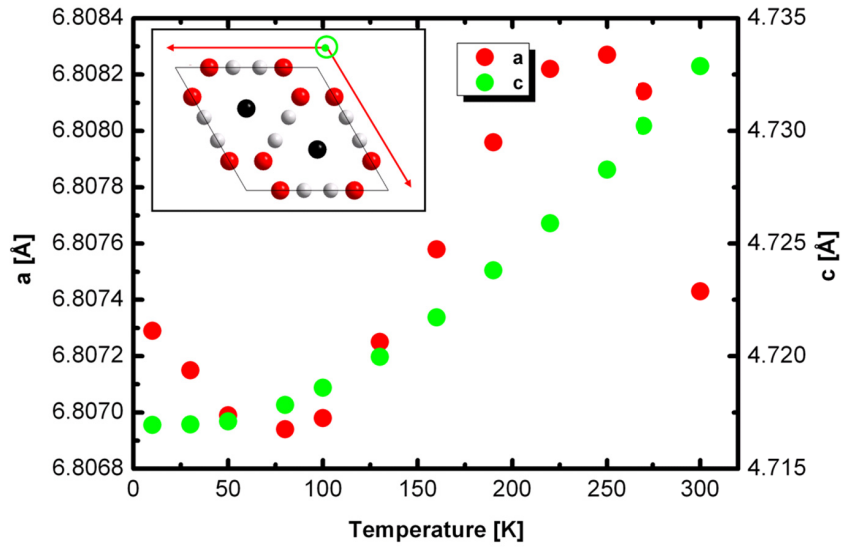


**Figure 7.20:** Lattice constants  $a$  and  $c$  of  $\text{Mn}_{5-x}\text{Fe}_x\text{Si}_3$   $x=4$  as function of temperature. Colors of points in diagram refer to colors of marked lattice constants in unit cell in the inset. Error bars are smaller than points in diagram.

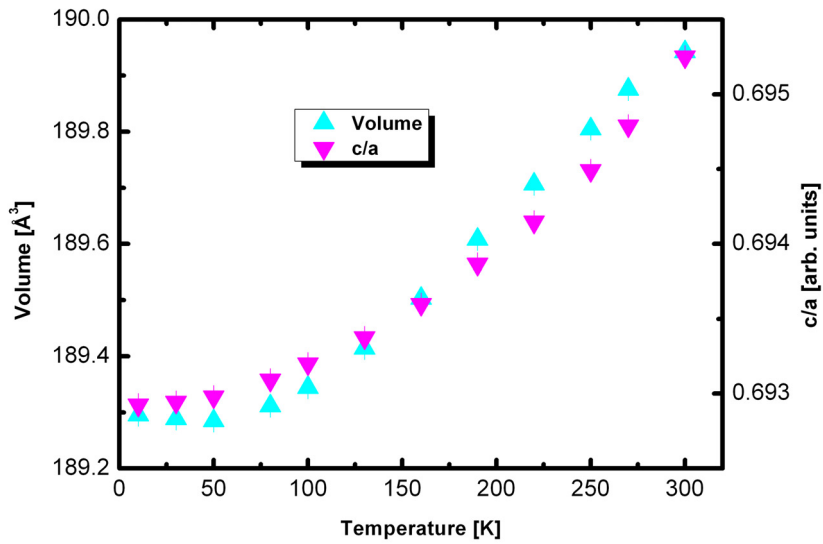


**Figure 7.21:** Volume and  $c/a$  of  $\text{Mn}_{5-x}\text{Fe}_x\text{Si}_3$   $x=4$  as function of temperature. Error bars are smaller than points in diagram.

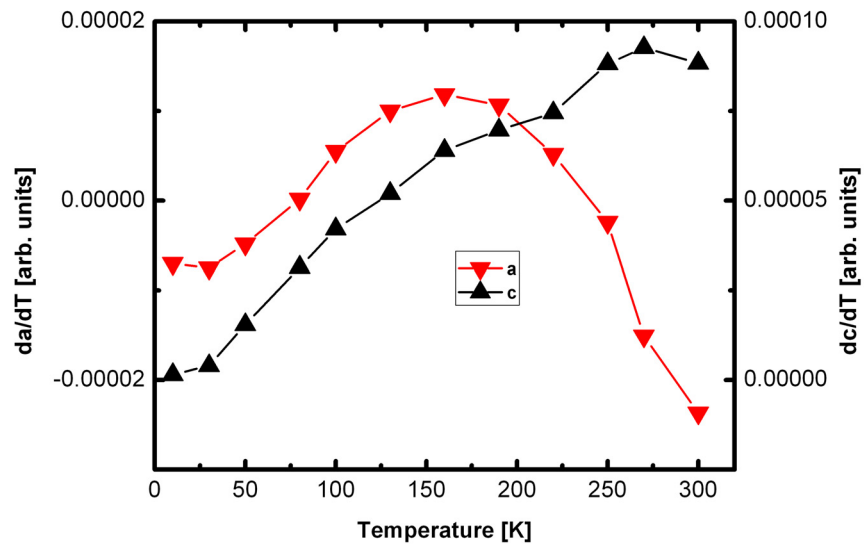


**Figure 7.22:** Derivatives of lattice constants of  $Mn_{5-x}Fe_xSi_3$   $x=4$  as function of temperature. Lines between points in diagram are guides to the eye. Error bars are smaller than points in diagram.

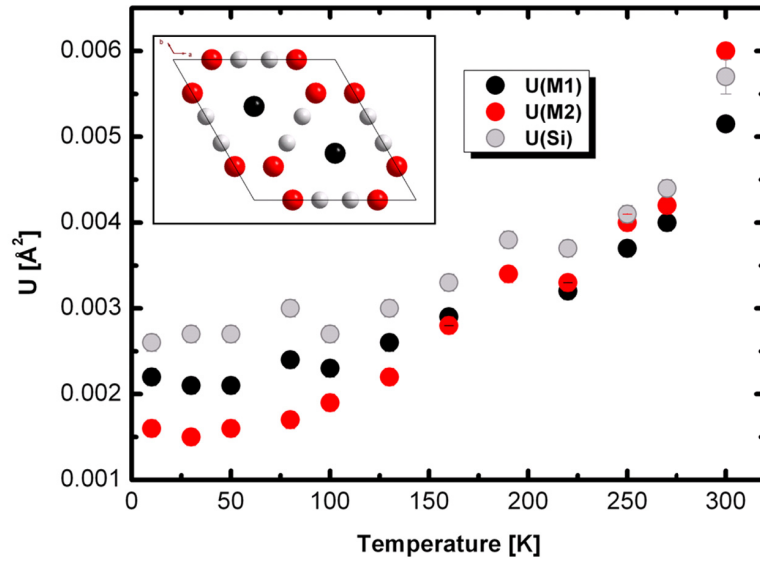


**Figure 7.23:** Atomic displacement parameters of  $Mn_{5-x}Fe_xSi_3$   $x=4$  as function of temperature. Colors of points in diagram refer to colors of atoms in unit cell in the inset.

visible in the temperature dependence of any of the derivatives. The bump between 70K and 250K in the derivative of  $a$  can be considered anomalous.

The influence of the phase transition is clearly visible in the dependence of temperature of the isotropic atomic displacement parameters in figure 7.23. Values of all parameters undergo a jump between 270K and 300K. Furthermore, there are only small discrepancies which might have originated from the quality of the data, i.e. the presence of the reflections of the impurity.

An anomaly is visible between 190K and 220K. This anomaly could have originated by the same phenomenon which induced the unusual temperature dependence of lattice constant  $a$ .

Finally, it can be concluded that atomic displacement parameters meet physical expectations, since they go down in temperature and indicate the presence of the phase transition.

### Magnetic structure of $\text{Mn}_{5-x}\text{Fe}_x\text{Si}_3$ $x=4$

Magnetization measurements clearly indicate ferromagnetic behaviour in compound  $\text{Mn}_{5-x}\text{Fe}_x\text{Si}_3$   $x=4$  with  $T_C=302(1)\text{K}$  (figure 5.1 (e,f)). Additionally, it is also useful to compare two diffraction patterns with each other since magnetic ordering effects intensities. In the ferromagnetic case one would expect increase of intensities. In figure 7.24 two diffraction patterns with refinements are compared with each other. Reflection (2-11) (green arrows) increases in intensity at low temperatures. A diffraction pattern with refinement that did not include magnetism is presented in figure 7.25 with refined parameters presented in table 7.12. According to literature [28, 77] no phenomenon is proposed to take place except magnetic ordering close to room temperature. Therefore refining diffraction patterns with a model including magnetism seems to be reasonable. The inset in the figure clearly shows reasonable quality of the refinement confirming ferromagnetic behaviour. In figure 7.26 the used magnetic model with magnetic moments aligned parallel to  $c$ -axis is presented. The used magnetic form factors are discussed in section A.4.

			M1		M2		Si	
M	$a$ [ $\text{\AA}$ ]	$c$ [ $\text{\AA}$ ]	$U$ [ $\text{\AA}^2$ ]	$M$ [ $\mu_B$ ]	$U$ [ $\text{\AA}^2$ ]	$M$ [ $\mu_B$ ]	$U$ [ $\text{\AA}^2$ ]	GOF
Y	6.80729(1)	4.71694(2)	0.0022(1)	1.07(7)	0.0016(1)	2.84(3)	0.0026(1)	1.25
N	6.80729(1)	4.71694(2)	0.0021(1)	-	0.0016(1)	-	0.0012(1)	1.17

**Table 7.12:** Refined atomic parameters and GOF-values of two refinements both performed on a diffraction pattern taken on  $\text{Mn}_{5-x}\text{Fe}_x\text{Si}_3$   $x=4$  at 10K. First column indicates if magnetism was applied on M1 ("Y") or not ("N").

Values of the refined magnetic moments confirm ferromagnetic structure (figure 5.1 (e,f)) since on both atomic positions the values increase at lower temperatures especially regarding the total momentum of the unit cell (figure 7.27).

The magnetic nature of the atoms occupying positions M1 and M2 is completely different. While the magnetic moment refined on position M1 tends to remain small, the magnetic moment on M2 seems to dominate the magnetism, especially at temperatures above 200K (figure 7.27).

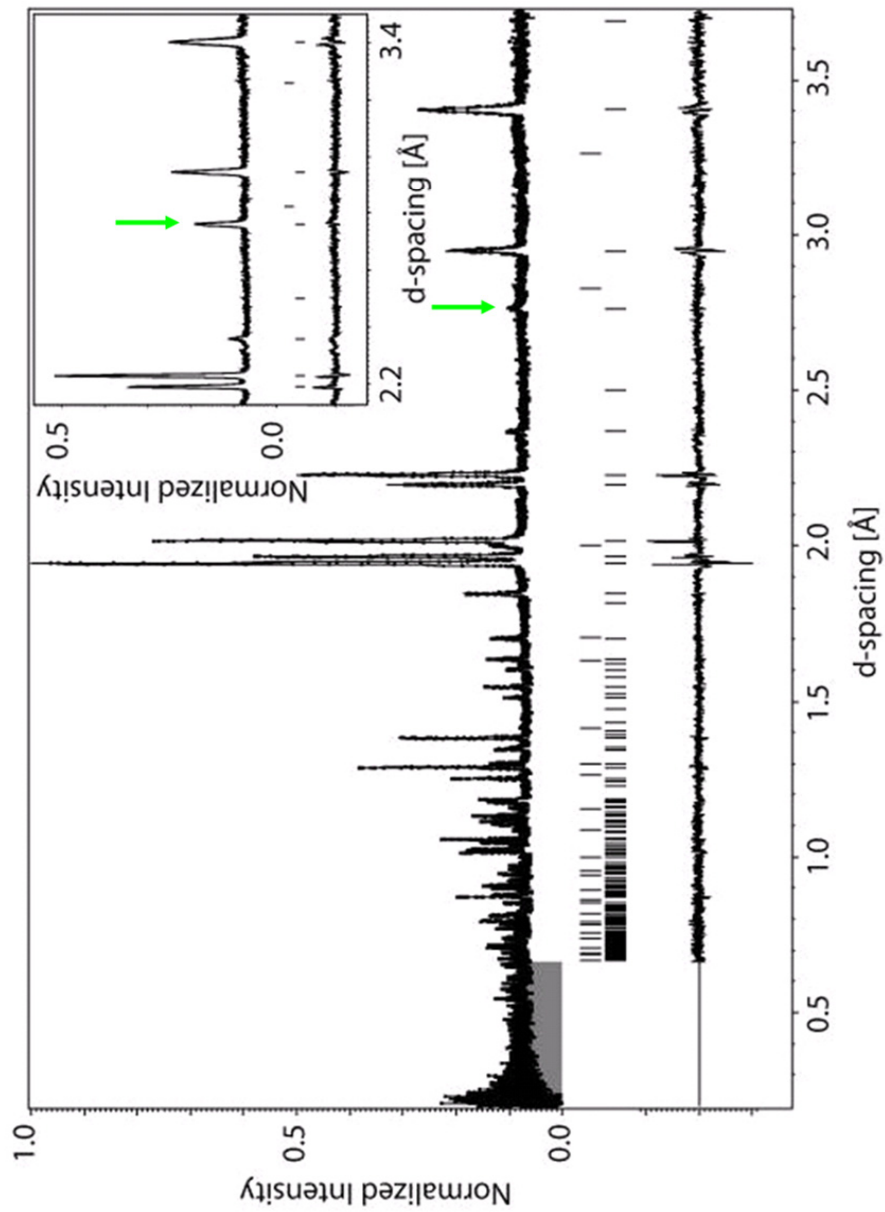


**Figure 7.24:** Block with center at  $45^\circ$  of powder diffraction pattern of  $Mn_{5-x}Fe_xSi_3$   $x=4$  taken at 300K with refinement. Inset presents block with center at  $45^\circ$  of powder diffraction pattern of  $Mn_{5-x}Fe_xSi_3$   $x=4$  taken at 10K with refinement. Green arrows point at reflection (2-11).



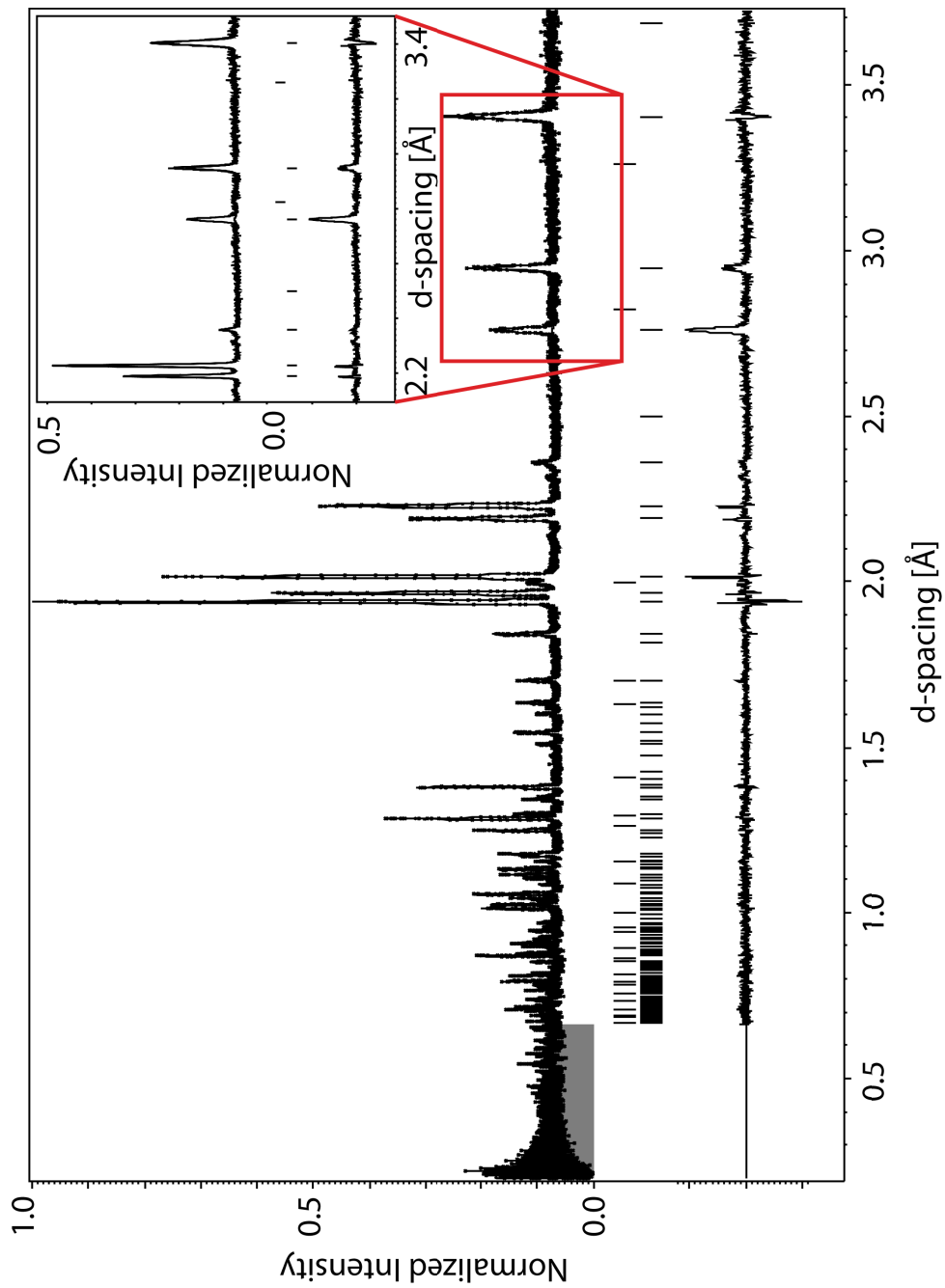


**Figure 7.25:** Block with center at  $45^\circ$  of powder diffraction pattern of  $\text{Mn}_{5-x}\text{Fe}_x\text{Si}_3$   $x=4$  taken at 10K with refinement. Inset presents block with center at  $45^\circ$  of powder diffraction pattern of  $\text{Mn}_{5-x}\text{Fe}_x\text{Si}_3$   $x=4$  taken at 10K with refinement. No magnetic moments were applied in the used model.

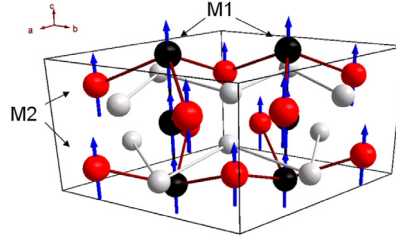


**Figure 7.26:** Unit cell with magnetic moments applied parallel to  $c$ -axis used as model for refinements on diffraction patterns taken on  $Mn_{5-x}Fe_xSi_3$   $x=4$ . Black and red spheres represent Mn or Fe while silver spheres Si atoms, respectively.

The presence of two different magnetic moments has already been reported in [28, 38]. The extracted magnetic moments are  $1.4\mu_B$  on M1 and  $2.5\mu_B$  on M2 at 8K [38]. In [28] values of  $1.0(1)\mu_B$  on M1 and  $1.5\mu_B$  for Fe and  $1.2\mu_B$  for Mn on M2 at 4.2K have been proposed.

The refined values of the magnetic moments on M1 in [38] are comparable to the results in figure 7.27. They do not agree with each other, since the moments in the figure on M1 is smaller and on M2 larger than in this publication. Additionally, they propose magnetic moments aligned with an angle of  $40^\circ$  to the  $c$ -axis, which is in contrast to the results in [28] and in this thesis. This could explain the difference to the values in figure 7.27. Maybe they made use of an experimental setup allowing them to capture reflections at higher  $d$ -spacing. Due to the applied setup on POWGEN diffraction patterns did not exceed  $3.52\text{\AA}$ . Therefore, useful information about the magnetism could be missing.

The values in [28] were published in 1973 which did not provide the opportunity to take diffraction patterns with a quality comparable to POWGEN, a recently introduced instrument, in 2010. This is probably the reason for the difference between their and the results presented in this thesis.

At 300K the phase transition is still in progress which can explain the large magnetic moment refined on position M1 at that temperature.

The function used for fitting the magnetic moments is

$$m = m_{sat} \left( \frac{T_C - T}{T_C} \right)^\beta \quad (7.1)$$

and was used analog to [96, 97].  $m_{sat}$  is the saturated magnetic moment at  $T=0K$ .  $T_C$  is the phase transition temperature. This function provides extraction of those two values that can be compared to publications. Values, corresponding to M1 at temperatures above 240K had to be excluded since the nature of the magnetism on this site is still unclear due to small refined magnetic moments and since equation 7.1 is only valid below the ordering temperature. With respect to this restriction all magnetic moments obey this equation. The results of the fittings of the moments of  $Mn_{5-x}Fe_xSi_3$   $x=4$  is presented in table 7.13. These values are not reliable since equation 7.1 is usually only valid close to the phase transition. However, as a first impression of the conditions of phase transitions it can be very useful here.

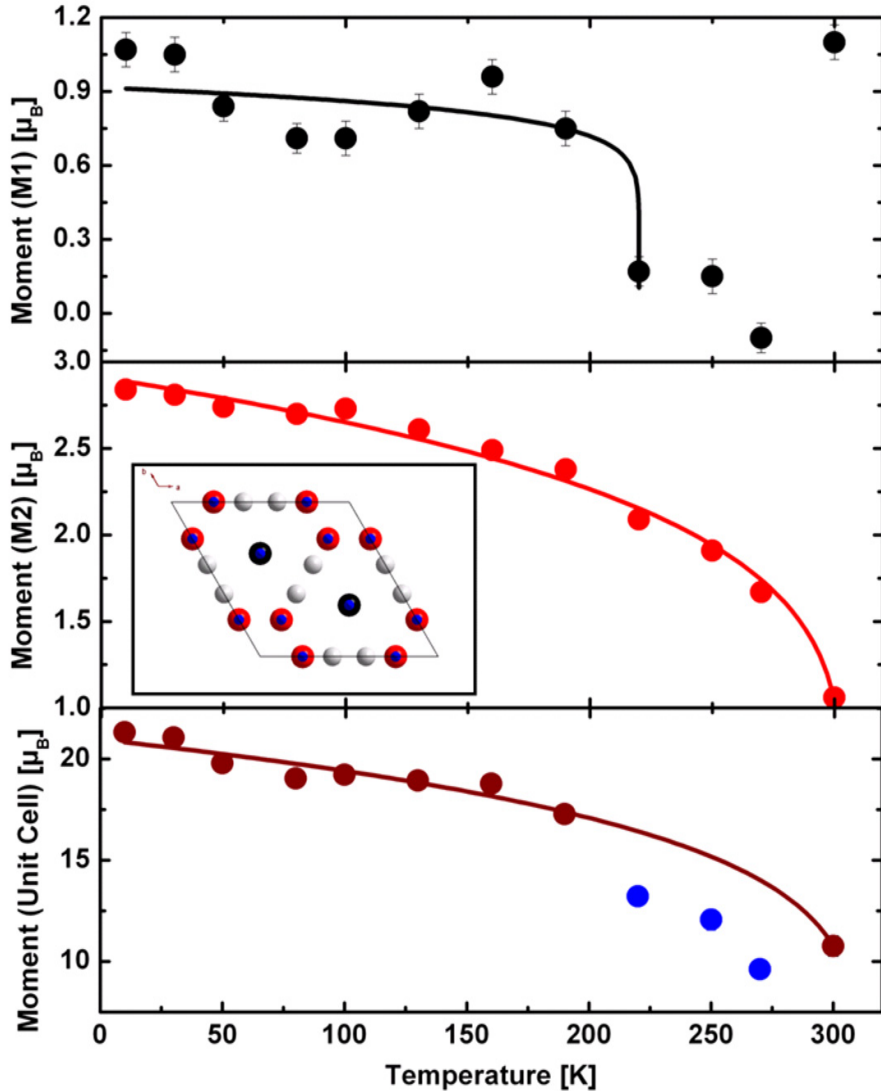


**Figure 7.27:** Magnetic moments refined on atomic positions M1, M2 and the whole unit cell of  $Mn_{5-x}Fe_xSi_3$   $x=4$  as function of temperature. Magnetic moments are applied parallel to the  $c$ -axis. Colors of points in diagram refer to colors of atoms in unit cell in the inset. Blue points were excluded from fitting. The refined magnetic moments on site M1 are obviously not reliable.

Those fits indicate different ordering temperatures for each atomic site. This indicates different ordering of the two atomic sites. To the best of the knowledge of the author of this thesis, no publication reports about the different ordering temperatures of the two atomic sites so far.

The error of  $T_C$  of the whole unit cell is large, because the lack of points of measurements

Atom	$T_C$ [K]	$m_{sat}$ [ $\mu_B$ ]	$\beta$
M1	220(1)	0.9(5)	0.1(1)
M2	304(2)	2.9(3)	0.23(2)
Unit cell	311(9)	21(5)	0.20(4)

**Table 7.13:**  $T_C$ ,  $m_{sat}$  and  $\beta$ , all extracted from the refined magnetic moments.

(the three blue points were not included for fitting). With respect to that error the transition temperatures of M2 and the whole unit cell are in agreement with each other. Therefore, the ordering of the magnetic moment on position M2 seems to mark the transition between para- and ferromagnetism. The ordering temperature of 304(2)K is in agreement with the value of  $T_C=302(1)$ K extracted from the magnetization measurement (section 5.2).

The saturated moments of equation 7.1 are valid at  $T=0$ K, making it impossible to measure them directly. The values extracted from the fittings meet expectations, since they are in a similar order as the refined values at 10K. Discrepancies are only visible for the magnetic moment on M1. This could be due to its small value.

The bump in lattice constant  $a$  (figure 7.20) and the anomaly in the atomic displacement (figure 7.23) at temperatures of  $\sim 220$ K might correspond to the ordering of the magnetic moment on M1. Still, no sign of any anomaly is visible in the derivative of lattice constant  $a$  (figure 7.22) and the magnetization measurements (figure 5.1 (e,f)).

The different ordering temperatures of the two magnetic sites must be linked to the MCE in this compound. The entropy change depends on the magnetization (equation 1.2) which is driven by the alignment of the magnetic moments. The fact that the magnetic moment on site M1 seems to be unordered close to the phase transition implies that larger magnetic fields have to be applied for alignment of these moments. This does not necessarily have to be the case since a magnetic field of 100Oe is obviously strong enough to merge the ordering of the two magnetic sites into a single phase transition (figure 5.1 (e)). Since the value of the magnetic moment is "technically"  $0\mu_B$  it can only give a nonzero contribution when the field (a value of at least 100Oe is considered) is applied.

$$\Delta S_m = \left( \frac{M_{M1}(T_2, B=0) + M_{M2}(T_2, B=0) - (M_{M1}(T_1, B=0) + M_{M2}(T_1, B=0))}{T_1 - T_2} \right) \Delta B + \left( \frac{M_{M1}(T_2, B>0) + M_{M2}(T_2, B>0) - (M_{M1}(T_1, B>0) + M_{M2}(T_1, B>0))}{T_1 - T_2} \right) \Delta B \quad (7.2)$$

The fact that the magnetic moment on site M1 seems to be unordered close to the phase transition implies

$$M_{M1}(T_2, B=0) = M_{M1}(T_1, B=0) = 0. \quad (7.3)$$

Therefore, equation 7.2 can be simplified to

$$\Delta S_m = \left( \frac{M_{M2}(T_2, B=0) - M_{M1}(T_1, B=0)}{T_1 - T_2} \right) \Delta B + \left( \frac{M_{M1}(T_2, B > 0) + M_{M2}(T_2, B > 0) - (M_{M1}(T_1, B > 0) + M_{M2}(T_1, B > 0))}{T_1 - T_2} \right) \Delta B. \quad (7.4)$$

The unordered character of the magnetic moment (assuming its value properly refined) could have caused the increase of the magnetization at low temperatures in figures 5.1 (e,f).

This effect can be further investigated when comparing this compound to a material with a similar magnetic structure. Only the ordering temperatures in this compound would have to be equivalent or very close to each other. Maybe such a structure is exhibited by one of the Co-doped compounds. Also, the model for ferromagnets in the context of the MCE presented in [94] could be used for theoretical investigations. Magnetic sites M1 and M2 could be considered as two sublattices, here.

			M1		M2		Si	
M	$a$ [Å]	$c$ [Å]	U [Å <sup>2</sup> ]	M [ $\mu_B$ ]	U [Å <sup>2</sup> ]	M [ $\mu_B$ ]	U [Å <sup>2</sup> ]	GOF
Y	6.80814(2)	4.73022(2)	0.0040(1)	-0.1(6)	0.0042(1)	1.67(4)	0.0044(1)	1.18
N	6.80814(2)	4.73021(2)	0.0040(1)	-	0.0042(1)	1.67(4)	0.0044(1)	1.18

**Table 7.14:** Refined atomic parameters and GOF-values of two refinements both performed on a diffraction pattern taken on  $Mn_{5-x}Fe_xSi_3$   $x=4$  at 270K. First column indicates if magnetism was applied on M1 ("Y") or not ("N").

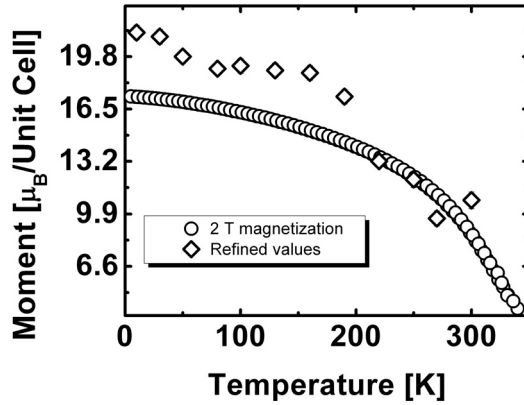


**Figure 7.28:** Magnetic moment of the whole unit cell refined on atomic positions M1 and M2 and magnetization measurement performed on  $Mn_{5-x}Fe_xSi_3$   $x=4$  as function of temperature.

The value of the magnetic moment on position M1 is very small above 200K. Actually, the magnetic moment could already be too small to have been refined properly on a powder diffraction pattern. Also, the value of  $0\mu_B$  (within error bars) at 270K can be explained that way. Concerning the magnetic order on M1 two refinements are compared with each other in table

7.14, one includes magnetism on M1 the other does not. Besides, a very small change in the lattice constant  $a$ , the two refinements are exactly the same including value of GOF. Therefore, the magnetic moment on M1 could not be refined properly. Especially the value of the ordering temperature is not reliable. Even the proposal of the existence of the two ordering temperatures has not been given evidence. This moment could have been ordered at 260K with a very small value. Still, the magnetic moment on this atom can be considered unordered at high T.

The magnetic moment on position M2 meets physical expectations since ferromagnetic character was already revealed by magnetization measurements. The value of this moment is large. At low temperatures a value of  $2.84(3) \mu_B$  was refined. Since high refined magnetic moments must have originated from "high intensities" these values can be considered reliable and reasonable.

The magnetic moment of the whole unit cell is obviously strongly affected by the unordered small magnetic moment on M1, since those changes exactly coincide with each other. The unordered character (assuming it does not originate from the quality of the data) of the magnetic moment on M1 could also explain why the magnetization as function of temperature does not remain flat at low T.

In figure 7.28 refined magnetic moments are plotted in the magnetization measurement performed at 2T. It is expected that refined values should be above the magnetization curve. This is due to the performance of the magnetization measurement on a polycrystalline sample. Points of refined and magnetization data coincide at high temperatures with each other. Here, the lack of information of the magnetic moment on M1 might play the important role.

T [K]	$a$ [Å]	$c$ [Å]	M1		M2		Si	GOF
			U [Å <sup>2</sup> ]	M [ $\mu_B$ ]	U [Å <sup>2</sup> ]	M [ $\mu_B$ ]		
300	6.80743(1)	4.73287(2)	0.00515(8)	1.1(7)	0.0060(1)	1.06(4)	0.0057(2)	1.11
270	6.80814(2)	4.73022(2)	0.0040(1)	-0.1(6)	0.0042(1)	1.67(4)	0.0044(1)	1.18
250	6.80827(2)	4.72828(2)	0.0037(1)	0.15(7)	0.0040(1)	1.91(4)	0.0041(1)	1.23
220	6.80822(2)	4.72590(2)	0.0032(1)	0.17(6)	0.0033(1)	2.09(3)	0.0037(1)	1.18
190	6.80796(1)	4.72381(2)	0.0034(1)	0.75(7)	0.0034(1)	2.38(3)	0.0038(1)	1.13
160	6.80758(1)	4.72172(2)	0.0029(1)	0.96(7)	0.0028(1)	2.49(3)	0.0033(1)	1.16
130	6.80725(1)	4.71997(2)	0.0026(1)	0.82(7)	0.0022(1)	2.61(3)	0.0030(1)	1.18
100	6.80698(1)	4.71860(2)	0.0023(1)	0.71(7)	0.0019(1)	2.73(3)	0.0027(1)	1.2
80	6.80694(1)	4.71783(2)	0.0024(1)	0.71(6)	0.0017(1)	2.70(3)	0.0030(1)	1.18
50	6.80699(1)	4.71710(2)	0.0021(1)	0.84(6)	0.0016(1)	2.74(3)	0.0027(1)	1.16
30	6.80715(1)	4.71697(2)	0.0021(1)	1.05(7)	0.0015(1)	2.81(3)	0.0027(1)	1.18
10	6.80729(1)	4.71694(2)	0.0022(1)	1.07(7)	0.0016(1)	2.84(3)	0.0026(1)	1.17

**Table 7.15:** Refined atomic parameters and GOF-values.

## 7.3 $\text{Mn}_{1-x}\text{Co}_x\text{Fe}_4\text{Si}_3$ and $\text{MnFe}_{4-x}\text{Co}_x\text{Si}_3$

### 7.3.1 Experimental setups

$\text{Mn}_{1-x}\text{Co}_x\text{Fe}_4\text{Si}_3$ $x=0.1$	
Temperatures [K]	310, 288, 167, 247, 99, 50, 12
$\text{Mn}_{1-x}\text{Co}_x\text{Fe}_4\text{Si}_3$ $x=0.2$	
Temperatures [K]	310, 290, 250, 100, 12
$\text{MnFe}_{4-x}\text{Co}_x\text{Si}_3$ $x=0.2$	
Temperatures [K]	310, 288, 268, 248, 99, 12
$\text{MnFe}_{4-x}\text{Co}_x\text{Si}_3$ $x=0.5$	
Temperatures [K]	310, 289, 268, 250, 200, 99, 50, 12

**Table 7.16:** Samples and temperatures at which measurements were taken. Ranges between 0.56 Å and 4.24 Å were covered in all diffraction patterns

In table 7.16 details of instrumental setups are presented. It was chosen to perform measurements at these temperatures to investigate the magnetism discussed in section 5.3.

### 7.3.2 Details of refinements

#### General qualities

Every diffraction pattern was cut off at a minimum value of  $d=0.6$  Å. For the transformation from  $t$ - to  $d$ -spacing the formula of Jason Hodges was used on every diffraction pattern.

The background of every diffraction pattern was created and treated manually, so that no additional parameters had to be refined. For this Jana2006 provides the opportunity to evaluate linear interpolation using a given number of background points. For Co-doped materials 50 points for linear interpolation of background of every diffraction pattern was applied. After this the background points of every model were checked carefully. In some cases one or two points for background treatment were added if it was considered necessary. The number of points for linear interpolation never exceeded 52.

All parameters of the profile of peaks (Pseudo Voigt in TOF-setting) including asymmetry were determined with the reference sample except Sig2 and Gam1 which were refined, respectively.

Atomic occupations were only refined on diffraction patterns taken at 310K for all samples. Displacement parameters (setting with isotropic model), and atomic positions were constantly refined with respect to space group.

Atomic displacement of impurities has not been refined on patterns taken at 310K. The values were taken from literature.

The total numbers of refined parameters, i.e. lattice constants, phase fractions, atomic displacement, atomic occupations, absorption correction, Sig2, Gam1 and scale factor are presented in

	$Mn_{1-x}Co_xFe_4Si_3$		$MnFe_{4-x}Co_xSi_3$	
	x=0.1	x=0.2	x=0.2	x=0.5
310K	30	30	23	28
below 310K	28	28	22	28

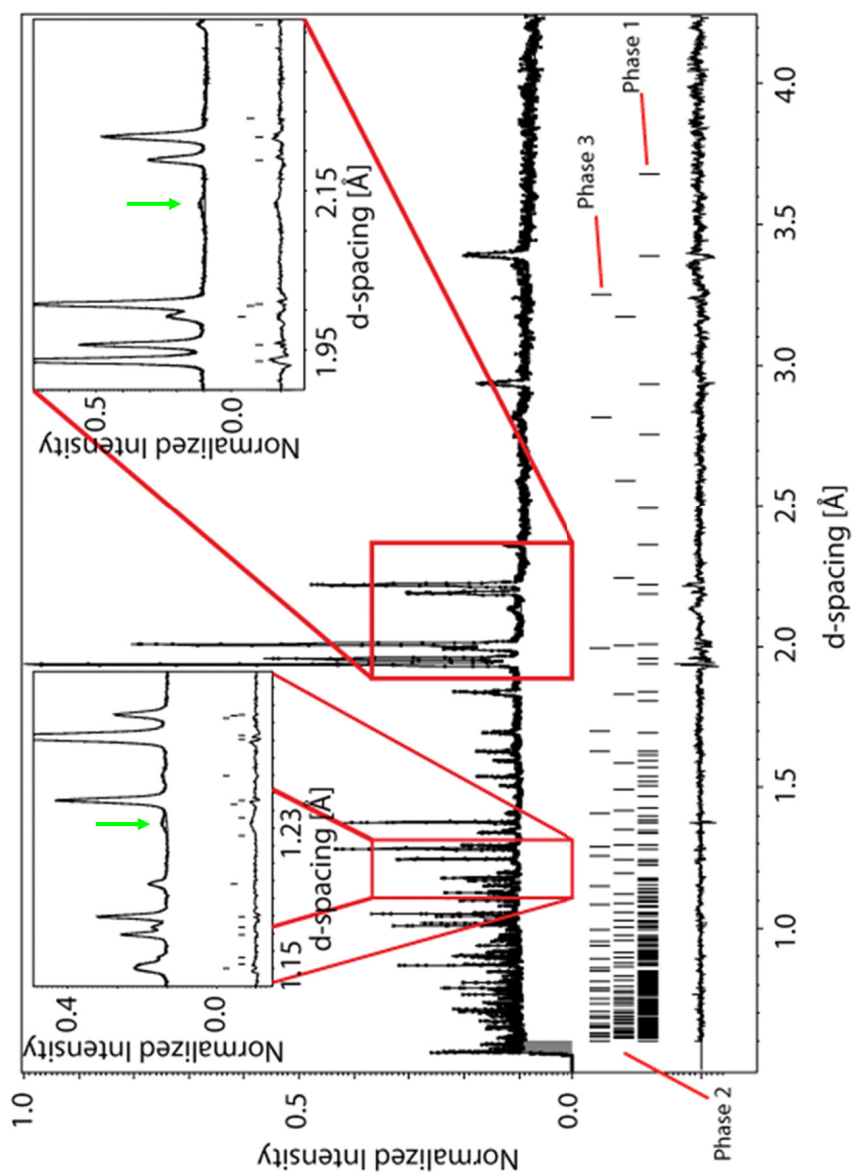
**Table 7.17:** Total number of refined parameters used in refinements performed on data taken at mentioned temperatures.

table 7.17. There was only one impurity detected in sample  $MnFe_{4-x}Co_xSi_3$   $x=0.2$ . At 310K no magnetic moments were refined on diffraction pattern taken on  $MnFe_{4-x}Co_xSi_3$   $x=0.5$ . On diffraction patterns taken at temperatures below 310K atomic occupations were not refined anymore.

In figure 7.29 a typical diffraction pattern with refinement is presented. There are small differences indicated (line below 0.0 normalized intensity) between calculated model and measured data. The quality of the refinement seems to be reasonable. Data presented in those figures were collected at 310K.

Stripes at the very bottom denoted "Phase 2" and "Phase 3" are related to impurity structures  $Mn_{1-y-z}Fe_yCo_zSi$  and  $Mn_{3-y-z}Fe_yCo_zSi$ . "Phase 1" is related to the "base compounds" which are not impurities. Same is valid for every refinement in this chapter. Insets present regions in d-spacing where reflections appear that are not indexed with one of the phases.





**Figure 7.29:** Powder diffraction pattern of  $\text{Mn}_{1-x}\text{Co}_x\text{Fe}_4\text{Si}_3$   $x=0.1$  taken at 310K with refinement. Green arrows in insets indicate peaks that do not fit to one of the three phases included in the model of the refinement.

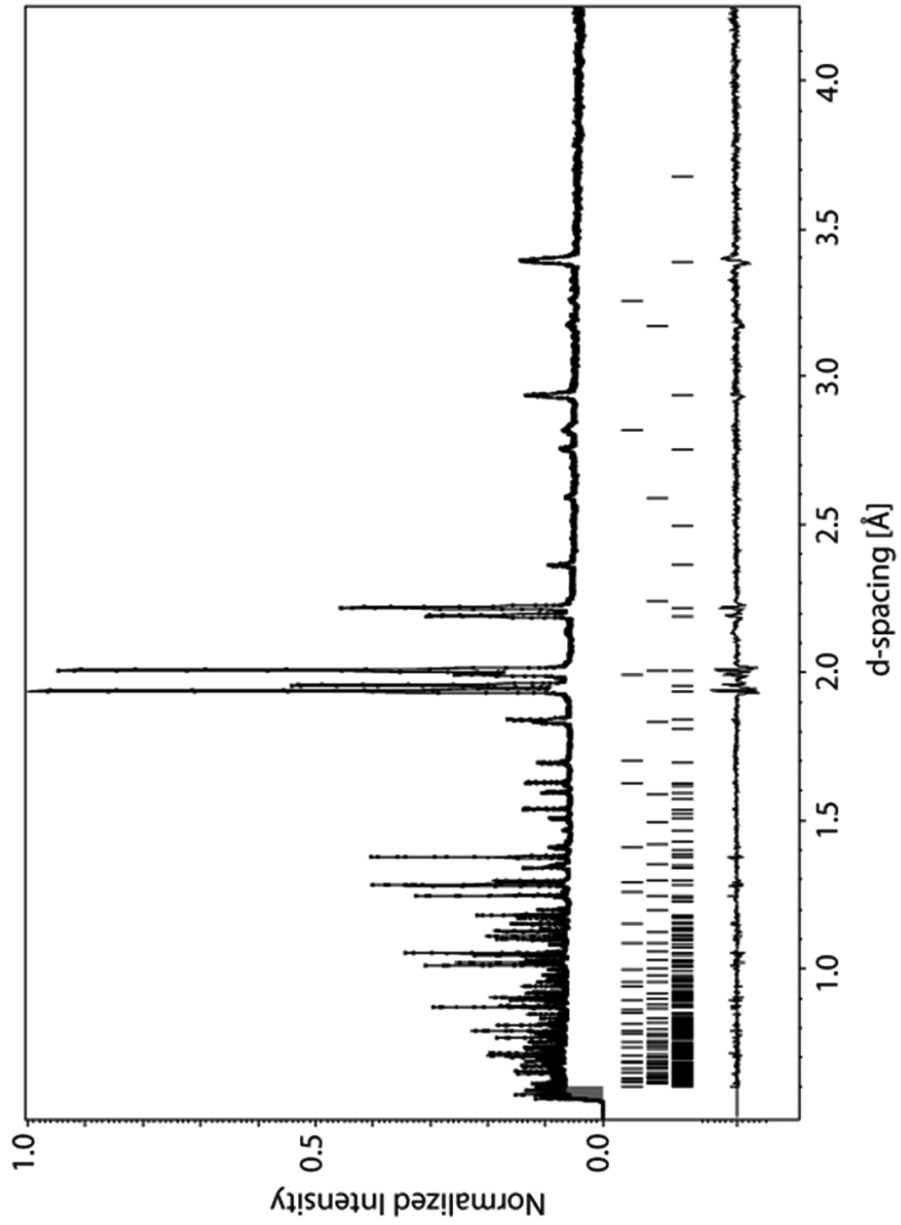


**Figure 7.30:** Powder diffraction pattern of  $Mn_{1-x}Co_xFe_4Si_3$   $x=0.2$  taken at 310K with refinement.

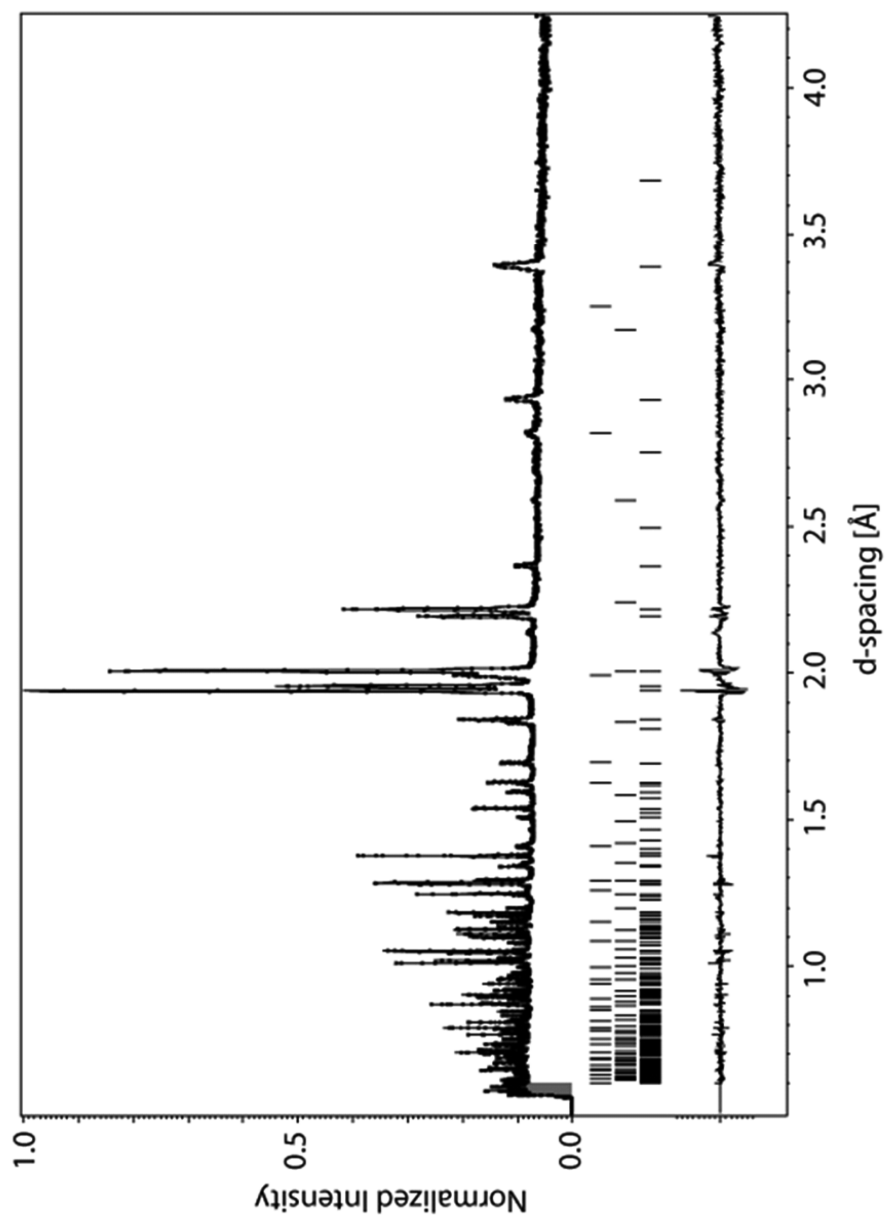


**Figure 7.31:** Powder diffraction pattern of  $\text{MnFe}_{4-x}\text{Co}_x\text{Si}_3$   $x=0.5$  taken at 310K with refinement.

### Impurity phases

After having refined the model with hexagonal space group  $P6_3/mcm$  (193) on each diffraction pattern taken on a sample at 310K, peaks which do not fit to this structure were identified. Those peaks could be due to shifting of the space group because of Co-doping or due to the presence of impurities in the samples. In the first case Co-doping must have forced the structure to undergo a phase transition.

Two of the impurities could be identified as structures  $Mn_{1-y-z}Fe_yCo_zSi$  and  $Mn_{3-y-z}Fe_yCo_zSi$ , which are isometric (according to refinements performed by the author of this thesis) to compounds  $FeSi$ ,  $MnSi$ ,  $CoSi$  [86, 98, 99] and  $Fe_3Si$  and  $Mn_3Si$  [86, 87]. Content and composition vary with sample. In the sample which was supposed to crystallize in pure  $MnFe_{4-x}Co_xSi_3$   $x=0.2$  impurity  $Mn_{1-y-z}Fe_yCo_zSi$  was absent.

There is at least one additional impurity in every diffraction pattern since there are reflections at  $d=1.233 \text{ \AA}$  and  $d=2.14 \text{ \AA}$  which do not fit to one of the structures that are included in the model. Green arrows in insets in figure 7.29 point these reflections out. Structures of many compounds consisting of at least one of the four elements used for preparation were checked without having succeeded in indexing those reflections.

From here on phrases like " $Mn_{1-x}Co_xFe_4Si_3$   $x=0.1$ " will refer to all the compounds that could be detected in this sample. Mentioning a material like " $Mn_{0.95(1)}Co_{0.11(1)}Fe_{3.94(3)}Si_3$ " will only refer to this one compound that could be detected in a sample. Phrases like "base material" will be related to a non-impurity compound.

Results of refinements of the structure of the base compounds can only be influenced by impurities if peaks from both structures overlap each other. There are a lot of reflections in every diffraction pattern referring to the hexagonal structure with only small differences between calculated and measured pattern. Furthermore, reflections generated by the unidentified impurity are very small in intensity ( $\sim 2(1)\%$  of the highest intensity in a diffraction pattern) in indicating that there is only a small amount of this impurity in samples. Therefore, the effect of the unidentified impurity can be discarded.

The assumption that impurities originate from oxygen contamination can be almost excluded, due to the accurate sample preparation (section 4.3). If the crystallization of those impurities is due to the preparation its origin remains unclear. Maybe the phases  $Mn_{1-x}Co_xFe_4Si_3$  and  $MnFe_{4-x}Co_xSi_3$  are unstable at certain temperatures, or the impurities crystallize under similar conditions.

The purpose was to investigate magnetocaloric effect materials  $Mn_{1-x}Co_xFe_4Si_3$   $x=0.1;0.2$  and  $MnFe_{4-x}Co_xSi_3$   $x=0.2;0.5$ . This might give rise to question if phases of impurities have to be included in refinements at all. In table 7.18 results of refinements, including and excluding phases of impurities are compared to each other. All refinements were performed on diffraction patterns taken at 310K. Reasonable differences are clearly visible in the results of every refinement. For example including phases of impurities decreases values of error bars and GOF significantly. Error bars of the results of the refinement of phase  $Mn_{0.817(8)}Co_{0.13(1)}Fe_{4.04(2)}Si_3$  are more than doubled when phases of impurities are excluded.

Mn <sub>1-x</sub> Co <sub>x</sub> Fe <sub>4</sub> Si <sub>3</sub> x=0.1								
			M1		M2		Si	
Imp.	a [Å]	c [Å]	U [Å <sup>2</sup> ]	M [μ <sub>B</sub> ]	U [Å <sup>2</sup> ]	M [μ <sub>B</sub> ]	U [Å <sup>2</sup> ]	GOF
Y	6.7762(1)	4.71795(8)	0.0063(2)	1.2(1)	0.0059(3)	1.1(1)	0.0066(4)	2.1
N	6.7744(2)	4.7167(2)	0.0043(4)	-0.4(2)	0.0067(7)	1.4(1)	0.0059(6)	4.21
Mn <sub>1-x</sub> Co <sub>x</sub> Fe <sub>4</sub> Si <sub>3</sub> x=0.2								
			M1		M2		Si	
Imp.	a [Å]	c [Å]	U [Å <sup>2</sup> ]	M [μ <sub>B</sub> ]	U [Å <sup>2</sup> ]	M [μ <sub>B</sub> ]	U [Å <sup>2</sup> ]	GOF
Y	6.77536(9)	4.72200(7)	0.0046(2)	-0.1(1)	0.0053(2)	1.09(7)	0.0051(3)	3.46
N	6.7734(3)	4.7207(2)	0.0023(5)	-0.5(2)	0.0064(6)	1.4(2)	0.0051(8)	10.77
MnFe <sub>4-x</sub> Co <sub>x</sub> Si <sub>3</sub> x=0.2								
			M1		M2		Si	
Imp.	a [Å]	c [Å]	U [Å <sup>2</sup> ]	M [μ <sub>B</sub> ]	U [Å <sup>2</sup> ]	M [μ <sub>B</sub> ]	U [Å <sup>2</sup> ]	GOF
Y	6.78242(9)	4.72437(7)	0.0046(2)	-0.2(1)	0.0050(3)	0.92(8)	0.0056(2)	3.23
N	6.7820(1)	4.7241(1)	0.0039(2)	-0.4(1)	0.0054(3)	1.0(1)	0.0060(4)	5.02
MnFe <sub>4-x</sub> Co <sub>x</sub> Si <sub>3</sub> x=0.5								
			M1		M2		Si	
Imp.	a [Å]	c [Å]	U [Å <sup>2</sup> ]	M [μ <sub>B</sub> ]	U [Å <sup>2</sup> ]	M [μ <sub>B</sub> ]	U [Å <sup>2</sup> ]	GOF
Y	6.7744(1)	4.73046(9)	0.0049(2)	-	0.0050(2)	-	0.0054(3)	3.41
N	6.7717(3)	4.7286(2)	0.0027(4)	-	0.0064(6)	-	0.0050(7)	8.11

**Table 7.18:** Comparing results of refinements of base (non-impurity) compounds when phases of impurities are included (marked with Y) and not included (marked with N) in the refinement. Refinements were conducted on data taken at 310K.

### Refining base compounds at 310K

Having three different Rietveld models refined on data might easily overload the refinement with parameters. This is very important to be mentioned, since attempts to refine occupations of the base compounds in Mn<sub>1-x</sub>Co<sub>x</sub>Fe<sub>4</sub>Si<sub>3</sub> x=0.1;0.2 and MnFe<sub>4-x</sub>Co<sub>x</sub>Si<sub>3</sub> x=0.2;0.5 and impurities at the same time as starting point failed. The resulted compositions did not make any sense. Therefore regions with reflections overlapping with peaks emerging from at least one of the impurities were first excluded. Doing so led to atomic position M1 being only occupied by Fe and Co and atomic position M2 being only occupied by Mn and Fe. Those results are due to the emergence of atomic occupations of 0 or even smaller in the refinement. Such atoms were excluded from the corresponding position. That was a crucial step for moving closer to final results. No vacancies were proposed.

In figure 7.32 a typical diffraction pattern with refinement only including the base compound and no impurities is presented. The purpose was to exclude not more regions than necessary. After having performed some cycles of refining excluded regions were modified. The same excluded regions were used for every refinement performed on a diffraction pattern taken on one of the samples at 310K. The only exception was MnFe<sub>4-x</sub>Co<sub>x</sub>Si<sub>3</sub> x=0.2 with less excluded regions because of the absence of the second impurity.

To evaluate atomic distributions qualitatively (M1: Co and Fe, M2: Fe and Mn) was the first

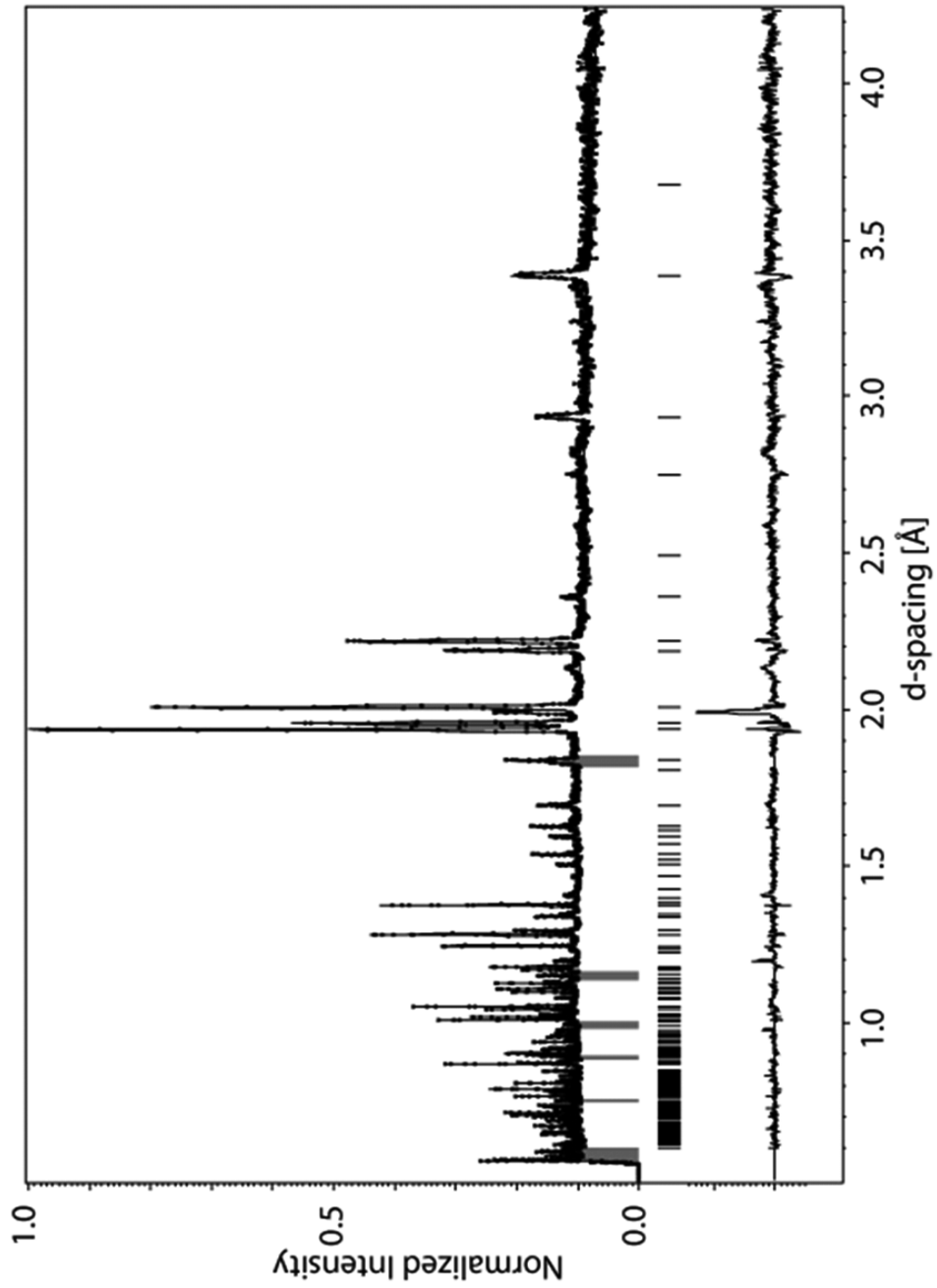


**Figure 7.32:** Powder diffraction pattern of  $Mn_{1-x}Co_xFe_4Si_3$   $x=0.1$  taken at 310K with refinement and excluded regions. No impurities are included in the model. GOF-value is 3.4.

step. Evaluating all atomic parameters, including occupations of the base compounds quantitatively was the second step. Since atomic values (displacement parameters, occupations and atomic positions) strongly depend on intensities of peaks, the impurity phases were introduced into every model (in case of  $\text{MnFe}_{4-x}\text{Co}_x\text{Si}_3$   $x=0.2$  only one impurity). No regions were excluded anymore.

In table 7.19 the refined occupations of the base materials are presented. The occupation of Si was not refined in either of the materials, leaving this element as reference for the refined scale factors, fractions and occupations. Due to the emergence of impurities in every sample, it is no surprise that compositions do not fit exactly to the proposed pure materials.

	$\text{Mn}_{1-x}\text{Co}_x\text{Fe}_4\text{Si}_3$		$\text{MnFe}_{4-x}\text{Co}_x\text{Si}_3$	
	$x=0.1$	$x=0.2$	$x=0.2$	$x=0.5$
Occup. Co on M1	0.009(1)	0.011(1)	0.016(1)	0.033(1)
Occup. Fe on M1	0.157(1)	0.155(1)	0.150(1)	0.133(1)
Occup. Fe on M2	0.1710(9)	0.1818(7)	0.1659(6)	0.1621(6)
Occup. Mn on M2	0.0790(9)	0.0681(7)	0.0841(6)	0.0879(6)
Final Comp. Mn	$\text{Mn}_{0.95(1)}$	$\text{Mn}_{0.817(8)}$	$\text{Mn}_{1.009(7)}$	$\text{Mn}_{1.055(7)}$
Final Comp. Co	$\text{Co}_{0.11(1)}$	$\text{Co}_{0.13(1)}$	$\text{Co}_{0.19(1)}$	$\text{Co}_{0.40(1)}$
Final Comp. Fe	$\text{Fe}_{3.94(3)}$	$\text{Fe}_{4.04(2)}$	$\text{Fe}_{3.79(2)}$	$\text{Fe}_{3.54(2)}$
Final Comp. Si	$\text{Si}_3$	$\text{Si}_3$	$\text{Si}_3$	$\text{Si}_3$

**Table 7.19:** Refined atomic occupations of the base compounds.

### Refining impurities at 310K

For all refinements on data taken at 310K isometric atomic displacement of impurities were taken from compounds FeSi and  $\text{Fe}_3\text{Si}$  on icsd homepage [100] in order to reduce the number of refined parameters. Reflections generated by impurities are small in intensity and the effect of atomic displacement on the calculated diffraction pattern scales with intensity. Therefore, the influence of atomic displacement parameters of impurities on the quality of the refinement of the base compounds is considered small. Finally, the focus of this work is to investigate base compound  $\text{MnFe}_4\text{Si}_3$  with Co-doping.

Concerning impurities, magnetization measurements do not indicate the presence of any additional phases except  $\text{MnFe}_{4-x}\text{Co}_x\text{Si}_3$   $x=0.5$ . Although this measurement does not provide evidence for the existence of another phase. Maybe the parts of the corresponding sample used for such measurements were pure.

In tables 7.20 and 7.21 the refined impurities with fractions are presented. With those values the total content of one element in the sample was calculated. Results are presented in table 7.22. The final contents do not fit to prepared mixtures of elements (table 7.22), especially contents of Fe and Si. The presence of at least one additional phase might play an important role for those differences. The total number of refined parameters of models has probably overloaded the refinement. This would also explain why the contents of sample  $\text{MnFe}_{4-x}\text{Co}_x\text{Si}_3$   $x=0.2$  is closest to expected values (table 7.17).

	$Mn_{1-x}Co_xFe_4Si_3$	
	x=0.1	x=0.2
Phase 1	<b>Mn</b> <sub>0.95(1)</sub> <b>Co</b> <sub>0.11(1)</sub> <b>Fe</b> <sub>3.94(3)</sub> <b>Si</b> <sub>3</sub>	<b>Mn</b> <sub>0.817(8)</sub> <b>Co</b> <sub>0.13(1)</sub> <b>Fe</b> <sub>4.04(2)</sub> <b>Si</b> <sub>3</sub>
Fraction	0.636(9)	0.589(7)
Phase 2	<b>Mn</b> <sub>0.67(1)</sub> <b>Co</b> <sub>0.05(1)</sub> <b>Fe</b> <sub>0.27(1)</sub> <b>Si</b>	<b>Mn</b> <sub>0.494(9)</sub> <b>Co</b> <sub>0.189(9)</sub> <b>Fe</b> <sub>0.317(9)</sub> <b>Si</b>
Fraction	0.126(4)	0.147(3)
Phase 3	<b>Mn</b> <sub>0.46(1)</sub> <b>Co</b> <sub>0.22(1)</sub> <b>Fe</b> <sub>2.32(1)</sub> <b>Si</b>	<b>Mn</b> <sub>1.2(2)</sub> <b>Co</b> <sub>0.76(2)</sub> <b>Fe</b> <sub>1.00(2)</sub> <b>Si</b>
Fraction	0.238(8)	0.264(7)

**Table 7.20:** Refined atomic occupations of all compounds including impurities. Phases of base compounds are marked in bold.

	$MnFe_{4-x}Co_xSi_3$	
	x=0.2	x=0.5
Phase 1	<b>Mn</b> <sub>1.009(7)</sub> <b>Co</b> <sub>0.19(1)</sub> <b>Fe</b> <sub>3.79(2)</sub> <b>Si</b> <sub>3</sub>	<b>Mn</b> <sub>1.055(7)</sub> <b>Co</b> <sub>0.40(1)</sub> <b>Fe</b> <sub>3.54(2)</sub> <b>Si</b> <sub>3</sub>
Fraction	0.933(5)	0.657(9)
Phase 2		<b>Mn</b> <sub>0.47(2)</sub> <b>Co</b> <sub>0.22(2)</sub> <b>Fe</b> <sub>0.30(2)</sub> <b>Si</b>
Fraction		0.099(3)
Phase 3	<b>Mn</b> <sub>0.97(9)</sub> <b>Co</b> <sub>0.46(9)</sub> <b>Fe</b> <sub>1.57(9)</sub> <b>Si</b>	<b>Mn</b> <sub>1.22(4)</sub> <b>Co</b> <sub>0.84(4)</sub> <b>Fe</b> <sub>0.94(9)</sub> <b>Si</b>
Fraction	0.067(5)	0.244(9)

**Table 7.21:** Refined atomic occupations of all compounds including impurities. Phases of base compounds are marked in bold.

	$Mn_{1-x}Co_xFe_4Si_3$		$MnFe_{4-x}Co_xSi_3$	
	x=0.1	x=0.2	x=0.2	x=0.5
Mn	0.74(3)	0.88(3)	1.01(2)	1.04(4)
Co	0.12(1)	0.31(2)	0.21(2)	0.49(3)
Fe	2.87(7)	2.69(6)	3.64(5)	2.59(6)
Si	2.10(4)	2.18(3)	2.87(4)	2.31(4)

**Table 7.22:** Total observed contents of elements Mn, Co, Fe and Si in the samples (including impurities).

	$Mn_{1-x}Co_xFe_4Si_3$		$MnFe_{4-x}Co_xSi_3$	
	x=0.1	x=0.2	x=0.2	x=0.5
Mn	0.9	0.8	1.0	1.0
Co	0.1	0.2	0.2	0.5
Fe	4.0	4.0	3.8	2.5
Si	3.0	3.0	3.0	3.0

**Table 7.23:** Total expected contents of elements Mn, Co, Fe and Si in the samples (including impurities).



Instrumental parameters

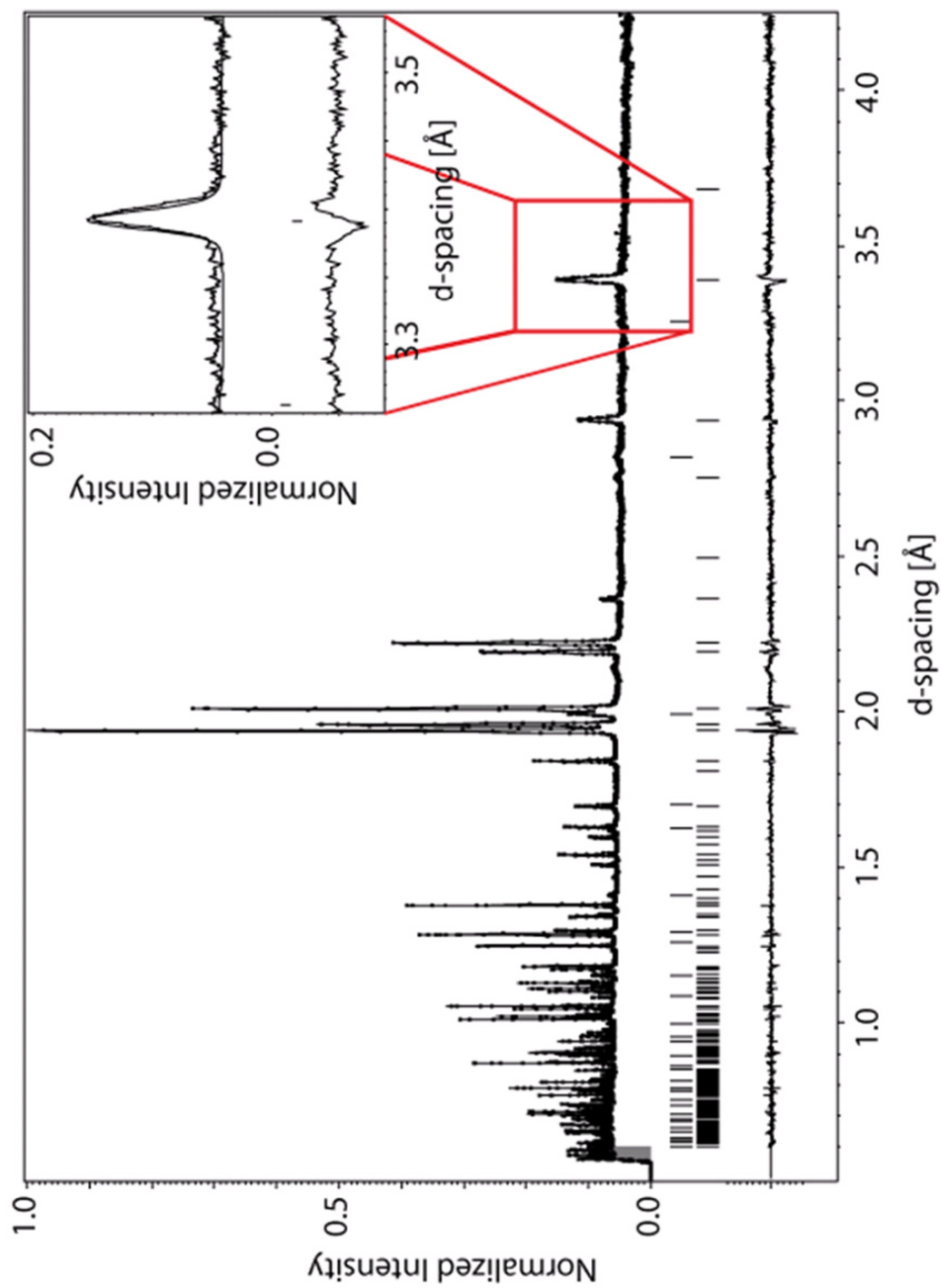


Figure 7.33: Powder diffraction pattern of  $\text{MnFe}_{4-x}\text{Co}_x\text{Si}_3$   $x=0.2$  taken at 310K with refinement.

It might be the case that instrumental parameters, determined with refinements performed on a diffraction pattern taken on a reference sample, are not sufficient. In the inset of figure 7.33 a region in d-spacing is presented where discrepancies are visible between calculated and measured pattern. Although this might look like it was due to asymmetry parameters on first look, the fact that the position of calculated peak does not fit to measured data reveals insufficiency of instrumental parameters (the intensity seems to have been refined properly). Since this is the only reflection in the refinement the effect is considered small. Furthermore, refining instrumental parameters does not necessarily improve the quality of the results even though the profile might be better. Those values would be less reliable, since the refinement would not base on a diffraction pattern which was taken on the reference sample anymore.

At low temperatures ( $T < 310\text{K}$ ) atomic displacement parameters of impurities have been refined. Atomic occupations were fixed.

### Qualities of refinements

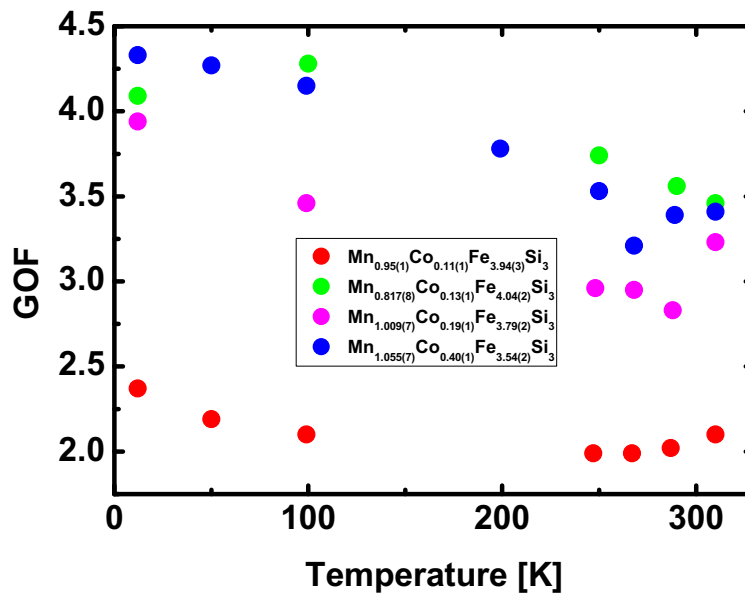


Figure 7.34: GOF-values of Co-doped materials as function of temperature.

Values of GOF of refinements as function of temperature are presented in figure 7.34. The smallest values emerged from refinements performed on diffraction patterns taken on  $Mn_{1-x}Co_xFe_4Si_3$   $x=0.1$ . This could be due to the fact that the Co-content does not affect the structure as much as it is the case for the other three materials. This gives rise to the assumption that the addition of Co induces phase transitions of the structures of the base compounds. For such investigations samples with higher Co contents have to be investigated.

The GOF-values were also influenced by the properties of the impurities. Points of phase transitions and details of the magnetic structures of the impurities are, to the best of the knowledge

of the author of this thesis, unknown in literature. Due to the small amounts of impurities which generate small reflections in comparison to the base compounds, the structures of impurities could not be determined.

### 7.3.3 Results of refinements

#### Nuclear structure of the Co-doped samples

The base phases of the models could be refined properly on diffraction patterns using hexagonal space group  $P6_3/mcm$  (193) with the very same atomic positions used for samples  $Mn_{5-x}Fe_xSi_3$   $x=0,1,2,3,4$  at room temperature. Though, atomic distributions were different. The best refinements, however, could be achieved with Fe and Co on position M1 and Mn and Fe on position M2. This setting leads to properly refined compositions close to the expected values. No crucial discrepancies, such as negative occupations or atomic displacement, were obtained. Furthermore, Co occupying position M1 makes physically sense, since the shell of Co consists of one additional electron in comparison to Fe. And in compound  $MnFe_4Si_3$  atomic position M1 is completely occupied by atom Fe. Therefore, one would expect Co to occupy position M1 first. Crystallographic details are presented in table 7.24.

Site	Atom	Coordination	Multiplicity	Wyckoff letter
M1	Co/Fe	(1/3,1/3,0)	4	d
M2	Mn/Fe	(x,0,1/4)	6	g
Si	Si	(x,0,1/4)	6	g

**Table 7.24:** Multiplicities and wyckoff letter of atoms of Co-doped samples.

Lattice constants as function of temperature are shown in figure 7.35. Kinks are clearly visible in lattice constant  $a$  for every composition. This is probably due to the magnetic phase transitions which affects all 4 samples (figures 5.5 and 5.6). Also, the kinks are always very close to the transition temperature. Notice that these effects are very small. Lattice constant  $a$  of material  $Mn_{0.95(1)}Co_{0.12(2)}Fe_{3.92(3)}Si_3$ , for example, seems to be affected by approximately 0.002 Å by the kink.

There is also a bump in lattice constant  $a$  of compounds  $Mn_{0.817(8)}Co_{0.13(1)}Fe_{4.04(2)}Si_3$  and  $Mn_{1.055(7)}Co_{0.40(1)}Fe_{3.54(2)}Si_3$  at 100K which similar to lattice constant  $a$  in  $Mn_{5-x}Fe_xSi_3$   $x=4$  (figure 7.20). These anomalies could be linked to the magnetism or to thermal activities. Since there is no hint for any transition in the magnetization measurements at these temperatures (figures 5.5 and 5.6), one would tend to discard first assumption.

Furthermore, lattice constant  $a$  increases in temperature for every composition except  $Mn_{0.95(1)}Co_{0.12(2)}Fe_{3.92(3)}Si_3$ . Here  $a$  remains more or less constant below 300K.

Temperature dependences of lattice constants  $c$  do not show anomalies for any composition. They just increase in temperature.

There are no anomalies visible in the temperature dependences of the volumes. The volume increases with the number of electrons per unit cell for all compounds except  $Mn_{1.009(7)}Co_{0.19(1)}Fe_{3.79(2)}Si_3$  (figure 7.37). This could be due to another electronic configuration.

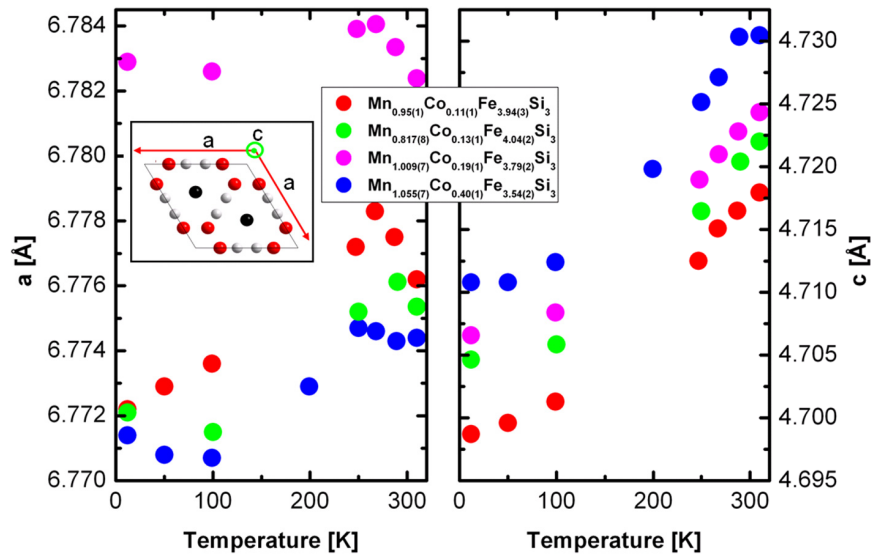


**Figure 7.35:** Lattice constants  $a$  (left) and  $c$  (right) of Co-doped materials as function of temperature. Inset presents the unit cell of these structures. Colors of points in diagram refer to colors of marked lattice constants in unit cell in the inset.

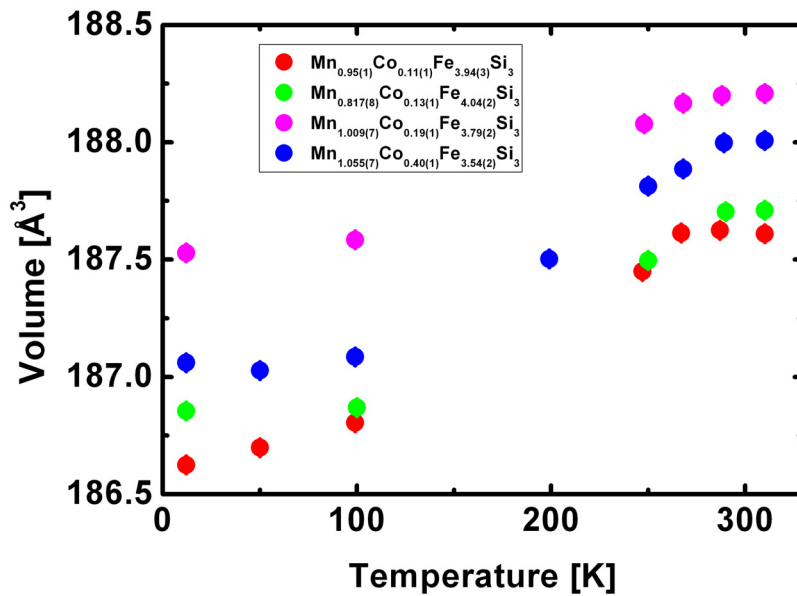


**Figure 7.36:** Volume of Co-doped materials as function of temperature.

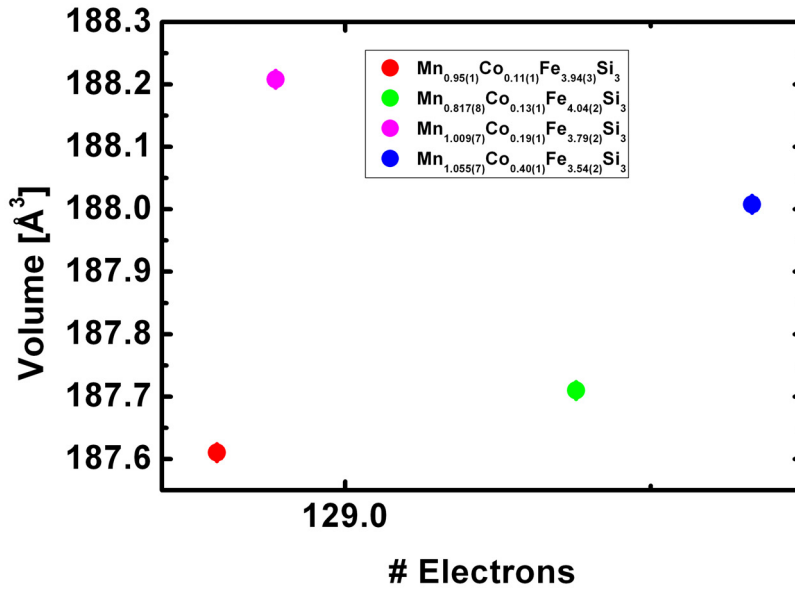


Figure 7.37: Volume of Co-doped materials as function of the number of electrons.

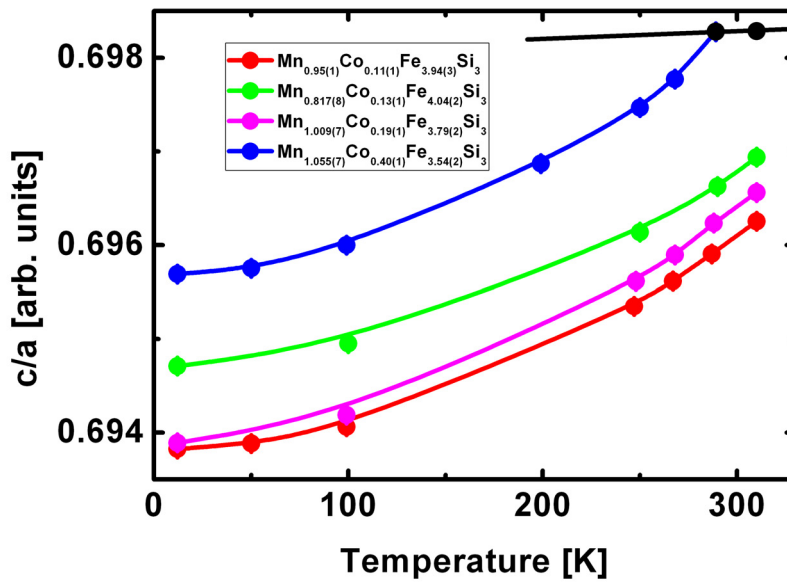
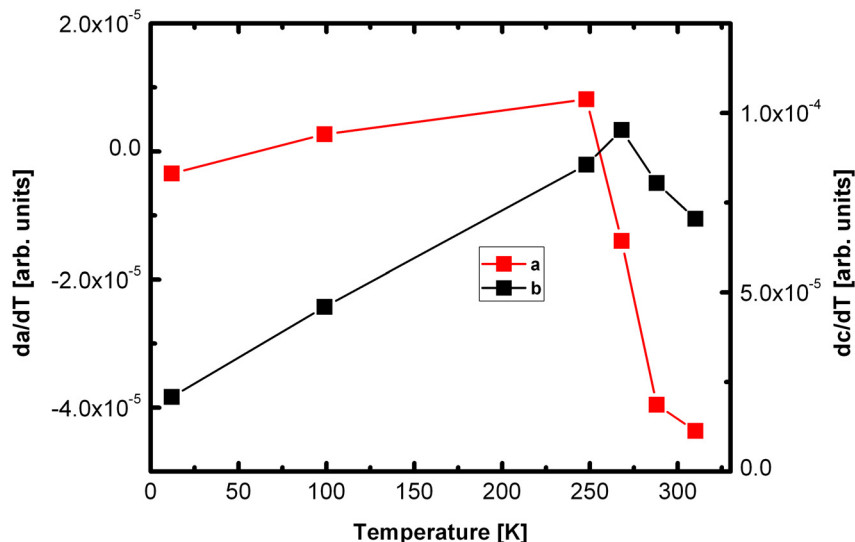


Figure 7.38: Value of c/a of Co-doped materials as function of temperature. Lines are only guides to the eye. Lines between points of measurements are only guides to the eye.



**Figure 7.39:** Derivatives of lattice constants of  $Mn_{1.009(7)}Co_{0.19(1)}Fe_{3.79(2)}Si_3$  as function of temperature. Lines between points in diagram are guides to the eye.

The quotient  $c/a$  shows only anomalies for composition  $Mn_{1.055(7)}Co_{0.40(1)}Fe_{3.54(2)}Si_3$  (figure 7.38). Here, the ratio seems to be constant, which is indicated by the black line. This anomaly could have been emerged due to the phase transition, since the compound is proposed to be in the paramagnetic phase at 310K (figure 5.6 (b)).

The derivatives of both compounds  $Mn_{1.009(7)}Co_{0.19(1)}Fe_{3.79(2)}Si_3$  (figure 7.39) and  $Mn_{1.055(7)}Co_{0.40(1)}Fe_{3.54(2)}Si_3$  (figure 7.40) seem to indicate the presence of phase transitions. This is due to the fact that sharp anomalies in the diagrams are clearly visible. Still, it has to be mentioned that the number of points of measurements is not sufficient to extract the exact ordering temperatures.

The derivatives of the lattice constants of  $Mn_{1.009(7)}Co_{0.19(1)}Fe_{3.79(2)}Si_3$  are obviously affected at different temperatures. The derivative of lattice constant  $a$  seems to be affected at  $\sim 250$ K and the derivative of lattice constant  $c$  at  $\sim 270$ K. This cannot be due to the ferromagnetic ordering since the transition temperature is 299(1)K (material  $MnFe_{4-x}Co_xSi_3$   $x=0.2$  in section 5.3). Here, no sign for any kind of transition could be detected between 250K and 270K. Therefore, those anomalies could not have emerged due to the magnetism.

Both derivatives of the lattice constants of  $Mn_{1.055(7)}Co_{0.40(1)}Fe_{3.54(2)}Si_3$  indicate sharp transitions at  $T \sim 270$ K (figures 7.39 and 7.40). Additional points of measurements could increase the resolution and maybe reveal small differences in the temperatures which are not visible now. In section 5.3 the phase transition is proposed to take place at  $T=288(1)$ K (material  $MnFe_{4-x}Co_xSi_3$   $x=0.2$ ). Diffraction patterns on this compound were taken at 310K, 289K, 268K and lower temperatures as already mentioned in section 7.3.1. These points of measurements are probably not enough to characterize a phase transition at 288(1)K.

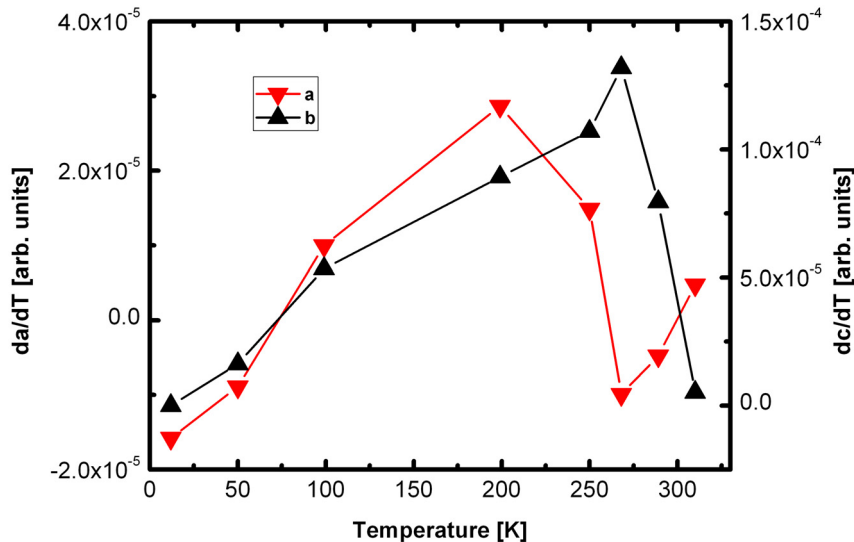


**Figure 7.40:** Derivatives of lattice constants of  $\text{Mn}_{1.055(7)}\text{Co}_{0.40(1)}\text{Fe}_{3.54(2)}\text{Si}_3$  as function of temperature. Lines between points in diagram are guides to the eye.

In figure 7.41 normalized Fe occupation on atomic positions M1 and M2 is presented. Since Co only occupies position M1 one would expect a linear dependence between Fe and Co. This is the case in the figure.

Position M2 is only occupied by Mn and Fe. The peak at content of Co=0.132 is due to the wrong ratio between Fe and Co, i.e. too much Fe.

The atomic displacements parameters given in figure 7.42 meet physical expectations, since they increase in temperature. Material  $\text{Mn}_{0.95(1)}\text{Co}_{0.12(2)}\text{Fe}_{3.92(3)}\text{Si}_3$  exhibits highest atomic displacement.

Bumps are visible in the thermal displacement of  $\text{Mn}_{0.95(1)}\text{Co}_{0.11(1)}\text{Fe}_{3.94(3)}\text{Si}_3$  at 267K. These anomalies cannot be linked to the phase transition, since it takes place above 300K (figure 5.5 (a)). This anomaly could be due to a reordering of the electronic configuration of an atom. In that case one would expect influences on other values such as magnetism, too. Only lattice constant  $a$  of this compound shows an abrupt increase at this temperature. The origin of these phenomena cannot be clarified here.

The phase transition in compound  $\text{Mn}_{1.055(7)}\text{Co}_{0.40(1)}\text{Fe}_{3.54(2)}\text{Si}_3$  takes place at  $T=299(1)\text{K}$  (section 5.3). There are indeed abrupt increases in the displacement of every atom visible, which is probably caused by the influence of the ferromagnetism. Still this effect is small (between  $0.0005 \text{ \AA}^2$  and  $0.001 \text{ \AA}^2$ ).

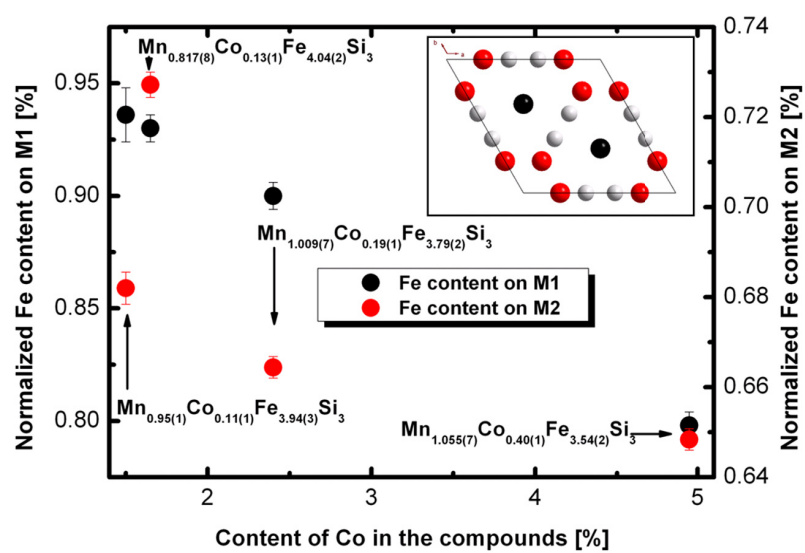


**Figure 7.41:** Normalized content of Fe on M1 and M2 as function of Co content. Inset presents the unit cell of these structures. Colors of points in diagram refer to colors of atoms in unit cell in the inset.



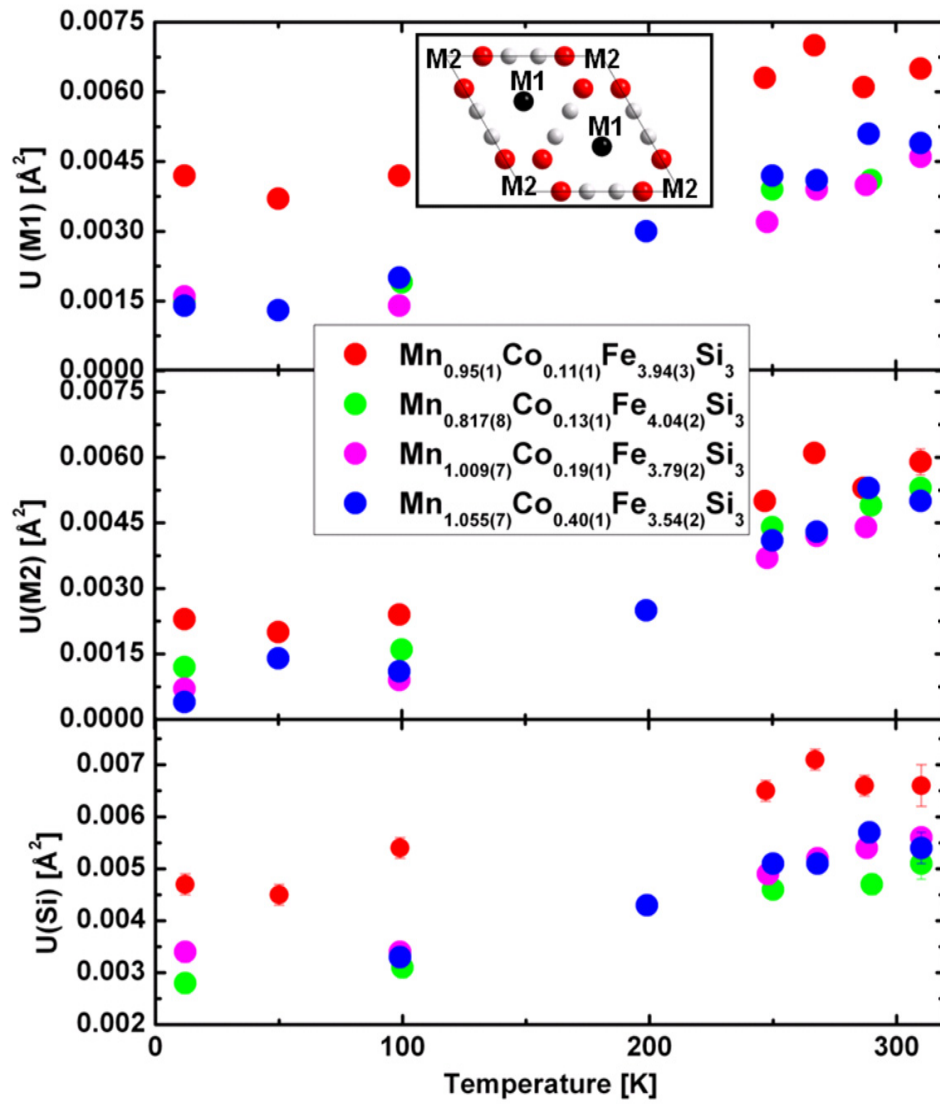


Figure 7.42: Atomic displacement parameters of Co-doped materials as function of temperature. The inset denotes the atomic sites. Si is grey in the unit cell.

### Magnetic structure of the Co-doped samples

The magnetic model used for the refinements on diffraction patterns is the same as for  $Mn_{5-x}Fe_xSi_3$   $x=4$  (shown in figure 7.26, magnetic form factors are discussed in section A.4.). This model can be used for all Co-doped compounds since magnetization measurements are indicating ferromagnetic behaviour. An increase of intensity at low temperatures (similar to increase of intensities in diffraction patterns taken on  $Mn_{5-x}Fe_xSi_3$   $x=4$ ) was also observed. Unfortunately, no results have been published about these impure compositions so far.

However, transition-metal monosilicides of composition TMSi (TM=Cr, Mn, Fe, Co) attract the attention of scientific groups due to various magnetic ground states [101]. FeSi, which is isometric to  $Mn_{1-y-z}Fe_yCo_zSi$ , is obviously a paramagnetic semiconductor [102]. No magnetic long range ordering could be detected via neutron powder diffraction [103]. MnSi orders antiferromagnetically below 30K [104]. A model for frustrated magnetic helices was obviously developed by the MnSi-structure [105]. CoSi is reported to exhibit diamagnetic [98] and no magnetic behaviour [106].

$Fe_3Si$ , isometric to  $Mn_{3-y-z}Fe_yCo_zSi$ , is a ferromagnet with a Curie temperature of 530°C [107, 108].  $Mn_3Si$  orders ferromagnetically below 23K [87].  $Co_3Si$  is proposed to be stable between 1170°C and 1210°C [109].

Also, compounds consisting of combinations of the elements Mn, Fe, Co and Si exhibit various structures. For example,  $Mn_{1-x}Co_xSi$  is reported to exhibit a spin-glass state [101].  $Fe_xCo_{1-x}Si$  has ferromagnetic behaviour between 8.8K and 43.5K for  $0.3 \leq x \leq 0.9$  [110].

Details of the magnetism of the exact compositions of any impurity could not be found. All these different magnetic structures mentioned above do not allow to apply magnetic models for the impurities anymore. This is due to the lack of information in the diffraction patterns. Also a magnetic model cannot be that easily developed, since substitution of elements can shift the magnetic behaviour immediately.

Therefore, the influence of the magnetic structures of the impurities on the refinement of the base compounds is considered small. Unfortunately the influence of the impurities on Magnetization and MCE measurements cannot be estimated.

The magnetic behaviour of the moments on the two atomic positions indicates ferromagnetism at high temperatures for the base materials. Since phase transitions are still in progress at 310K (290K for  $Mn_{1.055(7)}Co_{0.40(1)}Fe_{3.54(2)}Si_3$ ) (figures 5.5 and 5.6) refined values of magnetic moments are not reliable here. Therefore, negative values cannot be taken into account.

The magnetic moment refined on position M1 is much larger than any other refined moment of a base compound or even  $Mn_{5-x}Fe_xSi_3$   $x=4$  (section 7.2.6). This might give rise to doubt those values. Still, the refinements of sample  $Mn_{1-x}Co_xFe_4Si_3$   $x=0.2$  are promising due to the smallest GOF-values (figure 7.34) in the Co-doped compounds presented in this thesis. Therefore, the author of this thesis tends to consider this effect real.

The magnetic moments were fitted with equation 7.1, which has already been used for fitting magnetic moments of  $Mn_{5-x}Fe_xSi_3$   $x=4$ .

Fitted values on M1 are  $T_C=250(3)K$ ,  $m_{sat}=0.5(3)\mu_B$  and  $\beta=0.2(1)$  for base compound  $Mn_{1.055(7)}Co_{0.40(1)}Fe_{3.54(2)}Si_3$ . The ordering of the magnetic moment on M1 has probably induce the kink in lattice constant  $a$  (figure 7.35) and the kink in its derivative (figure 7.40). Even though the

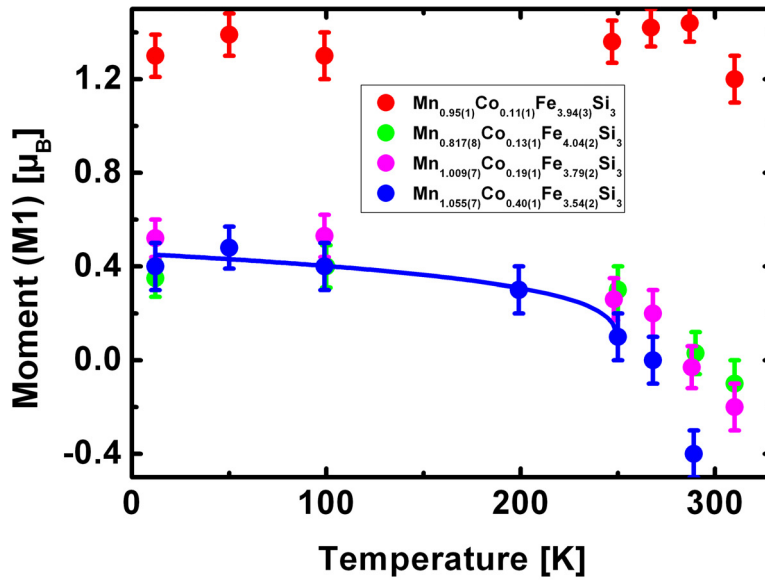


Figure 7.43: Magnetic moments  $M1$  of Co-doped materials as function of temperature.

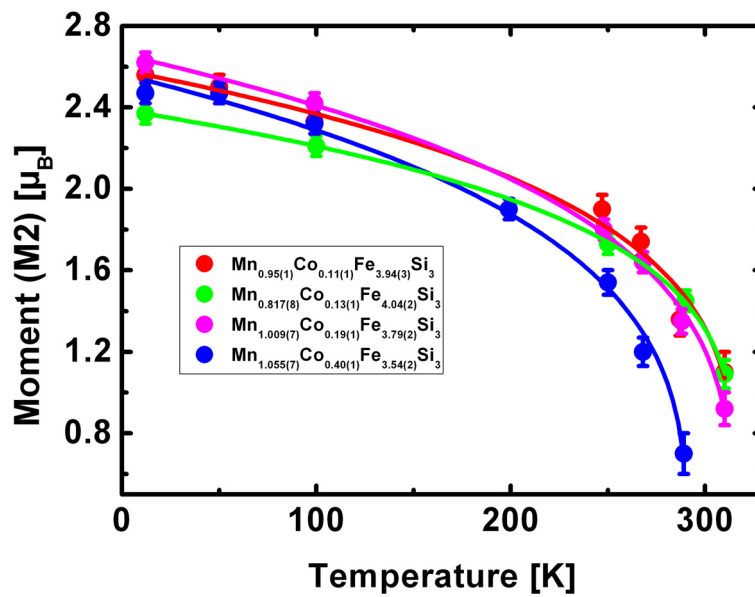
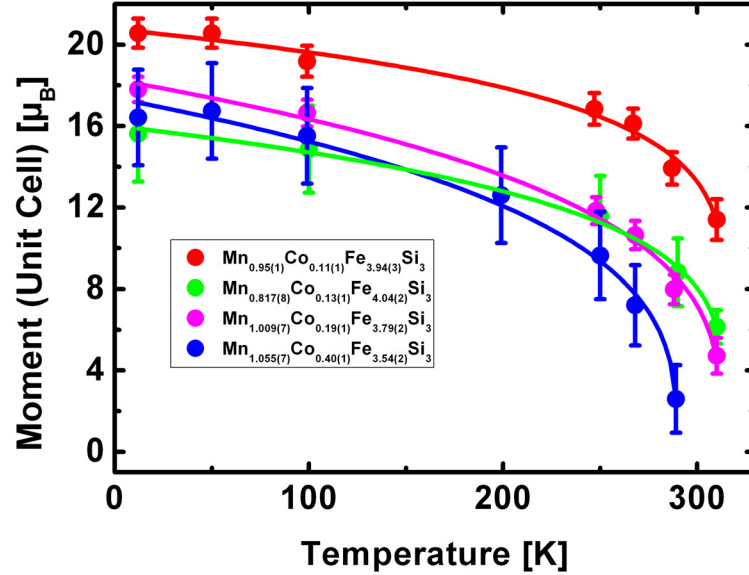


Figure 7.44: Magnetic moments of  $M2$  Co-doped materials as function of temperature.

exact values of the other ordering temperatures could not have been extracted, the temperatures dependences of  $a$  and its derivative (figure 7.39) of every base compound seem to be linked to



**Figure 7.45:** Magnetic moments of the unit cell of Co-doped materials as function of temperature.

the ordering temperatures (figures 5.5 and 5.6).

$T_C$ ,  $m_{sat}$  and  $\beta$  of M2 and the whole unit cell are presented in tables 7.25 and 7.26.

compound	$T_C(M2)$ [K]	$m_{sat}$ [ $\mu_B$ ]	$\beta$
$Mn_{0.95(1)}Co_{0.11(1)}Fe_{3.94(3)}Si_3$	317(6)	2.64(9)	0.23(3)
$Mn_{0.817(8)}Co_{0.13(1)}Fe_{4.04(2)}Si_3$	316.9(7)	2.39(4)	0.204(3)
$Mn_{1.009(7)}Co_{0.19(1)}Fe_{3.79(2)}Si_3$	315(2)	2.7(2)	0.26(1)
$Mn_{1.055(7)}Co_{0.40(1)}Fe_{3.54(2)}Si_3$	291(2)	2.6(3)	0.27(2)

**Table 7.25:**  $T_C$ ,  $m_{sat}$  and  $\beta$ , all extracted from magnetic moments on M2.

Transition temperatures of magnetic moments on M2 and of the whole unit cell are in agreement with each other with respect to error bars (tables 7.25 and 7.26). Therefore, moment M2 seems to order at higher temperatures marking the boundary between para- and ferromagnetism. The error bar of the fitted transition temperature of the magnetic moment on site M2 of  $Mn_{0.817(8)}Co_{0.13(1)}Fe_{4.04(2)}Si_3$  is quite small. This is due to the fact that it is the only compound with a refined magnetic moment below  $0.8\mu_B$  which has improved the quality of fitting.

The fitted temperature of phase transition of  $MnFe_{4-x}Co_xSi_3$   $x=0.2$  (section 5.3) is 299(1)K which is in contrast to the fitted values of the magnetic moment of the whole unit cell (table 7.26). This could be due to a lack of points of measurements closer to the phase transition. For  $MnFe_{4-x}Co_xSi_3$   $x=0.5$  the fitted phase transition temperature is 288(1)K (section 5.3) which is in agreement within the error bars with 289.(6)7K fitted with the magnetic moments of the whole unit cell (table 7.26). The fitted values of the transition temperatures of the other two

compound	$T_C$ [K]	$m_{sat}$ [ $\mu_B$ ]	$\beta$
$Mn_{0.95(1)}Co_{0.11(1)}Fe_{3.94(3)}Si_3$	315(3)	21(2)	0.15(2)
$Mn_{0.817(8)}Co_{0.13(1)}Fe_{4.04(2)}Si_3$	314(2)	16(2)	0.22(2)
$Mn_{1.009(7)}Co_{0.19(1)}Fe_{3.79(2)}Si_3$	313(2)	18(2)	0.29(2)
$Mn_{1.055(7)}Co_{0.40(1)}Fe_{3.54(2)}Si_3$	289.6(7)	17(2)	0.31(2)

**Table 7.26:**  $T_C$ ,  $m_{sat}$  and  $\beta$ , all extracted from magnetic moments of the whole unit cell.

compounds in table 7.26 cannot be compared to the magnetization measurements which is due to the lack of points of measurements above the phase transitions in figure 5.5.

Assuming the influence of the impurities on the MCE is small, which is probably the case for  $MnFe_{4-x}Co_xSi_3$   $x=0.2$  with a fraction of less than 10% of an impurity (tables 7.20 and 7.21) a connection between the MCE and the refined values of the magnetic moments can be proposed. Different temperatures of phase transitions of the two moments on the magnetic sites could be linked to the MCE as it is proposed to be the case for  $Mn_{5-x}Fe_xSi_3$   $x=4$  (equations 7.2-7.4 in section 7.2.6).  $Mn_{0.95(1)}Co_{0.11(1)}Fe_{3.94(3)}Si_3$  ( $Mn_{1-x}Co_xFe_4Si_3$   $x=0.1$ ) exhibits a larger MCE than  $Mn_{5-x}Fe_xSi_3$   $x=4$  (figure 6.2). This could be due to the fact the the magnetic moment on site M1 is already aligned close to room temperature with a value of  $1.2(1)\mu_B$ . The equivalent magnetic moment in  $Mn_{5-x}Fe_xSi_3$   $x=4$  is still not ordered. Therefore, the the alignment of the magnetic moment on M1 when no field is applied does not weaken but improve the MCE.

Similar assumptions can be done for the other Co-doped samples. The MCE seems to scale with the value of the saturated magnetic moment of the whole unit cell (table 7.26).  $Mn_{0.817(8)}Co_{0.13(1)}Fe_{4.04(2)}Si_3$  and  $Mn_{1.055(7)}Co_{0.40(1)}Fe_{3.54(2)}Si_3$  exhibit the smallest MCEs (figure 6.2) and the smallest magnetic moment of the whole unit cell. The differences in the ordering temperatures of the two magnetic atoms of these compounds (figures 7.43 and 7.44) seem to be comparable to  $Mn_{5-x}Fe_xSi_3$   $x=4$  (figure 7.27).

The fact that the MCE measurements depend on the value of the magnetic moments agrees with theory, since the entropy change depends on the magnetization of the sample (equation 1.2).

The value of the refined magnetic moment scales with the measured intensity of magnetic reflections. In section 7.2.6 sensitivity of small magnetic moments ( $\sim 0.5\mu_B$ ) was analysed. Qualities of refinements of  $Mn_{5-x}Fe_xSi_3$   $x=4$  were obviously not sufficient for refining the magnetic moment on site M1 properly.

Earlier, discrepancies of the profile functions of peaks were reported. But this affected only the position of peaks. Since magnetism is only affected by intensities here, this issue probably had no impact on the magnetic moments in the refinement.

In this work error bars were directly taken from Jana 2006. It has to be mentioned that the presence of impurities weakens the quality of the analysis. This is because overlapping of peaks, and a lot of parameters which influence each other. Still, final refinements give a convincing impression.

$Mn_{0.95(1)}Co_{0.11(1)}Fe_{3.94(3)}Si_3$								
			M1		M2		Si	
T [K]	$a$ [Å]	$c$ [Å]	U [Å <sup>2</sup> ]	M [ $\mu_B$ ]	U [Å <sup>2</sup> ]	M [ $\mu_B$ ]	U [Å <sup>2</sup> ]	GOF
310	6.7762(1)	4.71795(8)	0.0063(2)	1.2(1)	0.0059(3)	1.1(1)	0.0066(4)	2.1
287	6.7775(1)	4.7165(1)	0.0061(2)	1.44(8)	0.0053(2)	1.36(8)	0.0066(2)	2.02
267	6.7783(1)	4.7151(1)	0.0070(3)	1.42(8)	0.0061(2)	1.74(7)	0.0071(2)	1.99
247	6.7772(1)	4.71251(9)	0.0063(3)	1.36(9)	0.0050(2)	1.90(7)	0.0065(2)	1.99
99	6.7736(1)	4.7013(1)	0.0042(2)	1.3(1)	0.0024(2)	2.33(6)	0.0054(2)	2.1
50	6.7729(1)	4.6996(1)	0.0037(2)	1.39(9)	0.0020(2)	2.50(6)	0.0045(2)	2.19
12	6.7722(1)	4.69871(9)	0.0042(2)	1.3(9)	0.0023(2)	2.56(6)	0.0047(2)	2.37
$Mn_{0.817(8)}Co_{0.13(1)}Fe_{4.04(2)}Si_3$								
			M1		M2		Si	
T [K]	$a$ [Å]	$c$ [Å]	U [Å <sup>2</sup> ]	M [ $\mu_B$ ]	U [Å <sup>2</sup> ]	M [ $\mu_B$ ]	U [Å <sup>2</sup> ]	GOF
310	6.77536(9)	4.72200(7)	0.0046(2)	-0.1(1)	0.0053(2)	1.09(7)	0.0051(3)	3.46
290	6.77612(9)	4.72042(7)	0.0041(1)	0.03(9)	0.0049(1)	1.45(5)	0.0047(2)	3.56
250	6.7752(1)	4.71647(7)	0.0039(1)	0.3(1)	0.0044(1)	1.73(5)	0.0046(2)	3.74
100	6.7615(1)	4.70585(8)	0.0019(1)	0.40(9)	0.0016(1)	2.21(5)	0.0031(2)	4.28
12	6.7721(1)	4.70464(8)	0.0015(1)	0.35(8)	0.0012(1)	2.37(5)	0.0028(2)	4.09
$Mn_{1.009(7)}Co_{0.19(1)}Fe_{3.79(2)}Si_3$								
			M1		M2		Si	
T [K]	$a$ [Å]	$c$ [Å]	U [Å <sup>2</sup> ]	M [ $\mu_B$ ]	U [Å <sup>2</sup> ]	M [ $\mu_B$ ]	U [Å <sup>2</sup> ]	GOF
310	6.78239(9)	4.72435(7)	0.0046(2)	-0.2(1)	0.0050(3)	0.92(8)	0.0051(2)	3.23
288	6.78335(9)	4.72280(6)	0.0040(1)	-0.03(9)	0.0044(2)	1.35(6)	0.0054(2)	2.83
268	6.78406(9)	4.72099(7)	0.0039(1)	0.2(1)	0.0042(3)	1.64(5)	0.0052(2)	2.95
248	6.78391(9)	4.71899(7)	0.0032(1)	0.26(9)	0.0037(3)	1.80(5)	0.0049(2)	2.96
99	6.7826(1)	4.70839(7)	0.0014(1)	0.53(9)	0.0009(3)	2.42(5)	0.0034(2)	3.46
12	6.7829(1)	4.70668(7)	0.0016(1)	0.52(8)	0.0007(3)	2.62(5)	0.0034(2)	3.94
$Mn_{1.055(7)}Co_{0.40(1)}Fe_{3.54(2)}Si_3$								
			M1		M2		Si	
T [K]	$a$ [Å]	$c$ [Å]	U [Å <sup>2</sup> ]	M [ $\mu_B$ ]	U [Å <sup>2</sup> ]	M [ $\mu_B$ ]	U [Å <sup>2</sup> ]	GOF
310	6.7744(1)	4.73046(9)	0.0049(2)	-	0.0050(2)	-	0.0054(3)	3.41
289	6.7743(1)	4.73035(9)	0.0051(2)	-0.4(1)	0.0053(2)	0.7(1)	0.0057(2)	3.39
268	6.7746(1)	4.72712(9)	0.0041(1)	0.0(1)	0.0043(2)	1.20(7)	0.0051(2)	3.21
250	6.7747(1)	4.72514(9)	0.0042(2)	0.1(1)	0.0041(2)	1.54(6)	0.0051(2)	3.53
199	6.7729(1)	4.71983(9)	0.0030(2)	0.3(1)	0.0025(2)	1.90(5)	0.0043(2)	3.78
99	6.7707(1)	4.7124(1)	0.0020(2)	0.4(1)	0.0011(2)	2.32(5)	0.0033(2)	4.15
50	6.7708(1)	4.7108(1)	0.0013(2)	0.48(9)	0.0014(2)	2.47(5)	0.0004(2)	4.27
12	6.7714(1)	4.7108(1)	0.0014(2)	0.4(1)	0.0004(2)	2.47(5)	0.0004(2)	4.33

**Table 7.27:** Refined atomic parameters and GOF-values.

## 7.4 Co-doped materials and $\text{Mn}_{5-x}\text{Fe}_x\text{Si}_3$ $x=4$ at room temperature

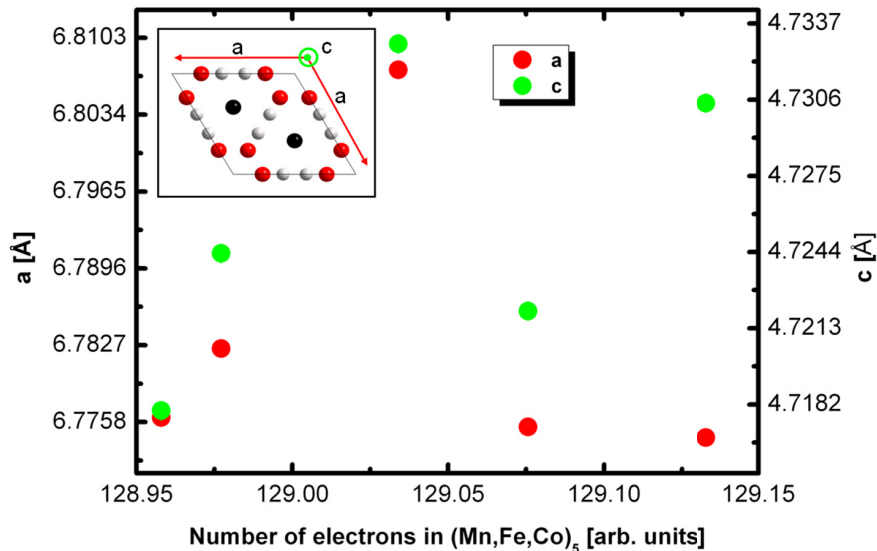


**Figure 7.46:** Lattice constants  $a$  and  $c$  of Co-doped materials and  $\text{Mn}_{5-x}\text{Fe}_x\text{Si}_3$   $x=4$  as function of the number of electrons in  $(\text{Mn,Fe,Co})_5$ . All taken from refinements on diffraction patterns taken at 310K except  $\text{Mn}_{5-x}\text{Fe}_x\text{Si}_3$   $x=4$ , which was taken at 300K. Colors of points in diagram refer to colors of marked lattice constants in unit cell in the inset. Error bars are smaller than points in diagram. Material that referring to a certain number of electrons can be taken from 7.47.

Analog to section 7.2.4 lattice constants, volumes of unit cells,  $c/a$ -values and atomic displacement parameters of the Co-doped base compounds can be compared to the corresponding results of  $\text{Mn}_{5-x}\text{Fe}_x\text{Si}_3$   $x=4$ . All results were extracted from data taken at 310K except  $\text{Mn}_{5-x}\text{Fe}_x\text{Si}_3$   $x=4$ , which were taken at 300K.

The lattice constants as function of the electrons in  $(\text{Mn,Fe,Co})_5$  are presented in figure 7.46. There is no general trend visible in the lattice constants in this figure. They do not obey Vegard's law, instead the dependence seems to be more complex. More points of measurements would be useful to understand any kind of tendency, assuming that a tendency exists.

There is also no general pattern visible in the volume of the unit cell in figure 7.47. The ratio  $c/a$ , on the other hand, seems to increase with the number of electrons. More points of measurements are needed for linear fitting.

All these dependencies, except the volume of the unit cell, have developed local (or even absolute) minima at 129.03. The qualitative dependence seems to be repeated in these figures. There is no reason to question the results of the Co-doped base compounds here. Even though

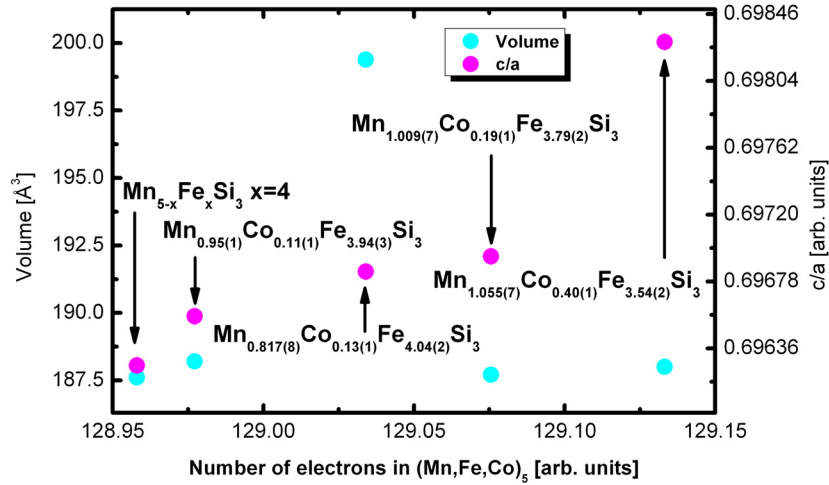


**Figure 7.47:** Volume and  $c/a$  Co-doped materials and  $Mn_{5-x}Fe_xSi_3$   $x=4$  as function of the number of electrons in  $(Mn,Fe,Co)_5$ . All taken from refinements on diffraction patterns taken at 310K except  $Mn_{5-x}Fe_xSi_3$   $x=4$ , which was taken at 300K. Error bars are smaller than points in diagram.

the presence of several impurities could be detected the quality of the refinements seems to be reasonable.

Regarding the dependencies discussed in this section and those in section 7.2.4, the links between nuclear structure and magnetism are in agreement. The nuclear structure is not affected that much by doping anymore, since the magnetic behaviour, which is ferromagnetic, is not shifted in the Co-doped base compounds. Therefore, one might conclude that nuclear and magnetic structure are presumably linked to each other, even in the paramagnetic states. The next step is to further investigate this kind of coupling in the context of the MCE, which is proposed to take place due to the interplay between those two qualities (section 1.3.1).



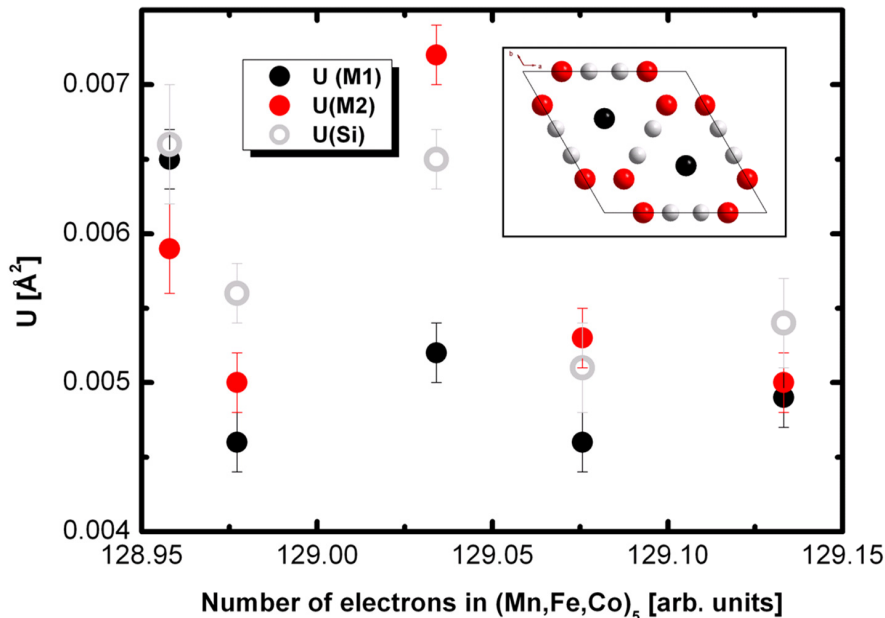


**Figure 7.48:** Isotropic displacement parameters of Co-doped materials and  $\text{Mn}_{5-x}\text{Fe}_x\text{Si}_3$   $x=4$  as function of the number of electrons in  $(\text{Mn,Fe,Co})_5$ . All taken from refinements on diffraction patterns taken at 310K except  $\text{Mn}_{5-x}\text{Fe}_x\text{Si}_3$   $x=4$ , which was taken at 300K. Inset presents the unit cell of these structures. Colors of points in diagram refer to colors of atoms in unit cell in the inset. Material that referring to a certain number of electrons can be taken from 7.47.

## 7.5 Summary

Refinements on diffraction patterns taken on the compounds  $\text{Mn}_{5-x}\text{Fe}_x\text{Si}_3$   $x=0,1,2,3,4$  confirmed hexagonal structure  $P6_3/mcm$  at room temperature. Antiferromagnetic structures of  $\text{Mn}_{5-x}\text{Fe}_x\text{Si}_3$   $x=0$  and ferromagnetism of  $\text{Mn}_{5-x}\text{Fe}_x\text{Si}_3$   $x=4$  were refined at low temperatures. Co-doped compounds  $\text{Mn}_{0.95(1)}\text{Co}_{0.11(1)}\text{Fe}_{3.94(3)}\text{Si}_3$ ,  $\text{Mn}_{0.817(8)}\text{Co}_{0.13(1)}\text{Fe}_{4.04(2)}\text{Si}_3$ ,  $\text{Mn}_{1.009(7)}\text{Co}_{0.19(1)}\text{Fe}_{3.79(2)}\text{Si}_3$  and  $\text{Mn}_{1.055(7)}\text{Co}_{0.40(1)}\text{Fe}_{3.54(2)}\text{Si}_3$  also crystallize in hexagonal unit cell  $P6_3/mcm$ . The refined magnetic structures are similar to compound  $\text{Mn}_{5-x}\text{Fe}_x\text{Si}_3$   $x=4$ .

The refined compositions of  $\text{Mn}_{5-x}\text{Fe}_x\text{Si}_3$   $x=0,1,2,3,4$  almost exactly agree with the proposed compounds as proposed in [28, 77]. An impurity with the composition  $\text{Mn}_{1.69(3)}\text{Fe}_{1.31(3)}\text{Si}$  could be detected in the batch of the sample which was supposed to crystallize in pure  $\text{Mn}_{5-x}\text{Fe}_x\text{Si}_3$   $x=4$ . No traces of impurities could be detected in any other sample of these compounds.

Anomalies were revealed in the Fe content dependence of lattice constant  $a$ , the quotient of the lattice constants  $c/a$  and thermal displacement parameters of  $\text{Mn}_{5-x}\text{Fe}_x\text{Si}_3$   $x=0,1,2,3,4$ . The magnetism in this family of compounds seems to be directly linked to these anomalies, even though they are all paramagnetic at room temperature except  $\text{Mn}_{5-x}\text{Fe}_x\text{Si}_3$   $x=4$ . This is due to the fact that points of anomalies fall together with the change of the magnetic properties at low

temperatures in the dependence of the Fe content. The large magnetic moment on site M2 is proposed to play an important role for the magnetic behaviour of this family of compounds.

The diffraction pattern taken on  $\text{Mn}_{5-x}\text{Fe}_x\text{Si}_3$   $x=0$  at 100K could be refined with the same hexagonal unit cell which was used for room temperature measurements. The antiferromagnetic structure of  $\text{Mn}_{5-x}\text{Fe}_x\text{Si}_3$   $x=0$  at 90K (and above 60K) could be refined with the orthorhombic unit cell with is the same space group proposed in [39]. The magnetism at that temperature is driven by Mn atoms on site M22 with a refined value of  $1.53(6)\mu_B$ . At 60K and below the magnetic structure could be refined with a monoclinic space group which has never been done in literature before. Weak ferromagnetism ( $\sim 0.5\mu_B$ ) could also be detected on one atomic site at these temperatures. The maximum value of the magnetic moments is  $\sim 3\mu_B$  at 40K. In the case of an applied magnetic field the weak ferromagnetism is annihilated. This could cause the orthorhombic phase to be more stable than the monoclinic one when a field is applied.

Anomalies are visible in the temperature dependence of lattice constant  $a$  and atomic displacement of  $\text{Mn}_{5-x}\text{Fe}_x\text{Si}_3$   $x=4$ . Both phenomena are proposed to be linked to the magnetism. The ferromagnetic behaviour of  $\text{Mn}_{5-x}\text{Fe}_x\text{Si}_3$   $x=4$  was investigated at low temperatures confirming structure  $P6_3/mcm$  with magnetic moments applied parallel to the  $c$ -axis as proposed in [28]. The value of the ordering temperature on site M1 is not reliable due to the small magnetic moment. The ordering temperature of the magnetic moment on site M2 is higher and its value much larger than on site M1. The value of the moment on site M1 does not exceed  $1.2\mu_B$ . The fitted saturation moments is in agreement with the results of the refinements. Discrepancies in refinements appeared on site M1 due to its small value ( $\sim 0.2\mu_B$  at 220K). The nature of the magnetism of the two atomic sites seems to be linked to the MCE (equations (7.2) to (7.4)).

The different setting (formula of Jason Hodges for transformation from d-spacing to time) used for refinements on the Co-doped samples were taken proved value. The quality of the refinements could be improved in comparison to  $\text{Mn}_{5-x}\text{Fe}_x\text{Si}_3$   $x=4$ . This affects especially the magnetism due to small magnetic moments ( $\sim 0.5\mu_B$ ) on one atomic site. In all samples impurities with fractions of up to 41.11(7)% could be refined.

The temperature dependence of the lattice constants is similar to  $\text{Mn}_{5-x}\text{Fe}_x\text{Si}_3$   $x=4$ . Anomalies are visible in lattice constant at and above 250K which are proposed to be linked to the magnetism on one atomic site, too.

The quotient  $c/a$  exhibited an anomaly for the base compound  $\text{Mn}_{1.055(7)}\text{Co}_{0.40(1)}\text{Fe}_{3.54(2)}\text{Si}_3$ , which could be due to the magnetism. Still, additional points of measurements would be needed to confirm this assumption, since there are not enough points of measurements available.

Derivatives of the lattice constants as function of temperature indicate the presence of two different phase transitions for base compounds  $\text{Mn}_{1.009(7)}\text{Co}_{0.19(1)}\text{Fe}_{3.79(2)}\text{Si}_3$  and  $\text{Mn}_{1.055(7)}\text{Co}_{0.40(1)}\text{Fe}_{3.54(2)}\text{Si}_3$ .

The atomic displacement parameters as function of temperature exhibited only anomalies for compound  $\text{Mn}_{0.95(1)}\text{Co}_{0.11(1)}\text{Fe}_{3.94(3)}\text{Si}_3$ . Its origination could not be understood here.

Ferromagnetic structures of the Co-doped base compounds could be refined using the same setting as for  $\text{Mn}_{5-x}\text{Fe}_x\text{Si}_3$   $x=4$  (magnetic moments applied parallel to the  $c$ -axis). The presence of two different ordering temperatures of the magnetic moments on the two atomic sites is similar to  $\text{Mn}_{5-x}\text{Fe}_x\text{Si}_3$   $x=4$ . The resulted saturation moments of the applied model fit well to

the refined parameters. All compounds exhibit large magnetic moments on site M2 similar to  $\text{Mn}_{5-x}\text{Fe}_x\text{Si}_3$   $x=4$ .

Both, the presence of two magnetic sites ordering at different temperatures and the absolute values of the moments seem to influence the MCE. This is in agreement with theory of the MCE.

# Chapter 8

## Inelastic neutron scattering

### 8.1 Experimental setups and data treatment

Inelastic neutron scattering measurements on 2T1 at LLB were performed on the single crystal  $\text{Mn}_{5-x}\text{Fe}_x\text{Si}_3$   $x=4$  at 3.17K. For every measurement the number of monitored neutrons was not smaller than 5000 and never exceeded 10000. In order to extract both, magnon and phonon branches, energy scans at constant Q and q-scans at constant energies were performed.

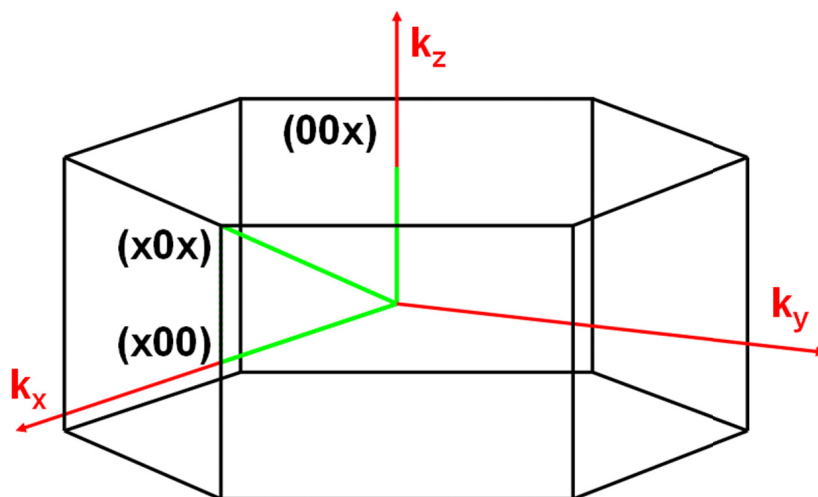


**Figure 8.1:** Brillouin zone with scan directions (solid green lines). Red arrows indicated directions in k-space.

Scans were performed along directions  $(x00)$ ,  $(00x)$  and  $(x0x)$ . Those directions are indicated in k-space in figure 8.1.

Energy scans at constant Q were performed in steps of 0.1 r.l.u., q-scans at energies never exceeding a value of 14meV.

The alignment of the single crystal was not perfect. Therefore, Bragg reflections were measured for modification of the orientation matrix.

## 8.2 Analyzing and fitting of data

### 8.2.1 Phonons

Before fitting, every spectrum was analyzed carefully looking for spurions. Regions with spurions were cut out. For data analysis program Aprox, which provides options to fit spectra with Gaussian or Lorentzian curves, was used. Every peak (generated by magnetic or phonon excitations) was fitted with a Gaussian curve and the background linear and usually without slope.

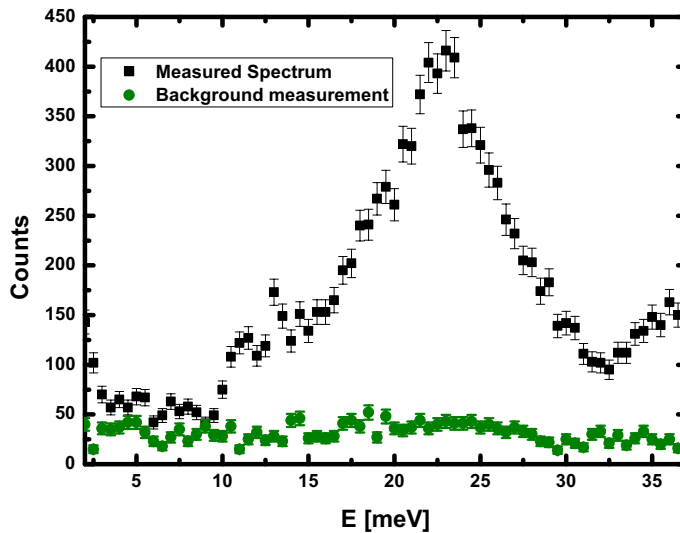


**Figure 8.2:** Constant Q-scan performed on (4,0,0.5) with and without sample in Q-space.

In order to estimate the influence of the sample environment on a spectrum, measurements with sample holder and without sample were performed. In figure 8.2 an energy spectrum is compared to the background measurement both taken at (4,0,0.5). The influence of the background on the spectrum is small, since intensities of peaks do not seem to be affected. Since the goal of these measurements is to evaluate positions of peaks, linear fitting of the background seems to be reasonable.

Here, q-scans at constant energies were mainly carried out at low energies looking for acoustic phonons and magnon branches close to 0meV. Such scans were always conducted between intervals of +q and -q. Therefore every peak (if an excitation could be detected) was measured in focussing and defocussing mode. The exact position of a transverse acoustic phonon was evaluated by taking the average of focussing and defocussing value. In figure 8.3 such a typical is scan presented. Due to the presence of spurious only a limited number of scans were taken in focusing and defocusing modes. The background was fitted linear with a slope, here.

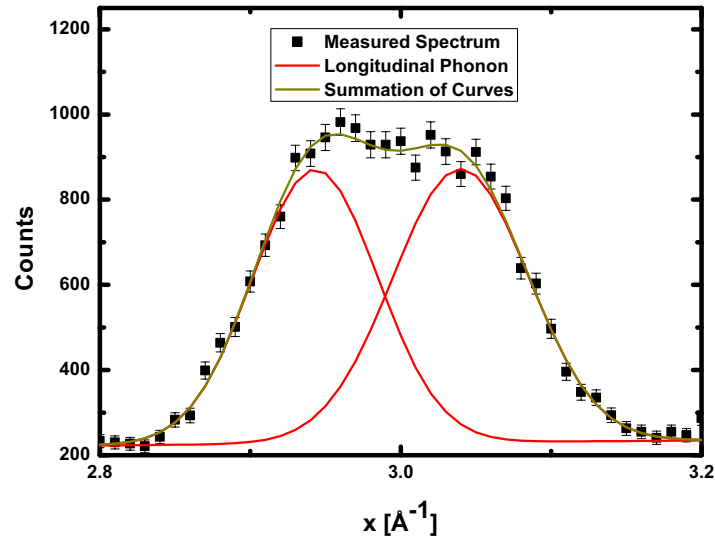


**Figure 8.3:** Q-scan  $(x,0,0)$  performed at  $E=3\text{meV}$  in order to detect the accoustical phonon.

In figure 8.4 a longitudinal energy scan performed at  $(0,0,2.4)$ , which was fitted with 5 peaks, is presented. In comparison with the fitted energy scan performed at  $(4,0,0.4)$ , different intensities and shapes of the peaks are clearly visible. For example, the acoustic branch in figures 8.4 and 8.5 (peak at lowest energy in both spectra) in  $(0,0,2.4)$  is higher in intensity than the one in  $(4,0,0.4)$ . The broad shape of the peaks of the optical branches could be due to the quality of the single crystal. Diffraction patterns taken on Laue equipment confirmed the hexagonal symmetry without any discrepancies.

Branches were always determined combining collections of measurements performed close to the same Q-point. For example in figure 8.5 between  $18\text{meV}$  and  $27\text{meV}$  two peaks were fitted. Those two peaks could have been fitted with only one Gaussian curve properly, which is presented in figure 8.4. Still, two peaks were detected in that energy interval at  $Q=(4,0,0.1)$ , which is presented in figure 8.5. Therefore it is very clear that one single Gaussian curve could not be reasonable in the physical sense, even though the summation of the fitted curves in figure 8.4 can be considered reasonable, too.

The acoustic phonon was too small in intensity for having been fitted in spectrum presented in figure 8.6.

Fitting cannot only be performed in the mathematical way, i.e. fitting each spectrum by only counting the number of excitations. In order to strengthen the qualities of such fitting, intensity of a peak as function of  $q$  can be plotted. In figure 8.7 intensities of all peaks fitted in transversal spectra  $(x,0,0)$  and  $(0,0,x)$  in dependence of  $q$  are presented.

Discrepancies of the fitted intensities are visible at  $q=0$  which is due to the different configuration which was applied when the spectrum was taken. In excitation a large increase in intensity

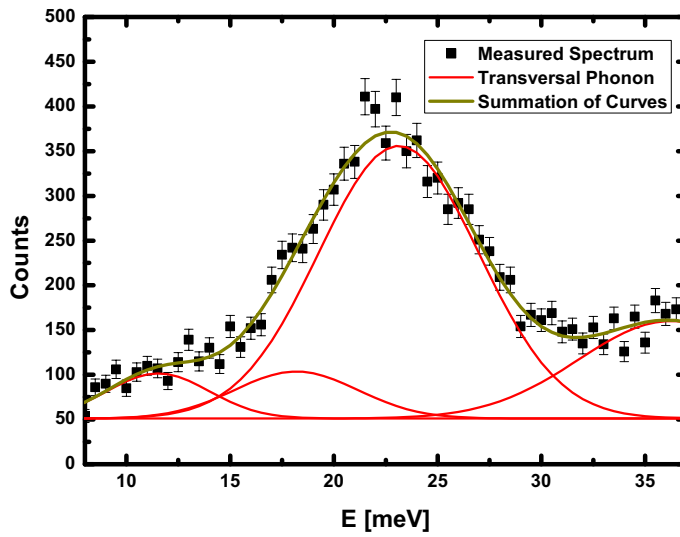


Figure 8.4: Constant Q-scan performed on (0,0,2.4) in Q-space.

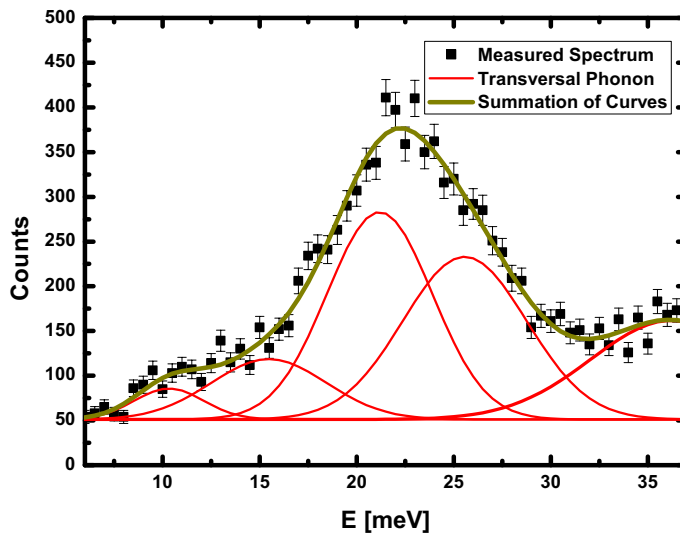


Figure 8.5: Constant Q-scan performed on (4,0,0.4) in Q-space.

appears at (0.5,0,0). Since the spectrum seems to have been fitted mathematically on a proper way, this effect could be considered real. Disregarding this, the fitted intensities are comparable

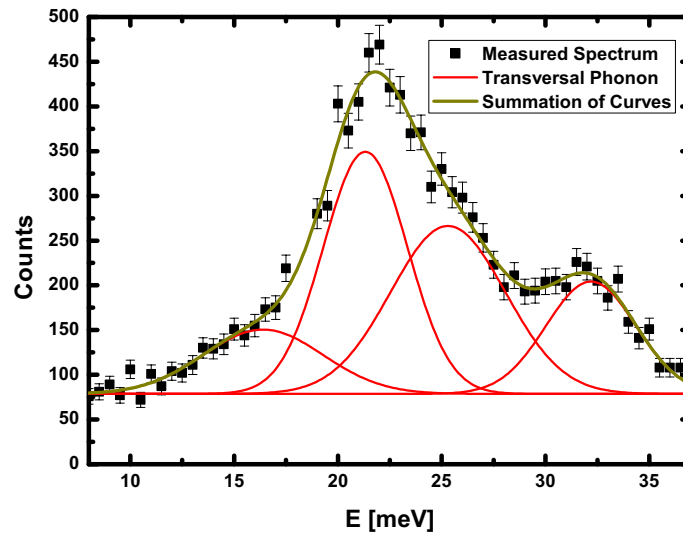


Figure 8.6: Constant Q-scan performed on  $(4,0,0.1)$  in Q-space.

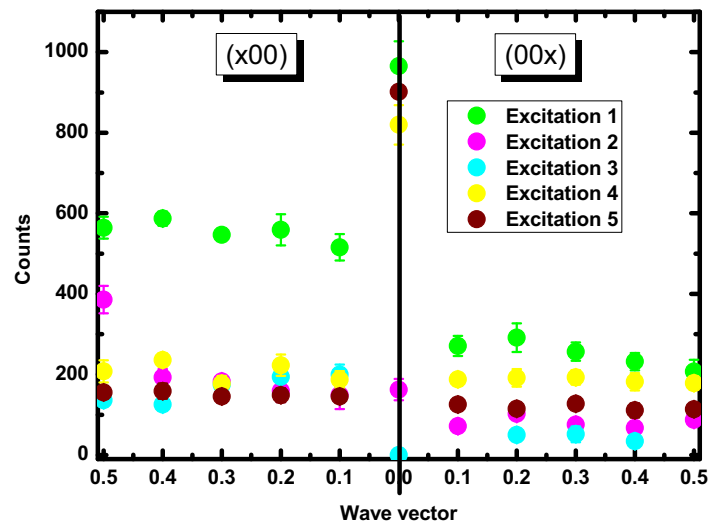


Figure 8.7: Intensities of peaks fitted in transverse configurations.

for every peak for each  $q$ .



### 8.2.2 Magnons

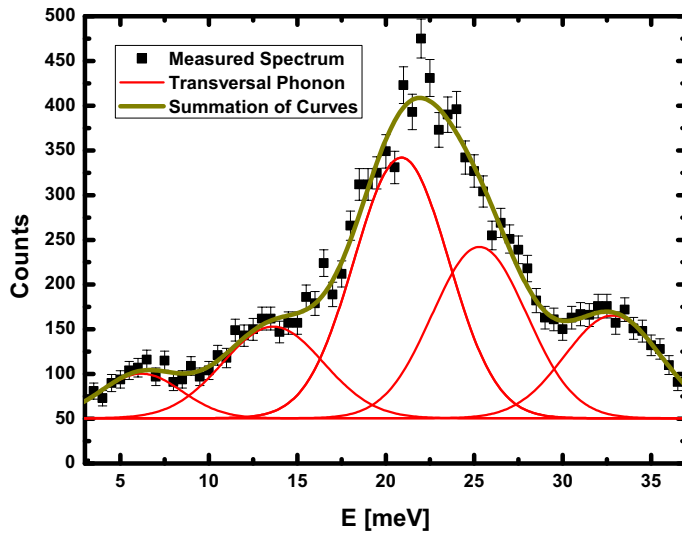


Figure 8.8: Constant Q-scan performed on (4,0,0.2) in Q-space.

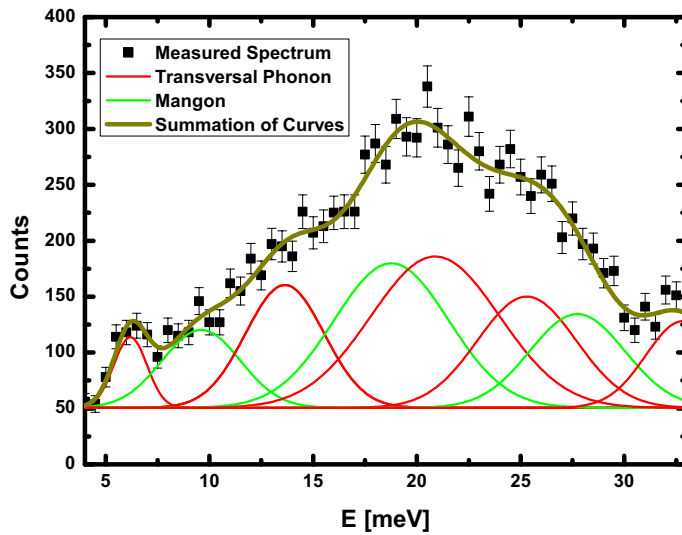


Figure 8.9: Constant Q-scan performed on (2,0,0.2) in Q-space.

Magnon branches were determined comparing energy spectras taken at high and low  $Q$ , i.e. measurements performed close to  $(2,0,0)$  and  $(4,0,0)$ . It was assumed that magnetic excitations generate peaks with large intensities close to  $(2,0,0)$  while intensities of peaks of phonons were considered small and vice versa at  $(4,0,0)$ . Therefore, peaks appearing in spectras close to  $(2,0,0)$  which are absent in spectras close to  $(4,0,0)$  were considered magnon excitations. It has to be mentioned that, even though this assumption is reasonable, this method does not provide evidence for excitations to be magnetic or not.

Comparing figures 8.8 and 8.9, for example, three additional peaks could be detected (marked green) at  $(2002)$  which were considered to have been generated by a magnetic excitation.

## 8.3 Results

### 8.3.1 Dispersion relation

The dispersion relation in  $\text{Mn}_{5-x}\text{Fe}_x\text{Si}_3$   $x=4$  is presented in figure 8.10. In some cases, for example the transversal acoustic branch at  $(0,0,0.5)$ , points of branches are missing. This is due to intensities which are too small, or due to the presence of spurions. Therefore such peaks cannot be fitted properly.

The longitudinal acoustic phonon at  $(0,0,0.2)$  is lower in energy than the transversal branch, which could be due to misalignments.

The dynamic properties of the acoustic lattice vibrations seem to be anisotropic. Anisotropic behaviour is exhibited by the acoustic phonons. For example longitudinal and transverse acoustic branches are clearly separated in direction  $(x00)$ . In direction  $(00x)$  they seem to coincide with each other at low  $q$ . This is in contrast to direction  $(x0x)$ . Here, the two branches seem to fall together at high  $q$ .

At high energies  $\sim 35\text{meV}$  the phonon branches can be considered isotropic. There are only small differences visible, since the dispersion remains almost completely flat.

Anisotropic effects have been revealed in calculations and inelastic neutron scattering measurements on GaS [111], which crystallizes in hexagonal  $P6_3/mmc$ .

These anisotropics are product of the symmetries of the structure. The symmetries of the lattice vibrations (i.e. phonons) have to obey the symmetry of the unit cell. There are numerous publications demonstrating how to analyze lattice vibrations by taking symmetry conditions into account (for example [112]). In the case of  $\text{Mn}_{5-x}\text{Fe}_x\text{Si}_3$   $x=4$  directions  $(00x)$ ,  $(x00)$  and  $(x0x)$  are not equivalent to each other.

In [113] measured and calculated phonon DOS and dispersion relations are presented for FeSi and CoSi. These two compounds crystallize in cubic unit cells [114, 115]. Still, the elements of those materials are very similar to the composition of  $\text{Mn}_{5-x}\text{Fe}_x\text{Si}_3$   $x=4$ . In comparison to those compounds the acoustic phonons get excited at lower energies in  $\text{Mn}_{5-x}\text{Fe}_x\text{Si}_3$   $x=4$ . Measurements and calculations reveal exciting energies for phonons of  $\sim 22\text{meV}$ . In  $\text{Mn}_{5-x}\text{Fe}_x\text{Si}_3$   $x=4$  the energies do not exceed a value of  $15\text{meV}$ .

Anisotropies concerning magnon branches are hard to extract from the results. The magnon branch with lowest energy in (00x)-direction seems to be similar to the magnon branch in (x0x)-direction. Still, additional points of measurements would be useful to analyze anisotropies of magnetic branches.

### 8.3.2 Properties of the magnon

In order to extract the magnetic interaction and anisotropy parameters of the system equation 2.30 has to be calculated. This equation can be solved by fitting the data with a model describing the magnetic exchange of the unit cell. In (0,0,x)-direction 6 points of measurements can be used for fitting. Three points of measurements are probably not enough.

In figure 8.11 the nearest neighbours of magnetic atoms are indicated with green lines. Only the z-component was taken into account which is due to having measured only this value in (0,0,x)-direction. The distances in c-direction is 0.5 (two times) and 0.25.

In figure 8.12 the magnon with the fit is presented. Even though the fit looks like it was describing the data properly it cannot be considered reasonable in the mathematical way due to large error bars, and in the physical way due to the fact that this curve does not seem to converge for  $0 < q < 1$ . The value at  $q=1$  is 330 meV.

This could be due to the fact that the model used for the fitting is not sufficient. Considering three single exchange does obviously provide reasonable results. Also, the number of points of measurements is very low. To get reliable results additional inelastic neutron scattering measurements are proposed.

Furthermore, this model is only an approximation since calculating spin waves can easily get very complex. More promising model are presented in [69] and [116]. Here, two or three sublattices are considered. This could be very useful for developing another model due to the presents of two atomic sites carrying magnetic moments. In these publications however, every model deals with a matrix which has to be diagonalized.

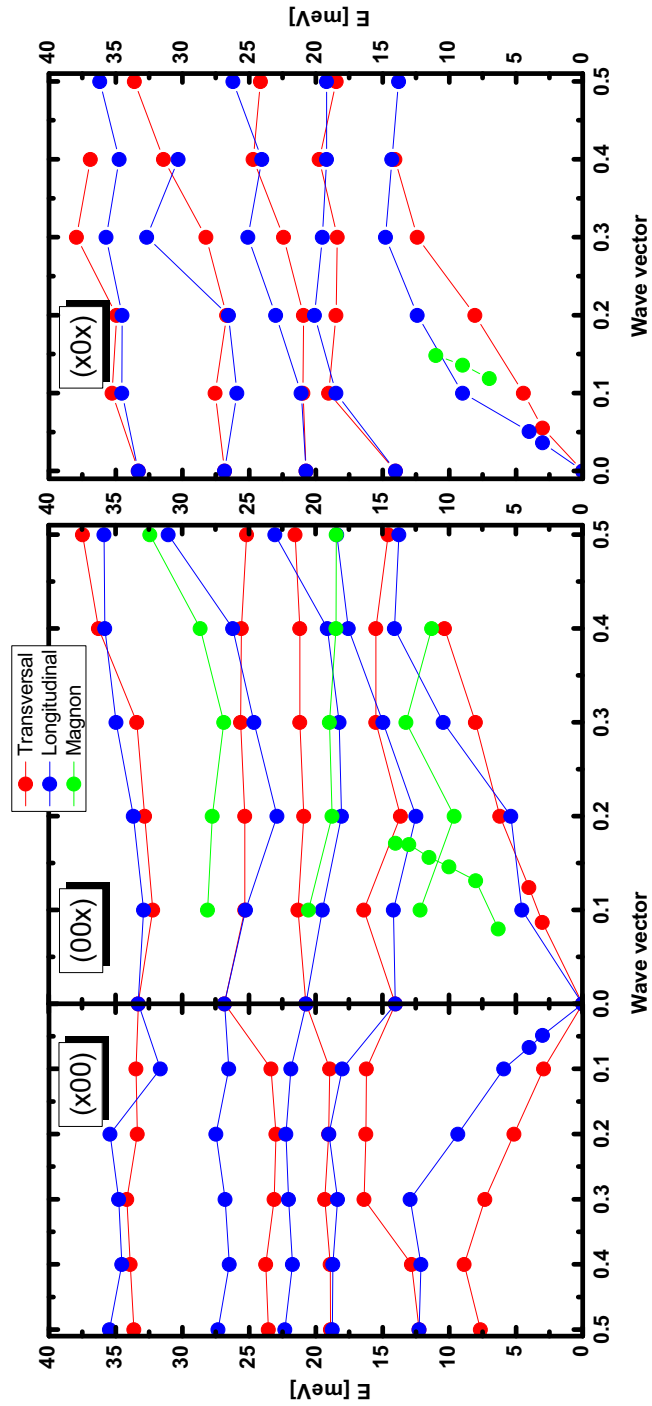


**Figure 8.10:** Dispersion relation of  $\text{Mn}_{5-x}\text{Fe}_x\text{Si}_3$   $x=4$  extracted from inelastic neutron scattering data.

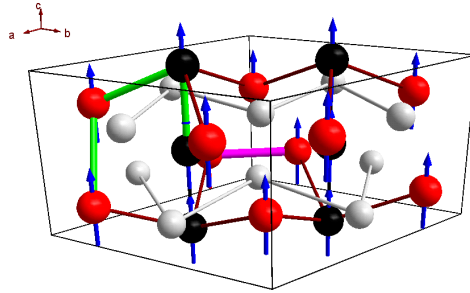


**Figure 8.11:** Magnetic unit cell of  $\text{Mn}_{5-x}\text{Fe}_x\text{Si}_3$   $x=4$  with green bars indicating magnetic exchange which was considered for the model. Interactions in plane similar to the pink line were not considered.

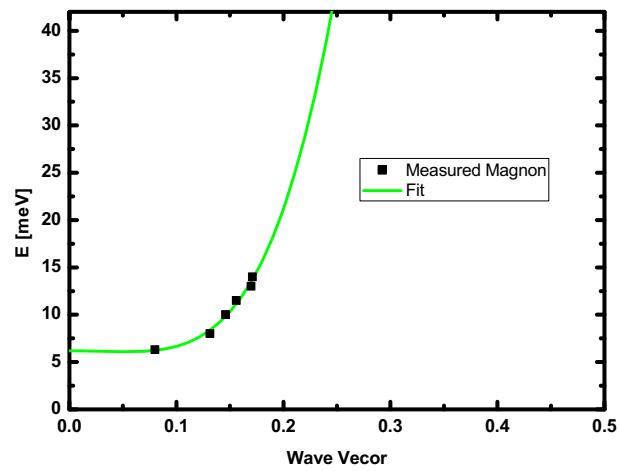


**Figure 8.12:** Dispersion relation of the magnon in  $\text{Mn}_{5-x}\text{Fe}_x\text{Si}_3$   $x=4$  with fit of polynom of second degree. The formula of the the fitted polynom is  $e = 6(3) - 6(5) \cdot 10^6 \cdot (1 - \cos(0.5x)) + 2(2) \cdot 10^7 \cdot (1 - \cos(0.25x))$ .

## 8.4 Summary

Inelastic neutron data were collected on sample  $\text{Mn}_{5-x}\text{Fe}_x\text{Si}_3$   $x=4$  on thermal neutron triple axis spectrometer 2T1 at LLB.

Phonon and magnon branches could be extracted from the data with fitting of Gaussian curves. Magnons could be separated from phonons since measurements were performed at high and low  $q$ . The dispersion relation of the phonons reveal anisotropies which are proposed to have appeared due to the hexagonal symmetries.

The proposed model for fitting the magnon branch could not provide additional information. Neither the anisotropy parameter nor the exchange parameters of the used model could be extracted from the data.



# Chapter 9

## Conclusion

In this dissertation polycrystalline samples of compositions  $\text{Mn}_{5-x}\text{Fe}_x\text{Si}_3$   $x=0,1,2,3,4$ ,  $\text{Mn}_{1-x}\text{Co}_x\text{Fe}_4\text{Si}_3$   $x=0.1,0.2$  and  $\text{MnFe}_{4-x}\text{Co}_x\text{Si}_3$   $x=0.2,0.5$  were prepared. All samples were characterized with magnetization measurements revealing antiferromagnetic and ferromagnetic ordering. The crystallographic structures of all samples at room temperature were refined on neutron powder diffraction patterns taken on POWGEN using a hexagonal setting. Inelastic neutron scattering measurements on a single crystal with composition  $\text{Mn}_{5-x}\text{Fe}_x\text{Si}_3$   $x=4$  were carried out as first step experiment to analyze dynamics and their link to the MCE.

The diffraction pattern taken at 100K on  $\text{Mn}_{5-x}\text{Fe}_x\text{Si}_3$   $x=0$  was refined with the same hexagonal unit cell which was used for room temperature measurements. The antiferromagnetic structure of  $\text{Mn}_{5-x}\text{Fe}_x\text{Si}_3$   $x=0$  at  $60\text{K}<T<100\text{K}$  was refined with the orthorhombic unit cell which was proposed in [39]. Diffraction patterns taken at  $T<60\text{K}$  on  $\text{Mn}_{5-x}\text{Fe}_x\text{Si}_3$   $x=0$  provided data which was refined with a monoclinic unit cell which has not been done in literature so far. Furthermore, the existence of weak ferromagnetism ( $\sim 0.5\mu_B$ ) could also be detected on one atomic site at these temperatures. An applied magnetic field of 4T at 50K annihilates the weak ferromagnetism of  $\text{Mn}_{5-x}\text{Fe}_x\text{Si}_3$   $x=0$  resulting in a phase transition to the orthorhombic structure. This feature concerning the influence of the applied magnetic field seems to be the driving force of the inverse MCE at  $\sim 62\text{K}$  in this material. MCE measurements of  $\text{Mn}_{5-x}\text{Fe}_x\text{Si}_3$   $x=0$  only provided values of the entropy change which are below zero and are therefore in contrast to [36].

The nuclear and magnetic structure of  $\text{Mn}_{5-x}\text{Fe}_x\text{Si}_3$   $x=4$  at low temperatures could be refined using the hexagonal unit cell (space group  $P6_3/mcm$ ) with magnetic moments applied parallel to the  $c$ -axis as it is proposed in [28]. Anomalies are visible in the temperature dependence of lattice constant  $a$  and atomic displacement parameters. Both phenomena are proposed to be linked to the magnetism due to the different ordering temperatures of the two atomic sites ( $\sim 220\text{K}$  and  $\sim 304\text{K}$ ). The existence of two magnetic moments is proposed to play an important role for the MCE in this compound. The measured entropy change of  $\text{Mn}_{5-x}\text{Fe}_x\text{Si}_3$   $x=4$  was carried out at a different applied magnetic field as it was done in [36]. Still, they seem to complement one another.

Inelastic neutron scattering measurements carried out on single crystal  $\text{Mn}_{5-x}\text{Fe}_x\text{Si}_3$   $x=4$  revealed anisotropies in the phonon branches. This phenomenon seems to be linked to the hexagonal symmetry.

Material  $\text{Mn}_{5-x}\text{Fe}_x\text{Si}_3$   $x=4$  was doped with Co opening a door to families of compounds that can be investigated in the context of the MCE. Neutron diffraction data revealed the presence of impurities in every phase of the Co-doped compounds. Refinements of the magnetic moments



of the unit cell (same hexagonal setting as for  $\text{Mn}_{5-x}\text{Fe}_x\text{Si}_3$   $x=4$ ) revealed two different ordering temperatures for the two atomic sites similar to  $\text{Mn}_{5-x}\text{Fe}_x\text{Si}_3$   $x=4$ . Enhanced entropy changes could be measured for  $\text{Mn}_{1-x}\text{Co}_x\text{Fe}_4\text{Si}_3$   $x=0.1$  (maximum is  $\sim 1.11\text{J/kgK}$ ) in comparison to  $\text{Mn}_{5-x}\text{Fe}_x\text{Si}_3$   $x=4$  (maximum is  $\sim 1.09\text{J/kgK}$ ), while the entropy changes of all other Co-doped materials are smaller than the MCE in  $\text{Mn}_{5-x}\text{Fe}_x\text{Si}_3$   $x=4$  (minimum is  $\sim 0.9\text{J/kgK}$ ). The maximum of the entropy change in each material strongly varies with  $T_C$ . Due to the presence of up to 41.11(7)% of impurity phases the origin of the MCE in some Co-doped samples remains unclear.

# Chapter 10

## Outlook

### 10.1 Further modification of the MCE in $\text{Mn}_{5-x}\text{Fe}_x\text{Si}_3$ $x=0$ and $\text{Mn}_{5-x}\text{Fe}_x\text{Si}_3$ $x=4$ with doping

The approach starting with an MCE material crystallizing in a complex structure proved value. The door is still open to various elements that could be used for doping using  $\text{Mn}_{5-x}\text{Fe}_x\text{Si}_3$   $x=4$  or  $\text{Mn}_{5-x}\text{Fe}_x\text{Si}_3$   $x=0$  as mother compounds.

#### 10.1.1 $\text{Mn}_{5-x}\text{Fe}_x\text{Si}_3$ $x=0$

In  $\text{Mn}_{5-x}\text{Fe}_x\text{Si}_3$   $x=0$  Si has already been substituted with Ge [117]. The transition temperature decreased with the content of Ge. Still, the family  $\text{Mn}_5\text{Si}_{3-x}\text{Ge}_x$  could be an interesting candidate for studies concerning the indirect effect of Si/Ge. Composition  $\text{Mn}_5\text{Ge}_3$  orders ferromagnetically [118]. This gives rise to the propose a rich phase diagram similar to  $\text{Mn}_{5-x}\text{Fe}_x\text{Si}_3$ .

#### 10.1.2 $\text{Mn}_{5-x}\text{Fe}_x\text{Si}_3$ $x=4$

Here, since Mn, Fe and Co have already been substituted with each other, investigations of the MCE introducing elements with higher atomic radii are proposed. Tc, Ru and Rh could be introduced (always starting with small ratios). Using results of investigations of those compounds one could decide if it is reasonable doping elements of another group of elements.

$\text{Mn}_{5-x}\text{Fe}_x\text{Si}_3$   $x=4$  could be doped with Ge. Similar approaches were done in  $\text{Mn}_5\text{Ge}_{3-x}\text{Si}_x$  [117] and  $\text{Mn}_5\text{Ge}_{3-x}\text{Sb}_x$  [119], both crystallizing in hexagonal  $P6_3/mmc$ . Investigating this material could help understanding the indirect role of Si similar to the doping in  $\text{Mn}_{5-x}\text{Fe}_x\text{Si}_3$   $x=0$ .

In  $\text{Mn}_{5-x}\text{Fe}_x\text{Si}_3$   $x=4$  Fe could be substituted with Si or Al. Similar substitutions have been done in  $\text{LaFe}_{13}$  which opened a door to new types of structures with unusual magnetic properties [120, 121].

Ferromagnetic structure and the unordered character of magnetic moments on position M1 at high temperatures ( $200\text{K} < T < 310\text{K}$ ) make not only undoped compound  $\text{Mn}_{5-x}\text{Fe}_x\text{Si}_3$   $x=4$  as

promising candidate for further studies in the context of MCE. For example as next step investigations Si could be substituted with Ge, i.e.  $\text{MnFe}_4\text{Si}_{3-x}$   $x=0.1,0.2$ . Analyzing the nuclear and magnetic structures could provide results that might help to understand the impact of Si on the magnetism in this family of compounds.

## 10.2 Neutron diffraction measurements on single crystals

In order to investigate the complex antiferromagnetic structures in  $\text{Mn}_{5-x}\text{Fe}_x\text{Si}_3$   $0 < x < 4$ , neutron diffraction measurements on single crystals could be performed. Reflections that fall together in powder experiments can be treated separately here.

The nature of the two atomic sites in  $\text{Mn}_{5-x}\text{Fe}_x\text{Si}_3$   $x=4$  can be confirmed with single crystal measurements. Also, the angle of the momentum to the c-axis on site M1 could be investigated.

## 10.3 Inelastic neutron scattering measurements

Additional neutron scattering measurements without magnet could be performed to complete the phonon and magnon dispersion at low temperatures. Also, measurements could be performed at high temperatures (still in the ferromagnetic phase) to clearly distinguish between magnetic and vibrational excitations.

In order to investigate the influence of an applied magnetic field on sample, further inelastic neutron scattering measurements could be performed. In future, inelastic neutron scattering experiments could be performed with applied magnetic field on the single crystal  $\text{Mn}_{5-x}\text{Fe}_x\text{Si}_3$   $x=4$ . Publications such as [49], for example, could serve as reference. Here, above 3T the emergence of another magnetic excitation could be detected.

Measurements for investigations of the influence of an applied magnetic field could be performed in reciprocal space at points equivalent to the brown circle in figure 10.1. At such points phonon and magnon branches cross each other.

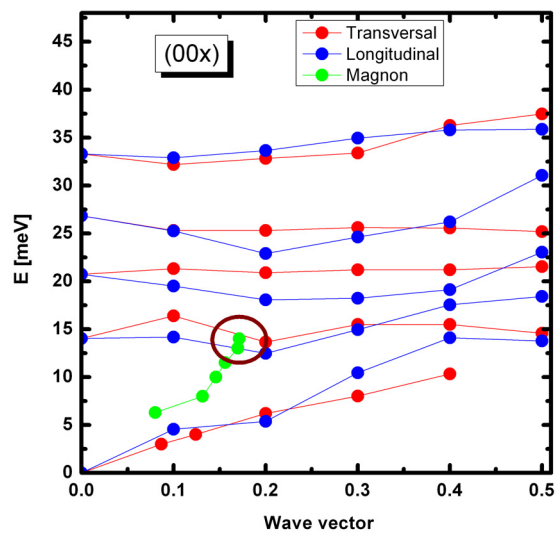


**Figure 10.1:** Dispersion relation of  $\text{Mn}_{5-x}\text{Fe}_x\text{Si}_3$   $x=4$ . The brown circle marks points where a magnon branch crosses a phonon branch.



# Chapter 11

## Acknowledgements

All results of on  $\text{Mn}_{5-x}\text{Fe}_x\text{Si}_3$   $x=0$  on POWGEN and HB2A are based on publication. Sections dealing with that topic do not present additional but also not less information than included in this publication.

Concerning this publication all samples used for neutron diffraction measurements, first refinements and first draft of paper were prepared by M. Gottschlich. Concerning performance of refinements and corrections of paper this work was accommodated by O. Gourdon, M. Ohl, J. Persson and T. Brueckel. M. Gottschlich and O. Gourdon performed theoretical calculations together which were included in the paper by O. Gourdon. When measurements were performed on POWGEN, O. Gourdon was second instrument responsible. J. Persson taught M. Gottschlich how to prepare samples. C. de la Cruz was instrument responsible of HB2A. V. Petricek provided support for program Jana2006 which was used for refinements. All gave feedback for writing and improving the quality of the publication. M. Ohl was head of the JCNS group at SNS (Spallation Neutron Source) at Oak Ridge National Laboratory. T. Brueckel was head of the JCNS group in Juelich. Both were in charge of this dissertation on hand and people involved in this work.

I want to thank the following people, who contributed a lot to the outcome of this work:

**Prof. Thomas Brückel** for the opportunity to work on this very interesting subject with a lot of freedom in choosing the direction of my investigation. I could profit from a rich pool of methods and know how working in this group.

**Georg Roth** who agreed to take the second revision of this thesis.

**Olivier Gourdon, Michael Ohl and Jörg Perßon** for an extremely well mentoring. I always enjoyed discussions with you. You had an open door for me every day and the patience to sustain my eagerness to solve a problem. I would also like to thank you for the nice beamtimes we carried out together.

**Jörg Voigt, Karen Friese and Kirill Nemkovski** for a lot of fruitful discussions about elastic and inelastic neutron scattering. This collaboration could not have been better. Additional acknowledges for the RBS analysis together with **Willi Zander**.

**Carsten Thomas** for the help with sample preparation.

**Philipp Bourges, Clarina Dela Cruz, Vasile Ovidiu Garlea** for their help and scientific support at the different x-ray and neutron experiments (2T1, HB2A).

**Benedikt Klobes** for the assistance at the CCMS.

**M. McGuire** member of the Condensed Matter Sciences Division at Oak Ridge National laboratory performed the magnetization measurements on sample  $\text{Mn}_{5-x}\text{Fe}_x\text{Si}_3$   $x=4$  which was used to calculate the MCE in that compound. The author of the thesis hereby would like to thank M. McGuire for this support.

**Elisabeth Josten, Alice Klapper, Paul Zakalek, Alexander Weber, Markus Schmitz, Dimitrios Bessas and Yinguo Xiao** for helpful discussions and the enjoyable atmosphere.

I want to thank my mother, my brother and my stepfather for everything.

Last but not least I'm very grateful for the lovely atmosphere at the institute for scattering methods. I enjoyed working with everybody and getting some insight in very different fields of investigation, too.

# Appendix A

## Additional Information

### A.1 The Curie Weiss law

$$\chi = \frac{c}{T - T_C} = \frac{N_A \mu_0 \mu_{eff}}{3k_B(T - T_C)} \quad (\text{A.1})$$

$$c = \frac{N_A \mu_0 \mu_{eff}}{3k_B} \quad (\text{A.2})$$

$c$  = Curie-Weiss-constant

$N_A$  = Avogadro constant

$\mu_0$  = magnetic permeability

$\mu_{eff}$  = effective moment

$k_B$  = Boltzmann constant

### A.2 Profile function for TOF-diffraction

Detailed explanations for the peak shapes in TOF-data is given in [57, 59].

$$\Omega(x) = \int_{-\infty}^{\infty} P(x-t)E(t)dt \quad (\text{A.3})$$

$$E(t) = 2Ne^{\alpha t}, t \leq 0, E(t) = 2Ne^{-\alpha t}, t > 0, N = \frac{\alpha\beta}{2(\alpha + \beta)} \quad (\text{A.4})$$

$$P(x-t) = \eta L(x-t) + (1 - \eta)G(x-t) \quad (\text{A.5})$$

$$G(t-x) = \frac{1}{\sqrt{2\pi\sigma^2}} \exp\left[-(x-t)^2/2\sigma^2\right] \quad (\text{A.6})$$



$$L(t-x) = \frac{\Gamma}{2\pi} \frac{1}{(\Gamma/2)^2 + (t-x)^2} \quad (\text{A.7})$$

$$\eta = 1.36603(\gamma/\Gamma) - 0.47719(\gamma/\Gamma)^2 + 0.11116(\gamma/\Gamma)^3 \quad (\text{A.8})$$

$$\Gamma = \sqrt[5]{\Gamma_g^5 + 2.69269\Gamma_g^4\gamma + 2.42843\Gamma_g^3\gamma^2 + 4.47163\Gamma_g^2\gamma^3 + 0.07842\Gamma_g\gamma^4 + \gamma^5} \quad (\text{A.9})$$

$$\sigma^2 = \sigma_0^2 + \sigma_1^2 d^2 + \sigma_2^2 d^4 = \frac{H^2}{8\ln(2)} \quad (\text{A.10})$$

$$\gamma = \gamma_0 + \gamma_1 d + \gamma_2 d^2 \quad (\text{A.11})$$

$$\frac{1}{\alpha} = n\alpha^e + (1-n)\alpha^t, \alpha^e = \alpha_0^e + \alpha_1^e d, \alpha^t = \alpha_0^t - \frac{\alpha_1^t}{d_h} \quad (\text{A.12})$$

$$\frac{1}{\beta} = n\beta^e + (1-n)\beta^t, \beta^e = \beta_0^e + \beta_1^e d, \beta^t = \beta_0^t - \frac{\beta_1^t}{d_h} \quad (\text{A.13})$$

Here,  $n=n_{cross}$  as introduced in section 2.2.6.

### A.3 Instrumental parameters for CW-diffraction

The shift parameter introduces an offset to the measured angle of the data:  $\Delta\theta = 2\theta + shift$ . The parameters *sycos* and *sysin* shift the angle with a cos or sin dependence:

$$\Delta\theta = sycos \cdot \cos\theta, \Delta\theta = sysin \cdot \sin\theta \quad (\text{A.14})$$

### A.4 Magnetic form factors

The magnetic form factor is computed

$$f_m = \sum_i^4 A_i \exp[-B_i(k/4\pi)^2] + \left(\frac{2}{g} - 1\right) \sum_i^4 A'_i \exp[-B'_i(k/4\pi)^2] \quad (\text{A.15})$$

$g$  is the Lande splitting factor. The first summation in equation A.15 is the magnetic and the second the orbital contribution. For first row transition metals the second summation can be neglected since  $g \approx 2$ . The parameters used in the refinements for the form factor are presented in table A.1.

	A <sub>1</sub>	B <sub>1</sub>	A <sub>2</sub>	B <sub>2</sub>	A <sub>3</sub>	B <sub>3</sub>	A <sub>4</sub>	B <sub>4</sub>
Fe	0.378	11.38	0.656	4.592	-0.035	0.483	0.001	0.036
Mn	0.376	12.566	0.66	5.133	-0.037	0.563	0.001	0.039

**Table A.1:** Parameters of formula used for transformation from t- to d-spacing in Jana2006 and FullProf.

## A.5 X-ray powder diffraction

This refinement converged after the 17th cycle with the parameters which are presented below.

```

COMM Mn5-xFexSi3+Si_x=2
! Files => DAT-file: , PCR-file: C:\Mn5-xFexSi3\Messungen\X-Ray\Rt\Mn5-xFexSi3
_x=2_mit_Si
!Job Npr Nph Nba Nex Nsc Nor Dum Iwg Ilo Ias Res Ste Nre Cry Uni Cor Opt Aut
  0  5  2 15  0  0  1  1  0  0  1  0  1  0  0  0  0  0  1  1
!
!Ipr Ppl Ioc Mat Pcr Ls1 Ls2 Ls3 NLI Prf Ins Rpa Sym Hkl Fou Sho Ana
  1  2  1  1  1  0  4  0  0 -3 10 -1  1  1  0  0  0  1
!
! lambda1 Lambda2 Ratio Bkpos Wdt Cthm muR AsyLim Rpolarz ->
Patt# 1
  1.540560 1.540560 1.0000 50.000 8.0000 1.0000 1.0000 57.00 0.0000
!
!NCY Eps R_at R_an R_pr R_gl Thmin Step Thmax PSD
  50 0.01 0.33 0.35 0.35 0.35 20.0300 0.005000 98.7150 0.000
Sent0
  0.000
!
!2Theta/TOF/E(Kev) Background for Pattern# 1
  22.138 6158.387 11.000
  24.935 5580.724 21.000
  31.029 5628.026 31.000
  35.125 5507.383 41.000
  42.817 5315.216 51.000
  51.409 5223.326 61.000
  53.706 5131.543 71.000
  60.599 5088.467 81.000
  65.095 4953.975 91.000
  70.589 4900.279 101.000
  74.486 4633.599 111.000
  78.881 4523.589 121.000
  84.176 4623.513 131.000
  90.969 4009.435 141.000
  97.662 3629.472 151.000
!
!
  25 !Number of refined parameters
!
```

Appendix A Additional Information

```

! Zero   Code   SyCos   Code   SySin   Code   Lambda   Code MORE -> Patt# 1
  0.33946  0.0 -0.25317  0.0  0.13217  0.0  1.000000  0.00  0
-----
! Data for PHASE number:  1 ==> Current R_Bragg for Pattern#  1:  0.00
-----
Si
!
!Nat Dis Ang Pr1 Pr2 Pr3 Jbt Irf Isy Str Furth      ATZ   Nvk Npr More
   0  0  0  0.0  0.0  1.0  2  2  0  0  0      64710.145  0  5  0
!
! d 3 m          <--Space group symbol
!-----> Profile Parameters for Pattern #  1
! Scale      Shape1      Bov      Str1      Str2      Str3      Strain-Model
  0.39244E-07  0.25633  0.00000  0.00000  0.00000  0.00000  0
   0.00000  0.000  0.000  0.000  0.000  0.000
!      U      V      W      X      Y      GauSiz  LorSiz
   0.016781 -0.034757  0.040915  0.014075  0.000000  0.000738  0.000000
   0.000  0.000  0.000  0.000  0.000  0.000  0.000
Size-Model
  0
!      a      b      c      alpha      beta      gamma      #Cell Info
   5.435688  5.435688  5.435688  90.000000  90.000000  90.000000
   0.00000  0.00000  0.00000  0.00000  0.00000  0.00000
! Pref1 Pref2 Asy1 Asy2 Asy3 Asy4
   1.03378  0.00000 -0.59567 -0.09789  1.43957  0.34172
   0.00  0.00  0.00  0.00  0.00  0.00
-----
! Data for PHASE number:  2 ==> Current R_Bragg for Pattern#  1:  0.00
-----
Mn3 Fe2 Si3
!
!Nat Dis Ang Pr1 Pr2 Pr3 Jbt Irf Isy Str Furth      ATZ   Nvk Npr More
   5  0  0  0.0  0.0  1.0  0  0  0  0  0      5236.341  0  5  0
!
193
!-----> Profile Parameters for Pattern #  1
!Atom  Typ      X      Y      Z      Basis      Occ      In Fin N_t Spc
/Codes
Mn1  Mn      0.33330  0.66670  0.00000  0.00000  0.08804  0  0  0  0
      0.00  0.00  0.00  0.00  201.00
Fe1  Fe      0.33330  0.66670  0.00000  0.00000  0.56404  0  0  0  0
      0.00  0.00  0.00  0.00  201.00
Mn2  Mn      0.23280  0.00000  0.25000  0.00000  0.81799  0  0  0  0
      241.00  0.00  0.00  0.00  231.00
Fe2  Fe      0.23280  0.00000  0.25000  0.00000  0.16799  0  0  0  0
      241.00  0.00  0.00  0.00  231.00
Si   Si      0.59830  0.00000  0.25000  0.00000  1.00000  0  0  0  0
      0.00  0.00  0.00  0.00  0.00
!-----> Profile Parameters for Pattern #  1
! Scale      Shape1      Bov      Str1      Str2      Str3      Strain-Model
  0.52399E-03  0.25600  1.24519  0.00000  0.00000  0.00000  0

```

```

180.03125    0.000    251.000    0.000    0.000    0.000
!   U         V         W         X         Y         GauSiz   LorSiz
  0.016781  -0.034757  0.040915  0.005690  0.000000  0.002535  0.000000
    0.000    0.000    0.000    211.000    0.000    0.000    0.000
Size-Model
  0
!   a         b         c         alpha    beta         gamma    #Cell Info
  6.863102  6.863102  4.764036  90.000000  90.000000  120.000000
 171.00000 171.00000 161.00000  0.000000  0.000000  171.00000
! Pref1   Pref2     Asy1     Asy2     Asy3     Asy4
  0.99828  0.00000  0.11028  0.06903  0.00000  0.00000
    0.00    0.00   191.00  221.00   0.00    0.00
! 2Th1/TOF1  2Th2/TOF2  Pattern # 1
    20.030    98.715    1

```

## A.6 Magnetization measurements

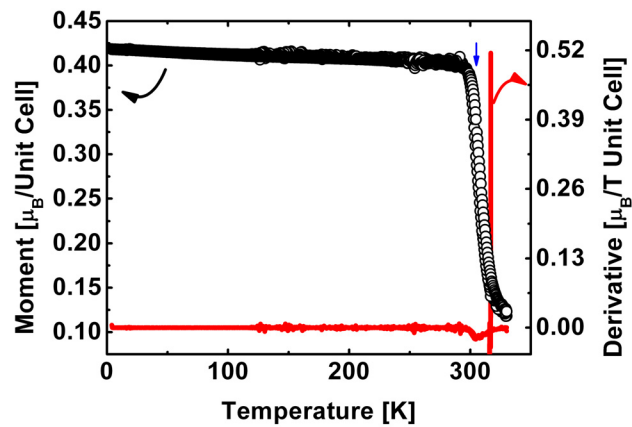


Figure A.1: Magnetization measurement performed at an applied field of 100Oe with derivative. The blue arrow indicates the point of phase transition.

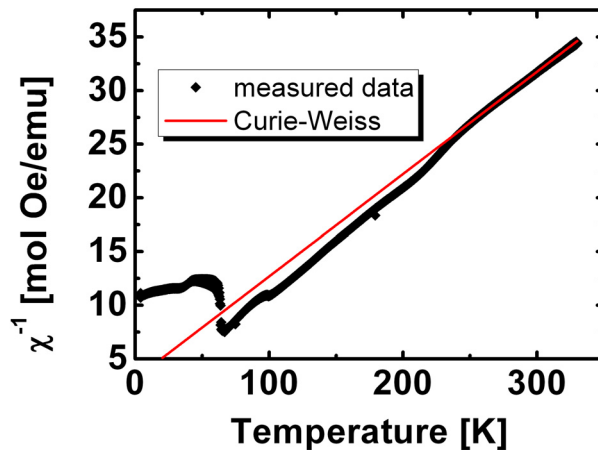


Figure A.2: Inverse susceptibility of  $\text{Mn}_{5-x}\text{Fe}_x\text{Si}_3$   $x=0$  with Curie-Weiss fit.

## A.7 Neutron powder diffraction

### A.7.1 $\text{Mn}_{5-x}\text{Fe}_x\text{Si}_3$

### A.7.2 Details of the refinement performed on sample $\text{MnFe}_{4-x}\text{Co}_x\text{Si}_3$ $x=0.2$ at 310K

Refinement program

The following lines were read as a control data :

```
=>cycles 100 autkeys 0 convchck 0 damp 0.3 corr 0.000009<=
=>restric Fe1 1 Co1<=
=>restric Fe2 1 Mn2<=
=>restric Mn5 1 Fe5 Co5<=
=>restric Mn6 1 Fe6 Co6<=
```

```
*****
* Run parameters *
*****
```

Structure refinement in 100 cycles with damping 0.3 will be performed

The damping factor will be reduced by the factor 2 if Rwp is larger by more than 10% from the previous value

In the case that in 3 consecutive cycles refinement converge, the damping factor will change back

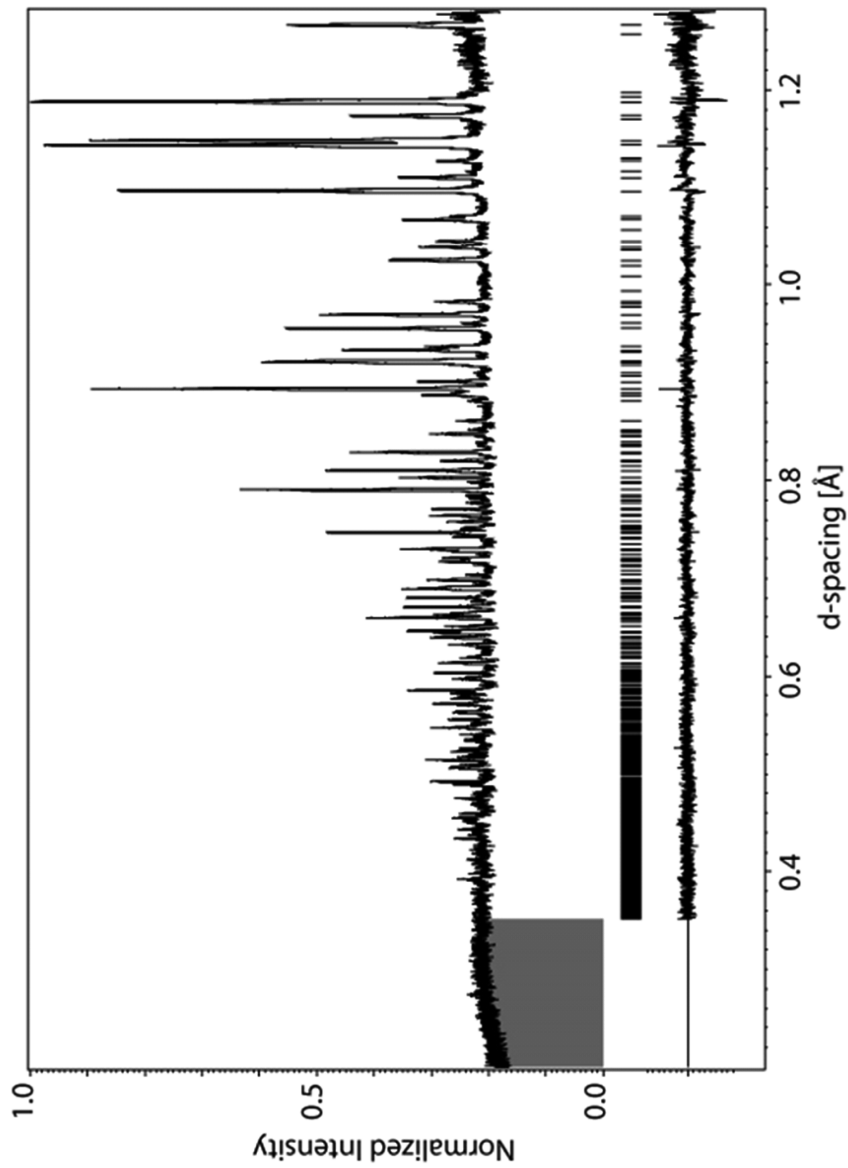


**Figure A.3:** Block with center at  $115^\circ$  of powder diffraction pattern of  $\text{Mn}_{5-x}\text{Fe}_x\text{Si}_3$   $x=1$  taken at 300 K with refinement. GOF-value of this block is 0.99.

Atoms reaching  $U_{iso} > 0.2$  will be disabled from the refinement  
 Calculation of  $\text{sig}(I)$  is as minimum from profile fit and error propagation formula  
 Only not-matching reflections flagged by # (see below) will be printed  
 Print of reflections after last cycle of refinement  
 Reflections with  $I < 3\text{sig}(I)$  will be classified as unobserved - flag \*  
 Reflections with  $|F_o - F_c| > 3\text{sig}(I)$  will be flagged by #

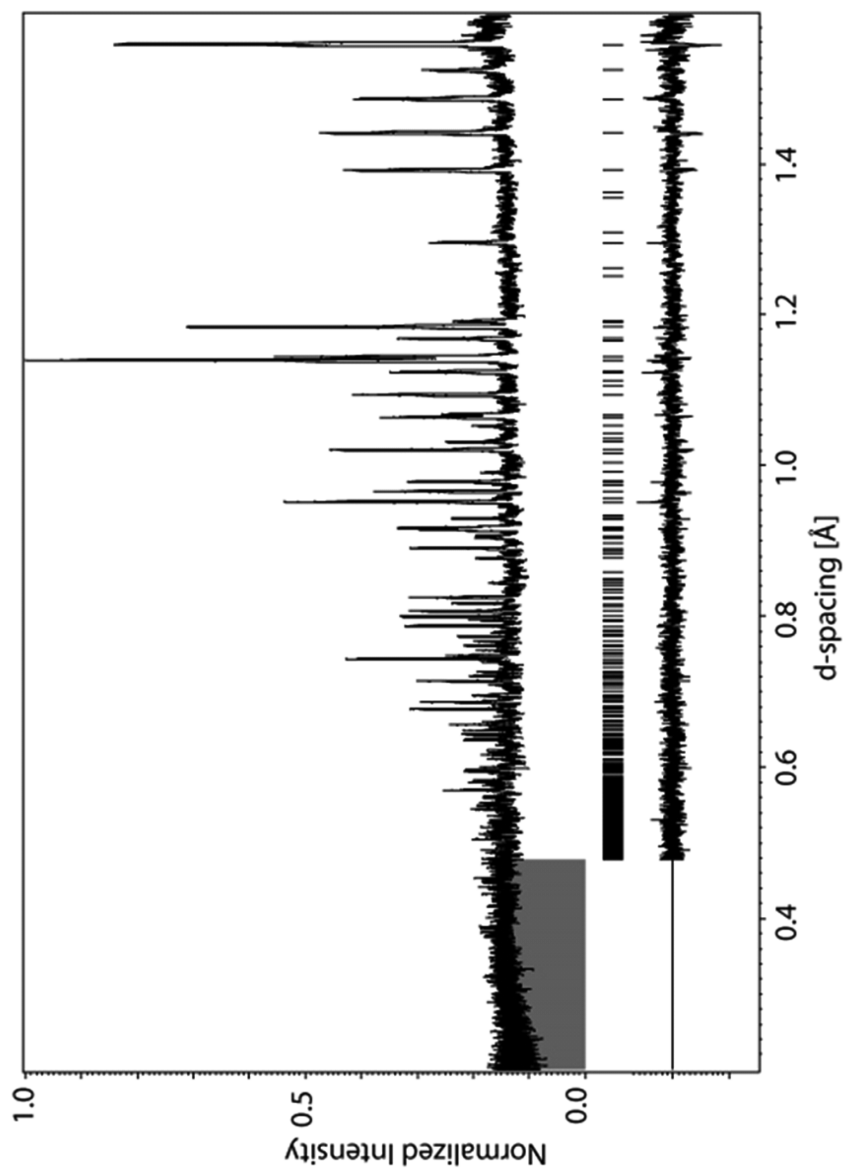


**Figure A.4:** Block with center at  $85^\circ$  of powder diffraction pattern of  $\text{Mn}_{5-x}\text{Fe}_x\text{Si}_3$   $x=2$  taken at 300 K with refinement. GOF-value of this block is 1.04.

Correlations larger than 0 will be printed  
 Automatic procedure for setting of refinement keys will be applied

```
*****
* Powder parameters *
*****
```

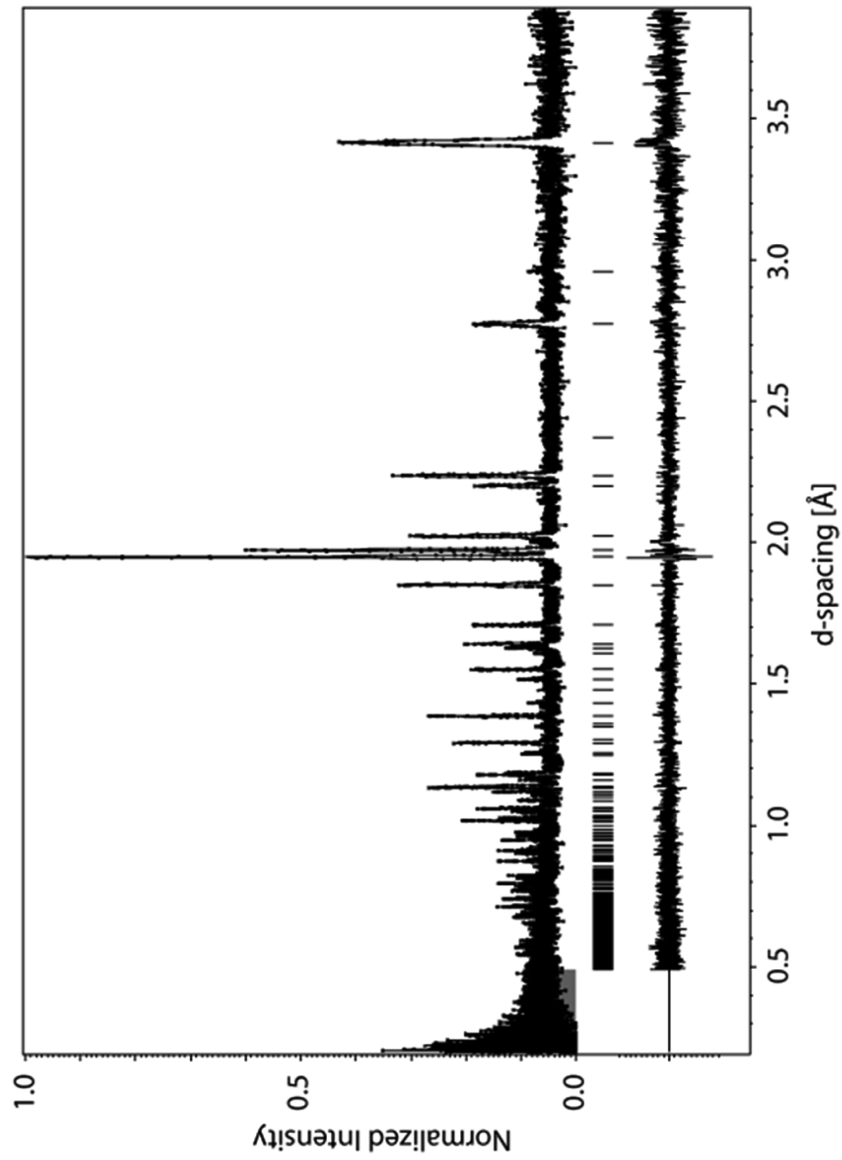


**Figure A.5:** Block with center at  $45^\circ$  of powder diffraction pattern of  $\text{Mn}_{5-x}\text{Fe}_x\text{Si}_3$   $x=3$  taken at 270 K with refinement. GOF-value of this block is 1.21.

Manual background will be used

Profile function convoluted with exponential rise/decay function - Jason Hodges

Phase#1

=====



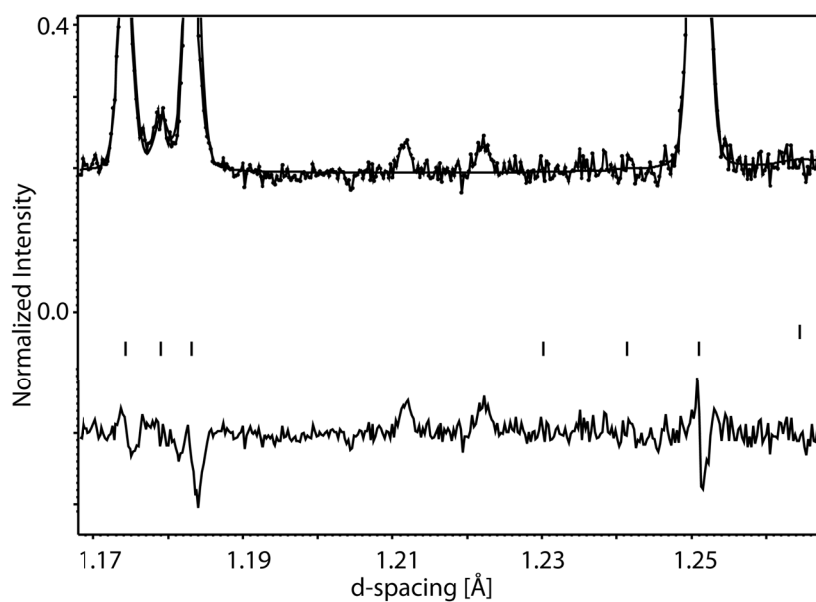


**Figure A.6:** Part of block with center at  $115^\circ$  of powder diffraction pattern of  $\text{Mn}_{5-x}\text{Fe}_x\text{Si}_3$   $x=4$  taken at 300 K with refinement. Ghosting peaks appear at  $d=1.21 \text{ \AA}$  and  $d=1.22 \text{ \AA}$ .

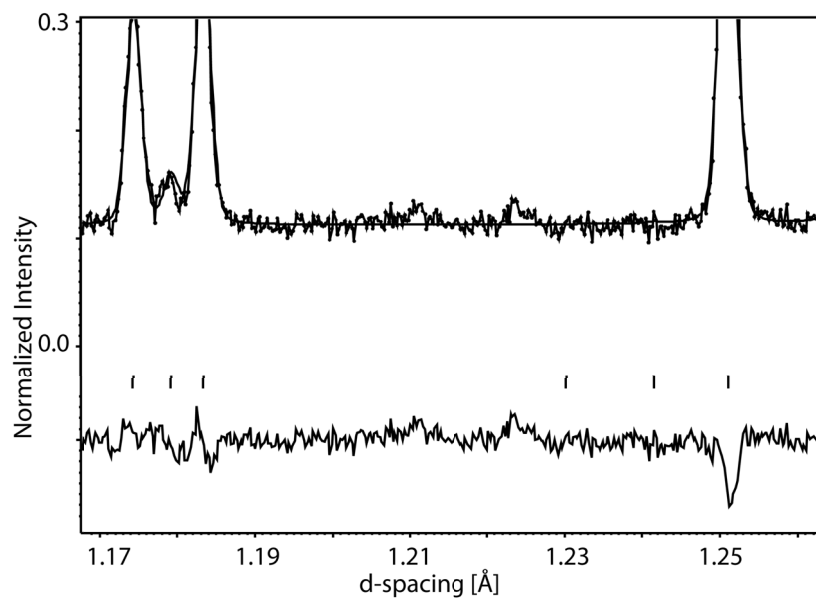


**Figure A.7:** Part of block with center at  $85^\circ$  of powder diffraction pattern of  $\text{Mn}_{5-x}\text{Fe}_x\text{Si}_3$   $x=3$  taken at 300 K with refinement. Ghosting peaks appear at  $d=1.21 \text{ \AA}$  and  $d=1.22 \text{ \AA}$ .

Pseudo-Voigt profile function  
The profile is cut outside  $8 \cdot \text{FWHM}$  range

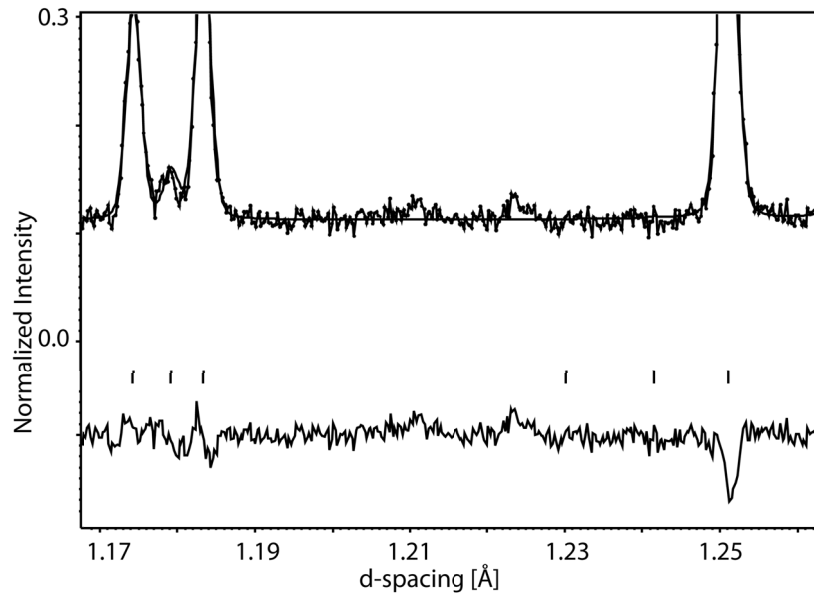


**Figure A.8:** Part of block with center at  $45^\circ$  of powder diffraction pattern of  $\text{Mn}_{5-x}\text{Fe}_x\text{Si}_3$   $x=3$  taken at 300 K with refinement. No ghosting peaks in this diffraction pattern.

Phase#3

=====

Pseudo-Voigt profile function

The profile is cut outside  $8 \times \text{FWHM}$  range

\*\*\*\*\*

\* Radiation \*

\*\*\*\*\*

Radiation type: Neutrons - time of flight

\*\*\*\*\*

\* Structure data - Phase#1 \*

\*\*\*\*\*

Cell parameters	:	6.7824	6.7824	4.7244
Reciprocal parameters	:	0.170249	0.170249	0.211669
90.000	90.000	120.000	Volume :	188.2
90.000	90.000	60.000	Volume :	0.005313

Refinement program

structure : Fe3 Si

Appendix A Additional Information

---

Centrosymmetric space group: P63/mc̄0m̄0

List of centring vectors:

0.000000 0.000000 0.000000

Symmetry operators:

x	y	z	m
-y	x-y	z	m
-x+y	-x	z	m
-x	-y	z+1/2	m
y	-x+y	z+1/2	m
x-y	x	z+1/2	m
y	x	-z+1/2	-m
x-y	-y	-z+1/2	-m
-x	-x+y	-z+1/2	-m
-y	-x	-z	-m
-x+y	y	-z	-m
x	x-y	-z	-m
-x	-y	-z	m
y	-x+y	-z	m
x-y	x	-z	m
x	y	-z+1/2	m
-y	x-y	-z+1/2	m
-x+y	-x	-z+1/2	m
-y	-x	z+1/2	-m
-x+y	y	z+1/2	-m
x	x-y	z+1/2	-m
y	x	z	-m
x-y	-y	z	-m
-x	-x+y	z	-m

Neutron scattering lengths

Mn	-3.730	0.000
Fe	9.450	0.000
Co	2.490	0.000
Si	4.149	0.000

Magnetic form factors

Fe4+	0.378	11.380	0.656	4.592	-0.035	0.483	0.001	0.036
------	-------	--------	-------	-------	--------	-------	-------	-------

F(000) for X-rays : 342.3755

F(000) for neutrons : 90.0672

Equations induced by symmetry :

Refinement program  
structure : Fe3 Si

x[Fe1]=0.33333  
y[Fe1]=0.66667  
z[Fe1]=0  
mx0[Fe1]=0  
my0[Fe1]=0  
x[Co1]=0.33333  
y[Co1]=0.66667  
z[Co1]=0  
y[Fe2]=0  
z[Fe2]=0.25  
mx0[Fe2]=0  
my0[Fe2]=0  
y[Mn2]=0  
z[Mn2]=0.25  
y[Si1]=0  
z[Si1]=0.25  
alpha[Phase#1]=90  
beta[Phase#1]=90  
gamma[Phase#1]=120  
b[Phase#1]=a[Phase#1]

\*\*\*\*\*  
\* Structure data - Phase#3 \*  
\*\*\*\*\*

Cell parameters : 5.6386 5.6386 5.6386  
Reciprocal parameters : 0.177350 0.177350 0.177350  
90.000 90.000 90.000 Volume : 179.3  
90.000 90.000 90.000 Volume : 0.005578

Centrosymmetric space group: Fm-3m

List of centring vectors:

0.000000 0.000000 0.000000  
0.000000 0.500000 0.500000  
0.500000 0.000000 0.500000  
0.500000 0.500000 0.000000

Symmetry operators:

```
x   y   z
-x  -y  z
-x  y   -z
x   -y  -z
z   x   y
z   -x  -y
-z  -x  y
-z  x   -y
y   z   x
-y  z   -x
y   -z  -x
-y  -z  x
y   x   -z
```

Refinement program  
structure : Fe3 Si

```
-y  -x  -z
y   -x  z
-y  x   z
x   z   -y
-x  z   y
-x  -z  -y
x   -z  y
z   y   -x
z   -y  x
-z  y   x
-z  -y  -x
-x  -y  -z
x   y   -z
x   -y  z
-x  y   z
-z  -x  -y
-z  x   y
z   x   -y
z   -x  y
-y  -z  -x
y   -z  x
-y  z   x
y   z   -x
-y  -x  z
y   x   z
-y  x   -z
y   -x  -z
-x  -z  y
```

```
x  -z  -y
x   z   y
-x  z  -y
-z  -y  x
-z  y  -x
z   -y  -x
z   y   x
```

Neutron scattering lengths

```
Fe          9.450  0.000
Co          2.490  0.000
Mn         -3.730  0.000
Si          4.149  0.000
```

```
F(000) for X-rays :    365.7902
F(000) for neutrons :   64.8118
```

Equations induced by symmetry :

```
x[Fe5]=0
y[Fe5]=0
```

Refinement program  
structure : Fe3 Si

```
z[Fe5]=0
x[Mn5]=0
y[Mn5]=0
z[Mn5]=0
x[Fe6]=0.25
y[Fe6]=0.25
z[Fe6]=0.25
x[Mn6]=0.25
y[Mn6]=0.25
z[Mn6]=0.25
x[Si5]=0.5
y[Si5]=0.5
z[Si5]=0.5
x[Co5]=0
y[Co5]=0
z[Co5]=0
x[Co6]=0.25
y[Co6]=0.25
z[Co6]=0.25
```

alpha[Phase#3]=90  
beta[Phase#3]=90  
gamma[Phase#3]=90  
b[Phase#3]=a[Phase#3]  
c[Phase#3]=a[Phase#3]

\*\*\*\*\*  
\* User defined constrains/restrains \*  
\*\*\*\*\*

Restrictions defined by user :

Occupational restriction of atoms : Fe1      Co1  
... sum of occupations will be kept to 0.166667  
... coordinates, ADP and modulation will be kept identical

Occupational restriction of atoms : Fe2      Mn2  
... sum of occupations will be kept to 0.250000  
... coordinates, ADP and modulation will be kept identical

Occupational restriction of atoms : Mn5      Fe5      Co5  
... sum of occupations will be kept to 0.020833  
... coordinates, ADP and modulation will be kept identical

Occupational restriction of atoms : Mn6      Fe6      Co6  
... sum of occupations will be kept to 0.041667  
... coordinates, ADP and modulation will be kept identical

\*\*\*\*\*  
\* User defined keep commands \*  
\*\*\*\*\*

Refinement program  
structure : Fe3 Si

None

Refinement program  
structure : Fe3 Si

Refinement program  
structure : Fe3 Si

Last screen information window:

```

-----
|R factors for Phase#1 : [218=185+33/11]
|R(obs)= 2.22  Rw(obs)= 2.85  R(all)= 2.22  Rw(all)= 2.85
|R factors for Phase#3 : [39=39+0/4]
|R(obs)= 3.38  Rw(obs)= 3.37  R(all)= 3.38  Rw(all)= 3.37
|=====
|Profile R factors : [4888/10+13],  Damping factor: 0.3000
|GOF  = 3.22  Rp   = 3.36  Rwp  = 3.27
|Last Rwp: 3.27 3.27 3.27 3.27 3.27 3.27 3.27
|Maximum change/s.u. : 0.0049 for ZeroT
-----

```

There were 253 correlations larger than 0.000 in last refinement cycle

```

-0.979 correlation : CE/a[Phase#1]
-0.955 correlation : CE/c[Phase#1]
-0.928 correlation : phvol2/ai[Fe5]
 0.915 correlation : a[Phase#1]/c[Phase#1]
-0.882 correlation : phvol2/ai[Fe6]
-0.814 correlation : Sig2[Phase#1]/Gam1[Phase#1]
-0.804 correlation : Sig2[Phase#3]/Gam1[Phase#3]
 0.751 correlation : ai[Fe5]/ai[Fe6]
-0.749 correlation : ZeroT/CE
 0.746 correlation : scale1/TOFAbs
 0.728 correlation : scale1/Uiso[Si1]
-0.696 correlation : ai[Fe1]/Uiso[Si1]
 0.689 correlation : ZeroT/a[Phase#1]
 0.670 correlation : ZeroT/c[Phase#1]
 0.666 correlation : TOFAbs/Uiso[Fe1]
-0.610 correlation : ai[Fe2]/Uiso[Si1]
 0.605 correlation : ai[Fe1]/ai[Fe2]
 0.596 correlation : ai[Fe2]/Uiso[Fe2]
 0.484 correlation : TOFAbs/Uiso[Fe2]
-0.476 correlation : scale1/ai[Fe1]
 0.440 correlation : scale1/Uiso[Fe1]
 0.411 correlation : TOFAbs/Uiso[Si1]
-0.400 correlation : scale1/ai[Fe2]
-0.401 correlation : CE/a[Phase#3]
 0.396 correlation : a[Phase#1]/a[Phase#3]
 0.387 correlation : c[Phase#1]/a[Phase#3]
 0.375 correlation : ai[Fe1]/Uiso[Fe1]
 0.365 correlation : Mz0[Fe1]/Mz0[Fe2]
-0.360 correlation : scale1/ai[Fe5]
-0.345 correlation : Mz0[Fe1]/Uiso[Fe2]
-0.331 correlation : scale1/ai[Fe6]
 0.292 correlation : scale1/phvol2

```



Appendix A Additional Information

---

0.282 correlation : ZeroT/a[Phase#3]  
0.283 correlation : scale1/Uiso[Fe2]  
-0.251 correlation : ai[Fe2]/Mz0[Fe2]  
-0.235 correlation : Mz0[Fe1]/ai[Fe2]  
-0.226 correlation : x[Fe2]/x[Si1]  
0.204 correlation : ai[Fe1]/Mz0[Fe1]  
-0.197 correlation : Uiso[Fe2]/Mz0[Fe2]  
0.173 correlation : Uiso[Fe1]/Uiso[Si1]  
0.159 correlation : Uiso[Fe1]/Mz0[Fe2]  
0.149 correlation : TOFAbs/Mz0[Fe2]  
0.147 correlation : Uiso[Fe1]/Mz0[Fe1]  
0.133 correlation : phvol2/ai[Fe2]  
-0.131 correlation : phvol2/Uiso[Si1]  
-0.123 correlation : scale1/Mz0[Fe1]  
0.117 correlation : phvol2/ai[Fe1]  
0.115 correlation : ai[Fe2]/x[Fe2]  
0.110 correlation : phvol2/Gam1[Phase#3]  
0.110 correlation : scale1/Mz0[Fe2]  
-0.108 correlation : TOFAbs/Mz0[Fe1]  
0.101 correlation : scale1/Gam1[Phase#1]  
-0.097 correlation : Gam1[Phase#1]/ai[Fe5]  
0.096 correlation : Uiso[Fe2]/x[Si1]  
0.090 correlation : TOFAbs/Gam1[Phase#3]  
-0.088 correlation : Mz0[Fe1]/Uiso[Si1]  
-0.079 correlation : TOFAbs/Sig2[Phase#3]  
-0.080 correlation : Uiso[Fe1]/ai[Fe2]  
-0.079 correlation : Mz0[Fe1]/x[Fe2]  
0.080 correlation : scale1/Gam1[Phase#3]  
0.077 correlation : Gam1[Phase#3]/Uiso[Fe1]  
0.076 correlation : x[Fe2]/Uiso[Fe2]  
0.074 correlation : TOFAbs/Gam1[Phase#1]  
0.073 correlation : Uiso[Fe2]/Uiso[Si1]  
-0.065 correlation : scale1/Sig2[Phase#3]  
-0.063 correlation : Gam1[Phase#1]/Gam1[Phase#3]  
0.062 correlation : Mz0[Fe2]/Uiso[Si1]  
-0.062 correlation : x[Fe2]/Mz0[Fe2]  
0.061 correlation : phvol2/x[Fe2]  
-0.062 correlation : Sig2[Phase#3]/Uiso[Fe2]  
-0.062 correlation : Mz0[Fe1]/x[Si1]  
0.058 correlation : Gam1[Phase#3]/Uiso[Fe2]  
-0.058 correlation : x[Fe2]/ai[Fe5]  
-0.056 correlation : ai[Fe1]/x[Si1]  
0.056 correlation : Sig2[Phase#1]/ai[Fe5]  
0.056 correlation : Uiso[Fe1]/Uiso[Fe2]  
0.056 correlation : Sig2[Phase#1]/Uiso[Fe1]  
-0.055 correlation : ai[Fe2]/ai[Fe6]

Refinement program  
structure : Fe3 Si

-0.052 correlation : Gam1[Phase#1]/Uiso[Fe1]  
-0.050 correlation : scale1/Sig2[Phase#1]  
-0.048 correlation : Sig2[Phase#3]/Uiso[Fe1]  
0.049 correlation : scale1/x[Si1]  
0.049 correlation : Mz0[Fe1]/ai[Fe5]  
-0.045 correlation : Uiso[Fe1]/x[Si1]  
0.044 correlation : phvol2/Gam1[Phase#1]  
-0.043 correlation : x[Si1]/ai[Fe6]  
0.041 correlation : TOFAbs/x[Si1]  
0.042 correlation : ai[Fe1]/Mz0[Fe2]  
-0.039 correlation : Gam1[Phase#1]/ai[Fe6]  
-0.040 correlation : x[Fe2]/ai[Fe6]  
-0.037 correlation : TOFAbs/Sig2[Phase#1]  
-0.038 correlation : phvol2/Sig2[Phase#3]  
-0.037 correlation : CE/x[Fe2]  
0.036 correlation : Gam1[Phase#3]/ai[Fe2]  
-0.035 correlation : ai[Fe2]/ai[Fe5]  
0.036 correlation : Sig2[Phase#1]/Gam1[Phase#3]  
0.036 correlation : Gam1[Phase#3]/ai[Fe1]  
0.034 correlation : TOFAbs/ai[Fe2]  
0.034 correlation : c[Phase#1]/x[Fe2]  
0.034 correlation : Uiso[Si1]/ai[Fe5]  
0.033 correlation : a[Phase#1]/x[Fe2]  
-0.032 correlation : phvol2/Mz0[Fe1]  
0.032 correlation : Sig2[Phase#1]/Uiso[Si1]  
0.032 correlation : Mz0[Fe1]/ai[Fe6]  
0.032 correlation : ai[Fe1]/x[Fe2]  
-0.031 correlation : Gam1[Phase#1]/Uiso[Si1]  
-0.030 correlation : Uiso[Fe2]/ai[Fe6]  
0.030 correlation : Gam1[Phase#1]/Sig2[Phase#3]  
0.028 correlation : Gam1[Phase#3]/ai[Fe6]  
-0.028 correlation : x[Fe2]/Uiso[Si1]  
-0.028 correlation : Sig2[Phase#3]/Uiso[Si1]  
0.029 correlation : a[Phase#3]/x[Fe2]  
0.027 correlation : Uiso[Si1]/ai[Fe6]  
-0.027 correlation : phvol2/Sig2[Phase#1]  
0.027 correlation : Uiso[Fe1]/x[Fe2]  
-0.026 correlation : Sig2[Phase#3]/ai[Fe6]  
0.026 correlation : Uiso[Fe1]/ai[Fe5]  
0.026 correlation : ZeroT/Sig2[Phase#3]  
-0.025 correlation : Gam1[Phase#1]/x[Si1]  
0.025 correlation : phvol2/Uiso[Fe2]  
-0.024 correlation : Sig2[Phase#1]/Sig2[Phase#3]

Appendix A Additional Information

---

-0.024 correlation : Sig2[Phase#3]/ai[Fe2]  
0.024 correlation : Mz0[Fe2]/x[Si1]  
0.023 correlation : ZeroT/x[Fe2]  
0.023 correlation : Sig2[Phase#1]/ai[Fe6]  
0.023 correlation : TOFAbs/x[Fe2]  
0.023 correlation : Gam1[Phase#3]/ai[Fe5]  
-0.023 correlation : c[Phase#1]/Gam1[Phase#1]  
0.022 correlation : ZeroT/Sig2[Phase#1]  
0.022 correlation : TOFAbs/ai[Fe1]  
0.022 correlation : a[Phase#3]/Gam1[Phase#3]  
-0.022 correlation : Gam1[Phase#1]/x[Fe2]  
-0.020 correlation : ZeroT/Gam1[Phase#1]  
0.019 correlation : Sig2[Phase#1]/x[Si1]  
0.019 correlation : Sig2[Phase#1]/x[Fe2]  
0.017 correlation : c[Phase#1]/Sig2[Phase#1]  
0.017 correlation : Sig2[Phase#3]/Mz0[Fe1]  
0.017 correlation : Gam1[Phase#3]/Uiso[Si1]  
-0.017 correlation : Sig2[Phase#1]/Mz0[Fe1]  
-0.018 correlation : ZeroT/Uiso[Si1]  
-0.018 correlation : a[Phase#1]/x[Si1]  
0.018 correlation : a[Phase#3]/ai[Fe1]  
-0.018 correlation : Uiso[Fe2]/ai[Fe5]  
-0.016 correlation : TOFAbs/ai[Fe5]  
0.016 correlation : CE/x[Si1]  
-0.016 correlation : ZeroT/Uiso[Fe2]  
0.015 correlation : phvol2/ZeroT  
0.015 correlation : CE/Mz0[Fe1]  
0.014 correlation : ai[Fe2]/x[Si1]  
0.015 correlation : a[Phase#3]/Uiso[Fe1]  
-0.015 correlation : phvol2/Uiso[Fe1]  
0.015 correlation : ZeroT/ai[Fe1]  
0.014 correlation : Sig2[Phase#3]/x[Fe2]  
-0.013 correlation : ai[Fe1]/ai[Fe6]  
-0.013 correlation : TOFAbs/ai[Fe6]  
0.013 correlation : a[Phase#3]/ai[Fe2]  
-0.013 correlation : Sig2[Phase#3]/ai[Fe5]  
0.013 correlation : a[Phase#1]/Sig2[Phase#3]  
-0.013 correlation : c[Phase#1]/Mz0[Fe1]  
-0.013 correlation : c[Phase#1]/x[Si1]  
0.013 correlation : phvol2/x[Si1]  
0.013 correlation : phvol2/a[Phase#3]  
-0.013 correlation : ZeroT/TOFAbs  
-0.013 correlation : c[Phase#1]/ai[Fe1]  
-0.012 correlation : a[Phase#1]/Mz0[Fe1]  
0.012 correlation : CE/ai[Fe1]  
0.012 correlation : CE/Gam1[Phase#1]  
0.011 correlation : a[Phase#3]/Sig2[Phase#3]

---

-0.011 correlation : ZeroT/ai [Fe5]  
-0.011 correlation : CE/Sig2 [Phase#1]  
-0.011 correlation : CE/Sig2 [Phase#3]  
0.011 correlation : ZeroT/Uiso [Fe1]  
-0.011 correlation : a [Phase#1] / ai [Fe1]  
0.011 correlation : Sig2 [Phase#1] / Uiso [Fe2]  
0.010 correlation : c [Phase#1] / ai [Fe6]  
-0.010 correlation : Mz0 [Fe2] / ai [Fe5]  
-0.010 correlation : x [Si1] / Uiso [Si1]  
-0.010 correlation : Gam1 [Phase#3] / Mz0 [Fe1]  
-0.010 correlation : ZeroT / x [Si1]  
-0.010 correlation : scale1 / ZeroT  
-0.010 correlation : phvol2 / TOFAbs  
0.009 correlation : Mz0 [Fe2] / ai [Fe6]  
Refinement program  
structure : Fe3 Si

0.009 correlation : Uiso [Fe1] / ai [Fe6]  
0.008 correlation : scale1 / x [Fe2]  
-0.008 correlation : x [Si1] / ai [Fe5]  
0.008 correlation : Gam1 [Phase#1] / ai [Fe2]  
-0.008 correlation : Gam1 [Phase#3] / x [Si1]  
-0.009 correlation : Sig2 [Phase#1] / a [Phase#3]  
-0.008 correlation : Gam1 [Phase#3] / Mz0 [Fe2]  
-0.008 correlation : a [Phase#3] / Mz0 [Fe2]  
-0.008 correlation : c [Phase#1] / Mz0 [Fe2]  
0.008 correlation : CE / TOFAbs  
-0.008 correlation : a [Phase#1] / Mz0 [Fe2]  
0.009 correlation : CE / Mz0 [Fe2]  
-0.007 correlation : a [Phase#1] / Gam1 [Phase#3]  
0.007 correlation : c [Phase#1] / Sig2 [Phase#3]  
-0.007 correlation : TOFAbs / c [Phase#1]  
0.007 correlation : Sig2 [Phase#1] / Mz0 [Fe2]  
0.007 correlation : Sig2 [Phase#1] / ai [Fe1]  
-0.007 correlation : scale1 / a [Phase#3]  
-0.007 correlation : a [Phase#1] / Uiso [Fe2]  
-0.006 correlation : TOFAbs / a [Phase#1]  
-0.006 correlation : ai [Fe1] / ai [Fe5]  
0.006 correlation : a [Phase#1] / Sig2 [Phase#1]  
-0.006 correlation : a [Phase#3] / Uiso [Si1]  
0.006 correlation : Gam1 [Phase#1] / Mz0 [Fe1]  
-0.006 correlation : Sig2 [Phase#3] / x [Si1]  
-0.006 correlation : a [Phase#3] / x [Si1]  
-0.006 correlation : phvol2 / Mz0 [Fe2]  
-0.006 correlation : Gam1 [Phase#1] / ai [Fe1]  
-0.006 correlation : a [Phase#3] / Uiso [Fe2]  
-0.006 correlation : Gam1 [Phase#3] / x [Fe2]

Appendix A Additional Information

---

0.005 correlation : a[Phase#1]/ai [Fe6]  
-0.004 correlation : CE/ai [Fe6]  
-0.005 correlation : ZeroT/ai [Fe6]  
-0.005 correlation : ZeroT/Gam1 [Phase#3]  
-0.004 correlation : Sig2[Phase#1]/ai [Fe2]  
-0.004 correlation : a[Phase#3]/Mz0 [Fe1]  
-0.004 correlation : a[Phase#1]/Uiso [Si1]  
0.005 correlation : CE/Uiso [Si1]  
-0.005 correlation : ZeroT/Mz0 [Fe2]  
-0.004 correlation : Sig2[Phase#3]/ai [Fe1]  
-0.004 correlation : ai [Fe1]/Uiso [Fe2]  
0.005 correlation : Gam1 [Phase#1]/Uiso [Fe2]  
0.005 correlation : CE/Uiso [Fe2]  
-0.004 correlation : phvol2/c [Phase#1]  
-0.004 correlation : a[Phase#1]/Gam1 [Phase#1]  
0.003 correlation : ZeroT/ai [Fe2]  
0.003 correlation : CE/ai [Fe5]  
0.003 correlation : c [Phase#1]/Uiso [Si1]  
0.003 correlation : a [Phase#1]/Uiso [Fe1]  
-0.003 correlation : Sig2 [Phase#3]/Mz0 [Fe2]  
0.002 correlation : a [Phase#3]/ai [Fe6]  
0.002 correlation : CE/Gam1 [Phase#3]  
-0.002 correlation : CE/ai [Fe2]  
-0.002 correlation : phvol2/a [Phase#1]  
0.002 correlation : Gam1 [Phase#1]/a [Phase#3]  
-0.002 correlation : c [Phase#1]/Uiso [Fe1]  
-0.002 correlation : CE/Uiso [Fe1]  
0.002 correlation : Gam1 [Phase#1]/Mz0 [Fe2]  
-0.002 correlation : c [Phase#1]/Uiso [Fe2]  
0.001 correlation : c [Phase#1]/ai [Fe2]  
0.001 correlation : a [Phase#3]/ai [Fe5]  
0.001 correlation : c [Phase#1]/ai [Fe5]  
-0.001 correlation : ZeroT/Mz0 [Fe1]  
-0.001 correlation : scale1/a [Phase#1]  
-0.001 correlation : TOFAbs/a [Phase#3]  
-0.001 correlation : phvol2/CE  
-0.001 correlation : scale1/c [Phase#1]  
0.001 correlation : scale1/CE  
0.000 correlation : c [Phase#1]/Gam1 [Phase#3]  
0.000 correlation : a [Phase#1]/ai [Fe2]  
0.000 correlation : a [Phase#1]/ai [Fe5]

Relative phase amounts in mass

Phase#1 0.92(2)  
Phase#3 0.076(17)





# Appendix B

## Bibliography

- [1] <http://green.blogs.nytimes.com/tag/magnetocaloric-effect/>.
- [2] E. Warburg. Magnetische Untersuchungen. *Annalen der Physik und Chemie*, 13:1441, 1881.
- [3] W. F. Giauque. A thermodynamic treatment of certain magnetic effects. a proposed method of producing temperatures considerably below, 1 absolute. *Journal of the American Chemical Society*, 49:1864–1870, 1927.
- [4] P. Debye. Some observations on magnetisation at a low temperature. *Annalen der Physik*, 81(25):1154–1160, 1926.
- [5] Montreal protocol on substances that deplete the ozone layer (with annex). Concluded at montreal on 16 september 1987. *United Nations - Treaty Series*, 1522, 1987.
- [6] F. Drake, M. Purvis, and J. Hunt. Business appreciation of global atmospheric change: the united kingdom refrigeration industry. *Public Understanding of Science*, 10(2):187–211, 2001.
- [7] C. Zimm, A. Jastrab, A. Sternberg, V. Pecharsky, K. Gschneidner, M. Osborne, and I. Anderson. Description and performance of a near-room temperature magnetic refrigerator. *Advances in Cryogenic Engineering, Vol 43 Pts A and B*, 43:1759–1766, 1998.
- [8] A. M. Tisin and Y. I. Spichkin. *The magnetocaloric effect and its applications*. Bristol: Institute of Physics Publishing, 2003.
- [9] Andrej Kitanovski and Peter W. Egolf. Application of magnetic refrigeration and its assessment. *Journal of Magnetism and Magnetic Materials*, 321(7):777–781, 2009.
- [10] K. A. Gschneidner, V. K. Pecharsky, and A. O. Tsokol. Recent developments in magnetocaloric materials. *Reports on Progress in Physics*, 68(6):1479–1539, 2005.
- [11] Liu Min and Yu Bing-feng. Development of magnetocaloric materials in room temperature magnetic refrigeration application in recent six years. *Journal of Central South University of Technology*, 16(1):1–12, 2009.
- [12] V. K. Pecharsky and K. A. Gschneidner. Giant magnetocaloric effect in  $\text{Gd}_5(\text{Si}_2\text{Ge}_2)$ . *Physical Review Letters*, 78(23):4494–4497, 1997.
- [13] V. K. Pecharsky and K. A. Gschneidner. Tunable magnetic regenerator alloys with a giant magnetocaloric effect for magnetic refrigeration from similar to 20 to similar to 290 K. *Applied Physics Letters*, 70(24):3299–3301, 1997.



- [14] A. Giguere, M. Foldeaki, B. R. Gopal, R. Chahine, T. K. Bose, A. Frydman, and J. A. Barclay. Direct measurement of the "giant" adiabatic temperature change in  $\text{Gd}_5\text{Si}_2\text{Ge}_2$ . *Physical Review Letters*, 83(11):2262–2265, 1999.
- [15] A. O. Pecharsky, K. A. Gschneidner, and V. K. Pecharsky. The giant magnetocaloric effect of optimally prepared  $\text{Gd}_5\text{Si}_2\text{Ge}_2$ . *Journal of Applied Physics*, 93(8):4722–4728, 2003.
- [16] Y. I. Spichkin, V. K. Pecharsky, and K. A. Gschneidner. Preparation, crystal structure, magnetic and magnetothermal properties of  $\text{Gd}_x\text{R}_{5-x}\text{Si}_4$ , where  $r=\text{pr}$  and  $\text{tb}$ , alloys. *Journal of Applied Physics*, 89(3):1738–1745, 2001.
- [17] N. Hirano, S. Nagaya, M. Takahashi, T. Kuriyama, K. Ito, and S. Nomura. Development of magnetic refrigerator for room temperature application. *Advances In Cryogenic Engineering, Vol 47, Pts A and B*, 613, 2002.
- [18] A. M. Rowe and J. A. Barclay. Design of an active magnetic regenerator test apparatus. *Advances In Cryogenic Engineering, Vol 47, Pts A and B*, 613, 2002.
- [19] A. M. Rowe and J. A. Barclay. Static and dynamic force balancing in reciprocating active magnetic refrigerators. *Advances In Cryogenic Engineering, Vol 47, Pts A and B*, 613, 2002.
- [20] M. A. Richard, A. M. Rowe, and R. Chahine. Magnetic refrigeration: Single and multimaterial active magnetic regenerator experiments. *Journal of Applied Physics*, 95(4):2146–2150, 2004.
- [21] P. Clot, D. Viallet, F. Allab, A. Kedous-Lebouc, J. M. Fournier, and J. P. Yonnet. A magnet-based device for active magnetic regenerative refrigeration. *IEEE Transactions on Magnetics*, 39(5):3349–3351, 2003.
- [22] V. K. Pecharsky, K. A. Gschneidner, A. O. Pecharsky, and A. M. Tishin. Thermodynamics of the magnetocaloric effect. *Phys. Rev. B*, 64:144406, 2001.
- [23] O. Tegus. *Novel Materials for Magnetic Refrigeration*. PhD thesis, University of Amsterdam, 2003.
- [24] T. Krenke, E. Duman, M. Acet, E. F. Wassermann, X. Moya, L. Manosa, and A. Planes. Inverse magnetocaloric effect in ferromagnetic Ni-Mn-Sn alloys. *Nature Materials*, 4(6):450–454, 2005.
- [25] V. K. Sharma, M. K. Chattopadhyay, and S. B. Roy. Large inverse magnetocaloric effect in  $\text{Ni}_{50}\text{Mn}_{34}\text{In}_{16}$ . *Journal of Physics D-Applied Physics*, 40(7):1869–1873, 2007.
- [26] N. Kurti. L'antiferromagnetisme aux basses temperatures. *Journal de Physique et le Radium*, 12(3):281–290, 1951.
- [27] C. G. B. Garrett. Experiments with an anisotropic magnetic crystal at temperatures below 1K. *Proceedings of the Royal Society of London Series A-Mathematical and Physical Sciences*, 206(1085):242–257, 1951.
- [28] H. Binczycka, Z. Dimitrijevic, B. Gajic, and A. Szytula. Atomic and magnetic structure of  $\text{Mn}_{5-x}\text{Fe}_x\text{Si}_3$ . *Physica Status Solidi (a)*, 19:K13–K17, 1973.

- [29] E. Bruck, O. Tegus, D. T. Cam Thanh, Nguyen T. Trung, and K. H. J. Buschow. A review on mn based materials for magnetic refrigeration: Structure and properties. *International Journal of Refrigeration-revue Internationale Du Froid*, 31(5):763–770, 2008.
- [30] Fabiana Cristina Nascimento, Adenilson Oliveira dos Santos, Ariana de Campos, and Sergio ans Cardoso Lisandro Pavie Gama, S. A. Structural and magnetic study of the MnAs magnetocaloric compound. *Materials Research*, 9:111 – 114, 2006.
- [31] V. A. Chernenko, L. Wee, P. G. McCormick, and R. Street. Giant magnetoelastic response in mnas. *Journal of Applied Physics*, 85(11):7833–7837, 1999.
- [32] F. Ishikawa, K. Koyama, K. Watanabe, T. Asano, and H. Wada. First-order phase transition at the Curie temperature in MnAs and MnAs<sub>0.9</sub>Sb<sub>0.1</sub>. *Journal of the Physical Society of Japan*, 75(8):084604, 2006.
- [33] H. Wada and Y. Tanabe. Giant magnetocaloric effect of MnAs<sub>1-x</sub>Sb<sub>x</sub>. *Applied Physics Letters*, 79(20):3302–3304, 2001.
- [34] H. Wada, K. Taniguchi, and Y. Tanabe. Extremely large magnetic entropy change of MnAs<sub>1-x</sub>Sb<sub>x</sub> near room temperature. *Materials Transactions*, 43(1):73–77, 2002.
- [35] H. Wada, T. Morikawa, K. Taniguchi, T. Shibata, Y. Yamada, and Y. Akishige. Giant magnetocaloric effect of MnAs<sub>1-x</sub>Sb<sub>x</sub> in the vicinity of first-order magnetic transition. *Physica B-condensed Matter*, 328(1-2):114–116, 2003.
- [36] Songlin, Dagula, O. Tegus, E. Bruck, J. C. P. Klaasse, F. R. de Br, and K. H. J. Buschow. Magnetic phase transition and magnetocaloric effect in Mn<sub>5-x</sub>Fe<sub>x</sub>Si<sub>3</sub>. *Journal of Alloys and Compounds*, 334:249–252, 2002.
- [37] Nguyen H. Dung, Zhi Qiang Ou, Luana Caron, Lian Zhang, Dinh T. Cam Thanh, Gilles A. de Wijs, Rob A. de Groot, K. H. Jurgen Buschow, and Ekkes Bruck. Mixed magnetism for refrigeration and energy conversion. *Advanced Energy Materials*, 1(6):1215–1219, 2011.
- [38] A. Candini, O. Moze, W. Kockelmann, J. M. Cadogan, E. Bruck, and O. Tegus. Revised magnetic phase diagram for Fe<sub>x</sub>Mn<sub>5-x</sub>Si<sub>3</sub> intermetallics. *Journal of Applied Physics*, 95(11):6819–6821, 2004.
- [39] P. J. Brown and J. B. Forsyth. Antiferromagnetism in Mn<sub>5</sub>Si<sub>3</sub> - the magnetic-structure of the Af2 phase at 70K. *Journal of Physics-Condensed Matter*, 7(39):7619–7628, 1995.
- [40] P. J. Brown, J. B. Forsyth, V. Nunez, and F. Tasset. The low-temperature antiferromagnetic structure of Mn<sub>5</sub>Si<sub>3</sub> revised in the light of neutron polarimetry. *Journal of Physics-Condensed Matter*, 4(49):10025–10036, 1992.
- [41] J. Leciejewicz, B. Penc, A. Szytula, A. Jezierski, and A. Zygmunt. Magnetic properties of the Mn<sub>5</sub>Si<sub>3</sub> compound. *Acta Physica Polonica A*, 113(4):1193–1203, 2008.
- [42] A. Z. Menshikov, A. P. Vokhmyanin, and Y. A. Dorofeev. Magnetic-structure and phase-transformations in Mn<sub>5</sub>Si<sub>3</sub>. *Physica Status Solidi B-basic Research*, 158(1):319–328, 1990.

- [43] M. R. Silva, P. J. Brown, and J. B. Forsyth. Magnetic moments and magnetic site susceptibilities in  $\text{Mn}_5\text{Si}_3$ . *Journal of Physics-condensed Matter*, 14(37):PII S0953–8984(02)36762–6, 2002.
- [44] [http://www.bpc.edu/mathscience/chemistry/history\\_of\\_the\\_periodic\\_table.html](http://www.bpc.edu/mathscience/chemistry/history_of_the_periodic_table.html).
- [45] Song Lin, O. Tegus, E. Bruck, W. Dagula, T. J. Gortenmulder, and K. H. J. Buschow. Structural and magnetic properties of  $\text{MnFe}_{1-x}\text{Co}_x\text{Ge}$  compounds. *Ieee Transactions On Magnetics*, 42(11):3776–3778, 2006.
- [46] T. Tohei, H. Wada, and T. Kanomata. Large magnetocaloric effect of  $\text{Mn}_{3-x}\text{Co}_x\text{GaC}$ . *Journal of Magnetism and Magnetic Materials*, 272:E585–E586, 2004.
- [47] T. Svobodny and Z. Kalva. Magnetocaloric effect in ferromagnetic and superconducting materials. *Physica Status Solidi B-Basic Research*, 208(1):187–196, 1998.
- [48] T. Strassle, S. Janssen, F. Juranyi, A. Furrer, O. Moze, A. O. Pecharsky, V. K. Pecharsky, and K. A. Gschneidner. Inelastic neutron scattering study of the intra-lanthanide alloys  $\text{Er}_x\text{Pr}_{1-x}$  ( $x=0.6, 0.8$ ). *Physical Review B*, 68(13):134411, 2003.
- [49] R. Schedler, U. Witte, M. Rotter, M. Loewenhaupt, and W. Schmidt. Field dependence of the magnon dispersion in the Kondo lattice  $\text{CeCu}_2$  up to 12T. *Journal of Applied Physics*, 97(10):Phys Conf Inc., 2005.
- [50] B.K. Ponomarev. Magnetic properties of gadolinium in the region of paraprocess. *Journal of Magnetism and Magnetic Materials*, 61(1–2):129 – 138, 1986.
- [51] Arthur E. Clark and Earl Callen. Cooling by adiabatic magnetization. *Phys. Rev. Lett.*, 23:307–308, 1969.
- [52] Ch. Kuhrt, Th. Schittny, and K. Barner. Magnetic phase diagram of anion substituted  $\text{MnAs}$ . magnetocaloric experiments. *Physica Status Solidi (a)*, 91(1):105–113, 1985.
- [53] S. Yu. Dan’kov, A. M. Tishin, V. K. Pecharsky, and K. A. Gschneidner. Magnetic phase transitions and the magnetothermal properties of gadolinium. *Phys. Rev. B*, 57:3478–3490, 1998.
- [54] E.H. Kisi and C.J. Howard. *Application of Neutron Powder Diffraction*. Oxford University Press Inc., New York, 2008.
- [55] G. Arlt. Twinning in ferroelectric and ferroelastic ceramics: stress relief. *Journal of Materials Science*, 25:2655–2666, 1990.
- [56] A. Huq, J.P. Hodges, O. Gourdon, and L. Heroux. Powgen: A third-generation high-resolution high-throughput powder diffraction instrument at the spallation neutron source. *Kristallogr. Proc.*, 1:127–135, 2011.
- [57] A.C. Larson and R.B. Von Dreele. *General Structure Analysis System (GSAS)*. Los Alamos National Laboratory Report LAUR 86-748, 2004.
- [58] J. Rodriguez-Carvajal. *FullProf 2000*. Laboratoire Leon Brillouin (CEA-CNRS), <http://www.ill.eu/sites/fullprof/php/tutorials.html>, CEA/Saclay, 91191 Gif sur Yvette Cedex, FRANCE, 2001.

- 
- [59] J. Rodriguez-Carvajal. *Using FullProf to analyze Time of Flight Neutron Powder Diffraction Data*. Laboratoire Leon Brillouin (CEA-CNRS), <http://www.ccp14.ac.uk/ccp/web-mirrors/plotr/Tutorials&Documents/>, 2003.
- [60] V. Petricek and M. Dusek. *Jana2000 Crystallographic computing system, User manual, part 1*. Institute of Physics Academy of Science of the Czech Republic, <http://jana.fzu.cz/>, 2003.
- [61] A. Le Bail, H. Duroy, and J. L. Fourquet. Abinitio structure determination of LiSbWO<sub>6</sub> by x-ray-powder diffraction. *Materials Research Bulletin*, 23(3):447–452, 1988.
- [62] H. M. Rietveld. Line profiles of neutron powder-diffraction peaks for structure refinement. *Acta Crystallographica*, 22:151, 1967.
- [63] H. M. Rietveld. A profile refinement method for nuclear and magnetic structures. *Journal of Applied Crystallography*, 2:65, 1969.
- [64] E. Mueller-Hartmann. *Theoretische Festkoerperphysik I*. Universitaet Koeln, Institut fuer theoretische Physik, <http://www.thp.uni-koeln.de/lecturenotes.html>, WS 2005/06.
- [65] M. Angst, T. Brueckel, D. Richter, and R. Zorn, editors. *Scattering Methods for Condensed Matter Research: Towards Novel Applications at Future Sources*. Forschungszentrum Juelich, 2012.
- [66] I. A. Zaliznyak and S.-H. Lee. Magnetic neutron scattering, [http://neutrons.phy.bnl.gov/presentations/magneticneutronsattering\\_proofed\\_indexed\\_unlinked.pdf](http://neutrons.phy.bnl.gov/presentations/magneticneutronsattering_proofed_indexed_unlinked.pdf).
- [67] Ch. Kittel. *Einfuehrung in die Festkoerperphysik*. Oldenbourg Wissenschaftsverlag, 14 edition, 2006.
- [68] T. B. S. Jensen, N. B. Christensen, M. Kenzelmann, H. M. Ronnow, C. Niedermayer, N. H. Andersen, K. Lefmann, M. Jimenez-Ruiz, F. Demmel, J. Li, J. L. Zarestky, and D. Vaknin. Anomalous spin waves and the commensurate-incommensurate magnetic phase transition in LiNiPO<sub>4</sub>. *Physical Review B*, 79(9):092413, 2009.
- [69] Z. D. Zhang. Spin waves in several Heisenberg systems: Three-sublattice with different exchange constants ( $j(ab) \neq j(bc) \neq j(ca)$ ) and a superlattice with the elementary unit of four or three different layers. *Physical Review B*, 55(18):12408–12423, 1997.
- [70] <http://neutrons.ornl.gov/powgen/>.
- [71] <http://neutrons.ornl.gov/instruments/HFIR/HB2A/>.
- [72] [http://www-llb.cea.fr/en/fr-en/pdf/2t1\\_llb.pdf](http://www-llb.cea.fr/en/fr-en/pdf/2t1_llb.pdf).
- [73] Poster, M. Beyss, and H. Gier. *Schmelzverfahren fuer die Herstellung von Reinstmaterialien*. Forschungszentrum Juelich GmbH, Institut fuer Festkoerperforschung, Germany, 52425 Juelich.
- [74] Europaeische Patentschrift 0345542B1, H. Gier, and M. Beyss. Kalt-Schmelz-Tiegel, 03 1993.
- [75] K.-Th. Wilke. *Kristallzuechtung*. 1973.
- [76] [http://www.mineralogie\\_erleben.de/syn.htm](http://www.mineralogie_erleben.de/syn.htm).

- [77] V. Johnson, D. B. Rogers, J. F. Weiher, and CG Frederic. Magnetic and mossbauer-effect studies of  $\text{Mn}_5\text{Si}_3\text{Fe}_5\text{Si}_3$  solid-solutions. *Journal of Solid State Chemistry*, 4(2):311–&, 1972.
- [78] G. H. Lander, P. J. Brown, and J. B. Forsyth. Antiferromagnetic structure of  $\text{Mn}_5\text{Si}_3$ . *Proceedings of the Physical Society of London*, 91(572P):332–&, 1967.
- [79] N.W. Ashcroft and D.N. Mermin. *Festkoerperphysik*. Oldenbourg Wissenschaftsverlag, 3 edition, 2007.
- [80] K. G. Sandeman, R. Daou, S. Özcan, J. H. Durrell, N. D. Mathur, and D. J. Fray. Negative magnetocaloric effect from highly sensitive metamagnetism in  $\text{CoMnSi}_{1-x}\text{Ge}_x$ . *Phys. Rev. B*, 74:224436–224442, 2006.
- [81] T. Tohei, H. Wada, and T. Kanomata. Negative magnetocaloric effect at the antiferromagnetic to ferromagnetic transition of  $\text{Mn}_3\text{GaC}$ . *Journal of Applied Physics*, 94(3):1800–1802, 2003.
- [82] Jingfang Duan, Peng Huang, Hu Zhang, Yi Long, Guangheng Wu, Rongchang Ye, Yongqin Chang, and Farong Wan. Negative and positive magnetocaloric effect in Ni-Fe-Mn-Ga alloy. *Journal of Magnetism and Magnetic Materials*, 309(1):96–99, 2007.
- [83] Pramod Kumar, Niraj K. Singh, K. G. Suresh, A. K. Nigam, and S. K. Malik. Multiple magnetic transitions and the magnetocaloric effect in  $\text{Gd}_{1-x}\text{Sm}_x\text{Mn}_2\text{Ge}_2$  compounds. *Journal of Physics-Condensed Matter*, 19(38):386210, 2007.
- [84] Anis Biswas, Tapas Samanta, S. Banerjee, and I. Das. Inverse magnetocaloric effect in polycrystalline  $\text{La}_{0.125}\text{Ca}_{0.875}\text{MnO}_3$ . *Journal of Physics-condensed Matter*, 21(50):506005, 2009.
- [85] P. J. von Ranke, V. K. Pecharsky, K. A. Gschneidner, and B. J. Korte. Anomalous behavior of the magnetic entropy in  $\text{PrNi}_5$ . *Physical Review B*, 58(21):14436–14441, 1998.
- [86] Guowu Li, Nicheng Shi, Ming Xiong, Zhesheng Ma, Wenji Bai, and Qingsong Fang. X-ray diffraction investigation of native Si-Fe alloy minerals from luobusha, tibet. *Frontiers of Earth Science in China*, 1:21–25, 2007.
- [87] T. Jeong. Magnetic properties of  $\text{Mn}_3\text{Si}$  from first-principles studies. *Physica B-Condensed Matter*, 407(5):888–890, 2012.
- [88] Th. Hahn, editor. *INTERNATIONAL TABLES FOR CRYSTALLOGRAPHY*, volume A. International Union of Crystallography, 2006.
- [89] A. R. Denton and N. W. Ashcroft. Vegard law. *Physical Review A*, 43(6):3161–3164, 1991.
- [90] S. Yoon and J. G. Booth. Magnetic-properties and structures of some ordered  $(\text{FeMn})_3\text{Si}$  alloys. *Journal of Physics F-metal Physics*, 7(6):1079–1095, 1977.
- [91] T. ERSEZ, G. T. ETHERIDGE, and T. J. HICKS. Demagnetization effects in  $\text{Fe}_3\text{-xMn}_x\text{Si}$  alloys. *Journal of Magnetism and Magnetic Materials*, 148(3):L381–L383, 1995.
- [92] S. Yoon and J. G. Booth. Structural and magnetic-properties of  $\text{Fe}_{3-x}\text{Mn}_x\text{Si}$  alloys. *Physics Letters A*, A 48(5):381–382, 1974.

- [93] J Vannimenus and G Toulouse. Theory of the frustration effect. ii. Ising spins on a square lattice. *Journal of Physics C: Solid State Physics*, 10(18):L537, 1977.
- [94] P. J. von Ranke, N. A. de Oliveira, B. P. Alho, E. J. R. Plaza, V. S. R. de Sousa, L. Caron, and M. S. Reis. Understanding the inverse magnetocaloric effect in antiferro- and ferromagnetic arrangements. *Journal of Physics-Condensed Matter*, 21(5):056004, 2009.
- [95] N. A. de Oliveira and P. J. von Ranke. Theoretical aspects of the magnetocaloric effect. *Physics Reports-Review Section of Physics Letters*, 489(4-5):89–159, 2010.
- [96] C. M. N. Kumar. *Crystal and spin structure and their relation to physical properties in some geometrical and spin spiral multiferroics*. PhD thesis, Rheinisch-Westfaelische Technische Hochschule Aachen, 2011.
- [97] B. Morosin. Exchange striction effects In MnO and MnS. *Physical Review B*, 1(1):236–&, 1970.
- [98] K. Motoya, H. Yasuoka, Y. Nakamura, and J. H. Wernick. Magnetic-properties of MnSi-CoSi solid-solution alloys. *Journal of the Physical Society of Japan*, 44(5):1525–1532, 1978.
- [99] E. G. Moroni, W. Wolf, J. Hafner, and R. Podloucky. Cohesive, structural, and electronic properties of Fe-Si compounds. *Physical Review B*, 59(20):12860–12871, 1999.
- [100] [http://www.fiz.karlsruhe.de/icsd\\_home.html](http://www.fiz.karlsruhe.de/icsd_home.html).
- [101] J. Teyssier, E. Giannini, V. Guritanu, R. Viennois, D. van der Marel, A. Amato, and S. N. Gvasaliya. Spin-glass ground state in  $\text{Mn}_{1-x}\text{Co}_x\text{Si}$ . *Physical Review B*, 82(6):064417, 2010.
- [102] K. Koyama, T. Goto, T. Kanomata, and R. Note. Precise magnetization measurements of single-crystalline FeSi under high pressure. *Journal of the Physical Society of Japan*, 68(5):1693–1698, 1999.
- [103] H. Watanabe, H. Yamamoto, and K. Ito. Neutron diffraction study of the intermetallic compound FeSi. *Journal of the Physical Society of Japan*, 18(7):995, 1963.
- [104] Ishikawa Y., K. Tajima, D. Bloch, and M. Roth. Helical spin structure in manganese silicide Mnsi. *Solid State Communications*, 19(6):525–528, 1976.
- [105] Viacheslav A. Chizhikov and Vladimir E. Dmitrienko. Frustrated magnetic helices in MnSi-type crystals. *Physical Review B*, 85(1):014421, 2012.
- [106] N. Manyala, Y. Sidis, J. F. Ditusa, G. Aeppli, D. P. Young, and Z. Fisk. Large anomalous hall effect in a silicon-based magnetic semiconductor. *Nature Materials*, 3(4):255–262, 2004.
- [107] W. A. Hines, A. H. Menotti, J. I. Budnick, T. J. Burch, T. Litrenta, V. Niculescu, and K. Raj. Magnetization studies of binary and ternary alloys based on  $\text{Fe}_3\text{Si}$ . *Physical Review B*, 13(9):4060–4068, 1976.
- [108] V. A. Niculescu, T. J. Burch, and J. I. Budnick. A local environment description of hyperfine fields and atomic moments in  $\text{Fe}_{3-x}\text{T}_x\text{Si}$  alloys. *Journal of Magnetism and Magnetic Materials*, 39(3):223–267, 1983.

- [109] Vandenbo. J and F. M. A. Carpay. Eutectoid  $\text{Co}_3\text{Si}$  phase in Co-Si system. *Acta Metallurgica*, 20(4):473–&, 1972.
- [110] J. Beille, D. Bloch, V. Jaccarino, and J. H. Wernick. Effects of hydrostatic pressure on the magnetic properties of disordered monosilicide  $\text{Fe}_x\text{Co}_{1-x}\text{Si}$  alloys. *Le Journal de Physique*, 38:339–343, 1977.
- [111] B. M. Powell, S. Jandl, J. L. Brebner, and F. Levy. Anisotropic phonon dispersion in gas. *Journal of Physics C-solid State Physics*, 10(16):3039–3049, 1977.
- [112] W. D. Teuchert and R. Geick. Symmetry of lattice-vibrations in selenium and tellurium. *Physica Status Solidi B-Basic Research*, 61(1):123–136, 1974.
- [113] Olivier Delaire, Karol Marty, Matthew B. Stone, Paul R. C. Kent, Matthew S. Lucas, Douglas L. Abernathy, David Mandrus, and Brian C. Sales. Phonon softening and metalization of a narrow-gap semiconductor by thermal disorder. *Proceedings of the National Academy of Sciences of the United States of America*, 108(12):4725–4730, 2011.
- [114] R. Wartchow, S. Gerighausen, and M. Binnewies. Redetermination of the crystal structure of iron silicide, FeSi. *Zeitschrift Fur Kristallographie-New Crystal Structures*, 212(3):320–320, 1997.
- [115] B. Boren. Roentgenuntersuchung der Legierungen von Silicium mit Chrom, Mangan, Kobalt und Nickel. *Arkiv for Kemi, Mineralogi och Geologi*, A 11:1–28, 1934.
- [116] Z. D. Zhang and T. Zhao. Spin waves at low temperatures in two-sublattice heisenberg ferromagnets and ferrimagnets with different sublattice anisotropies. *Journal of Physics-condensed Matter*, 9(38):8101–8118, 1997.
- [117] F. Q. Zhao, W. Dagula, O. Tegus, and K. H. J. Buschow. Magnetic-entropy change in  $\text{Mn}_5\text{Ge}_3\text{-xsix}$  alloys. *Journal of Alloys and Compounds*, 416(1-2):43–45, 2006.
- [118] J. B. Forsyth and P. J. Brown. The spatial-distribution of magnetization density in  $\text{Mn}_5\text{Ge}_3$ . *Journal of Physics-Condensed Matter*, 2(11):2713–2720, 1990.
- [119] Songlin, Dagula, O. Tegus, E. Bruck, F. R. de Bör, and K. H. J. Buschow. Magnetic and magnetocaloric properties of  $\text{Mn}_5\text{Ge}_{3-x}\text{Sb}_x$ . *Journal of Alloys and Compounds*, 337:PII S0925–8388(01)01935–1, 2002.
- [120] T. T. M. Palstra, J. A. Mydosh, G. J. Nieuwenhuys, A. M. Vanderkraan, and K. H. J. Buschow. Study of the critical-behavior of the magnetization and electrical-resistivity in cubic  $\text{La}(\text{Fe}, \text{Si})_{13}$  compounds. *Journal of Magnetism and Magnetic Materials*, 36(3):290–296, 1983.
- [121] T. T. M. Palstra, H. G. C. Werij, G. J. Nieuwenhuys, J. A. Mydosh, F. R. Deboer, and K. H. J. Buschow. Metamagnetic transitions in cubic  $\text{La}(\text{Fe}_x\text{Al}_{1-x})_{13}$  intermetallic compounds. *Journal of Physics F-metal Physics*, 14(8):1961–1966, 1984.

# Appendix C

## List of Figures

1.1	Performance of one cycle of magnetocaloric refrigeration taken from [1]. a) A magnetic material is considered. b) When applying a magnetic field the magnetic moments align. Therefore the magnetic part of the entropy is decreased forcing the lattice part of the entropy to increase keeping the change of total entropy zero for an adiabatic process. This causes the material to heat up. c) After heat is pumped away due to the contact with an external heat bath the material's temperature is lower and reaches the equilibrium value of step a. Notice that magnetic moments are still aligned. d) The magnetic field is turned off causing the magnetic part of the entropy to rise and the lattice part to decrease. Finally the temperature of the material is lower than at the beginning a). From here on the material can be used for the performance of more cycles of cooling. . . . .	7
1.2	Schematic drawing of entropy change. . . . .	9
1.3	Periodic table of elements taken from [44]. . . . .	11
2.1	Schematic magnetization measurements performed at constant temperatures under varying the applied magnetic field. . . . .	13
2.2	Schematic drawing of a diffraction experiment. . . . .	14
2.3	Schematic drawing of scattering at two planes of atoms with respect to Bragg's law. . . . .	15
2.4	Schematic drawing of powder diffraction instrument. . . . .	17
2.5	Schematic drawing of a monochromator. . . . .	18
2.6	Schematic drawing of CW instrument used for powder diffraction. . . . .	18
2.7	Schematic drawing of TOF instrument used for powder diffraction. Reflections impinging on the detector bank are drawn at two different time frames. In the right part a spectrum of intensities of a pulse of neutrons as a function of wave length is illustrated. . . . .	19
2.8	Powder diffraction pattern performed on $Mn_{5-x}Fe_xSi_3$ , $x=0$ at 100 K with refinement. Red arrow points at line of difference pattern. . . . .	24
2.9	Scattering with illustration of the values $\vec{Q}$ , $\vec{q}$ , $\vec{k}_i$ and $\vec{k}_f$ . . . . .	25
2.10	Dispersion of one branch in defocussing (left) and focussing (right) mode. . . . .	26
3.1	Schematic picture of TOF instrument POWGEN at SNS Oak Ridge National Laboratory. Detectors are planned to be placed around the sample holder taken from [70]. . . . .	27
3.2	Technical layout of TOF-instrument POWGEN taken from [70]. . . . .	28
3.3	Proposed outgoing beam of neutron with (red) and without (black) using choppers. . . . .	28



3.4	Schematic picture of CW instrument HB2A at HFIR Oak Ridge National Laboratory taken from [71]. . . . .	29
3.5	Schematic picture of triple axis spectrometer 2T1 at LLB taken from [72]. . . . .	30
4.1	Technical layout of the KST taken from [73]. . . . .	32
4.2	Diffraction pattern taken on $Mn_{5-x}Fe_xSi_3$ $x=2$ with refinement. Si was used as reference. . . . .	33
4.3	Czochralski method for single crystal preparation taken from [76]. . . . .	34
5.1	RSO-magnetization measurements performed on $Mn_{5-x}Fe_xSi_3$ at 100Oe and 200Oe (only $Mn_{5-x}Fe_xSi_3$ $x=4$ ). Red arrows indicate points of phase transitions. . . . .	38
5.2	Phase diagram of $Mn_{5-x}Fe_xSi_3$ redetermined by magnetization measurements. . . . .	40
5.3	DC-magnetization measurements performed on $Mn_{5-x}Fe_xSi_3$ $x=4$ at 1T (left) and 2T (right). . . . .	41
5.4	Inverse susceptibilities with Curie-Weiss fits. . . . .	42
5.5	RSO-magnetization measurements performed on $Mn_{1-x}Co_xFe_4Si_3$ . Numbers in boxes in diagrams indicate applied fields when measurement was performed. . . . .	43
5.6	RSO-magnetization measurements performed on $MnFe_{4-x}Co_xSi_3$ . Numbers in boxes in diagrams indicate applied fields when measurement was performed. . . . .	44
5.7	VSM-magnetization measurements performed on sample $MnFe_{4-x}Co_xSi_3$ $x=0.5$ at applied fields of 0T and 140Oe. . . . .	45
6.1	MCE in $Mn_{5-x}Fe_xSi_3$ $x=0$ with $\Delta B=3T$ . Error bars are smaller than the points in the diagram. The line between points of measurement is only a guide to the eye. . . . .	48
6.2	MCE of $Mn_{5-x}Fe_xSi_3$ $x=4$ , $Mn_{1-x}Co_xFe_4Si_3$ and $MnFe_{4-x}Co_xSi_3$ and with $\Delta B=1T$ . Error bars are smaller than the points in the diagram. Lines between points of measurement are only guides to the eye. . . . .	49
6.3	MCE in dependence of number of electrons in one unit cell. Number of electrons of Si are not included. . . . .	50
7.1	Block with center of wave lengths CWL=1.066 of powder diffraction pattern performed on $Mn_{5-x}Fe_xSi_3$ $x=0$ at 100K with refinement. The intensity was normalized to the peak with the highest intensity. . . . .	53
7.2	Block with CWL=3.198 of powder diffraction pattern performed on $Mn_{5-x}Fe_xSi_3$ , $x=0$ at 100K with refinement. . . . .	54
7.3	Neutron powder diffraction pattern taken on $Mn_{5-x}Fe_xSi_3$ $x=0$ at 50K with a wave length of 2.41. A magnetic field of 4T was applied. . . . .	55
7.4	Block with center at $115^\circ$ of powder diffraction pattern of $Mn_{5-x}Fe_xSi_3$ $x=4$ taken at 300K with refinement. GOF-value of this block is 1.32. Stripes in the upper line marked with "phase 2" emerged from impurity (section 7.2.3). . . . .	57
7.5	Block with center at $85^\circ$ of powder diffraction pattern of $Mn_{5-x}Fe_xSi_3$ $x=4$ taken at 300K with refinement. GOF-value of this block is 1.08. . . . .	58
7.6	Block with center at $45^\circ$ of powder diffraction pattern of $Mn_{5-x}Fe_xSi_3$ $x=4$ taken at 300K with refinement. GOF-value of this block is 1.21. Left inset presents the part in d-spacing where "ghosting" reflections appeared in the patterns of the other two blocks. . . . .	59

---

7.7	GOF-values of refinements performed on diffraction patterns of $Mn_{5-x}Fe_xSi_3$ as function of $x$ and temperature. All diffraction patterns taken at 300K except $Mn_{5-x}Fe_xSi_3$ $x=3$ , which was taken at 270K. . . . .	61
7.8	Projection along the $c$ -axis of the unit cell of $Mn_{5-x}Fe_xSi_3$ for compositions $0 < x < 4$ . Black and red spheres represent Mn or Fe while silver spheres Si atoms, respectively. . . . .	62
7.9	From left to right: $1_{\infty}[\square(M2)_3]$ chains, $1_{\infty} [M1Si_3]$ chains and unit cell from above indicating the two chains. . . . .	63
7.10	Lattice constants $a$ and $c$ of $Mn_{5-x}Fe_xSi_3$ as function of $x$ . All taken from refinements on diffraction patterns taken at 300K except $Mn_{5-x}Fe_xSi_3$ $x=3$ , which was taken at 270K. Black lines are linear fits. The green curve is a guide to the eye. Colors of points in diagram refer to colors of marked lattice constants in unit cell in the inset. Error bars are smaller than points in diagram. . . . .	63
7.11	Volume and $c/a$ of $Mn_{5-x}Fe_xSi_3$ as function of $x$ . All taken from refinements on diffraction patterns taken at 300K except $Mn_{5-x}Fe_xSi_3$ $x=3$ , which was taken at 270K. The black line is a linear fit. The other two lines are only guides to the eye. . . . .	64
7.12	Occupations of Fe of the two atomic positions M1 and M2 in $Mn_{5-x}Fe_xSi_3$ as function of $x$ . All taken from refinements on diffraction patterns taken at 300K except $Mn_{5-x}Fe_xSi_3$ $x=3$ , which was taken at 270K. Inset presents the unit cell of these structures. Colors of points in diagram refer to colors of atoms in unit cell in the inset. Error bars are smaller than points in diagram. . . . .	65
7.13	Isotropic displacement parameters of $Mn_{5-x}Fe_xSi_3$ as function of $x$ . All taken from refinements on diffraction patterns taken at 300K except $Mn_{5-x}Fe_xSi_3$ $x=3$ , which was taken at 270K. Inset presents the unit cell of these structures. Colors of points in diagram refer to colors of atoms in unit cell in the inset. Lines between points of measurements are only guides to the eye. . . . .	66
7.14	Unit cell with magnetic moments applied parallel to $c$ -axis used as model for refinements on diffraction patterns taken on $Mn_{5-x}Fe_xSi_3$ $x=4$ . Atomic positions of Mn are denoted in both parts. . . . .	67
7.15	Magnetic unit cell of $Mn_{5-x}Fe_xSi_3$ $x=0$ extracted from refinement performed on diffraction pattern taken at 90K. . . . .	69
7.16	Magnetic unit cell of $Mn_{5-x}Fe_xSi_3$ $x=0$ extracted from refinement performed on diffraction pattern taken at 70K. . . . .	70
7.17	Magnetic unit cell of $Mn_{5-x}Fe_xSi_3$ $x=0$ extracted from refinement performed on diffraction pattern taken at 60K. The second atom on position M21 has disappeared due to the different space group in comparison to the unit cell at 70K 7.16. . . . .	70
7.18	Block with $CWL=1.066$ of powder diffraction pattern performed on $Mn_{5-x}Fe_xSi_3$ $x=0$ at 60K on POWGEN with refinement. . . . .	71
7.19	Block with $CWL=1.066$ of powder diffraction pattern performed on $Mn_{5-x}Fe_xSi_3$ $x=0$ at 50K on HB2A at an applied field of 4T with refinement. . . . .	72
7.20	Lattice constants $a$ and $c$ of $Mn_{5-x}Fe_xSi_3$ $x=4$ as function of temperature. Colors of points in diagram refer to colors of marked lattice constants in unit cell in the inset. Error bars are smaller than points in diagram. . . . .	76
7.21	Volume and $c/a$ of $Mn_{5-x}Fe_xSi_3$ $x=4$ as function of temperature. Error bars are smaller than points in diagram. . . . .	76

---

7.22	Derivatives of lattice constants of $\text{Mn}_{5-x}\text{Fe}_x\text{Si}_3$ $x=4$ as function of temperature. Lines between points in diagram are guides to the eye. Error bars are smaller than points in diagram. . . . .	77
7.23	Atomic displacement parameters of $\text{Mn}_{5-x}\text{Fe}_x\text{Si}_3$ $x=4$ as function of temperature. Colors of points in diagram refer to colors of atoms in unit cell in the inset. . . . .	77
7.24	Block with center at $45^\circ$ of powder diffraction pattern of $\text{Mn}_{5-x}\text{Fe}_x\text{Si}_3$ $x=4$ taken at 300K with refinement. Inset presents block with center at $45^\circ$ of powder diffraction pattern of $\text{Mn}_{5-x}\text{Fe}_x\text{Si}_3$ $x=4$ taken at 10K with refinement. Green arrows point at reflection (2-11). . . . .	79
7.25	Block with center at $45^\circ$ of powder diffraction pattern of $\text{Mn}_{5-x}\text{Fe}_x\text{Si}_3$ $x=4$ taken at 10K with refinement. Inset presents block with center at $45^\circ$ of powder diffraction pattern of $\text{Mn}_{5-x}\text{Fe}_x\text{Si}_3$ $x=4$ taken at 10K with refinement. No magnetic moments were applied in the used model. . . . .	80
7.26	Unit cell with magnetic moments applied parallel to $c$ -axis used as model for refinements on diffraction patterns taken on $\text{Mn}_{5-x}\text{Fe}_x\text{Si}_3$ $x=4$ . Black and red spheres represent Mn or Fe while silver spheres Si atoms, respectively. . . . .	81
7.27	Magnetic moments refined on atomic positions M1, M2 and the whole unit cell of $\text{Mn}_{5-x}\text{Fe}_x\text{Si}_3$ $x=4$ as function of temperature. Magnetic moments are applied parallel to the $c$ -axis. Colors of points in diagram refer to colors of atoms in unit cell in the inset. Blue points were excluded from fitting. The refined magnetic moments on site M1 are obviously not reliable. . . . .	82
7.28	Magnetic moment of the whole unit cell refined on atomic positions M1 and M2 and magnetization measurement performed on $\text{Mn}_{5-x}\text{Fe}_x\text{Si}_3$ $x=4$ as function of temperature. . . . .	84
7.29	Powder diffraction pattern of $\text{Mn}_{1-x}\text{Co}_x\text{Fe}_4\text{Si}_3$ $x=0.1$ taken at 310K with refinement. Green arrows in insets indicate peaks that do not fit to one of the three phases included in the model of the refinement. . . . .	88
7.30	Powder diffraction pattern of $\text{Mn}_{1-x}\text{Co}_x\text{Fe}_4\text{Si}_3$ $x=0.2$ taken at 310K with refinement. . . . .	89
7.31	Powder diffraction pattern of $\text{MnFe}_{4-x}\text{Co}_x\text{Si}_3$ $x=0.5$ taken at 310K with refinement. . . . .	90
7.32	Powder diffraction pattern of $\text{Mn}_{1-x}\text{Co}_x\text{Fe}_4\text{Si}_3$ $x=0.1$ taken at 310K with refinement and excluded regions. No impurities are included in the model. GOF-value is 3.4. . . . .	93
7.33	Powder diffraction pattern of $\text{MnFe}_{4-x}\text{Co}_x\text{Si}_3$ $x=0.2$ taken at 310K with refinement. . . . .	96
7.34	GOF-values of Co-doped materials as function of temperature. . . . .	97
7.35	Lattice constants $a$ (left) and $c$ (right) of Co-doped materials as function of temperature. Inset presents the unit cell of these structures. Colors of points in diagram refer to colors of marked lattice constants in unit cell in the inset. . . . .	99
7.36	Volume of Co-doped materials as function of temperature. . . . .	99
7.37	Volume of Co-doped materials as function of the number of electrons. . . . .	100
7.38	Value of $c/a$ of Co-doped materials as function of temperature. Lines are only guides to the eye. Lines between points of measurements are only guides to the eye. . . . .	100

---

7.39	Derivatives of lattice constants of $\text{Mn}_{1.009(7)}\text{Co}_{0.19(1)}\text{Fe}_{3.79(2)}\text{Si}_3$ as function of temperature. Lines between points in diagram are guides to the eye. . . . .	101
7.40	Derivatives of lattice constants of $\text{Mn}_{1.055(7)}\text{Co}_{0.40(1)}\text{Fe}_{3.54(2)}\text{Si}_3$ as function of temperature. Lines between points in diagram are guides to the eye. . . . .	102
7.41	Normalized content of Fe on M1 and M2 as function of Co content. Inset presents the unit cell of these structures. Colors of points in diagram refer to colors of atoms in unit cell in the inset. . . . .	103
7.42	Atomic displacement parameters of Co-doped materials as function of temperature. The inset denotes the atomic sites. Si is grey in the unit cell. . . . .	104
7.43	Magnetic moments M1 of Co-doped materials as function of temperature. . . . .	106
7.44	Magnetic moments of M2 Co-doped materials as function of temperature. . . . .	106
7.45	Magnetic moments of the unit cell of Co-doped materials as function of temperature. . . . .	107
7.46	Lattice constants $a$ and $c$ of Co-doped materials and $\text{Mn}_{5-x}\text{Fe}_x\text{Si}_3$ $x=4$ as function of the number of electrons in $(\text{Mn,Fe,Co})_5$ . All taken from refinements on diffraction patterns taken at 310K except $\text{Mn}_{5-x}\text{Fe}_x\text{Si}_3$ $x=4$ , which was taken at 300K. Colors of points in diagram refer to colors of marked lattice constants in unit cell in the inset. Error bars are smaller than points in diagram. Material that referring to a certain number of electrons can be taken from 7.47. . . . .	110
7.47	Volume and $c/a$ Co-doped materials and $\text{Mn}_{5-x}\text{Fe}_x\text{Si}_3$ $x=4$ as function of the number of electrons in $(\text{Mn,Fe,Co})_5$ . All taken from refinements on diffraction patterns taken at 310K except $\text{Mn}_{5-x}\text{Fe}_x\text{Si}_3$ $x=4$ , which was taken at 300K. Error bars are smaller than points in diagram. . . . .	111
7.48	Isotropic displacement parameters of Co-doped materials and $\text{Mn}_{5-x}\text{Fe}_x\text{Si}_3$ $x=4$ as function of the number of electrons in $(\text{Mn,Fe,Co})_5$ . All taken from refinements on diffraction patterns taken at 310K except $\text{Mn}_{5-x}\text{Fe}_x\text{Si}_3$ $x=4$ , which was taken at 300K. Inset presents the unit cell of these structures. Colors of points in diagram refer to colors of atoms in unit cell in the inset. Material that referring to a certain number of electrons can be taken from 7.47. . . . .	112
8.1	Brillouin zone with with scan directions (solid green lines). Red arrows indicated directions in $k$ -space. . . . .	115
8.2	Constant Q-scan performed on $(4,0,0.5)$ with and without sample in Q-space. . . . .	116
8.3	Q-scan $(x,0,0)$ performed at $E=3\text{meV}$ in order to detect the accoustical phonon. . . . .	117
8.4	Constant Q-scan performed on $(0,0,2.4)$ in Q-space. . . . .	118
8.5	Constant Q-scan performed on $(4,0,0.4)$ in Q-space. . . . .	118
8.6	Constant Q-scan performed on $(4,0,0.1)$ in Q-space. . . . .	119
8.7	Intensities of peaks fitted in transvere configurations. . . . .	119
8.8	Constant Q-scan performed on $(4,0,0.2)$ in Q-space. . . . .	120
8.9	Constant Q-scan performed on $(2,0,0.2)$ in Q-space. . . . .	120
8.10	Dispersion relation of $\text{Mn}_{5-x}\text{Fe}_x\text{Si}_3$ $x=4$ extracted from inelastic neutron scattering data. . . . .	123
8.11	Magnetic unit cell of $\text{Mn}_{5-x}\text{Fe}_x\text{Si}_3$ $x=4$ with green bars indicating magnetic exchange which was considered for the model. Interactions in plane similar to the pink line were not considered. . . . .	124

---

8.12	Dispersion relation of the magnon in $Mn_{5-x}Fe_xSi_3$ $x=4$ with fit of polynom of second degree. The formula of the the fitted polynom is $e = 6(3) - 6(5) \cdot 10^6 \cdot (1 - \cos(0.5x)) + 2(2) \cdot 10^7 \cdot (1 - \cos(0.25x))$ . . . . .	124
10.1	Dispersion relation of $Mn_{5-x}Fe_xSi_3$ $x=4$ . The brown circle marks points where a magnon branch crosses a phonon brnach. . . . .	131
A.1	Magnetization measurement performed at an applied field of 100Oe with derivative. The blue arrow indicates the point of phase transition. . . . .	139
A.2	Inverse susceptibility of $Mn_{5-x}Fe_xSi_3$ $x=0$ with Curie-Weiss fit. . . . .	140
A.3	Block with center at $115^\circ$ of powder diffraction pattern of $Mn_{5-x}Fe_xSi_3$ $x=1$ taken at 300 K with refinement. GOF-value of this block is 0.99. . . . .	141
A.4	Block with center at $85^\circ$ of powder diffraction pattern of $Mn_{5-x}Fe_xSi_3$ $x=2$ taken at 300 K with refinement. GOF-value of this block is 1.04. . . . .	142
A.5	Block with center at $45^\circ$ of powder diffraction pattern of $Mn_{5-x}Fe_xSi_3$ $x=3$ taken at 270 K with refinement. GOF-value of this block is 1.21. . . . .	143
A.6	Part of block with center at $115^\circ$ of powder diffraction pattern of $Mn_{5-x}Fe_xSi_3$ $x=4$ taken at 300 K with refinement. Ghosting peaks appear at $d=1.21$ and $d=1.22$ . 144	
A.7	Part of block with center at $85^\circ$ of powder diffraction pattern of $Mn_{5-x}Fe_xSi_3$ $x=3$ taken at 300 K with refinement. Ghosting peaks appear at $d=1.21$ and $d=1.22$ . 144	
A.8	Part of block with center at $45^\circ$ of powder diffraction pattern of $Mn_{5-x}Fe_xSi_3$ $x=3$ taken at 300 K with refinement. No ghosting peaks in this diffraction pattern. 145	

# Appendix D

## List of Tables

2.1	Parameters of formula used for transformation from t- to d-spacing in Jana2006 and FullProf. . . . .	20
2.2	Influence of parameters of the model of the Rietveld refinement of reflections. . . . .	23
4.1	Weights of elements used for preparation. . . . .	33
5.1	Temperatures of phase transition determined with derivatives of magnetization measurements performed for this thesis (Diss) and proposed temperatures of phase transitions in publications of sample $Mn_{5-x}Fe_xSi_3$ $x=0$ . . . . .	39
5.2	Curie constants $C$ , Weiss temperatures $\Theta$ and effective magnetic moments $\mu_{eff}$ for $Mn_{5-x}Fe_xSi_3$ $x=0,1,2,3$ . . . . .	43
7.1	Details of instrumental setups for the various measurements. . . . .	52
7.2	Excluded regions defined in t-spacing used on every diffraction pattern taken on $x>0$ consisting of the three blocks. . . . .	56
7.3	Comparing results of refinements of non-impurity compounds when phases of impurities are included (first one, marked with Y) and not included (second one, marked with N) in the refinement. Conducted on data taken on sample $Mn_{5-x}Fe_xSi_3$ $x=4$ at 270K. . . . .	60
7.4	Multiplicities and Wyckoff letter of atoms in hexagonal space group $P6_3/mcm$ (193) of samples $Mn_{5-x}Fe_xSi_3$ [28, 88]. Name is reference which is used from now on for atoms occupying the corresponding Wyckoff position. . . . .	61
7.5	Lattice constants $a$ and $c$ , occupation of Fe on M1 and M2, $x(M2)$ , $x(Si)$ of $Mn_{5-x}Fe_xSi_3$ as function of $x$ . All taken from refinements on diffraction patterns at 300K and 270K just for $x=3$ . . . . .	67
7.6	Refined atomic parameters. . . . .	68
7.7	Refined atomic parameters at 60K. . . . .	74
7.8	Refined atomic parameters at 50K. . . . .	74
7.9	Refined atomic parameters at 40K. . . . .	74
7.10	Refined atomic parameters at 30K. . . . .	75
7.11	Refined atomic parameters at 12K. . . . .	75
7.12	Refined atomic parameters and GOF-values of two refinements both performed on a diffraction pattern taken on $Mn_{5-x}Fe_xSi_3$ $x=4$ at 10K. First column indicates if magnetism was applied on M1 ("Y") or not ("N"). . . . .	78
7.13	$T_C$ , $m_{sat}$ and $\beta$ , all extracted from the refined magnetic moments. . . . .	83

7.14	Refined atomic parameters and GOF-values of two refinements both performed on a diffraction pattern taken on $Mn_{5-x}Fe_xSi_3$ $x=4$ at 270K. First column indicates if magnetism was applied on M1 ("Y") or not ("N"). . . . .	84
7.15	Refined atomic parameters and GOF-values. . . . .	85
7.16	Samples and temperatures at which measurements were taken. Ranges between 0.56 and 4.24 were covered in all diffraction patterns . . . . .	86
7.17	Total number of refined parameters used in refinements performed on data taken at mentioned temperatures. . . . .	87
7.18	Comparing results of refinements of base (non-impurity) compounds when phases of impurities are included (marked with Y) and not included (marked with N) in the refinement. Refinements were conducted on data taken at 310K. . . . .	92
7.19	Refined atomic occupations of the base compounds. . . . .	94
7.20	Refined atomic occupations of all compounds including impurities. Phases of base compounds are marked in bold. . . . .	95
7.21	Refined atomic occupations of all compounds including impurities. Phases of base compounds are marked in bold. . . . .	95
7.22	Total observed contents of elements Mn, Co, Fe and Si in the samples (including impurities). . . . .	95
7.23	Total expected contents of elements Mn, Co, Fe and Si in the samples (including impurities). . . . .	95
7.24	Multiplicities and wyckoff letter of atoms of Co-doped samples. . . . .	98
7.25	$T_C$ , $m_{sat}$ and $\beta$ , all extracted from magnetic moments on M2. . . . .	107
7.26	$T_C$ , $m_{sat}$ and $\beta$ , all extracted from magnetic moments of the whole unit cell. . .	108
7.27	Refined atomic parameters and GOF-values. . . . .	109
A.1	Parameters of formula used for transformation from t- to d-spacing in Jana2006 and FullProf. . . . .	137

---

## Curriculum Vitae

- Family name: Gottschlich, Given name: Michael
- Male
- Born: September 11th, 1982; Köln, Deutschland
- Nationality: German
- Abitur: 2002
- Lehramt (physics and mathematics): 2002
- Diplom (physics): 2003-2009
- PhD: 2009-2013
- e-mail: [micha.gottschlich@yahoo.com](mailto:micha.gottschlich@yahoo.com)

### Publications (as first author)

- Study of the antiferromagnetism of  $Mn_5Si_3$ : an inverse magnetocaloric effect material, M.Gottschlich, O. Gourdon, J. Persson, C. d.l. Cruz, Vaclav Petricek and T. Brueckel, *J.mater.Chem.*, 22, 15275, 2012

### Conference talks

- Gottschlich, M.; Gourdon, O.; Ohl, M.; Brückel, T.; Perßon, J., Experimental and theoretical studies of the Magnetocaloric Effect (MCE) in the  $Mn_{5-x}Fe_xSi_3$  series, 75. Jahrestagung der DPG und DPG Frühjahrstagung, Dresden, 13.03.2011 - 18.03.2011
- Gottschlich, M.; Gourdon, O.; Ohl, M.; Persson, J.; Brückel, T., Experimental and Theoretical Studies of the Magnetocaloric Effect (MCE) in the  $Mn_{5-x}Fe_xSi_3$  Series, Konferenz der "American Crystallographic Association", Chicago, USA, 24.06.2010 - 29.06.2010

### Posters

- Gottschlich, M.; Gourdon, O.; Ohl, M.; Perßon, J.; Brückel, T., Experimental and theoretical studies of the Magnetocaloric Effect (MCE) in the  $Mn_{5-x}Fe_xSi_3$  series, 5th European Conference On Neutron Scattering, Prag, Tschechische Republik, 17.07.2011 - 22.07.2011
- Gottschlich, M., Experimental and theoretical studies of the magnetocaloric effect (MCE) in the  $Mn_5-xFe_xSi_3$  series International Conference "Neutrons for Global Energy Solutions" NGES 2010, Bonn, Germany, 26.09.2010 - 30.09.2010
- Gottschlich, M.; Gourdon, O.; Ohl, M.; Persson, J.; Brückel, T., Experimental and theoretical studies of the Magnetocaloric Effect (MCE) in the  $Mn_{5-x}Fe_xSi_3$  series, American Conference on Neutron Scattering, Ottawa, 26.06.2010 - 30.06.2010





Band / Volume 49

**Study of Molecule-Metal Interfaces by Means of the Normal Incidence  
X-ray Standing Wave Technique**

G. Mercurio (2012), XXII, 361 pp

ISBN: 978-3-89336-816-7

Band / Volume 50

**5th Georgian-German School and Workshop in Basic Science**

Tbilisi, Georgia/August 6 – 10, 2012. Batumi, Georgia/August 13 – 17, 2012.

Org. Committee: E. Abrosimova, A. Bakuridze, A. Kacharava, A. Kvitashvili, A. Prangishvili, H. Ströher (2012); CD-ROM

ISBN: 978-3-89336-818-1

Band / Volume 51

**Exploring the electronic properties of novel spintronic materials  
by photoelectron spectroscopy**

A. Herdt (2012), ii, 126 pp

ISBN: 978-3-89336-831-0

Band / Volume 52

**Quantum Information Processing**

Lecture Notes of the 44<sup>th</sup> IFF Spring School 2013

February 25 – March 8, 2013 Jülich, Germany

D. DiVincenzo (Ed.) ca. 1000 pp

ISBN: 978-3-89336-833-4

Band / Volume 53

**Real-Space Finite-Difference PAW Method for Large-Scale Applications  
on Massively Parallel Computers**

P.F. Baumeister (2012), vi, 212 pp

ISBN: 978-3-89336-836-5

Band / Volume 54

**Einfluss unkonventioneller Medien auf die  
Selektivität ThDP-abhängiger Enzyme**

T. Gerhards (2013), XIV, 199 pp

ISBN: 978-3-89336-846-4

Band / Volume 55

**Aufbau einer Vierspitzen-  
Rastertunnelmikroskop/Rasterelektronenmikroskop-Kombination  
und Leitfähigkeitsmessungen an Silizid Nanodrähten**

E. Zubkov (2013), 150 pp

ISBN: 978-3-89336-848-8

Band / Volume 56

**Interplay between magnetic and dielectric phenomena  
at transition metal oxide interfaces**

D. Schumacher (2013), IV, 128 pp

ISBN: 978-3-89336-855-6

Band / Volume 57

**Single NdPc<sub>2</sub> Molecules on Surfaces:  
Adsorption, Interaction, and Molecular Magnetism**

S. Fahrenndorf (2013), viii, 100 pp

ISBN: 978-3-89336-856-3

Band / Volume 58

**Heyd-Scuseria-Ernzerhof Screened-Exchange Hybrid Functional for  
Complex Materials: All-Electron Implementation and Application**

M. Schlipf (2013), XV, 170 pp

ISBN: 978-3-89336-857-0

Band / Volume 59

**Orbital-dependent exchange-correlation functionals in density-functional  
theory realized by the FLAPW method**

M. Betzinger (2013), vi, 173 pp

ISBN: 978-3-89336-858-7

Band / Volume 60

**Structural influences on electrical transport in nanostructures**

R. D. Frielinghaus (2013), viii, 190 pp

ISBN: 978-3-89336-867-9

Band / Volume 61

**Study of intermolecular interactions in hetero-organic thin films**

B. Stadtmüller (2013), viii, 198 pp

ISBN: 978-3-89336-871-6

Band / Volume 62

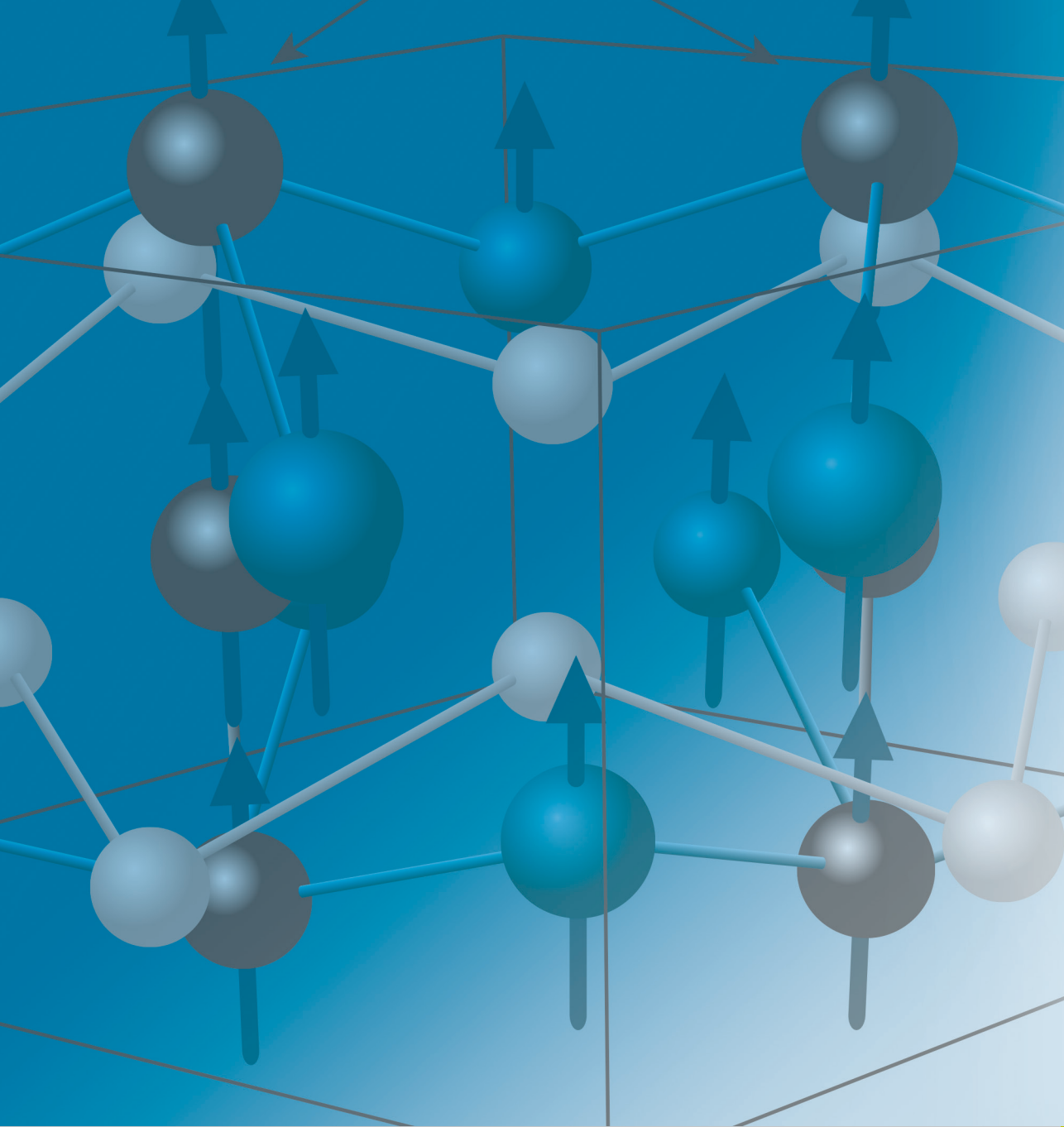
**Structure, magnetism and excitations in some  
Mn-based magnetocaloric effect compounds**

M. Gottschlich (2013), 175 pp

ISBN: 978-3-89336-874-7

Weitere **Schriften des Verlags im Forschungszentrum Jülich** unter  
<http://wwwzb1.fz-juelich.de/verlagextern1/index.asp>





**Schlüsseltechnologien / Key Technologies**  
**Band / Volume 62**  
**ISBN 978-3-89336-874-7**

